

ADHESION AND COHESION PROPERTIES OF DIAMOND-LIKE-CARBON COATINGS DEPOSITED ON BIOMATERIALS BY SADDLE FIELD NEUTRAL FAST ATOM BEAM SOURCE; MEASUREMENT AND MODELLING

A Thesis

Submitted to the Faculty of Engineering and Design, School of Mechanical and Manufacturing Engineering of Dublin City University
For the Degree of Doctor of Philosophy

By

Muhammad Monjur Morshed, B.Sc. Eng., M.Sc. Eng.

Materials Processing Research Centre and
National Centre for Plasma Science and Technology
Dublin City University



Research Supervisors

Dr. Brian P. McNamara

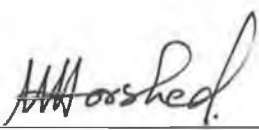
Professor David C. Cameron (B.Sc., Ph.D., CEng., MIEE)

Professor M. S. J. Hashmi (Ph.D., D.Sc., CEng., FIMechE., FIEI, MASME)

September 2003

DECLARATION

I hereby certify that this material, which I now submit for assesment on the programme of study leading to the award of Doctor of Philosophy is entirely my own work and has not been taken from the work of others save and to the extent that such work has been cited and acknowledged within the text of my work.

Signed: 

(Muhammad Monjur Morshed)

Student ID No.: 99144972

Date: 25-09-2003

ACKNOWLEDGEMENTS

My first vote of thanks must go to Dr. Brian P. McNamara, a man whom I have the greatest respect and admiration. His guidance and supervision were invaluable. I am extremely grateful for all advice and suggestions towards solving the problems. I am privileged to have worked with him. I also thank him sincerely for facilitating my entrance to the field of "Thin Film Technology".

I would like to thank Professor David Cameron for his unceasing enthusiasm, interest, constructive criticism and practical hand on assistance with the vacuum system and for putting up with me over the years. His expertise, availability to discuss ideas and willingness to give of his knowledge were instrumental in the completion of this thesis. I owe him much gratitude.

I will be forever indebted to Professor M. S. J. Hashmi who not only funded my project but also supported me unstintingly. Without his support and encouragement this research would not have been done.

My gratitude also extended to Dr. Bryan MacDonald for always making himself available to offer advice and to discuss the ideas about Finite Element Analysis (FEA).

I would also like to acknowledge our technicians Mr. Michael Tyrrell, Mr. Michael May, Mr. Christopher Crouch, Mr. Keith Hickey and Mr. Liam Domican. Special thanks to Mr. Michael Tyrrell and Mr. Michael May for their regular support.

Thanks are very much owing to Dr. Enda McGlynn, School of Physical Sciences, DCU and Dr. Patrick McNally, School of Electronic Engineering, DCU for assistance with the Raman and Micro Raman spectroscopy, Ger Insley of Styker Osteonics Howmedica, Limerick for adhesion testing and William F. Brennan, National Centre for Biomedical Engineering Science, NUI, Galway for nanohardness testing.

I am also grateful to Professor Ehsanul Haque (MME, BUET) and Professor Mizanur Rahman (IPE, BUET) who were selected me from the Department of Materials and

Metallurgical Engineering, BUET, Dhaka, Bangladesh for doing research in DCU. Thanks to my Masters supervisor Professor A. S. M. A. Haseeb (MME, BUET) for giving me knowledge about thesis and research paper writing. I would like to thanks Professor Mohiuddin Ahmed (IPE, BUET) for his assistance in coming to Ireland.

Many others friend and colleagues at this time in no particular order include Dr. Lisa Looney, Dr. Dermot Brabazon, Michelle Considine, Martina Reddy and a number of Bangladeshi students.

My most sincere gratitude is extended to my family, especially my mother, beloved father, and wife "Sumsun Naher" who have given their utmost support to all that I have tried to do. I can not ever repay them enough. Thanks for always encouraging me to learn and I hope there's room in the family for one more doctorate. Thanks are due to my sisters and nephew who continually inspired me from the family. Special thanks are due to my brothers in law Principal Khalilur Rahman and Mr. Shamsur Rahman who always supported me in every respect. I owe them a lot.

There are many, many unnamed individuals who have contributed in major and minor ways to this work. Thanks are due to them.

DEDICATION

*This Thesis is Dedicated to
My Beloved Father, Mother and Son
Mufid*

LIST OF ABBREVIATIONS

BWF	Breit-Wigner-Fano
CVD	Chemical Vapour Deposition
DC	Direct Current
DLC	Diamond Like Carbon
DCU	Dublin City University
ECR	Electron Cyclotron Resonance
ECWR	Electron Cyclotron Wave Resonance
EELS	Electron Energy Loss Spectroscopy
FAB	Fast Atom Beam
FCVA	Filtered Cathodic Vacuum Arc
FEA	Finite Element Analysis
FPB	Four Point Bend
FTIR	Fourier Transform Infrared Spectroscopy
FWHM	Full Width Half Maximum
GUI	Graphical User Interface
HPHT	High Pressure High Temperature
IR	Infrared Spectroscopy
KV	Kilo Volt
LVDT	Load Versus Displacement Technique
MSIB	Mass Selected Ion Beam
NEXAFS	Near Edge X-ray Absorption Fine Structure
NMR	Nuclear Magnetic Resonance
PBS	Plasma Beam Source
PECVD	Plasma Enhance Chemical Vapour Deposition
PLD	Pulsed Laser Deposition
PVD	Physical Vapour Deposition
RF	Radio Frequency
RH	Relative Humidity
RIE	Reactive Ion Etching
SEM	Scanning Electron Microscope
TEM	Transmission Electron Microscope
UHMWPE	Ultra High Molecular Weight Polyethylene
UV Raman	Ultra Violet Raman
VDOS	Vibrational Density Of State
XRD	X-Ray Diffraction

ADHESION AND COHESION PROPERTIES OF DIAMOND-LIKE-CARBON COATINGS DEPOSITED ON BIOMATERIALS BY SADDLE FIELD NEUTRAL FAST ATOM BEAM SOURCE; MEASUREMENT AND MODELLING

ABSTRACT

Muhammad Monjur Morshed, B.Sc. Eng., M.Sc. Eng.

Diamond-like-carbon (DLC) has been shown to be strategically important in respect to biomedical applications due to its biocompatibility. Despite decades of work on film deposition there is an insufficient understanding in respect of the film's adhesion characteristics, particularly on biomaterial substrates. The central aim of this study is two pronged. A programme of work has been undertaken to set-up, study, understand and optimise the production technique for DLC deposition, while on the other hand diamond like carbon films have been characterised to investigate the strength of adhesion and cohesive strength with particular reference to biomedical applications.

DLC films have been deposited on to substrates of 316L stainless steel, cobalt chrome (CoCr) and Ti6Al4V alloy using a saddle field neutral beam deposition system (Microvac 1200DB, Ion Tech Ltd) with acetylene and acetylene-argon mixture as the process gas. It is noted that numerous parameters influence coating adhesion including the stress in the film, contamination and chemical bonding between the film and the substrate, and the physical properties and roughness of the substrate. Discharge current vs. discharge voltage characteristics were investigated with different pressure and process gas. Uv absorption spectra were used to measure the photon energy and optical band gap of the films. The optical band gap was found in the range of ~0.85 and 0.85 -0.97 eV for lower and higher deposition current respectively. The adhesion of the films has been measured as a function of the duration of *in-situ* etching by a neutral argon beam and also as a function of source current, system pressure and process gas (pure C₂H₂ and C₂H₂+Ar gas mixture). The studies were performed on DLC films with thickness ~0.4 μm. The adhesion of the film was measured using pull-off and Rockwell C tests whereas four point bend (FPB) test was used to measure the cohesive strength of the films. Argon pre etching for 15 minutes is recommended to guarantee an optimal adhesion. The etching process also influenced the film structure in terms of the sp³/sp² ratio and stress. It was also found that this optimisation of the adhesion is correlated with a change in the structure and thickness of the native oxide layer on the steel surface of the

substrates. Substrate surface temperature during etching and deposition also influenced film structure and adhesion. Correlation between the residual stress and the adhesion of the films has also been established which helped to identify optimum process parameters for substrate-film adhesion properties. No significant change with deposition pressure has been observed but high anode currents may lead to higher sp^3 content. The adhesion strength has been found to be inversely proportional to residual stress and to increase at low deposition pressures. At source anode current of 0.6A, the adhesion is a monotonic function of pressure in the range examined where as with 1.0A source current the behaviour is more complex. The relationship between the stress and the sp^3 content of the films measured by analysis of Raman signature has also been investigated.

The experimental work of FPB has been used to support and develop a numerical (Finite Element) model for the determination and prediction of the film's cohesive strength. The model takes into account the film hardness, Young's modulus and thickness and has been shown to be capable of predicting the film's cohesive strength when combined with a theoretical formulation for brittle fracture. It has been observed that maximum stress developed at the outer surface of film during the bend test, which influenced the initiation of cracks at the outer surface of the film and their propagation through the film-substrate interface. This result has only been valid for films with higher Young's modulus compared with the substrate.

CONTENTS

Section No.	Description	Page No.
Declaration		i
Acknowledgements		ii
Dedication		iv
List of Abbreviations		v
Abstract		vi
Contents		viii

Chapter 1 Introduction

1.1 Introduction	1
------------------	---

Chapter 2 Synthesis of Diamond and Diamond Like Carbon Coatings and Surface Science

2.1 Introduction	4
2.1.1 The Geology of Diamond	4
2.2 Carbon as an Allotrope Element	6
2.2.1 Introduction	6
2.2.2 Hybridization	7
2.2.3 Hybridization Theory of Atomic Orbital	8
2.3 Synthesis of Diamond Films	14
2.4 Synthesis of Diamond Like Carbon Films	15
2.4.1 Introduction	15
2.4.2 DLC Films by Sputtering of a Solid Carbon Target	16
2.4.2.1 <i>Ion Beam Enhanced Deposition</i>	16
2.4.2.2 <i>Laser-Arc Assisted Deposition</i>	17
2.4.2.3 <i>Mass-Selected Ion Beam Deposition</i>	18
2.4.2.4 <i>Sputtering</i>	19
2.4.2.5 <i>Cathodic Arc</i>	20
2.4.3 DLC Films by Dissociation of Gaseous Hydrocarbon Source	22
2.4.3.1 <i>PECVD</i>	22
2.4.3.2 <i>RF Plasma-Assisted Deposition</i>	28
2.4.3.3 <i>Microwave and ECR-Assisted Discharges</i>	29
2.4.3.4 <i>Saddle Field Fast Atom Beam</i>	30
2.5 Surface Science	30
2.5.1 Surface Adsorption and Contamination	31
2.5.2 Surface Reactions	31
2.5.3 Growth Laws for Surface Films	32

2.6 Substrate Surface Polishing	34
2.6.1 Introduction	34
2.6.2 Polishing Methods	35
2.6.2.1 <i>Mechanical Polishing</i>	35
2.7 Substrate Cleaning	36
2.7.1 Solvent Cleaning	36
2.7.2 Glow Discharge Cleaning	37
2.7.3 Other Cleaning Methods	37

Chapter 3

Properties, Applications and Characterisation Techniques of Diamond and Diamond Like Carbon Coatings

3.1 Introduction	39
3.2 Properties of Diamond and DLC Coatings	39
3.2.1 Diamond Like Carbon Films	39
3.2.2 Diamond Films	41
3.3 Generation of Residual Stress	42
3.3.1 The Stoney Formula	42
3.3.2 Intrinsic Residual Stress	45
3.3.3 Thermal Residual Stress	46
3.4 Measurement of Residual Stress in Coating	47
3.4.1 Bending Beam Method	48
3.4.2 Bulge Test	48
3.4.3 X-Ray Diffraction Method	50
3.4.4 Raman Spectroscopy	50
3.5 Separation of Intrinsic and Thermal Stresses	51
3.6 Adhesion of Thin Films	53
3.6.1 Introduction	53
3.6.2 Measurement of Adhesion of Coatings	54
3.6.2.1 Mechanical Methods	55
3.6.2.1.1 <i>Tensile Type Test</i>	55
3.6.2.1.2 <i>Shear Type Test</i>	57
3.6.2.1.3 <i>Scratch Test</i>	57
3.6.2.1.4 <i>Indentation Type Test</i>	58
3.6.2.1.5 <i>Substrate Plastic Straining Test</i>	58
3.6.2.2 Pulse Laser Method	60
3.6.2.3 Nucleation Method	60
3.7 Film Thickness	60
3.7.1 Stylus Instruments	61
3.8 Film Hardness	62
3.8.1 Nanoindentation	62
3.8.2 Hardness and Elastic Modulus Measurement	64
3.9 Atomic Structure and Characterisation	69
3.9.1 Bonding	69

3.9.2 Raman Spectroscopy	71
3.10 Biomedical Application of Biomaterials, DLC and Diamond	79
3.10.1 Biomaterials	79
3.10.2 Biocompatibility of DLC	80
3.10.3 Diamond Like Carbon and Diamond	81
3.10.4 Environmental Stability of Coatings	83
3.11 Summary	84

Chapter 4

DLC Deposition Equipment

4.1 Introduction	86
4.2 History	86
4.3 Pump Down Chamber	86
4.4 Coating Equipment	86
4.5 Fast Atom Beam (FAB)	88
4.6 Evaluation of FAB Source	90
4.7 Beam Neutralisation	92
4.8 Advantage of Saddle Field Source	94

Chapter 5

Experimental Procedure

5.1 Introduction	96
5.2 Materials Used	96
5.3 Sample Preparation	96
5.4 Current-Voltage (A_c - A_v) Characteristics	97
5.5 UV Absorption of DLC Films	97
5.6 DLC Films Deposition on Implant Metals	97
5.7 Physical and Mechanical Characterisations	98
5.7.1 Film Density	98
5.7.2 Film Thickness	99
5.7.3 Determination of Stress in Films	99
5.7.4 Determination of Films Adhesion	100
5.7.4.1 <i>Pull-off Adhesion</i>	100
5.7.4.2 <i>Rockwell C Adhesion</i>	100
5.7.5 Determination of Film Hardness and Young's Modulus	100
5.8 Determination of Bonding Structure of Films	101
5.8.1 Raman Spectroscopy	101

Chapter 6

Results and Discussion

6.1 Current vs. Voltage Characteristics	102
6.2 UV Absorption Spectra	104
6.3 Effect of Process Parameters	109
6.3.1 Deposition Rate	110

6.3.2 Raman Spectroscopy	111
6.3.3 Films Stress and Adhesion	114
6.3.4 Films Hardness and Young's Modulus	118
6.4 Effect of Surface Treatment of 316L Stainless Steel	120
6.4.1 Raman Spectroscopy	120
6.4.2 Films Stress and Adhesion	121
6.4.3 FTIR	126
6.5 Effect of Surface Treatment of 316L Stainless Steel, Cobalt Chrome (CoCr) and Ti6Al4V Alloys	128
6.5.1 Raman Spectroscopy	128
6.5.2 Adhesion	129
6.5.3 Effect of Temperature	131

Chapter 7

Modelling for Cohesive Strength of DLC Thin Film

7.1 Finite Element Analysis (FEA)	136
7.2 Engineering Problems	137
7.3 Numerical Method	137
7.4 Steps in the Finite Element Method	138
7.5 Four Point Bend Test (FPB)	139
7.5.1 Theoretical Background of Four Point Bend Test	139
7.6 Experimental Procedure	143
7.7 Results and Discussion	143
7.8 Study of the Stress Distribution Across the Coating Thickness by FEA	146
7.9 Results and Discussion	150

Chapter 8

Conclusions and Recommendation

8.1 Conclusions	158
8.1.1 Current vs. Voltage (A_c - A_v) Characteristics	159
8.1.2 UV Absorption of DLC Films	159
8.1.3 Effect of Process Parameters	159
8.1.4 Effect of Surface Treatment of 316L Stainless Steel	160
8.1.5 Effect of Surface Treatment of 316L stainless steel, Cobalt Chrome (CoCr) and Ti6Al4V Alloys	160
8.1.6 Finite Element Analysis	161
8.2 Recommendation and Future Work	161
References	R-1
Publications	P-1

Appendix

Appendix A1	A-1
Appendix A2	A-2
Appendix A3	A-3

Chapter 1

Introduction

1.1 Introduction

Amorphous carbon thin film technology is an expanding area of materials research due to the achievement of a unique combination of chemical, electrical, optical and mechanical properties [1]. For example, the high surface smoothness, high hardness and chemical inertness, in combination with low co-efficient of friction make the diamond like carbon (DLC) sub-group ideal candidates for wear protective applications, for optical components [2], metalworking tool [3] and biomedical prostheses [4]. Despite the success of the modern prosthetic hip device, the biomedical engineering community still recognises the need to improve the all-round performance of these implants. Loosening of the device is, to date, the most common reason for prosthesis failure and tends to be mediated through the production of wear debris from the main articulating surfaces [5]. Consequently, there has been a great deal of interest expressed in applying the excellent mechanical properties of diamond like carbon to improve the wear resistance of these devices. The superior adhesion, wear resistance and batch to batch consistency of these coatings make their use an attractive option. The demonstration that DLC can be grown at low temperatures and pressures has engendered a great deal of research world-wide. DLC films deposited at low temperatures do not suffer from thermally induced stress, neither do they have open corrosion paths like polycrystalline CVD or porous ceramics films [6]. It is known that numerous parameters have an influence on coating adhesion including stress in the film, contamination and chemical bonding between the film and the substrate, and the physical properties and roughness of the substrate [7]. A key mechanical characteristic to be evaluated is the adhesive strength of the film-substrate composite. Several methods are used, such as scratch test, pull-off test and Rockwell test. However, sometime they provide contradictory results.

Objective of the Present Study

The central aim of this project is concerned with the deposition of DLC thin film on biomaterial substrates (316L stainless steel, CoCr alloy and Ti6Al4V alloy) and evaluation of their chemical and mechanical characteristics. In particular, the study is intended to identify optimum process parameters for enhancement of substrate-film adhesion as well as cohesive properties. The experimental work is coupled with numerical analysis to identify interface stress magnitudes as a function of cohesive characteristic. The outcome

of this study is expected to provide a scientific basis for the production of well-adhered thin film on bioengineering materials.

A number of process including magnetron sputtering, laser ablation, chemical vapour deposition (CVD) and physical vapour deposition (PVD) have been applied to produce this film. This project focuses on the deposition of DLC films using a neutral beam saddle field source (Microvac 1200DB, Ion Tech Ltd.) and a low temperature deposition process that is a plasma enhanced chemical vapour deposition (PECVD) technique. Films have been prepared by introducing pure hydrocarbon gas (acetylene: C_2H_2) and an argon-acetylene gas mixture directly into the ionisation source. The saddle field source is suited to this application as the internal walls are carbon clad which minimise any contamination due to internal sputtering. The electrode configuration in the DC energised, cold-cathode source is such that the resulting electrostatic field confines electrons to long oscillatory paths, thereby increasing the efficiency of ionisation. The use of saddle field sources makes it possible to coat substrates with DLC either on a small scale in a conventional research vacuum system or in large production systems. Pressures in the range of 1.5×10^{-3} to 4.8×10^{-3} mbar with the substrate held near room temperature are used in this study.

One problem in DLC synthesis is the inadequate adhesion of many substrates. Relevant to this is the generation of residual stresses in the film. Residual stress is the main cause for spontaneous failure at the interface (debonding) and must be controlled. The reasons for deposition stress generation and ways to control it are still being investigated. For the above reasons, a saddle field fast atom source (FAB) rig was set up to study the effect of deposition parameters on the morphology and residual stress generated in DLC films deposited on biomaterials. Residual stresses in the DLC films have been obtained from the curvature of substrate before and after deposition. The effect of substrate treatment and its influence on the film structure in terms of sp^3/sp^2 ratio, film stress and adhesion has also been investigated. Correlation between the residual stress and the adhesion with various deposition parameters of the films has also been established which helped to identify optimum process parameters for substrate-film adhesion properties.

A method to determine the cohesive strength of the film using a four point bending test technique has also been developed. This facility is simple and quick in determining the films' cohesive strength. Film density, hardness and Young's modulus have also been

determined. This experimental work has been used to support and develop a numerical model (Finite Element) for the determination and prediction of film and film-substrate interface stress. The model has taken into account the film hardness, Young's modulus and thickness and has been shown to be capable of predicting the film's cohesive strength when combined with brittle fracture. These optimised process parameters may provide a good stepping stone for further research in this area.

This thesis contains eight chapters. Those are accordingly,

1. Introduction.
2. Synthesis of diamond and diamond like coating and surface science.
3. Properties, application and characterisation techniques of diamond and diamond like coating.
4. DLC deposition equipment.
5. Experimental procedure.
6. Results and discussion.
7. Modelling for cohesive strength of DLC film and
8. Conclusion.

The first chapter deals with the introduction to the objective of the present work. Chapter 2 and 3 are the literature review carried out for this research include the topic of DLC fabrication methods, materials selection, surface science and mechanical properties, application and characterisation techniques. DLC deposition equipment is described in chapter 4. Chapter 5 includes experimental procedure carried out, including sample preparation, deposition procedure and mechanical and chemical characterisations. Chapter 6 consists of discussion based on the experimental work and chapter 7 consists of discussion based on the modelling and experimental works. Finally chapter 8 contains the conclusion from this present research and provides suggestions for further work, which is related to this field of study.

Chapter 2

Synthesis of Diamond and Diamond Like Carbon Coatings and Surface Science

2.1 Introduction

Mankind has known the history of diamond as a gemstone at least since biblical times. Until the early 18th century diamonds were available only from the sediments of certain riverbeds in India and probably the oldest literary reference of diamonds are Indian in origin [8-10]. Incidentally, India also happens to be the birthplace for the oldest and the most celebrated solitaire diamond- Koh-i-noor, which now adorns the crown of Queen Elizabeth in England [11]. Büchner et al. [12] proposed that the primary source of diamond is rock of volcanic origin, which is called 'kimberlite' after the first important deposit discovered in South Africa. These deposits are strongly eroded by weathering and erosion and therefore most of the diamonds are found in the surrounding areas of old watercourses, alluvial deposits and sometimes on seabeds. Off the coast of Namibia, for example, diamond-containing clays are sucked up from the seabed and immediately concentrated on site. However, the properties of diamond have been properly understood only since the last century. The French chemist Antoine L. Lavoisier was the first to determine that diamond constitutes of pure carbon [13]. Later Bragg used x-ray to determine that carbon allotropes were cubic (diamond), hexagonal (graphite) and amorphous. This information helped researchers to attempt the synthesis of diamond.

Diamond has a unique combination of properties that makes it an exceptional material for a variety of uses. It is the hardest known material, premier thermal conductor at room temperature, resists acid, heat, and radiation, is a good insulator but can be doped to form p-and n-type semiconductor, transparent to visible, and infrared radiation and has a small dielectric constant. Though long recognized, most of these superior properties of diamond, except for the applications based on hardness, have remained unexploited mainly because diamond did not exist in a form suitable for many high-tech applications. Now chemical vapour deposition (CVD) makes diamond and its derivative diamond like carbon (DLC) available in thin sheets or as coatings. Once the current problems are overcome, the diamond CVD has the potential of transforming the present "silicon age" into a future "diamond age".

2.1.1 The Geology of Diamond

A great deal of mystery still surrounds the conditions under which diamond is formed in nature. In natural form, it has been found in meteorites and terrestrial rocks. There are

several hypotheses concerning the origin of diamond in meteorites [14]. It was first conjectured that the diamond crystallized out at high pressures in the depths of planetary bodies which produced the meteorites. Later, it was suggested that diamonds are formed in meteorites upon impact with the earth, as result of the high pressure generated. The most recent and widely accepted hypothesis is that diamonds in meteorites were formed by collisions of carbonaceous stones in space during travel through the asteroid belt.

In terrestrial rock, the growth environments of diamond are obtained by relating the inclusion data to other studies. The structure of the earth which is composed of several layers, is known only indirectly with the help of seismology. The earth which constitutes of a crust (90 to 33 km), a mantle (33 km to 2900 km) and a core (2900 km to 6370 km), has a dynamic, convecting mantle, that interacts with the crust and possibly the core. Most of the diamonds in terrestrial rocks are found in the Kimberlite pipes. These Kimberlite pipes, formed during volcanic eruption, serve as a window that lets us look into the earth and establish the probable conditions under which diamond is naturally formed. The likely pressure and temperature conditions under which diamond forms inside the earth can be predicted on the basis of evidence from upper mantle phase equilibria and that obtained from the inclusions in diamond (Fig 2.1). As can be seen the minimum formation pressure is 4.5 GPa, which corresponds to depth of about 150 km [15]. From the inclusion data, diamond from depth below 670 km has been established. Thus diamond in nature from under high pressure and high temperature conditions.

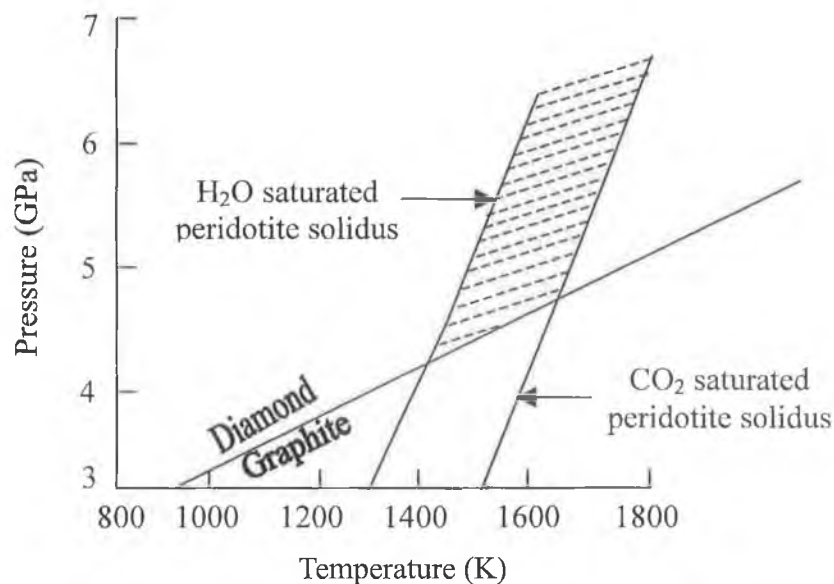


Figure 2.1: Pressure-temperature diagram showing the minimum conditions (dotted) for natural diamond formation [16].

2.2 Carbon as an Allotrope Element

2.2.1 Introduction

Carbon is an unusual material in that it exhibits both metallic and nonmetallic characteristics. Carbon exists in both crystalline and amorphous forms [17,18]. Crystalline carbon includes graphite, diamond and a family of fullerenes (Fig. 2.2) [19,20]. Graphite and diamond are infinite periodic network solids with a planar structure, whereas the fullerenes are a molecular form of pure carbon with a finite network with nonplanar structure.

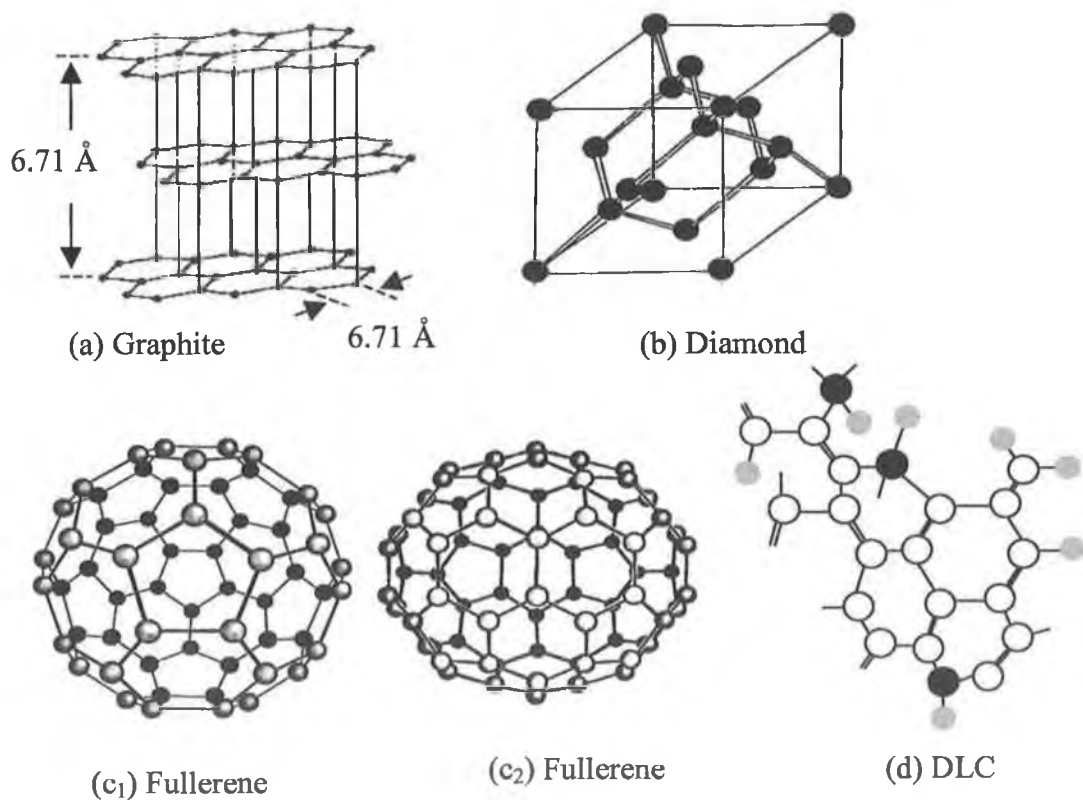


Figure 2.2: The structure of three known forms of crystalline carbon: (a) hexagonal structure of graphite; (b) modified face centered cubic (fcc) structure, two interpenetrating (fcc) lattices displaced by one quarter of the cube diagonal of diamond (each atom is bonded to four others that form the corners of the pyramidal structure called tetrahedron; (c₁ and c₂) structure of two most common forms of fullerenes: (c₁) soccer ball C₆₀ and (c₂) rugby ball C₇₀ molecules [19]; and (d) schematic representation of DLC structure: ●, sp³ carbon atom; O, sp² carbon atom; ⊙, hydrogen atom [21].

The diamond crystal structure is face centered cubic with one atom per lattice site. Each carbon atom is tetrahedral coordinated to four other carbon atoms and make strong, directional σ bonds using hybrid sp^3 atomic orbital. Graphite the stable allotrope has a layered structure with strong trigonal sp^2 bonds. The spare fourth electron in the outer shell of graphite forms a weak van der waals bond leading to electrical conductivity and lubricity.

Fullerenes (C_{60} , C_{70} etc.) and carbon nanotubes [22] have recently been developed by chemical vapor deposition [23] which have important advantages in the point of scientific basis. One of the fullerene molecules is C_{60} , commonly known as Buckyball. Since the C_{60} molecules are very stable and do not require additional atoms to satisfy chemical bonding, they are expected have low adhesion to mating surface and low surface energy. The low surface energy, spherical shape of C_{60} molecules, weak intermolecular bonding and high load bearing capacity offers potential for various mechanical and tribological applications. The sublimed C_{60} coatings and fullerene particles as an additive to mineral oils and greases have been reported to be good solid lubricants comparable with graphite and MoS_2 [24-26]. There have been parallel developments in the field of disordered carbons, which called “diamond like carbon”. Amorphous carbon has no long range order and the short range order of carbon atoms can have one or more of three bonding configurations — sp^3 (diamond), sp^2 (graphite) or sp^1 (with two electrons forming strong σ bonds and remaining two electrons left in orthogonal P_y and P_z orbitals to form weak π bonds). Short range order controls the properties of amorphous materials and coatings. Hard amorphous carbon coatings commonly known as diamond like carbon or DLC coatings are a class of coatings which are mostly metastable amorphous materials but include a micro or nanocrystalline phase. The coatings are a random network of covalently bonded carbon in hybridized tetragonal (sp^3) and trigonal (sp^2) local coordination with some of the bonds terminated by hydrogen. These coatings have been successfully deposited by a variety of vacuum deposition techniques on variety of substrates at or near room temperature. The following section will discuss how does carbon form different structures.

2.2.2 Hybridization

Carbon forms a great variety of crystalline and disordered structures because it is able to exist in three hybridizations, sp^3 , sp^2 and sp^1 [27]. The electronic configuration of the carbon atom allows it to form a number of hybridized atomic orbitals. Carbon atoms in the

elemental substances (e.g., diamond, graphite, & fullerenes) bond to each other covalently by the sharing of electron pairs. The covalent bonds have directional properties. This in turn gives carbon the ability to adapt into various molecular and crystalline structures. The nature of these bonds underlies the varied chemical properties and physical properties of the carbon allotropes.

Carbon, like many of the first-row elements of the periodic table (Appendix A1) has atomic orbitals that can hybridize. This is because the s-orbital and p-orbitals of carbon's second electronic shell have very similar energies. As a result, carbon can adapt to form chemical bonds with different geometries.

2.2.3 Hybridization Theory of Atomic Orbital

One very powerful theory in the valence bond approach is the hybridization theory which helps to explain why carbon containing molecules have carbon with four bonds. According to the orbital diagram of a ground state normal carbon atom, there are only two unpaired valence electrons in the 2p orbitals of a carbon atom. This should result in a carbon atom only capable of forming two bonds. However, every neutral carbon atom is tetra-valent and therefore, should have four unpaired electrons from which to form four bonds. How can we account for the discrepancy and how do we explain the tetra-valency of carbon atom? Professor Linus Pauling from California Institute of Technology in California suggested an interesting theory to explain the discrepancy. The theory also offers an explanation why carbon containing molecules can have one of three geometries around each carbon atom in the molecule. This hybridization theory resulted in Pauling being awarded the Nobel Prize for Chemistry in 1945.

According to this theory, carbon atoms are capable of hybridizing the s and p valence orbitals in one of three different ways. This hybridization process is preceded by the formation of an excited state carbon atom where a 2s electron is promoted into a 2p orbital before the hybridization process begins. Hybridization is similar to the hybridizations that occur in the plant and animal kingdoms. This results in a hybrid species which has some of the characteristics of both parents. The 2s and 2p orbitals of the excited state carbon can form one of three types of hybridized atomic orbitals. All four partially filled orbitals (one 2s and three 2p orbitals) may undergo mixing or hybridization to form four equal energy hybridized orbitals referred to as sp^3 hybrid orbitals. Each of the four sp^3 orbitals has an

unpaired electron explaining the tetra-valency for such a sp^3 carbon. The four sp^3 hybrid orbitals are arranged around the nucleus of the sp^3 hybridized carbon atom with the orbitals pointing toward the corners of a tetrahedron. The angle separation between the hybrid orbitals is 109.5 degrees.

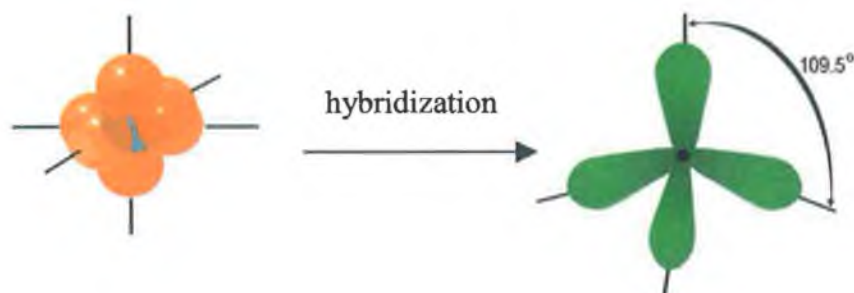


Figure 2.3 (a): Hybridization in carbon to create four sp^3 hybrids.

In order for other atoms to effectively overlap their orbitals with the sp^3 orbitals the atoms have to assume the same tetrahedral orientation. This results in a sp^3 carbon atom forming four single covalent bonds. If a carbon atom has four single bonds around it, and can be sure that it is hybridized sp^3 .

Another type of hybridization involves only the mixing of three of the orbitals (one 2s and two 2p orbitals). This forms three hybrid orbitals around the carbon nucleus called with one pure 2p orbital remained unhybridized. Each of the sp^2 hybrid orbitals and the pure p orbital have an unpaired electron which accounts for the tetra-valency of a sp^2 carbon. The sp^2 orbitals around and sp^2 hybridized carbon will have these orbitals pointing towards the corners of an equilateral triangle with the hybrid orbitals in the same plane as the carbon nucleus. The sp^2 hybrid orbitals will be 120 degree separated. This orientation of the hybrid orbitals establishes a trigonal planar orientation. This means that in order for other atoms to form effective maximum overlap with a sp^2 hybridized atom, these atoms must orient in the same geometrical orientation. These three orbitals can overlap with three other orbitals to account for three bonds, but what happened to the fourth bond? We are forgetting the 2p orbital that did not undergo hybridization. This double lobed orbital will be perpendicular to the plane where the hybrid orbitals are. This p orbital can overlap with another p orbital from another sp^2 hybrid carbon or from an oxygen atom. This is an effect make for the second bond between the two atoms hence a double co-valent bond. The

second bond is referred to as a "Pi" bond while the overlap between two sp^2 orbitals between the two carbons is called a sigma bond. Pi bonds are considerably weaker than any sigma bond which accounts for the fact that Pi bond makes available unpaired electrons which can be shared by other incoming atoms. These are quite understandably known as addition type reactions. In essence, if there is a double bond attached to the carbon, that carbon would be sp^2 hybridized.

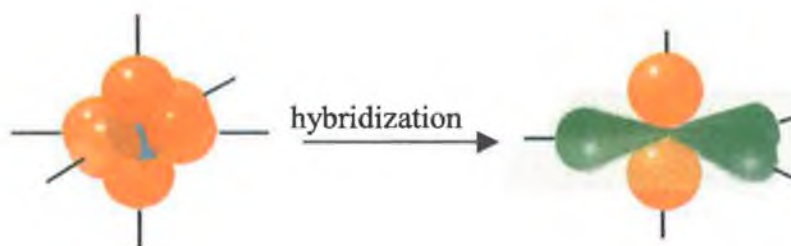


Figure 2.3 (b): Hybridization in carbon to create three sp^2 hybrids and the remaining p orbital extends perpendicular to the molecular plane.

A third way that carbon can hybridized its orbitals is the mixing of only two of the orbitals (one 2s and one 2p orbitals). This forms two orbitals known as sp orbitals with two pure 2p orbitals left unhybridized. Again each of the two sp hybrid orbitals and the two pure 2p orbitals left unhybridized. Again each of the two sp hybrid orbitals and the two pure 2p orbitals each have an unpaired electron to account for the tetra-valency of an sp hybrid carbon. The sp hybrid orbitals are oriented in a linear fashion with the hybrid orbitals 180 degrees separated. The two p orbitals are perpendicular to the linear arrangement of the sp hybrid orbitals and perpendicular to each other. Each p orbital can overlap with another p orbital from another sp hybrid atom to form a Pi bond for each. This would mean that the two sp hybrid atoms have a sigma bond (overlap between the sp orbitals) and two Pi bonds (overlap of the p orbitals) or a total of three bonds. Any carbon that has a triple bond to it will be sp hybridized.

Hybridization theory can also account for the fact that a carbon-carbon single bond length is longer (1.54 angstroms) than the carbon=carbon double bond length (1.31 angstroms) which in turn is longer than the carbon \equiv carbon triple bond length (1.2 angstrom). This tendency in bond length can be explained by using hybridization theory. Carbon-carbon single bonds involve sp^3 carbons. The characteristics of an sp^3 orbital, it could be found

that it is made out of the mixing of one s orbital which is characteristically less extended than p orbitals with three p orbitals which are more extended. It could say that the % of "s" character is 25% (1/4 of the orbitals used in the hybridization process are s). Using the same reasoning the sp^2 orbital is 33% s in character (1/3 of the orbitals used in the hybridization process are s). For the sp hybrid orbitals the percentage of s character is 50% (1/2 of the orbitals used in the hybridization process are s). Since the sp^3 orbitals that form a single bond between two carbons have the lowest percentage of s character, it would expect their orbitals to be the most extended. That means that the overlap of sp^3 orbitals by the carbon atoms can be effectively made when the nuclei are relatively far apart which would explain the relatively longer bond. The double bond between two sp^2 carbons would mean that the orbitals that needed to overlap would involve a higher percentage of s character which means that the hybrid orbitals would be relatively less extended compared to sp^3 orbitals. As a result the distance between the nuclei can be further apart for effective overlap to occur. A triple bond between two sp hybrid carbons means that the orbitals having the highest percentage of s character will be the orbitals least extended from the nuclei. As a result, the overlap between two sp hybrid carbons can not be effectively completed unless the nuclei of the two atoms are relatively close together. Hence the triple bond is the shortest.

From the above hybridization theory, it is recommended that carbon can exist in sp^3 , sp^2 and sp hybridization. The allotropes have different properties. Carbon soot and glassy carbon are primarily sp^2 bonded but amorphous carbon (a-C) and hydrogenated amorphous carbon (a-C:H) have a significant amount of sp^3 bonded carbon [28]. The sp^3 bonding of DLC confers on it many of the beneficial properties of diamond itself, such as its mechanical hardness, low friction, transparency, chemical and electrochemical inertness and wide band gap and hence is called "diamond like carbon" (DLC) film. While diamond films have well defined properties, the properties of cover a wide range of values between those of diamond on one extreme and graphite on the other. There is presently intense interest in these DLC films, which contain a mixture of both amorphous (sp^2) and crystalline (sp^3) phases. It is convenient to display the compositions of the various forms of amorphous C-H alloys on a ternary phase diagram as in figure 2.4 as first used by Jacob and Moller [29]. There are many a-Cs with disordered graphite ordering, such as soot, chars, glassy carbon, and evaporated a-C. These lie in the lower left-hand corner.

The hydrocarbon polymers polyethylene (CH₂)_n and polyacetylene (CH)_n define the limits of a triangle in the right hand corner beyond which interconnecting C-C networks cannot form, and only molecules form. Deposition methods have been developed to produce a-Cs with increasing degree of sp³ bonding. Sputtering can extend from sp² bonding some way towards sp³ bonding. If the fraction of sp³ bonding reaches a high degree, McKenzie [30] suggested that the a-C is denoted a tetrahedral amorphous carbon (ta-C) to distinguish it from sp² a-C. A range of deposition methods, such as plasma enhanced chemical vapour deposition (PECVD) is able to reach into the interior of the triangle. This produces a-C:H. Although this is diamond-like. It is seen from figure 2.4 that the content of sp³ bonding is actually not so large and its hydrogen content is rather large.

Thus, a more sp³ bonded material with less hydrogen which can be produced by high plasma density PECVD reactors is called hydrogenated tetrahedral amorphous carbon (ta-C:H) by Weiler et al. [33].

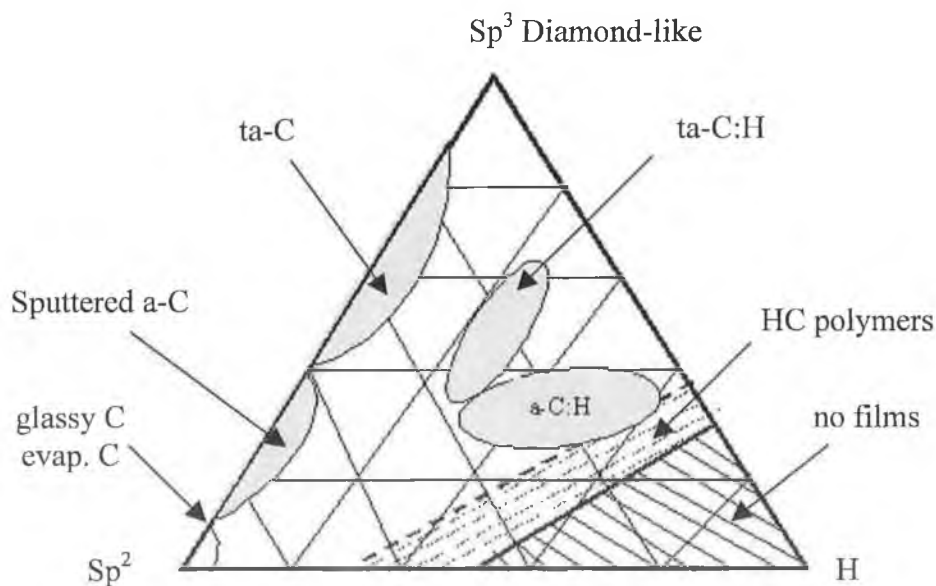


Figure 2.4: Ternary phase diagram of carbon [31,32]

The specific position of a diamond like material on this sp³-sp²-H ternary diagram is determined by the deposition system, i.e. precursor, method and parameters of the method. The energy of particles bombarding the growing film appears to be the most important parameter determining the position of the film on the ternary diagram. Another variation of

the diagram of figure 2.5 is presented in figure 2.4 [34], which shows that the diamond like carbon films comprising sp^3 , sp^2 and even sp^1 carbon bonds, have ranges of properties delimited by the properties of diamond, graphite and polymers.

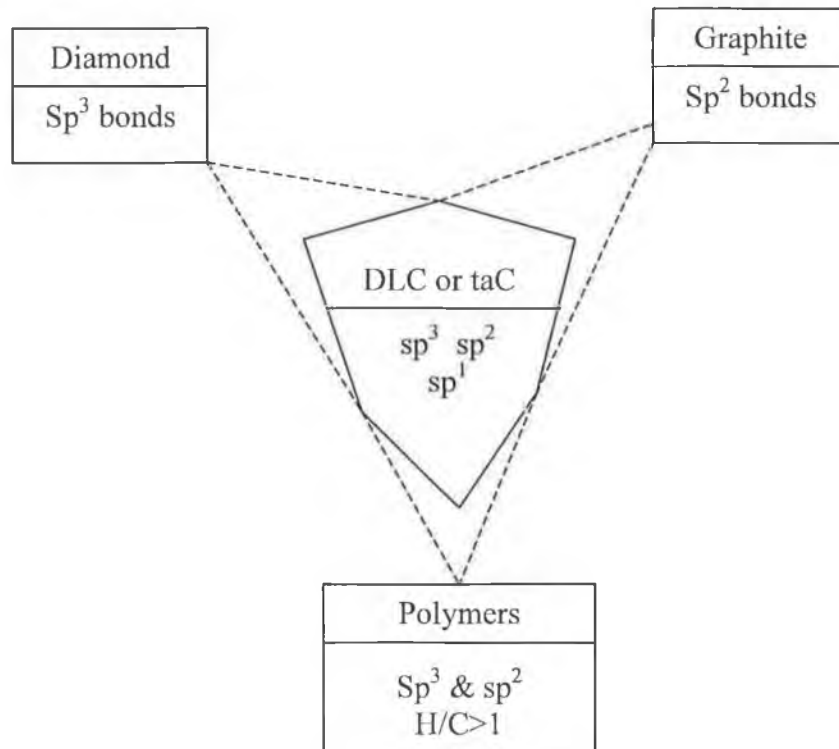


Figure 2.5: Delimitation of properties of diamond like carbon (after ref 34]

Both diamond and diamond like carbon films can be grown by chemical vapor deposition (CVD) of hydrocarbon containing gases. The CVD process involves decomposition of a gas mixture of carbon precursor and hydrogen or carbon precursor and hydrogen with some oxygen containing gas (like CO_2 , CO etc.) to atomic hydrogen, free radicals and sometimes ions which react to form the desired coating on a substrate. Deposition of diamond normally requires high substrate temperature (between 1000 and 1300 K), while deposition of DLC is done at substrate temperature below 600K. Temperature is not the only major factor differentiating the synthesis of these two materials. To grow a diamond film, the substrate and surface of growing film have to be continuously exposed to a large concentration of atomic hydrogen and/or oxygen to etch/prevent the formation of non-diamond phases through the mechanism. DLC is grown at lower temperature to prevent graphitisation under conditions of ion bombardment. The other difference is that, while diamond films are polycrystalline with crystallites up to tens of micrometers in size, DLC

films are metastable amorphous carbon containing a mixture of sp^3 , sp^2 and sp^1 hybridized carbon.

There are several methods available for deposition a diamond or diamond like carbon coatings. The following sections present a brief description of the various techniques and refer to relevant work in the literature for further details.

2.3 Synthesis of Diamond Films

Since the diamond in terrestrial rocks is formed under high pressure conditions, it was not surprising that the initial synthesis experiments tried to emulate this high pressure condition in the laboratory. General Electric in 1953 was the first to report a reproducible high pressure, high temperature (HPHT) synthesis of diamond [35,36]. The successful HPHT synthesis of diamond, however, resulted in product no better than those available with natural diamond. Thus synthesis of diamond films at near atmospheric pressure from hydrocarbons by Eversole [37] in 1958 was a significant step forward. Since then, diamond synthesis at low pressure has come a long way. Not only are the deposition conditions more or less perfected but also newer techniques with higher growth rates have emerged. The processing aspect of diamond films seems to have reached its peak. Today it is possible to coat almost all types of substrates and there is also the possibility for coating intricate shapes. Free standing diamond films are also now possible.

Development of DLC films seems to be as a spin-off of investigations in diamond coatings [38,39]. In the early days of diamond synthesis experiments, when the deposition conditions were not optimum, coatings which had properties between diamond and amorphous carbon, were formed. Aisenberg [40] first coined the name "diamond like carbon" in 1971 to describe these carbon coatings with high hardness. Soon these coatings due to some very useful properties developed as a new class of material in their own right. Today the dependent research in DLC films is probably as vast as it is for diamond films. There are several methods of depositing DLC films. One significant advantage of DLC film over diamond is that it is a low temperature process and so low temperature substrate like plastics can be easily coated.

2.4 Synthesis of Diamond Like Carbon (DLC) Films

2.4.1 Introduction

The first DLCs were prepared as thin films by Aisenberg and Chabot [40] who condensed a beam of C^+ ions in the presence of Ar and Ar^+ on a cold substrate to deposit an amorphous film containing no hydrogen, yet having some diamond like properties. It is possible to produce DLCs by wide range of deposition methods [41]. The methods can be categorized as to whether they are most suitable for laboratory studies or industrial production. The common feature of these methods is that the DLC film is condensed from a beam containing medium energy ($\sim 100\text{eV}$) carbon or hydrocarbon ions. It is the impact of these ions on the growing film that induces the sp^3 bonding — a physical process. This contrast with the chemical vapour deposition (CVD) of diamond, where a chemical process stabilises its sp^3 bonding. The best deposition process for DLC will provide a carbon ion flux at about 100eV per carbon atom, with narrow energy distribution, a single energetic species and a minimum number of non-energetic (generally neutral) species [33]. Robertson proposed that one of the common features is bombardment of the growing film with high-energy ions (usually in the range of 50 to 500 eV) to promote sp^3 bonding in an otherwise sp^2 bonded film [28,42].

Now DLC films can be deposited by a wide variety of techniques, such as ion beam deposition [43,44], mass selected ion beam deposition [45], dual ion beam [46,47], ion beam plating [48], fast atom beam [49], microwave plasma deposition [50], RF plasma [51] and DC plasma [52,53]. Deposition process for DLC films can be put into two classes depending on the source of carbon atoms [50]. The first class uses solid carbon itself (graphite target) sputtered by an ion beam [43-46] or a high energy laser beam [54], while the second one uses the dissociation of hydrocarbon gas by some form of glow discharge plasma [51,52]. Several comprehensive reviews of DLC films have been published [28,38,50,55-61].

Plasma basics

Plasmas, often referred to as the fourth state of matter are constituted of charged and neutral species. The charged species are predominantly positive ions and electrons, a contribution from negative ions is only present in plasmas of electronegative species. The

neutral species are atoms and molecules in the respective ground states or attainable excited states.

In low-pressure plasmas addressed here, the ions are produced by collisions between neutral and energetic electrons. An electric field supplies the energy for the electrons which are easily accelerated by external fields due to their small mass. Even a small mean free path length between two inelastic collisions with neutrals, electrons can extract a sufficient amount of energy from the external field to make production of ions through inelastic electron-neutral collisions an effective process. The big mass of ions, on the other hand, makes energy extraction from the field for these particles a slow process, so that their contribution to ionisation through inelastic ion-neutral collisions can be neglected.

Various physical quantities are used to characterise the state of plasma, of which density and temperature are the most important. The densities are the density of electrons (n_e), density of ions (n_i) and density of neutrals (n_n).

2.4.2 DLC Films by Sputtering of a Solid Carbon Target

2.4.2.1 Ion Beam Enhanced Deposition

This was the first technique used to deposit the diamond like carbon films [40]. The energy required for thin film nucleation and growth is obtained from the kinetic energy of an accelerated ion beam of the deposition material rather than heating the substrate. Changing the substrate potential can control the kinetic energy of the beam of ions. Thus DLC films with a wide variety of properties can be deposited. In figure 2.6 is shown a schematic of an ion beam deposition process.

Carbon ions are generated by sputtering carbon electrodes in an argon atmosphere in magnetically confined plasma and then accelerating them towards the substrates by a bias electrode. Since the substrate is isolated from the plasma, it is not subjected to bombardment by high-energy electrons and interaction with the radiation from the plasma is reduced [40]. The net effect is a reduced substrate temperature for ion beam, deposition compared with plasma methods. Thus a wide variety of temperature sensitive substrates can also be easily coated. Typical beam current densities are 1 to 2 mA/cm² with 500 eV ion energies and beam diameters up to 30 cm [50].

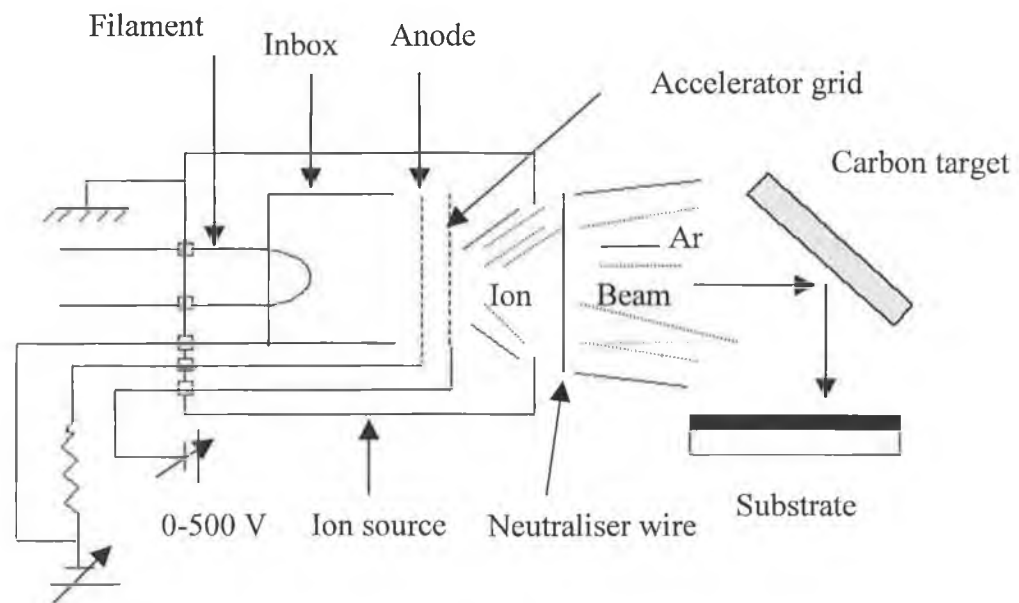


Figure 2.6: Schematic of single-ion beam sputtering deposition processes for DLC film [50].

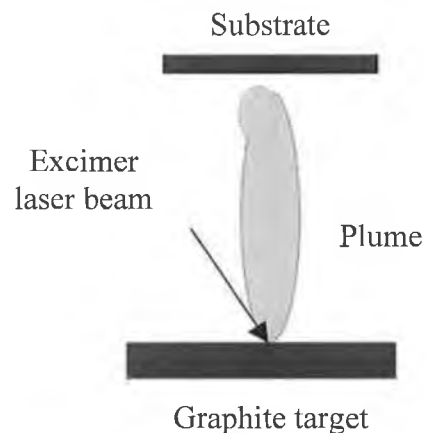
2.4.2.2 Laser-Arc Assisted Deposition

A carbon ion plasma can also be produced by laser ablation of a graphite target [54,62]. A high power Nd-YAG laser is used to strike a stable arc on a very pure carbon target to create a laser plasma plume. The plasma resembles that formed by a cathodic arc. The resulting film is diamond like if the laser power exceeds a certain threshold. The diamond like properties can be improved further by incorporating capacitive DC discharge energy with pulsed-laser evaporation [63].

Pulsed excimer lasers such as ArF give very short, intense energy pulses, which can be used to vaporise materials as an intense plasma [64-72]. The plasma then expands towards the substrates. The kinetic energy of this expansion gives ion energy analogous to the ion energy of MSIB or the cathodic arc. The mean ion energy is proportional to the laser fluence concentrated at the target spot [64]. In this way pulsed laser deposition (PLD) produces ta-C films similar to those from the MSIB and FCVA methods [70,72]. The dependence of properties on ion energy is similar [72]. The schematic diagram of pulse laser deposition system is shown in figure 2.7.

The advantage of PLD is that it is versatile laboratory scale method, which can be used to deposit many different materials from high temperature superconductor to hard coatings.

The PLD method for carbon has been reviewed by Voevodin and Donley [64] and by Siegal et al. [71].



(b) Pulsed laser deposition

Figure 2.7: Schematic of pulse laser deposition system

2.4.2.3 Mass-Selected Ion Beam Deposition

Deposition of a single ion species is possible if the ion beam is passed through a magnetic mass analyser for e/m selection. The analyser filters neutral, cluster species, graphitic fragments and impurities from the beam and allows only a pure beam of C^+ (or C^-) ions to reach the substrate. This mass-selected ion beam (MSIB) method was first used by Aksenov et al. [73] in 1970. This method results in a form of a-C with highest fraction of sp^3 bonding of those from any other DLC deposition process.

For laboratory work, it is desirable to have a controlled deposition from a single ion species at well-defined ion energy. This is achieved by mass selected ion beam deposition (MSIB) [74-78]. Carbon ions are produced in an ion source from a graphite target, such that the spread of ion energies is small, 1-10eV. The ions are then accelerated to 5-40 kV and passed through the magnetic filter. This filters out any neutrals and selects ions with an e/m ratio of the C^+ ion. The ion beam will diverge because of its Coulombic repulsion. The ions are then decelerated to the desired ion energy by electrostatic lens and the beam is focused onto the substrate in a vacuum of order 10^{-8} torr to produce a ta-C film. The advantages of MSIB are that it gives a controllable deposition species and energy, a filtering out of non-energetic species and the ability to dope by switching the ion species. The disadvantage is the low deposition rate of order $0.001 \text{Angstrom s}^{-1}$ and the high cost

and size of the apparatus. The MSIB method and its use have been reviewed by Lifshitz [74,75], and Hofsass and Ronning [78].

2.4.2.4 Sputtering

The most common industrial process for the deposition of DLC is sputtering [79-85]. The most common form uses the dc or rf sputtering of a graphite electrode by an Ar plasma. Because of the low sputter yield of graphite, magnetron sputtering is often used to increase the deposition rate. Figure 2.8 shows schematics of two sputtering deposition systems. Magnets are placed behind the target to cause the electrons to spiral and increase their path length and thus to increase the degree of ionisation of the plasma. As ion bombardment helps the formation sp^3 of bonding, the magnetic field can be configured to pass across to the substrate, so this causes the Ar ions to also bombard the substrate, to give an 'unbalanced magnetron'. A dc bias can be applied to the substrate to vary ion energy. The a-C:H can be produced by reactive sputtering by using a plasma of Ar and hydrogen or methane and a-CN_x can be produced using an argon-nitrogen plasma.

Alternatively, in ion beam sputtering (figure 2.8 a), a beam of Ar ions can be used to sputter from the graphite target to create the carbon flux [84]. A second Ar ion beam can be used to bombard the growing film to densify the film or encourage sp^3 bonding. This is called ion beam assisted deposition or ion plating.

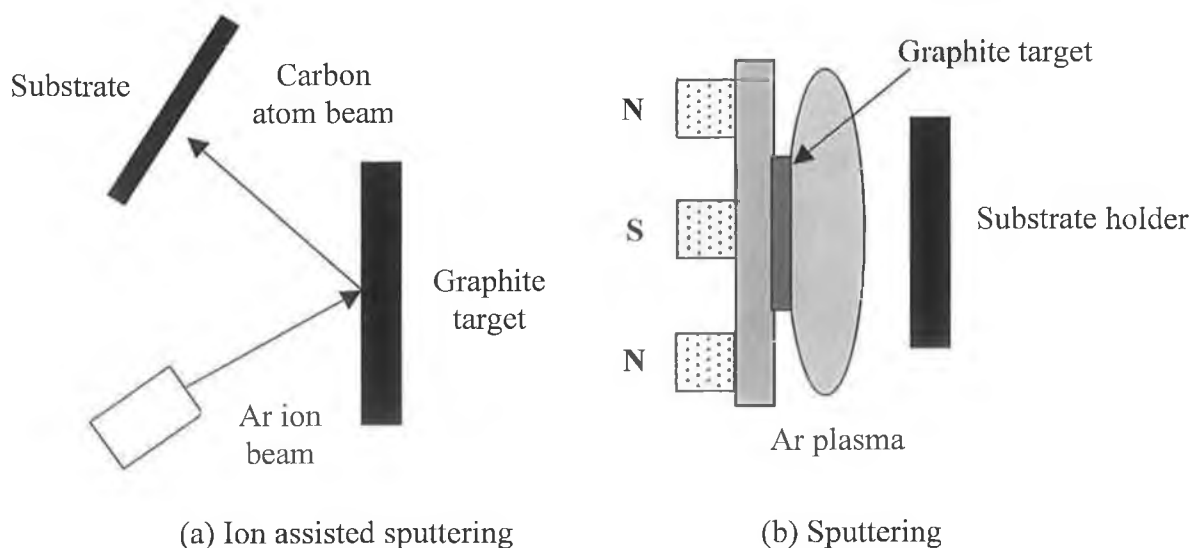


Figure 2.8: Schematics of sputtering deposition systems: (a) ion assisted sputtering, (b) sputtering.

Sputtering is preferred for industrial applications because of its versatility, its wide spread use to sputter many materials and its ease of scale up. Also the deposition conditions can be controlled by the plasma power and gas pressure but they are reasonably independent of the substrate geometry or conditions. A disadvantage of sputtering is, like ion beam deposition, that it can have a relatively low ratio of energetic ions to neutral species, so that it does not produce the hardest DLC films. However, sputtering methods with a very high fraction of ions have been developed by Schwan [83] and Cuomo et al.[84] to produce a-C with a relatively large sp^3 fraction, but this is at the expense of a low growth rate.

2.4.2.5 Cathodic Arc

An unusual method for laboratory and industrial use is the cathodic arc [86-99]. An arc is initiated in a high vacuum by touching the graphite cathode with a small carbon striker electrode and withdrawing the striker. This produces energetic plasma with a high ion density of up to 10^{13} cm^{-3} . A typical cathodic arc system is shown in figure 2.9 after Coll and Chowalla [100].

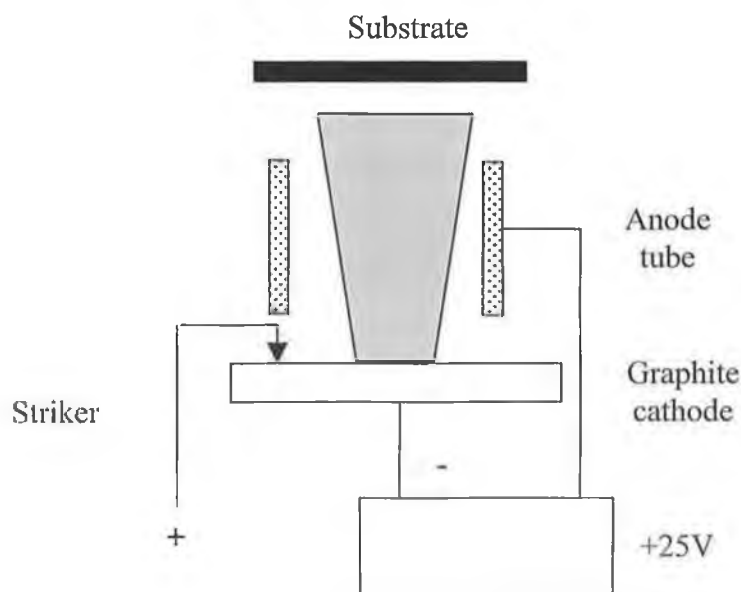


Figure 2.9: Schematic of cathodic vacuum arc deposition system.

The power supply is a low voltage, high current supply. The Cathodic arc is also widely used to deposit hard coating materials such as tin by the reactive deposition of Ti in a nitrogen atmosphere as reviewed by Brown [101]. The cathode spot is small, 1-10 μm and it carries a very high current density of 10^6 - 10^8 A cm^{-2} . The spot is formed by an explosive

emission process. This creates particulates as well as the desired plasma. The particulates can be filtered by passing the plasma along a toroidal magnetic filter duct [73] as shown in figure 2.10. This is known as filtered cathodic vacuum arc (FCVA).

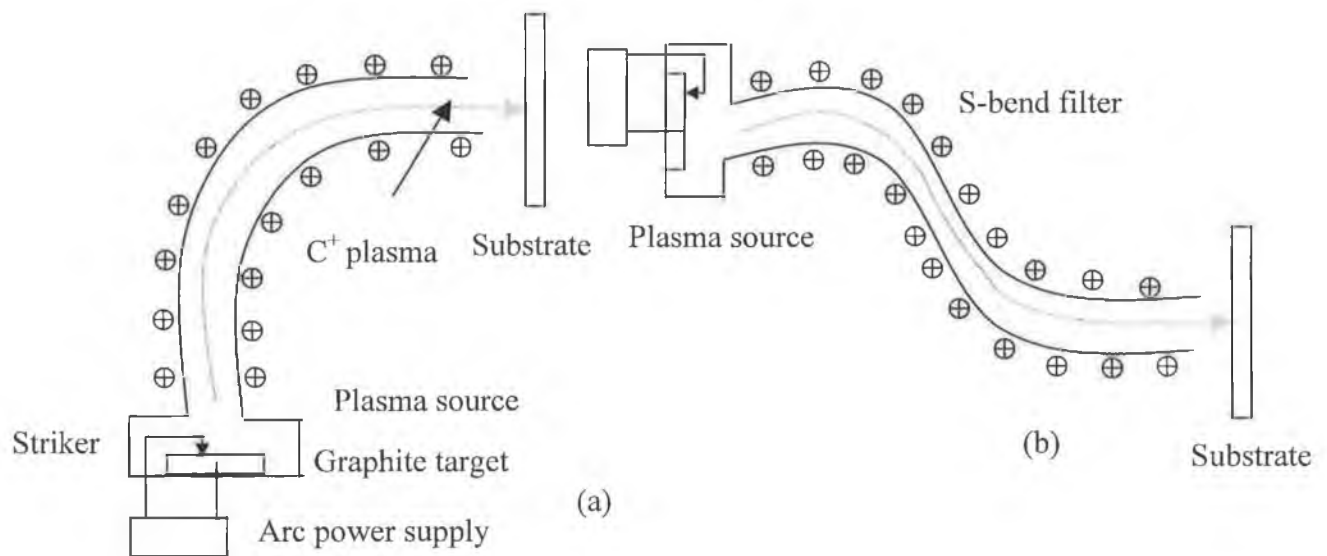


Figure 2.10: Schematic of filter cathodic vacuum arc: (a) single beam and (b) S-bend FCVA

The toroidal currents produce a magnetic field of about 0.1 T along the axis of the filter. The electrons of the plasma spiral around the magnetic field lines and so they follow them along the filter axis. This motion produces an electrostatic field, which causes the positive ions to follow the electrons around the filter. This produces an ambipolar transport of the plasma around the filter. The particulates cannot follow the field and they hit the walls and baffles on the walls. Alternatively, in the open filter system used by Brown [101] and Anders et al. [89], the particulates pass between the coils out of the filter zone into the chamber. The neutrals also hit the walls, so the filter raise the plasma ionization from about 30% to nearly 100% at the filter exit. The plasma beam is condensed onto a substrate to produce the ta-C. The advantages of the FCVA are that it produces a highly ionized plasma with an energetic species, a fairly narrow ion energy distribution and high growth rates of 1 nm s^{-1} for a low capital cost. It is used on an industrial scale. Unlike ion beam deposition, the deposition beam in FCVA is a neutral plasma beam so that it can deposit onto insulating substrates. The disadvantages are that the filtering is not sufficient for some applications, and that the cathode spot is unstable.

2.4.3 DLC Films by Dissociation of Gaseous Hydrocarbon Source

2.4.3.1 PECVD

The most popular laboratory deposition method is rf PECVD [102-112]. The reactor consists of two electrodes of different area. The rf power is usually capacitively coupled to the smaller electrode on which the substrate is mounted, and the other electrode (often including the reactor walls) is earthed. The rf power produces a plasma between the electrodes. The higher mobility of electrons than ions in the plasma creates a sheath next to the electrodes with an excess of ions. This has a positive space charge, so the plasma develops a positive voltage with respect to the electrodes, which equalises the mean electron and ion current to the wall [108], as shown in figure 2.11.

The sheaths act as a diode, so that the electrodes acquire dc self-bias voltages equal their peak rf voltage. The rf voltage divided between the sheaths of the two electrodes as in a capacitive divider according to their inverse capacitance. Thus the dc self bias voltage varies inversely with the electrode area [102,108],

$$\frac{V_1}{V_2} = \left(\frac{A_2}{A_1} \right)^2$$

The smaller electrode with smaller capacitance acquires the large bias voltage and becomes negative with respect to the large electrode. This is made the substrate electrode. The negative sheath voltage accelerates the positive ions to give the bombardment needed to create the sp³ bonding. In low pressure rf plasmas, the plasma is excited by an rf coupling to the sheaths. At higher pressures, the plasma is excited by Joule heating of the bulk plasma.

For DLC deposition, the plasma should be operated at the lowest possible pressure, in order to maximize the ion to radical fraction of the plasma. However, even at 50 m torr pressure, the ions are only about 10% of the film-forming flux. The ions can lose energy by collisions when being accelerated across the sheath. The ion energy is then no longer the sheath voltage. It is desirable to use a low pressure to minimise these collisions to maintain a narrow ion energy distribution. The sheath thickness decreases with increasing pressure P as [108]

$$d = kP^{-1/2}$$

(from the Debye length) while the ion mean free path decreases as $\lambda = k'/P$. Hence, the ratio λ/d scales as $P^{-1/2}$ and the mean free path becomes less than the sheath thickness at low enough pressures. It is necessary to use lower pressures, but this is not possible for conventional PECVD as the plasma will not longer strike. A lower pressure plasma can be created by using a magnetic field to confine the plasma to increase the electron path length and increase the ionisation efficiency. This allows a capacitively coupled plasma to continue to operate at 5×10^{-4} torr. At this pressure, the ion mean free path exceeds the sheath thickness and ion energy now has a narrow distribution.

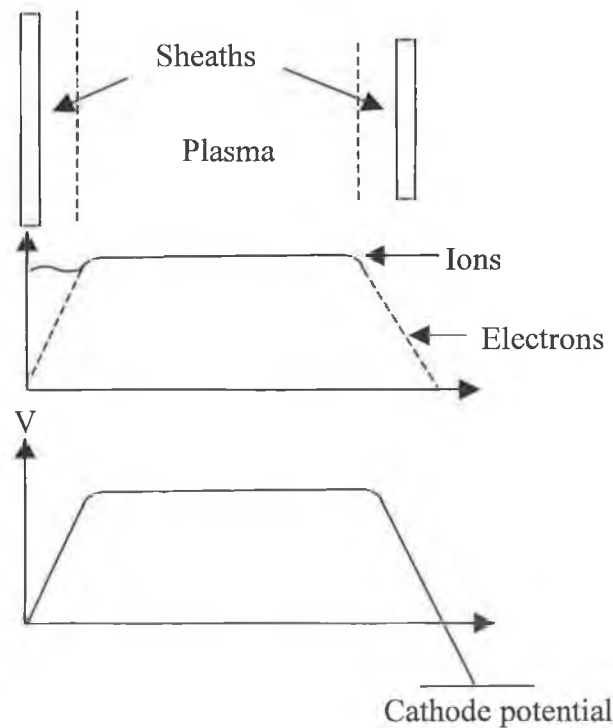


Figure 2.11: Electrons and ion distributions which create sheaths between the neutral plasma and wall.

This is the principle behind the plasma beam source (PBS) [110] shown in figure 2.12 (a). The PBS consists of magnetically confined plasma in which the plasma exits through a grid at earth potential. The rf is applied to a moveable electrode whose area is larger than the grid, so that this electrode acquires the positive self bias. This repels the positive ions

through the grid to form a plasma beam which then condenses on the substrate to form ta-C:H. The plasma beam is neutral so it can be used on insulating substrates.

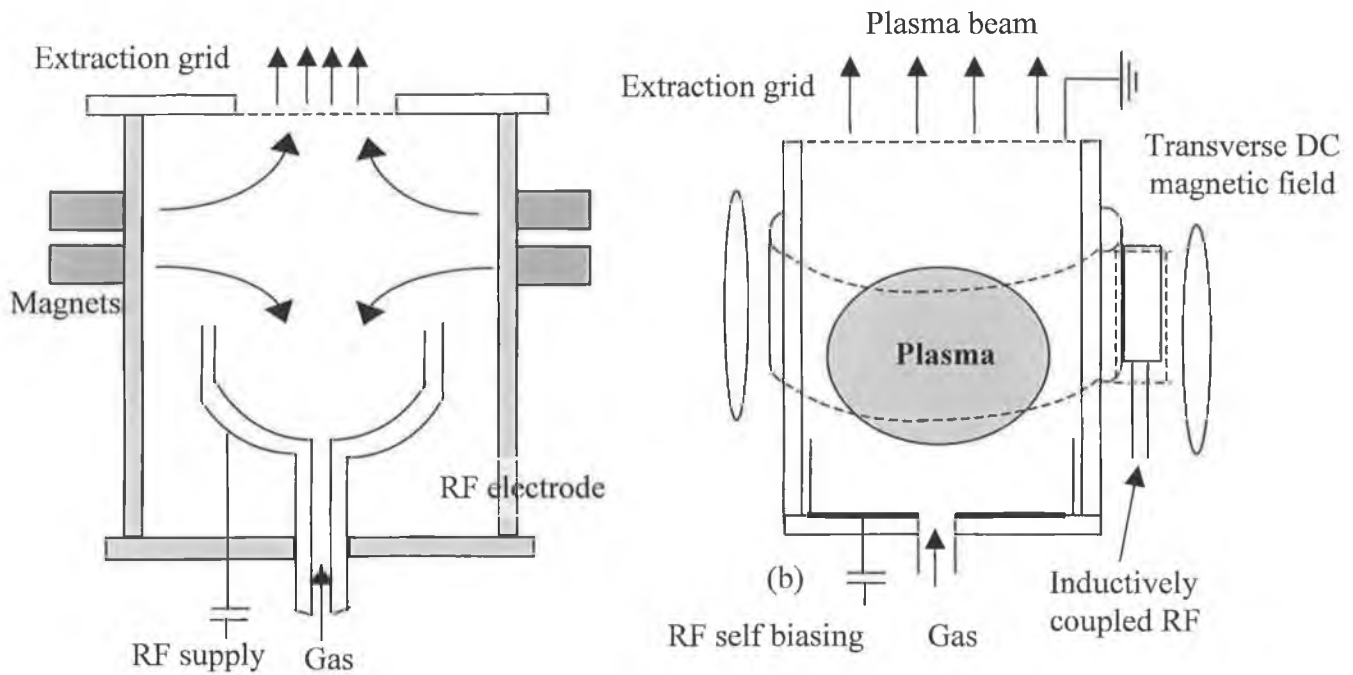


Figure 2.12: Schematic diagrams of the (a) plasma beam source and (b) ECWR source, after Weiler et al. [110,111].

In recent years, it has become clear that high density plasma sources are possible [108]. The two fundamental properties of the plasma are the plasma density n_0 and the electron temperature T_e . One aim is to maximise n_0 . The plasma electrons have a Maxwellian energy distribution, which defines the electron temperature, T_e

$$N(E) = n_0 \exp\left(-\frac{E}{kT_e}\right)$$

Electrons with energy above some threshold energy colliding with a neutral species will ionise or dissociate it according to the convolution

$$N_i = \int n_0(E, T_e) f_i(E) dE$$

where f_i is the ionisation probability. This is shown schematically in figure 2.13.

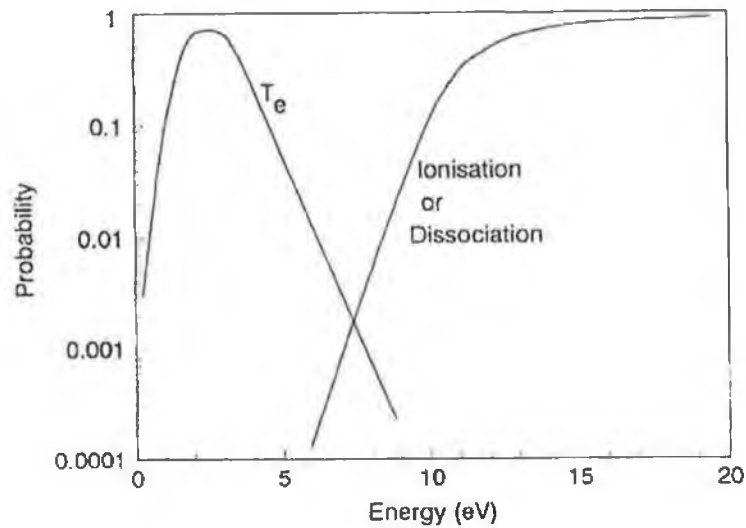


Figure 2.13: Electron temperature T_e and the dissociation/ionisation probability of a species.

Over a limited energy range, this gives

$$N_i \approx N_0 \exp\left(-\frac{E_i}{kT_e}\right)$$

where E_i is the ionisation potential. A high T_e maximises the ionisation. Similar relations hold for dissociated atomic species and excited species.

N_p and T_e are set by the requirements of energy and particle balance [108]. The particle balance sets T_e by equating the rate of generation of ions in the bulk plasma to the rate of loss of radicals and ions to the walls,

$$K_i N_g n_0 V = n_0 u_B A$$

This gives

$$\frac{K_i(T_e)}{u_B(T_e)} = \frac{1}{N_g l}$$

where l is the effective plasma length, A and V are the surface area and volume of plasma, n_0 is the plasma density, n_g is the density of atoms in the gas, K_i is the ionisation rate constant and u_B is the Bohm velocity of the electron. Here K_i and u_B are functions of T_e . The energy balance sets the plasma density n_0 by equating the power absorbed by the plasma W to the energy loss per ion E_T as ion energy and as ion loss to the walls. This gives

$$n_0 = \frac{W}{eu_B A E_T}$$

The most compact rf-powered, high plasma-density is the recently developed electron cyclotron wave resonance (ECWR) source [111] shown in figure 2.12 (b). The rf is inductively coupled to the plasma through a single turn coil. A transverse static magnetic field confines the plasma. This causes the rf electromagnetic wave in the plasma to form left and right hand circular polarised waves. The refractive index of one of these waves increases dramatically. This decreases the wavelength of the rf, so the rf can form a half wavelength standing wave across the chamber, which allows a resonant coupling of power into the plasma bulk. An rf signal is also capacitively coupled to a rear electrode to provide a self-bias voltage to vary the ion energy. The plasma can exit the chamber as a neutral beam through a grounded grid electrode. The ECWR is equivalent to the helicon, except for a different orientation of the fields and antennas.

The ECWR source produces an extremely high-density plasma of 10^{12} cm^{-3} or over with an independent control of the ion energy and ion current density [111]. The ECWR produces ta-C:H at a much higher growth rate (1.5 nm s^{-1}) than the PBS and gives uniform deposition over an diameter of 10 cm, which is scaleable to large values. It is the first industrialised high density PECVD source for DLC.

The gas used in PECVD has a significant effect on the a-C:H properties. In the early days, precursors with low ionisation potentials such as benzene were chosen as this gave a much higher growth rate. The deposition rate increases roughly exponentially with decreasing ionisation energy [103] as shown in figure 2.14. For mechanical applications, it is desirable to maximise the hardness, which minimising the incorporation of hydrogen. This requires using a precursor with small H/C ratio, such as acetylene, as this strongly affects the H/C ratio of the resulting film.

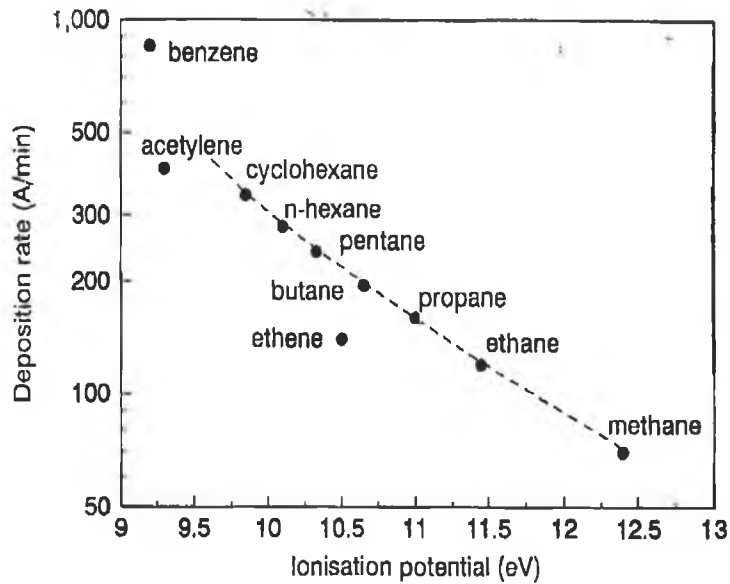


Figure 2.14: Growth rate of a-C:H by PECVD vs ionisation potential of the precursor gas. Data from Koidl et al. [113] and Zou et al. [107].

It is now known that DLC properties depend on the ion energy per carbon atom. Thus, a benzene ion $C_6H_n^+$ with six carbons requires 600V bias voltage to reach the desired 100 eV per carbon atom. Acetylene is more acceptable because only 200 V bias is needed to achieve 100 eV energy per carbon atom. Acetylene is in fact a very useful source gas for low pressure deposition because its strong $C\equiv C$ bonds means it has a simple dissociation pattern, giving mainly $C_2H_n^+$ ions [33].

Acetylene is the preferred source gas for mechanical application. However, acetylene is unsatisfactory for electronic applications because it is not available in high purity form and process as a substantial nitrogen impurity [112], which can cause a doping effect particularly if it is used in high density plasma. Methane remains a popular choice for

electronic applications because it is available in high purity, but the growth rate is lower and it gives high hydrogen content. Hydrogen dilution can be used to vary the hydrogen content.

2.4.3.2 RF Plasma-Assisted Deposition

One of the most popular methods is radio frequency (RF) plasma deposition from a hydrocarbon source gas. RF power is capacitively coupled to the substrate electrode and the counter electrode is either a second electrode or just the grounded walls of the deposition chamber. The powered electrode acquires a negative bias because of the large difference in electrode size and also in the electron and ion mobilities. The DC bias is largely dropped across an ion sheath in front of the cathode, which accelerates the ions towards the cathode. The deposition rate for a given source gas tends to vary linearly with bias voltage and gas pressure [50].

The rate is highest for gases of low ionisation potentials and large molecular weights. Films deposited from acetylene appear to have the best properties having the highest hardness [28]. A schematic of RF plasma-assisted CVD system is shown in figure 2.15.

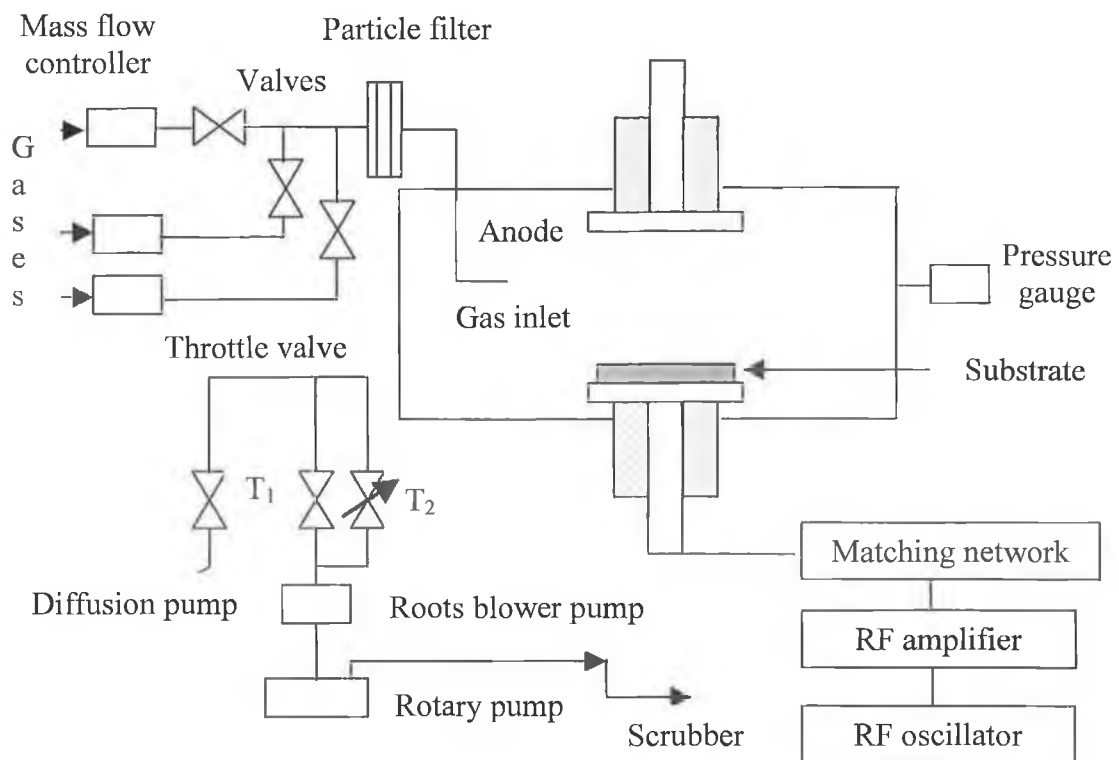


Figure 2.15: RF plasma-assisted CVD for diamond like carbon deposition [50].

2.4.3.3 Microwave and ECR-Assisted Discharges

Microwave discharges have been widely used in recent years because of their electrodeless nature together with their ability to create high densities of charge species in plasma discharge. Electron cyclotron resonance (ECR) discharge is basically a developed version of low pressure and low temperature microwave plasma. It utilizes a microwave energy coupled to natural resonant frequency of the electron gas in the presence of a static magnetic field [50]. The main advantage of using ECR is that it allows the microwave electric field to accelerate free electron continuously (between collision) throughout the full wave period which means that dense plasmas can be generated efficiently at low pressure.

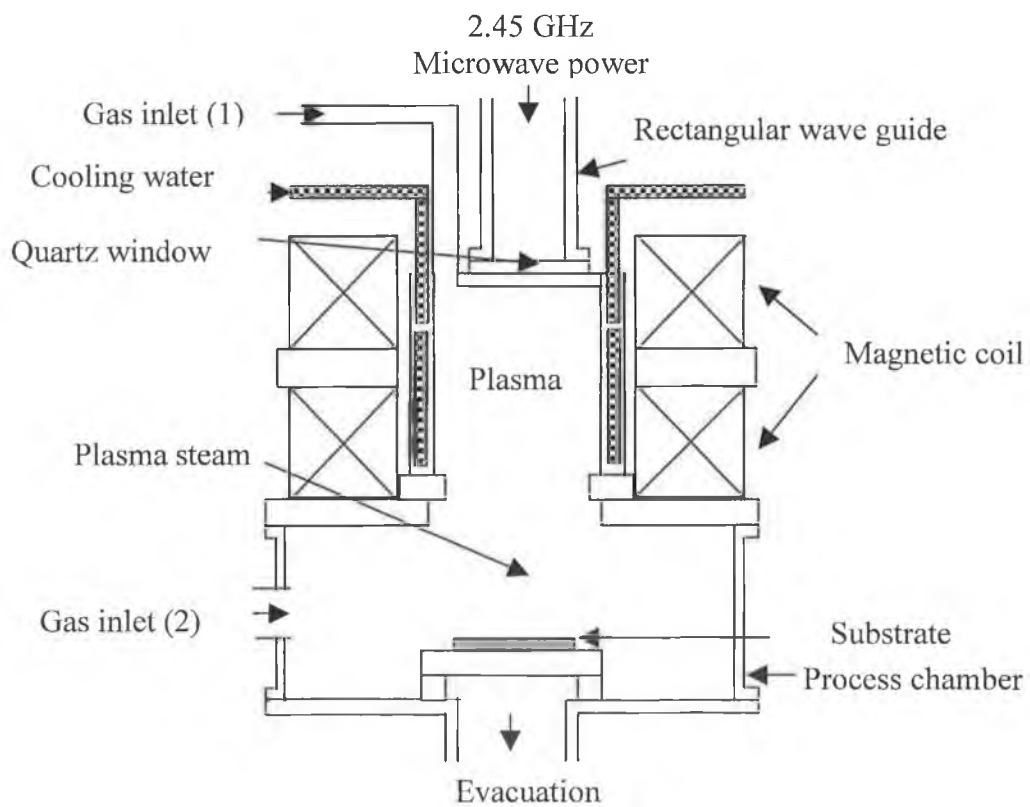


Figure 2.16: Schematic of an ECR deposition set up.

Other advantages include the absence of internal electrodes and direct control over the shape (through confinement), position (through resonance) and flow of plasma with magnetic field. These reduce the gas phase nucleation without heavy noble gas dilution and numerous undesirable powered electrode effects (such as contamination) are also eliminated. The ECR discharge-assisted deposition equipment is illustrated in figure 2.16.

2.4.3.4 Saddle Field Fast Atom Beam

Saddle field fast atom beam (FAB) offers an interesting option to grow diamond like carbon films. Indeed, one of the commercial manufacturers of such source (Atom Tech., Ltd., England) has engineered systems incorporating these sources to grow large area DLC films. Most importantly being essentially a neutral beam source, changing effect of the substrate while growing insulating films like DLC are not encountered. The fact that operation of the source does not require a radio frequency (rf) supply (or for that reason more complicated and expensive power supply as one requires to operate a conventional ion beam source) is decidedly a great advantage. DLC films are prepared almost neutral radicals using different hydrocarbon sources, namely methane (CH_4), acetylene (C_2H_2) gases and benzene (C_6H_6) vapour in the saddle field source. More details about the saddle field FAB source have described in Chapter 4.

2.5 Surface Science

In material science, much of the 'action' is at the surfaces and interfaces of the components. The quality of the surface is the most important property of the substrate since it is here that the film-substrate interaction occurs. Various types of irregularities make up the overall surface texture. The following categories of surface defects may be encountered [114]:

1. On the atomic scale: point defects, dislocation lines and monatomic ledges on cleavage planes.
2. Submicron features: polishing scratches, glass-drawing asperities and pores due to the less than theoretical density of the body.
3. Micron scale: grinding scratches, crystallite boundaries in polycrystalline materials, pores, glass-drawing lines.
4. Macrodefects: surface warp, glaze menisci, fused particles.

The different nature of these defects requires a variety of methods to determine or to characterise quantitatively the condition of substrate surfaces of the components. That is where loads are transferred from one component to another. It is where the system is exposed to the environment and where structural or microstructural instabilities are most likely to subsequent engineering failure. In this section will describe the effect of substrate surface of solid metals under ambient atmosphere.

2.5.1 Surface Adsorption and Contamination

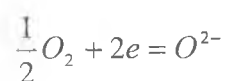
It is only rarely that free surface of a solid is unaffected by the environment. More typically, the solid surface is able to interact with a gaseous or liquid phase (air, water or a lubricant). When a clean surface reacts with a gaseous contaminant, the rate of contamination depends on the product of the rate of arrival of gas molecules with the probability that an arriving molecule will remain on the surface. This latter probability is termed the *sticking coefficient*. In a gaseous environment the arrival rate for gas molecules is given by the relation [115]:

$$R = \frac{3.15 \times 10^{22} x P}{\sqrt{T x M}}$$

R is in units of $\text{cm}^{-2}\text{s}^{-1}$, while P is in units of Torr, M is the molecular weight and T the absolute temperature. When a gaseous phase adheres to a clean surface the process is termed *adsorption* and is the first stage in surface contamination by the environment. The contamination rate at room temperature and a pressure of 10^{-6} torr, by an active gas with unit sticking coefficient is about one monolayer per second. This is the range of high vacuum. Ultra-high vacuum equipment, for the manufacture of solid state devices, is typically required to operate at pressure of 10^{-9} to 10^{-10} torr, which ensures that a surface can be preserved for several hours without appreciable surface contamination. Adsorption may occur without any chemical reaction to form an additional phase, resulting only in the reduction of the surface energy. The adsorbate is surface active.

2.5.2 Surface Reactions

If the bulk solid does react chemically with environment, then new phases are formed at the surface. The commonest example is the *oxidation* of metal. Gold is the only metal which is stable in air at room temperature. All other metals are oxidised to a greater or lesser extent. Growth of an oxide requires that both cathodic and anodic reactions occur (Fig. 2.17). In dry air the cathodic reaction at the surface of the oxide requires free electrons to create the negatively charged oxygen anions:



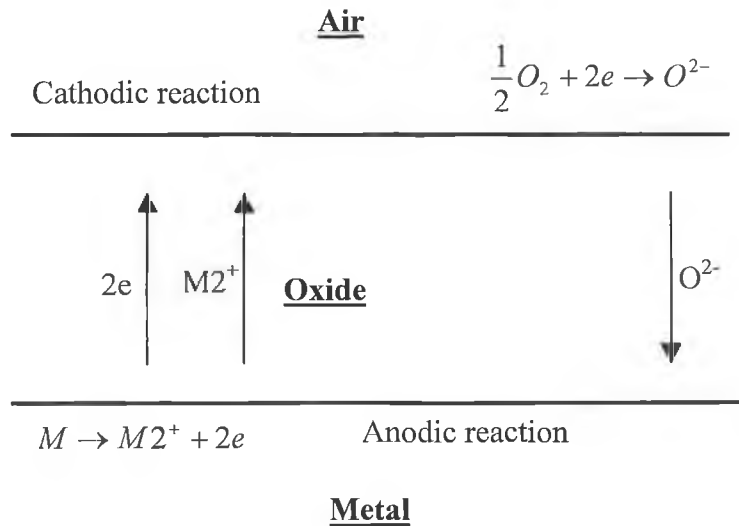
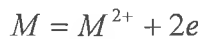


Figure 2.17: During oxidation, cathodic and anodic reactions take place at the free surface and at the oxide-metal interface respectively. Oxidation requires both electron transfer and diffusion of either anions or cations [115].

The corresponding anodic reaction occurs at the interface between the oxide and the metal and releases the free electrons to create positively charged cations:



2.5.3 Growth Laws for Surface Films

If the oxide is a stoichiometric insulator, then the electrons can only be transported across the film by quantum tunnelling across the potential barrier created by the non-conducting film. The tunnelling probability for electrons decreases exponentially with increasing thickness of the oxide, so that the rate of growth obeys a logarithmic law (and becomes negligible at room temperature when the film thickness is of the order of 2 nm). This is the basis for the protective (passivating) oxide film on metals and alloy which form stoichiometric oxides: Alumina on aluminium alloys and nickel-based superalloys, titania on titanium alloys and chromia on chromium plated components and chromium containing stainless steels. These films are much thinner than the wavelength of visible light, so that the polished metal surface retains its metallic reflectivity despite the presence of the thin oxide over layer.

Logarithmic growth is described by the equation:

$$d = k \cdot \log(at + b)$$

Where d is the thickness of the film, t is the time and parameters k , a and b are constants. Non-stoichiometric oxides are usually semiconductors whose electrical conductivity ensures adequate electron transport through the growing oxide. The growth rate of the oxide film is then controlled by the rate of ionic diffusion in the oxide. The driving force for ionic diffusion is usually provided by the difference in chemical potential associated with the ionic concentration gradients near the sites of the anodic and cathodic reactions. Alternatively, the driving for diffusion may derive from surface charge developed by the anodic and cathodic reactions, which creates an electric field across the oxide film.

The growth rate of the film is the product of the driving force for diffusion and the ionic mobility, which is directly proportional to the diffusion coefficient of the migrating ions. In general, either the cations or the anions dominate the diffusion process, while diffusion may occur by either a vacancy or an interstitial mechanism. If cation diffusion dominates, then the film grows outward from the original free surface of the metal, while if anion diffusion dominates the film grows in to the metal from the original surface (Fig 2.18).

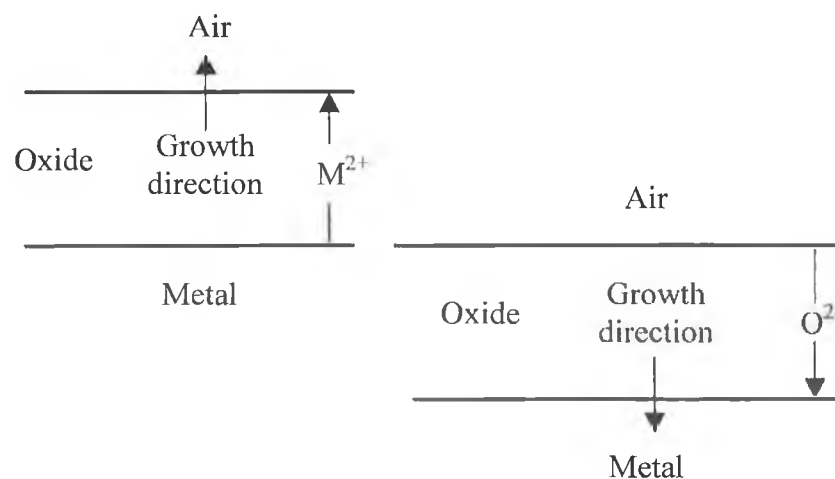


Figure 2.18: Oxide films growth outwards from the original metal surface, by diffusion of cations to the free surface, or into the metal by the diffusion of anions to the metal-oxide interface.

In many cases the oxide film is polycrystalline, in which case grain boundary diffusion may dominate the rate of growth. If the diffusion rate in an oxide film is constant, then ionic diffusion-controlled film growth leads to a parabolic dependence of film thickness on time:

$$d = k\sqrt{t} + a$$

Where the parameter k and a are again constants. Since the growth rate decreases with time, oxide film is partially protective. This type of growth is typical of many transition metals, such as copper, iron and nickel. Polished specimens of such metals eventually lose their reflectivity after exposure to dry air, since the film growth can continue to thickness well in excess of the wavelength of visible light ($\sim 0.5\mu\text{m}$). The ionic diffusion D is an exponential function of the temperature, so that the rate of film growth for non-stoichiometric oxides increases rapidly with increasing temperature:

$$D = D_0 \exp\left(\frac{-Q}{RT}\right)$$

Where D_0 is a pre-exponential factor, Q is the activation energy, T is the absolute temperature and R is the gas constant.

Finally, under some conditions the rate of film growth can be constant, so that the thickness increases linearly with time:

$$d = kt + a$$

2.6 Substrate Surface Polishing

2.6.1 Introduction

To reduce the surface roughness, substrate surface polishing is very important for thin film deposition. If two moving surfaces come in to contact with each other, friction arises between the two surfaces. When the friction force is higher than the atomic binding energy of the materials, atoms on the surface layer cannot resist the friction force and are deformed or chipped (called micro-chipped) away from the surface depending on the

brittleness of the material [116]. Producing portions of substrate experience higher friction forces and are easily chipped away by a process called micro-cleavage creating a smooth surface. The material removal rate increases as the contact or friction force increases. If a soft material and a hard material come into contact, the removal rate of the soft material is higher than that of the hard material. If an abrasive powder is used in this process, the material removal rate and the ultimate achievable roughness is related to the size of the abrasive powder used. Although the material removal rate is higher when a coarse powder is used, the traces (or grooves) produced by a coarse powder are deeper than these created by a fine powder. Consequently, coarse powders are used for lapping and fine powders are used for final polishing. In either case, polishing progress, the contact area increases. Therefore, if a constant contact force is applied, the shear force per unit contact area actually decrease with polishing time and the material removal rate decrease. To maintain a constant material removal rate, the contact force must be increased as a function of time to accommodate the increase in contact area. Diamond is hardest known material. The use of the diamond powder is the effective way of polishing a metal surface by this way.

2.6.2 Polishing Methods

There are different ways to reducing the surface roughness by polishing like mechanical polishing, thermo-chemical polishing, chemical assistant mechanical polishing and planarization, laser polishing, ion beam polishing, abrasive liquid jet polishing or solid particle impact etc. Mechanical polishing is the common and reliability straightforward process for surface polishing. There is no requirement for substrate heating. Theoretically, there are almost no limitations on the size of the sample that can be polished.

2.6.2.1 Mechanical Polishing

In mechanical polishing, samples are ground against a flat metal wheel covered with different grade emery papers (from coarse to fine grain size). In the case of diamond polishing to achieve smooth surface, diamond is the abrasive powder spread on the velvet cloth on the wheel. Sample surfaces to be polish is placed against the wheel that has been charged diamond powder and is rotated at a speed ~ 200 rpm. Sufficient loads ($\sim 5-10$ N) need to apply force the sample surface against the wheel. The final surface finish is to be controlled by the size of the abrasive powder used. A coarse powder ($> 1 \mu\text{m}$) is in the initial stage of polishing commonly refereed to as lapping, which allows for fast material

removal. A sequence of polishing steps using smaller and smaller diamond particles ($< 1\mu\text{m}$) can be used to obtain the desired final surface finish. However, as the particle size decreases, the polishing time increases.

2.7 Substrate Cleaning

The cleanliness of the substrate surface exerts a decisive influence on film growth and adhesion. A thoroughly cleaned substrate is a prerequisite for the preparation of films with reproducible properties. The choice of cleaning techniques depends on the nature of the substrate, the type of the contaminants and the degree of cleanliness required. Residues from the manufacturing, lint, fingerprints, oil and airborne particulate matter are examples of frequently encountered contaminants. The process of substrate cleaning requires that bonds are broken between contaminant molecules as well as between the contaminant and the substrate. This may be accomplished by chemical means as in solvent or by supplying sufficient energy to vaporise the impurity, for example, by heating or particle bombardment. There are several techniques to clean the substrate prior to deposition thin films. The most common methods are as follows

2.7.1 Solvent Cleaning

Suitable reagents for substrate cleaning include aqueous solutions of acids and alkalis as well as organic solvents such as alcohols, ketones and chlorinated hydrocarbons are generally used for thin film applications. The reagents depend on the nature of the substrate material. Ultrasonic cleaning is one of the most popular cleaning techniques for removal of chemical and organic materials on the substrate.

In ultrasonic cleaning, dissolution of residues is enhanced by the intense local stirring action of shock waves created in the solvent. Thus, solvent saturated with impurities is continuously carried away from the substrate surface and fresh, less saturated liquid is admitted. Mechanical vibrations induced in the substrate further aid in loosening gross contaminants such as particulate matter flakes. The parameters which affect the efficiency of ultrasonic cleaning are numerous. The frequency of vibration, applied power, type and temperature of the solvent, its surface tension and viscosity and the presence of nucleating

particles and dissolved gases are factors which play a role. The lowering the gas pressure above the agitated liquid may be detrimental in some cases but helpful in others. Low frequency ultrasonic agitation is the most effective in removing gross surface contaminants such as particles and finger prints. There are other solvent cleaning methods, like detergent cleaning, hot solvent cleaning etc. which are also used for substrate cleaning, but ultrasonic cleaning is the most effective method for substrate cleanliness.

2.7.2 Glow Discharge Cleaning

This is the most widely used technique to clean the substrates *in situ* and immediately prior to film deposition. Exposing the substrate to the plasma of a glow discharge effects it. Typically, the discharge is established between two electrodes positioned in the vicinity of the substrates such that the surface of the latter is immersed in the plasma. The discharge voltage may vary from 500 to 5,000 V. The electrodes are traditionally made of aluminium since this metal sputters very slowly in the presence of oxidising gases and therefore does not significantly deposit on the substrate surfaces. DC discharges are commonly used for two electrodes positioned close together.

During coating, the substrate is not part of the glow discharge circuit as it is in sputter cleaning. Although the latter is an effective cleaning method, it involves bombardment of the substrate with high-energy particles, sputtering and possible roughening of the substrate surface as well as deposition of foreign material from the counter electrode. In glow discharge cleaning, removal of impurities and other beneficial changes of the substrate surface are brought about by one or more of the following mechanisms:

1. Straightforward heating due to impingement of charged particles and their recombination.
2. Impurity deposition through electron bombardment of the chamber walls.
3. Impurity deposition resulting from low energy ion or neutral particle bombardment.
4. Volatilising of organic residues by chemical reaction with dissociated oxygen.
5. Modification of glass surfaces through the additional oxygen.
6. Enhanced nucleation during subsequent film deposition.

2.7.3 Other Cleaning Methods

In addition to the more general and widely used techniques discussed in the previous sections, there are less common cleaning methods, which are applicable in certain

situations. An example is the cleaving of single crystals to produce an intrinsically clean surface. This procedure is of course limited to material available in single crystalline form, which have a suitable cleavage plane such as rock salt.

A special dust removal technique involves coating of the substrate surface with an adhesive or lacquer, which is subsequently stripped, hopefully taking the dust with it. Results of this method have been published by Jorgenson and Wehner who considered dust to be prime cause of pinholes in their films [117].

Chapter 3

Properties, Applications and Characterisation Techniques of Diamond and Diamond Like Coatings

3.1 Introduction

As highlighted in section 2.2, while diamond films have a well-defined set of properties, DLC films cover a wide range of values with properties of diamond and graphite at the two extremes. Table 3.1 compares the properties and applications of DLC and diamond coatings. These coatings must have good adhesion to avoid failure during service. Residual stresses in the film impair the adhesion and cause cracking or debonding. Therefore, its development needs to be understood and carefully controlled.

3.2 Properties of Diamond and DLC Coatings

3.2.1 Diamond Like Carbon Films

DLC coatings, unlike diamond films are essentially amorphous and mostly hydrogenated and have a wide range of properties (see Table 3.1). The mechanical properties of DLC films are inferior to those of diamond because of the presence of sp^2 bonding and hydrogen atoms. The properties of DLC depend on [56,122]: a) the deposition technique, b) hydrogen content of the film, c) substrate bias voltage and d) sp^3 content of the films and so on.

In general, DLC films contain a significant amount of hydrogen. Depending on the deposition method, the hydrogen content can be anywhere between 10 to 60 at.% [123]. The total hydrogen content determines the film structure at atomic scale (the ratio of sp^3 and sp^2 co-ordinate carbon atoms) and therefore the physical properties of the film. The sp^3 to sp^2 ratio has a maximum with increasing hydrogen concentration [123]. Hydrogen content is also the key to obtain a wide optical gap and high electrical resistivity, as it passivates the dangling bonds in the amorphous structure [58].

The Young's modulus (E) and hardness (H) of DLC films depends both on the deposition technique [56,124] and whether the film is hydrogenated or not [56]. Young's modulus is function of bias voltage. It first increases with bias voltage due to the preponderance of sp^3 bonding and then declines at high bias because of the increasing sp^2 content [56].

The tribological behaviour of DLC films is largely controlled by the surface chemistry, which is in turn affected by the environment and the deposition method used. In nitrogen

Table3.1: Properties of various forms of carbons [52,58,59,120,118-121]

Property	Graphite	a-C	a-C:H	CVD diamond	Natural diamond	Application
Crystal structure	hexagonal; a=2.47Å; c=6.79Å	amorphous with both sp ³ and sp ² bonds	amorphous with both sp ³ and sp ² bonds	cubic; a=3.561; 3.601Å	cubic; a=3.567 Å	-
Form	plates	films; smooth to rough	films; smooth	facetted crystals	(001), (111); twins on (111)	-
Density (gcm ⁻³)	2.26	2.0-3.5	1.8-2.0	3.52	3.51	-
Vickers hardness (Kgmm ⁻²)	-	1200-3000	900-3000	3000-12000	7000-10000+	Drill bits, cutting tools, wear resistance films on windows, lenses, surgical cutting tools and magnetic tapes
Coefficient of friction	-	0.15-0.45	0.2-2.0	-	0.05-0.15	
Refractive index	2.15(∥C); 1.81 (⊥C)	1.5-3.1	1.8-2.2	-	2.42	Optical filters
Optical band gap (eV)	-	0.4-3.0	0.7-3.0	5.5	5.5	Semiconducting and electronic devices Hot transistors, lasers, solid state detectors
Electrical resistivity	0.04(∥C); 0.2(⊥C)	10 ⁵ -10 ¹⁴	10 ² -10 ¹³	>10 ⁹	IIa>10 ¹⁶ ; IIb 10-10 ³	
Chemical stability	inert-inorganic acids	inert-inorganic acids	inert- inorganic acids inert-inorganic solvents	Inert-inorganic acids	Inert- inorganic acids	Coating for reactor vessels; gas/slurry pipes
Residual stress	-	low intrinsic(-), low thermal	high intrinsic (-), low thermal	low intrinsic (+), high thermal	-	-

the preponderance of sp^3 bonding and then declines at high bias because of the increasing sp^2 content [56].

The tribological behaviour of DLC films is largely controlled by the surface chemistry, which is in turn affected by the environment and the deposition method used. In nitrogen at a relative humidity $RH < 1\%$, the friction coefficient between steel ball and DLC coated silicon wafer is found to be $\mu = 0.01$ and increase to 0.19 at $RH \cong 100\%$ [125].

Values as low as $\mu = 0.005$ have been measured in vacuum [125]. In conditions giving rise to very low values of μ , carbonaceous material from DLC is transferred on to the metal ball, while in the conditions of high friction the metal is transferred to the DLC surface [126]. This material transfer changes the chemistry of the surfaces in contact and leads to different values of μ under the different ambient conditions. Surface topography also plays a significant role in tribological behaviour of the DLC coatings. During wear of the slider against the carbon surface, planarisation of processing corrugations can increase greatly the contact area changing the friction coefficient. However the surface roughness and the contact area does not significantly change if there are a large number of pores, leaving the friction coefficient unaffected [127].

The characterisation methods and applications of DLC films have been discussed extensively in the literature but can be found in summary form in reviews such as Angus [60], Robertson [128], Tsai and Bogy [58], Matthews [129] and Grill et al [123]. A comparison of the properties of DLC films with those of diamond films has been presented by Angus and Hyman [38]. The wide interest in DLC coatings stems not only from the fact that these films have attractive properties but also that very smooth films can be deposited uniformly over wide areas on a large variety of substrates.

3.2.2 Diamond Films

Natural diamond has a unique combination of properties, as list in table 3.1. Synthetic diamond has properties very similar to the natural diamond. The properties of synthetic diamond films depend on several factors, few of these being a) hydrogen content, b) sp^2 content, c) gas mixture composition and d) substrate temperature.

3.3 Generation of Residual Stress

Whatever the application, the mechanical stability of the film is of critical importance. Internal stresses are central to the problems of cracking, delamination and buckling of the film during deposition and in service. Deposition of diamond and DLC films is always accompanied with internal stresses. Large stress comparable to the yield strength of many materials can develop during deposition. It has been reported that stresses of a few GPa typically developed during growth [130,131]. It is well established that [132,133] such large stresses can readily overcome the film-substrate adhesion and cause delamination of films, even when they are relatively thin. In addition, high stresses are expected to affect mechanical, optical, electronic and chemical properties of the film. Thus, a quantitative measure of film stresses is necessary both for understanding the stability issues and for the design of useful DLC material.

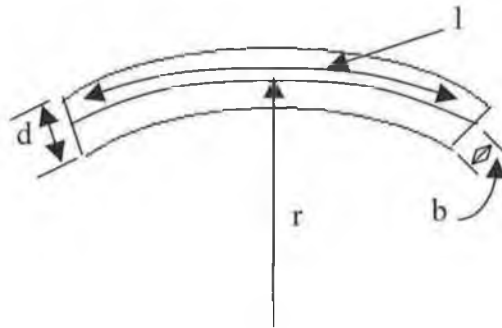
Residual stresses developed during the deposition process can either be deposition (intrinsic) or thermal. Any mechanism which impedes atomic rearrangement will lead to the development of stresses. It is important to understand and control the development of stress in a coating as excessive stresses in the coating may cause a component to fail by cracking, delamination and buckling. In addition, coating performance indicators such as adhesion strength, resistance to thermal shock, stability at high temperature, wear and erosion resistance and other mechanical properties are strongly influenced by the nature and magnitude of residual stresses. It also limits the maximum coating thickness that can be deposited without spallation. Internal stress may be affected by a number of processing parameters such as film deposition rate, angle of incidence of beam source, presence of residual gas in the film, deposition current, gas pressure and deposition temperature. Further, it is strongly dependent on the deposition technique.

3.3.1 The Stoney Formula [134]

If bar is bent into a curve due to differential stresses, assuming stress is zero at cross section b.

Length of bar at b is l

Angle subtended by bar, $\theta = \frac{l}{r}$



Length of bar at position x from inner edge

$$l(x) = r(x)\theta$$

$$l(x) = (r + x - b)\theta$$

$$\text{i.e. } \Delta l(x) = l - l(x)$$

$$\text{or, } \Delta l(x) = r\theta - (r + x - b)\theta$$

$$\text{or, } \Delta l(x) = (b - x)\theta$$

$$\therefore \text{Strain} = \frac{\Delta l(x)}{l} = \frac{(b - x)\theta}{r\theta} = \frac{b - x}{r}$$

$$\text{Stress} = E \times \text{Strain}$$

$$\text{i.e. } P = E \frac{(b - x)}{r}$$

Bending moment in bar at position x

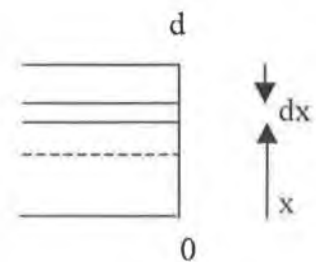
$$dM = P dx \times x = \frac{E}{r} (b - x) x dx$$

Total bending moment across the bar

$$= \int dM = 0$$

$$\text{i.e. } \int_0^d \frac{E}{r} (b - x) x dx = 0$$

$$\therefore b = \frac{2}{3} d$$



Net forces in bar must be equal to force in film

$$\text{Force in film} = P_f l$$

$$\begin{aligned} \text{Force in film} &= \int_0^d P(x) dx \\ &= \int_0^d \frac{E}{r} (b-x) dx \\ &= \frac{1}{6} E \frac{d^2}{r} \end{aligned}$$

$$\therefore \text{Stress in film, } P_f = \frac{1}{6} \frac{E d^2}{lr}$$

Taking Poisson's ratio into account

$$P_f = \frac{E d^2}{6(1-\nu)lr}$$

To calculate deflection

$$l = r\theta$$

$$z' = \sqrt{(l^2 + r^2)} - r = \sqrt{(r^2\theta^2 + r^2)} - r = r\sqrt{(1 + \theta^2)} - r$$

If $\theta \ll 1$

$$z' \approx r \left[1 + \frac{\theta^2}{2} - 1 \right] = \frac{r\theta^2}{2}$$

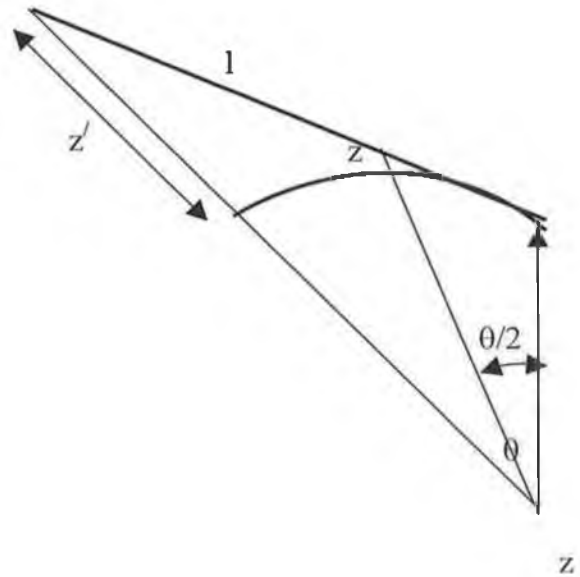
$$\text{but, } \theta = \frac{l}{r}$$

$$\therefore z' = \frac{l^2}{2r}$$

$$\text{Similarly, } z = \frac{l^2}{8r}$$

$$\therefore P_f = \frac{E d^2 z'}{3(1-\nu)l^2}$$

$$\text{or, } P_f = \frac{4E d^2 z}{3(1-\nu)l^2}$$



For DLC films, P_f is the residual stress, which is replaced by σ , E is the Young's modulus of the substrate designated by E_s , d is the substrate thickness designated by t_s , z is the deflection call δ and l is the film thickness which is replaced by t_f .

The equation is

$$\sigma = \frac{4E_s l_s^2 \delta}{3(1-\nu_f) l_f l^2} \quad 3.1$$

3.3.2 Intrinsic Residual Stress

During deposition, the stress generated in the film may be either tensile or compressive [135,136]. Essentially it arises either from the incorporation of excess vacancies (tensile) or from the “atomic peening” effect (compressive), when bombardment with high energy species occurs. The stresses can also arise from source such as impurity incorporation at the interface, incomplete structure ordering, or structural reordering [137]. However, the details of how this “intrinsic” or “deposition” stress develops and its dependence on processing conditions is a complex area, which is still not well understood. A multitude of qualitative models has been proposed to explain the generation of intrinsic residual stresses in coatings.

The intrinsic stress of almost every coating formed by condensation from vapours is tensile. This is explained in terms of a constrained relaxation during film growth from a disordered state to a more ordered state. Two different models have been proposed in literature to explain this phenomenon, both of which employ a constrained relaxation or constrained shrinkage mechanism during film growth to explain the tensile stress. The first model [137] assumes that the outer surface layer of a growing film is in a condition of high disorder, far from thermodynamic equilibrium. The regions beneath the surface layer relax toward a state of increased order and decreased volume. The decrease in volume results in the formation of tensile stresses. The second model [138] visualises the crystallites in the growing film as growing together until the gap between the two crystallites is on the order of the bulk lattice constant of the film material. The inter atomic forces then produce an elastic relaxation of the boundaries towards each other. This relaxation is constrained relaxation results in the formation of tensile stresses. However, the presence of impurities or deliberate addition of other gases in the deposition atmosphere of films deposited by vapour condensation can cause the stresses to become null or even compressive. Presumably impurities are adsorbed at the surface of the film from where they diffuse inward causing an increase in volume [137]. In a sputter film the intrinsic stress is almost always compressive, caused by the constant bombardment of the growing film by

energetic species [137,139]. The sputtered species have an average energy of tens of electron volts, whereas evaporated species have an average energy of only a few tenths of an electron volt. Thus, the growing film during sputter deposition is bombarded by high energy species and energetic neutrals. This bombardment of the growing film by these energetic species is referred to as “atomic peening”. The peening effect causes atoms to be incorporated into the growing film with a density higher than would be obtained otherwise [139]. The peening also causes the impurity and neutral atoms (like argon) to get trapped (i.e. generation of interstitial) in the coating [136]. Both of these mechanisms result in generation of intrinsic compressive stresses in the film. Compressive stresses in a film do not necessarily imply the formation of interstitial (At higher bombardment energies, however, interstitial may be the main cause for generation of compressive stresses).

The cause for generation of intrinsic stresses in diamond and diamond like carbon films are not the same. In diamond films, which are formed always by the CVD route and are crystalline in nature, the generation of intrinsic stress is attributable to the lattice parameter mismatch between the film and substrate and the distribution of defects within the films. Whereas, in DLC films, which are primarily formed by ion beam or sputtering methods and are mostly amorphous, atomic peening and generation of interstitial are the cause for development of intrinsic stress.

3.3.3 Thermal Residual Stress

If the coefficient of thermal expansion of a film and its substrate are not the same, heating or cooling will produce additional stress, which will tend to deform the film-substrate combination. This stress contribution known as thermal stress and its type and magnitude depend on the difference between the thermal expansion coefficient of the films and substrate. This thermal stress is predictable and easier to analyse the intrinsic stress. For a substrate of length L_0 and modulus E constrained at both ends, if its temperature reduced from T to T_0 it would change (contract) in length by an amount equal to $\alpha (T_0-T) L_0$, where α is the coefficient of linear expansion. Since the specimen is constrained it is effectively elongated in tension. The tensile strain ϵ is $\epsilon = \alpha (T_0-T)$ and the corresponding thermal stress, by Hooke's law, is $\sigma_f = E\alpha (T_0-T)$. Now for a film-substrate combination subjected to a temperature differential ΔT , the film and substrate strains are, respectively

$$\varepsilon_f = \alpha_f \Delta T + \frac{F_f(1-\nu_f)}{E_f d_f w} \quad 3.2$$

$$\varepsilon_s = \alpha_s \Delta T + \frac{F_f(1-\nu_s)}{E_s d_s w} \quad 3.3$$

where, w is the width of the specimen, F is the thermal mismatch force and subscripts f and s refer to film and substrate respectively. However, the strain compatibility requires that $\varepsilon_f = \varepsilon_s$, therefore, the thermal mismatch force is

$$F_f = \frac{w(\alpha_s - \alpha_f)\Delta T}{\left(\frac{1-\nu_f}{d_f E_f}\right) + \left(\frac{1-\nu_s}{d_s E_s}\right)} \quad 3.4$$

If the film is thin as compared to the substrate, that is,

$$\frac{d_s E_s}{(1-\nu_s)} \gg \frac{d_f E_f}{(1-\nu_f)} \quad 3.5$$

The thermal stress in the film, assuming that there is no plastic flow in the substrate, is

$$\sigma_f(T) = \frac{F_f}{d_f w} = (\alpha_s - \alpha_f)\Delta T \frac{E_f}{(1-\nu_f)} \quad 3.6$$

Diamond films, which are deposited at high substrate temperature, have a significant amount of thermal residual stress in them. Thermal stress calculated at room temperature (293K) in diamond film deposited at 1173K on Ti6Al4V alloy can be as high as 6.8 GPa [140]. DLC films, on the other hand, do not have significant thermal stresses, as they are deposited at much lower temperatures.

3.4 Measurement of Residual Stress in Coating

Interest in the mechanical properties of thin films has grown rapidly over the past few years, hand in hand with general interest in all other properties. However, attention had been made to certain aspects of mechanical behavior especially the stress present in growth films as early as the end of the nineteenth century (in 1877), when measurements were made on the stress present in films deposited chemically on glass thermometer bulbs.

Thirty two years later the subject was put on a more quantitative basis for electrodeposited films by Stoney [134]. Since these early beginnings interest has grown apace, so much so that over the last few years several authoritative reviews have been compiled and published, notably by Hoffman [141-143]. In view of the excellence of these reviews, the present author finds a little difficulty in adding new material and readers will of necessity be constantly referred these texts.

The ultimate goal is to find ways to reduce the stresses and therefore to achieve better film quality. If a film is deposited in stress on a thin substrate, the substrate will be bent by a measurable degree. A tensile stress will bend it so that the film surface is concave and a compressive stress so that is convex. The most common methods for measuring the stress in a thin film are based on this principle. The following sections explain in brief, both the techniques and the underlying principles used to measure the residual stresses in diamond and DLC films.

3.4.1 Bending Beam Methods

As pointed out above, films containing residual stresses bend the film-substrate combination to counteract the unbalanced moments. One of the most simple and widely used techniques is to measure the curvature of the film-substrate composite. The curvature of this composite can be used to establish the residual stress in the film, by using Stoney's formula (Eq. 3.1).

A number of techniques have been used to measure the curvature of the stressed film and substrate composite. In some experiments, a long thin substrate beam is clamped at one side and the deflection of the free end observed, while in others the substrate is held on knife edges and the centre deflection measured. In the case of cantilever beam, the deflection can be observed optically [144], through the capacitance change [145], or mechanically by using a surface analyser probe [146]. An optical interference technique can also be used to measure the curvature of the beam [138].

3.4.2 Bulge Test

In this technique a known pressure differential is applied between the front and back of the circular free standing membrane (Fig 3.1).

The deflection of the centre of the membrane is measured either by optical interference [147] or by a microscope with calibrated z-axis [148].

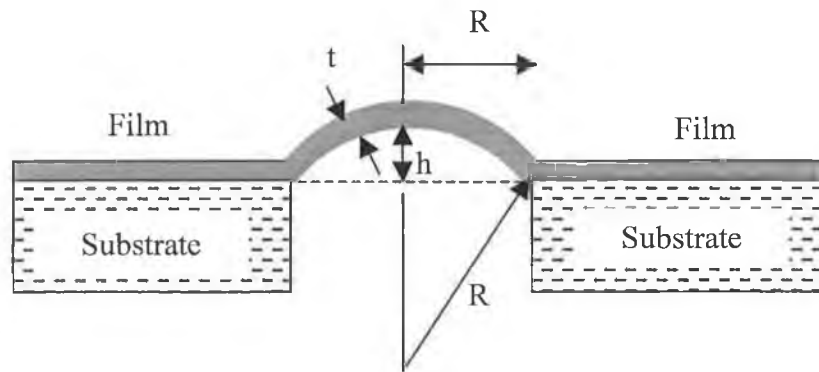


Figure 3.1: Illustrating the set up used for determining the stress in a free standing [147]

Assuming that the deflection of the membrane is small compared to its radius, the differential pressure (ΔP) as a function of membrane deflection (h) is found to be [147].

$$\Delta P = \frac{4t\sigma_f}{r^2}h + \frac{8t}{3r^4} \frac{E}{1-\nu} h^3$$

For a membrane with radius r , film thickness t , intrinsic stress σ_f and bulk modulus of the film $E/(1-\nu)$. By measuring the bulge height versus pressure and fitting the data to a polynomial with first and third order terms and using the known membrane thickness and radius, σ_f and $E/(1-\nu)$ can be easily determined.

Cardinale et al. [149] used this technique to measure the stresses as low as 0.8 MPa in microwave plasma deposited diamond films. The need for a freestanding film makes this technique destructive and limits its use for stress measurement. However, Cardinale et al. [149-151] and Field et al. [152] have adapted this technique to measure the stress in diamond film. They dissolved the circular section in the substrate to get a freestanding circular coating. However, their claim that the interface between the free standing and the etched circular hole in the sample is a well defined circle is open to suspicion. Yet another limitation is that this technique cannot easily be applied DLC films, because DLC films are prone to chemical attack and are often permeable [153].

3.4.3. X-Ray Diffraction Method

Internal stresses induce strain in the specimen, which lead to a change in lattice parameter [154]. This strain shifts the x-ray diffraction peak and can be used to measure the residual strain. If the elastic constant is known, the internal stress can be established. The same can be achieved by other diffraction methods such as electron diffraction or neutron diffraction. Electron diffraction techniques have better resolution. X-ray diffraction peaks can be analysed in two different ways to extract the value of internal stress in the film. This technique is however suitable only for studying crystalline materials like diamond films [155,156].

It should be noted that x-ray and electron diffraction techniques will give the strain and hence the stress in a crystalline lattice. This is not necessarily the same as that measured by substrate bending since the stress at the grain boundaries may not be same as that in the crystallites.

3.4.4 Raman Spectroscopy

Atoms in molecules and crystals vibrate with a fundamental frequency. The number of possible vibrational is $3n-6$ for non linear molecules and $3n-3$ for crystals, where n is the number of atoms in the molecule or in the primitive unit cell of the crystal. The Raman spectrum arises from the indirect coupling of high frequency radiation with the electron clouds that make up the chemical bonds. Thus in Raman spectroscopy an intense monochromatic light beam (usually a continuous gas laser) impinges on the sample and distorts the electron clouds that make up chemical bonds in the sample, storing some energy. When the field reverses as the wave passes, the distorted electron clouds relax and the stored energy is reradiated. Most of the energy is reradiated at the same frequency as that of the incident exciting light (the Rayleigh scattering). However, a small portion of the stored energy is transferred to the sample itself, exciting the vibrational modes. The vibrational energies are deducted from the energy of the incident beam and weak side bands appears in the spectrum at frequencies less than that of the incident beam (Stokes scattering). On the other hand, existing vibrations that have been excited by thermal process can be annihilated by coupling with the incident beam and can add their energies to that of the sources. These appear as side bands at higher wave numbers (anti-Stokes scattering). The anti-Stokes intensities are strongly temperature dependent. Thus most spectrometers are set up to display the wave number shift of Stokes lines from the

Rayleigh line directly. Because Raman spectra are extremely weak, stray light within the monochromator must be effectively suppressed. The spectrum is more sensitive to the lengths, strengths and arrangement of bonds in a material than it is to the chemical composition. The spectrum of crystals likewise responds more to details of defects and disorder than to trace impurities and related chemical imperfections.

Raman spectroscopy has been extensively used for probing the structure of coatings [157-160], and recently it has been used to measure film stress [130,140,160,161]. It is possible to obtain molecular specific information from Raman spectra for both amorphous and crystalline phase [162]. Molecular information relates to chemical bonding in the film and can unambiguously be used to infer localised stresses within the film. Internal stresses in a coating tend to shift the Raman peak and this shift can be correlated to the stress in the coating. In general a material which is under tensile stress will shift the Raman peak to a lower frequency, while the Raman peak of a material under a compressive stress is shifted to a high frequency [160,163,164]. Boppart et al. [165] has found that the Raman frequency shift $\Delta\omega/\omega$ is a linear function of stress in the crystal given approximately by the relation:

$$\sigma = \pm \frac{E_f}{(1-\nu_f)} \frac{\Delta\omega}{\omega}$$

where σ is the stress and $\Delta\omega$ (cm^{-1}) is the shift of the Raman peak for diamond film compared with the natural diamond ($\omega = 1333.3 \text{ cm}^{-1}$). The minus and plus signs are assigned to compressive and tensile stresses respectively.

Raman spectroscopic studies of diamond films have been widely carried out. The stress-induced shifts in diamond Raman frequency have been interpreted either in terms of the hydrostatic stress model [160] or a biaxial stress model [161,164] or a more general model developed by Ager et al. [140] to measure biaxial stress in polycrystalline diamond films.

3.5 Separation of Intrinsic and Thermal Stresses

Residual stress in a coating calculated at room temperature after the deposition is complete, is the total stress- a sum of intrinsic and thermal stresses. According to Maissel

and Carey et al. [114,166] the total stress σ observed in a film is equal to the sum of any externally applied stress plus thermal plus intrinsic components, i.e.,

$$\sigma = \sigma_{external} + \sigma_{thermal} + \sigma_{intrinsic}$$

Even though it is possible to calculate the intrinsic stress in the coating by separating the thermal contribution to the stress, it is not possible to know the history of stress generation during deposition. *In-situ* methods for measuring stresses in coatings while it is being deposited can give useful information about the way intrinsic stresses develop during deposition. Only an *in-situ* monitoring of stress can reveal that in most vapour deposited films. The stress increases rapidly during initial stages of growth and then decreases and becomes nearly constant [162]. In principal, all the methods described in section 3.4 can be used for in-situ study but there are several practical problems. Therefore, only a few methods have been successfully used to study *in-situ* generation in diamond films. To date, there has been no attempt to study real time stress generation DLC films.

An optical setup, similar to the optical setup developed by Flinn et al. [167] has been use to measure the change in curvature of the film-substrate composite *in-situ* during deposition of diamond film on the silicon substrates [168,169]. Martin et al. [170] used a laser interferometric method for *in-situ* measurements of stress of optical materials. In principal, this technique measures the deflection of the centre of freely supported thin substrate during deposition. Yet another method of *in-situ* stress measurement is by sensing the curvature of the sample during deposition capacitively using a miniature probe [145].

Raman spectroscopy can also be used for *in-situ* monitoring of film's intrinsic stress during deposition. The advantage of using Raman spectroscopy is that it can simultaneously also measure several other properties such as stoichiometry, grain orientation and impurity content and it can be used to analyse both single and multi layer films. In technological applications the total stress must be small. The intrinsic stress is the predominant component in many systems and has been the subject of most of the investigators.

3.6 Adhesion of Thin Films

3.6.1 Introduction

Adhesion is the most important attribute of a deposited film without which all other film characteristics are meaningless. Adhesion is defined as the sum of all the intermolecular interactions between two different juxtaposed materials [166]. Borges and Ohring et al. [171,172] defined adhesion as the condition in which two surfaces are held together by valence forces or by mechanical anchoring or by both together. Thus the type of interfacial region formed during deposition governs the adhesion. The work required to separate a unit area of two surfaces forming an interface, which is a measure of adhesion is affected by contributions from chemical interactions, interdiffusional effects, internal film stresses, interfacial impurities, imperfect contact etc. At least four types of interfaces have been distinguished and these are depicted in figure 3.2.

1. In the abrupt interface atoms change suddenly from the film to the substrate material. In this type of interface, stresses and defects are confined to a small region where stress gradients are high. Film adhesion in this case is generally poor because of easy interfacial fracture modes. Roughening of the substrate surface before coating will promote better adhesion.
2. The compound interface has a layer or multilayer structure, which is several atomic layers thick and is created by chemical reaction and diffusion between film and substrate atoms. Such an interface can generate high stresses through volumetric changes accompanying reaction. Adhesion is generally good if the interfacial layer is thin (reduce interfacial stresses), but it poor if thicker layers form (increase interfacial stresses).
3. In a diffusion interface, there is a gradual change in composition between film and substrate. The mutual solubility of film and substrate precludes the formation of interfacial compounds. Usually, interdiffusion results in good adhesion.
4. The mechanical interface is characterized by interlocking of the depositing material with a rough substrate surface. The adhesion strength in such cases depends on the mechanical properties of the film and substrate and on the interfacial geometry.

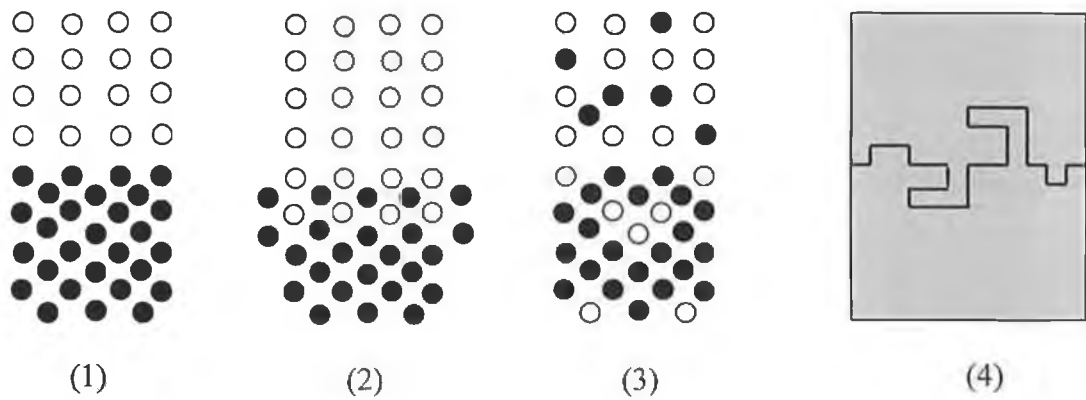


Figure 3.2: Different types of interfacial layers formed between film and substrate [172]. (1) abrupt interface, (2) compound interface, (3) diffusion interface and (4) mechanical anchoring at interface.

In diamond and DLC interface plays a significant role. The interface type depends on the substrate material used. Films growing on stable carbide forming substrate like Ti would form a compound interface and hence would have a better adhesion than films growing on a substrate, like steel, which forms a diffusion interface with carbon. Polishing the surface not only increases the nucleation density but also causes mechanical anchoring at the interface and hence gives better adhesion.

The following section review the various adhesion tests used to study coatings in general with particular emphasis on techniques used to study adhesion of diamond and DLC coatings.

3.6.2 Measurement of Adhesion of Coatings

For any intended application of a film, its adhesion to the substrate is of primary importance for any practical utilisation of the composite. However, it is difficult to measure this parameter quantitatively, especially when adhesion is acceptable. Mechanical methods of obtaining quantitative data and also qualitative analysis for adhesion are reviewed [173]. In this section, several adhesion test methods as well as concept and theory of the tests are discussed.

3.6.2.1 Mechanical Methods

There are essentially two types of tests, which are distinguished by the kind of stress generated in the interfacial region, namely, tensile and shear tests [173]. Direct tensile (pull-off, topple test), acceleration, and shock wave tests belongs to the tensile test group, where as adhesive tape, direct shear and peel and scratch tests belong to the shear test group. The choice of the test for measuring practical adhesion should be based upon the type of stresses the test specimen is going to encounter in practice [174]. Furthermore more, the ideal test should be nondestructive, automated and easy to perform, easy to interpret, reproducible and be quantitative. In the following, the principal tests for measuring practical adhesion are reviewed.

3.6.2.1.1 Tensile Type Test

These are one of the simplest and most commonly used tests and include tests like direct pull-off and topple test [173,175-177].

In the pull-off test, a loading fixture commonly called a dolly or stud made of aluminium is precoated with epoxy and bonded to the surface of the film. A special device is then used to apply with continuously increasing force until the coating debonds or the glue fails [178]. The pull is perpendicular to the surface, so tensile strength is being measured. This is different from tape test where shear is being measured. Therefore, the results obtained from the two different types of tests are not comparable. The schematic diagram of pull-off adhesion and topple tests are shown in figure 3.3.

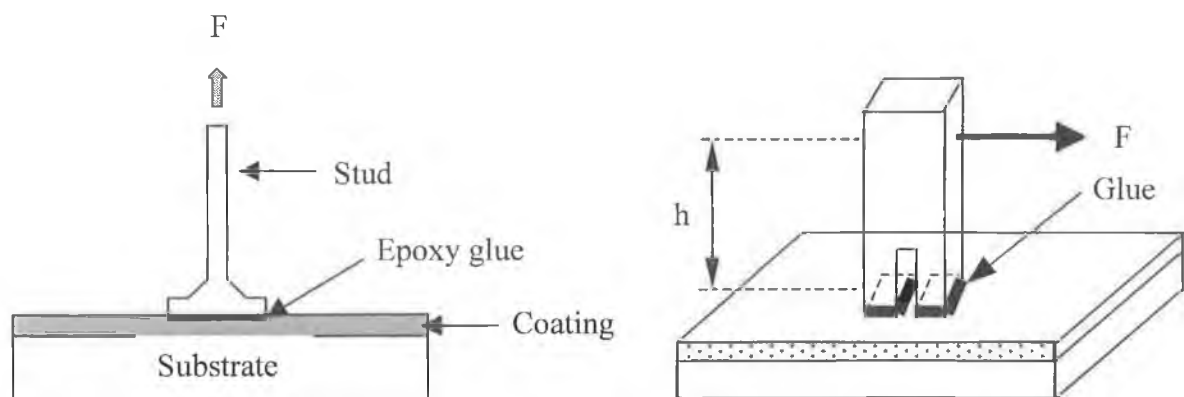


Figure 3.3: Schematic diagram of (a) pull-off adhesion and (b) topple tester [173].

A portable adhesion tester, loading fixtures and adhesive are needed for this test. The first step is to prepare the loading fixtures. These are supplied as smooth steel and must be cleaned so the glue will stick. This usually involves solvent cleaning. It is a good idea to roughen the bonding surface of the loading fixture either with sandpaper or light abrasive blasting. This will minimise the number of glue failures that occur. The coating surface must also be cleaned. Surface abrasions can induce flaws, so only fine sandpaper (400 grit or finer) should be used, if needed, to remove loose or weakly adherent contaminants such as chalking or dirt that cannot be washed off. Epoxy or acrylic adhesives are used to glue the loading fixture in place. The adhesive must cure for the amount of time recommended by the manufacturer. This can be several hours to a day, depending on the adhesive and the temperature. It is important that constant contact pressure be maintained as the adhesive sets and begins to cure. Magnetic or mechanical clamps work the best. For pull-off adhesion testing, at least three test fixtures per test area are normally required. The number of areas being tested will determine how many fixtures and clamps are needed. The fixtures can be taped in place with masking tape or duct tape if enough clamps are not available. There are two main types of commonly used adhesion testers. One is a fixed-alignment, mechanical adhesion tester, the other is a fixed-alignment, pneumatic adhesion tester. These instruments come in different force ranges, so the proper range instrument must be selected. No matter what instrument is being used, the load to the fixture should be increased continuously and smoothly at a rate not to exceed 1 MPa/s (145 psi/s). The load is applied until failure occurs (or until the maximum force has been applied). Any test fixtures that do not detach with the maximum load can be easily removed by tapping them on their side. In fact, this is a good demonstration of how easily the test fixtures can be removed in shear compared to the tensile failure mode of the actual test. More information about the pull-off test procedure can be found in ASTM D 4541 standard test method. Pull-off test is not suitable for porous films, as bonding material may diffuse inside the coating [173]. In the topple test misalignment problem associated with normal pulling are partially overcome by applying a bending moment.

A way to generate tensile stresses in the coating with the advantage of no glues and mechanical linkage is to subject it to large acceleration so that the coating is subjected to force of inertia. In the ultracentrifugal method [179] a coated cylinder is levitated electromagnetically and spun at ever-increasing speed until the coating debonds from the

substrate. The adhesion in such cases is related to the angular velocity at which debonding occurs [173].

3.6.2.1.2 Shear Type Test

The adhesive tape test provides the simplest and quickest qualitative measure of adhesion of weakly adherent film or coating [175,180].

Here it is necessary that the tape film bond be stronger than the film-substrate bond. The adhesion is characterized either by the area detached or by the peeling energy. The schematic diagram of shear type test is shown in figure 3.4.

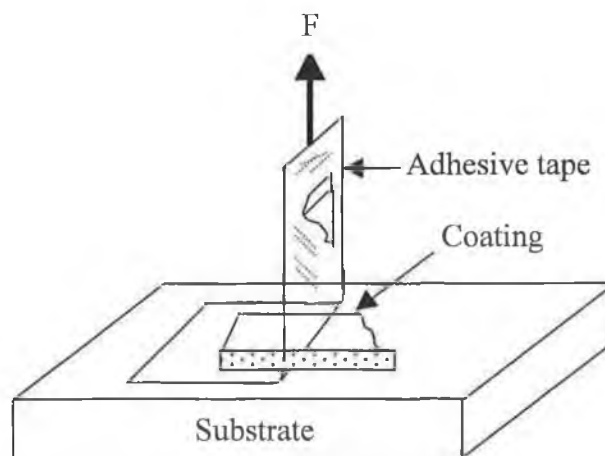


Figure 3.4: Schematic diagram of shear type adhesive tape test [173].

3.6.2.1.3 Scratch Test

All the above methods are limited to weakly adherent films i.e., the adhesion is lower than the bulk resistance of the bonding agent. In many cases tests that do not have any such constraint are needed. Among such techniques the scratch test [176,181] seems to be the most widely used method because the intensity of the stresses which can be exerted by it in the interfacial region is not limited. Coating adhesion is the load on the stylus at which the coating peels off. Theoretical analysis relating the critical load (L_c) to the specific adhesion force (F_c) is given by the relation [175]

$$L_c = \frac{KH_v F_c}{\pi R^2}$$

where the magnitude of the coefficient K depends on the model details (K can range from 0.2 to 1), H_v is the Vickers hardness and R is the radius of the stylus tip.

3.6.2.1.4 Indentation Type Test

Another method for adhesion test is indentation technique [181-183]. Here a conventional indenter type hardness machine like Rockwell, Vickers etc. is used to measure the adhesion characteristics of the film.

The Rockwell-C adhesion test is a qualitative method of measuring adhesion of coatings. The test was developed in Germany and is standardised in the VDI guidelines 3198 [184] and is expected to become a DIN standard in the near future [185]. Various researchers have used Rockwell-C test for film adhesion all over the world such as ref. [186,187]. The test method includes application of a minor load using the indenter to eliminate backlash in the load train and to causes the indenter to breakthrough slight roughness. Then the major load is applied which causes layer damage adjacent to the boundary of the indentation. When the indenter penetrates the coating, cracks propagate from the indentation point, in some cases the coating is peeled off from the substrate (Fig. 3.5). After indentation, the crack in the film is confirmed by using either an optical or scanning electron microscope. A scale is considered from HF1 to HF6 (HF is the German short form of adhesion strength) showing the adhesion properties in a sequential way as shown in figure 3.6. The advantage of this method is that it is easy to use, even in an industrial environment.

3.6.2.1.5 Substrate Plastic Straining Test

Agrawal and Raj [189] proposed a simple technique for exploring interfacial adhesion between a ductile substrate and a thin brittle coating. The substrate is subjected to an increasing tensile strain causing the film to crack and break up into segments. Strongly adhering films will break up into narrow segments, since the necessary stress level can be built up in the film over short distance. A variant of simple shear lag theory is used to obtain the following expression for the interfacial shear strength

$$\tau_* \approx \delta \rho_{\infty} \sigma_*$$

3.7

where δ is the film thickness. Equation 3.7 can be used to calculate τ^* . The film strength can be inferred from the change in crack spacing as straining continues. The advantage is that unlike other methods described above, this technique attempts to measure a fundamental property of the interface, which determines the adhesion. Other workers have used similar methods as well [49,190,191].

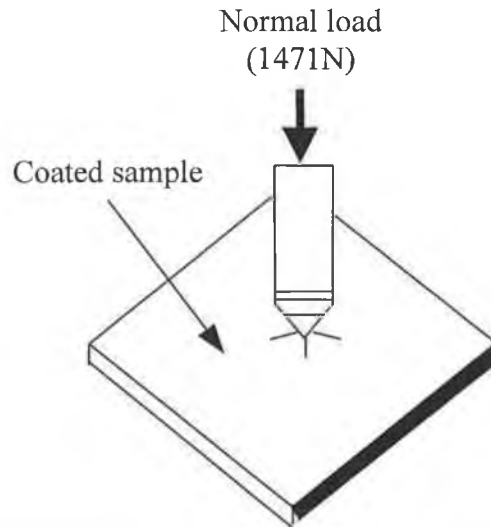


Figure 3.5: Rockwell C set-up for adhesion measurement [188].

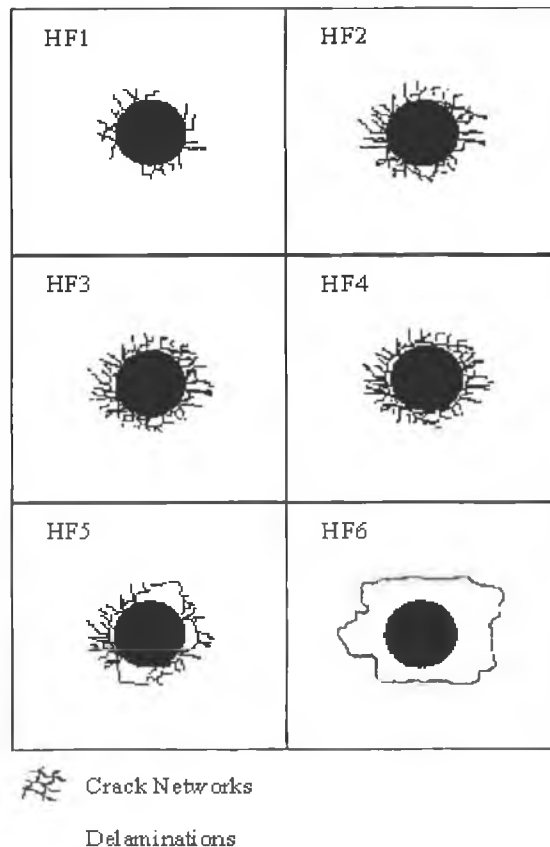


Figure 3.6: Rockwell indentation scale of adhesion characteristic value.

3.6.2.2 Pulse Laser Method

Pulsed laser [192] has also been used to measure adhesion force. In this test, a laser pulse generates successive compressive and tensile shock waves, which rapidly flex the substrate back and forth, detaching the coating in the process. The adhesion is characterized by the energy per unit area of the impulse responsible for detaching the coating.

3.6.2.3 Nucleation Method

On an atomic scale the removal of a film consists of the breaking of bonds between the individual atoms of the film and of the substrate so that macroscopic adhesion can be considered as the summation of individual atomic forces. In principle, therefore, it should be possible to relate the adsorption energy of a single atom on the substrate E_a to the total adhesion of a film. The adsorption energy of a single atom is also the term that helps to govern the behaviour of condensation atoms on a surface. It controls the lifetime before an arrived atom reevaporates and thus the nucleation of the film on the surface. Electron microscopical observations of the nucleation and initial stages of growth of a film can therefore give measurements from which E_a can be derived. The measurement of E_a using this method is details in ref. [114].

3.7 Film Thickness

In this section, the most useful techniques for determining the film thickness will be discussed in sufficient details to understand but references will be given for further details. References will also be given some film thickness measuring techniques, which are of limited applicability for general laboratory use. Some of the advantages and disadvantages of much film thickness measuring techniques have been listed in a recent article by Gillespie [193]. The best technique for a specific application or process depends upon the film type, the thickness of the film, the accuracy desire and the use of the film. These criteria include such properties as film thickness, film transparency, film hardness, thickness uniformity, substrate smoothness, and substrate optical properties and substrate size. In many cases there is no single best technique and the particular one chosen will be determined by the personal preferences of the investigator.

Since thin film thicknesses are generally of the order of a wavelength of light, various types of optical interference phenomena have been found to be most useful for the measurement of film thickness. In addition to the optical techniques, there are mechanical, electrical and magnetic techniques, which have been used for film thickness measurements. Among these, the one that has found the widest acceptance is the stylus technique, which is discussed in following section.

3.7.1 Stylus Instruments

Stylus instruments are widely used for the measurement of surface roughness and surface finishes. If a step is made in a deposited film by masking a portion of the substrate during deposition by removing part of the film from substrate, then a stylus instrument can also be used for the measurement film thickness. For the investigation of the substrate finish, the stylus should have a very small tip to produce the surface more accuracy and a very light load to limit possible penetration of the surface. In principle, the instrument compares the vertical movement of the stylus travelling across the sample surface with the movement of a "shoe" or "skid" on a smooth and flat reference surface. The latter may be an external flat or portions of the sample itself may serve the purpose. The difference of vertical displacement is converted to electrical signals by means of transducer. Various types of transducers can be used. The signal is then amplified and recorded on a strip chart, which also amplifies to a lesser extent the horizontal movement of the stylus relative to the sample surface. For the measurement of film thickness, the radius of the stylus tip can be increased to reduce the pressure and thus possible penetration of the stylus into the film.

Figure 3.7 shows the schematic of traces to measure the film thickness with stylus instrument. Because of the wide variety of vertical amplifications available with this instrument, it is possible to measure film thickness from about 20\AA up to $10\ \mu$ with an accuracy of a few percent.

In figure 3.7, film is deposited on to a substrate with part of the substrate protected by a mask so that a step can be formed on the sample. In this instance, the slopes in the trace on both sides of the step must be considered. The film thickness corresponds to the vertical distance between linear extrapolations of the lower and upper portions of the trace. With sloping traces, the thickness corresponds to the vertical distance rather than the

perpendicular distance between the upper and lower traces. This is because the vertical magnification is orders of magnitude greater than the horizontal magnification.

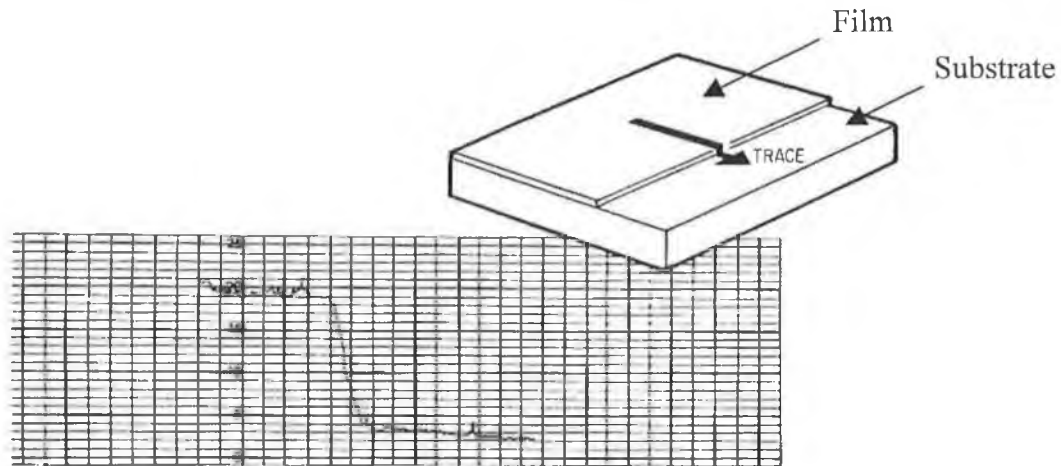


Figure 3.7: Schematic of film thickness measurement with stylus instrument.

3.8 Film Hardness

3.8.1 Nanoindentation

Indentation has been the most commonly used technique to measure the mechanical properties of materials because of the ease and speed with which it can be carried out. At the beginning of the 20th century, indentation tests were first performed by Brinell, using spherical and smooth balls from ball bearings as indenters to measure the plastic properties of materials [194,195]. The Brinell test was quickly adopted as an industrial tests method soon after its introduction and prompted the development of various macro and micro indentation tests [196]. Traditional indentation testing involves optical imaging of the indent. This clearly imposes lower limit on the length scale of the indentation. During the past two decades, the scope of indentation testing has been extended down to the nanometer range. This has been achieved principally through the development of instrument capable of continuously measuring load and displacement throughout an indentation [195,197-199]. In a recent developed system, loads as small a nanoNewton and displacements of 0.1 nm can be accurately measured. On the other hand, the recognition in the early 1970s that elastic modulus could potentially be measured from an indentation load-displacement curve [200] greatly promoted the development of instrumented indentation testing methodologies. In recent years, the study of mechanical properties of

materials on the nanoscale has received much attention, as these properties are size dependent [20,195, 201]. These studies have been motivated partly by the development nanocomposites and the application of nanometer thick film for miniaturisation of the engineering and electronic component [195, 202] and partly by newly available methods of probing mechanical properties in small volumes [195,198,199]. The nanoindenter is maturing as an important tool for probing the mechanical properties of small volumes of material. Indentation load-displacement data contain a wealth of information. From the load-displacement data, many mechanical properties such as hardness and elastic modulus can be determined without imaging the indentations [195,198]. The nanoindenter has also been used to estimate the fracture toughness of ultrathin films [203-205], which cannot be measured by conventional indentation tests.

Nanoindentation system measures mechanical properties in much the same way as conventional mechanical indentation testing systems; properties are derived from simple measurement of load, displacement and time. Figure 3.8 illustrates the most common nanoindentation test, in which a sharp diamond indenter is driven into and withdrawn from a film while the loads on and displacements of the indenter are measured.

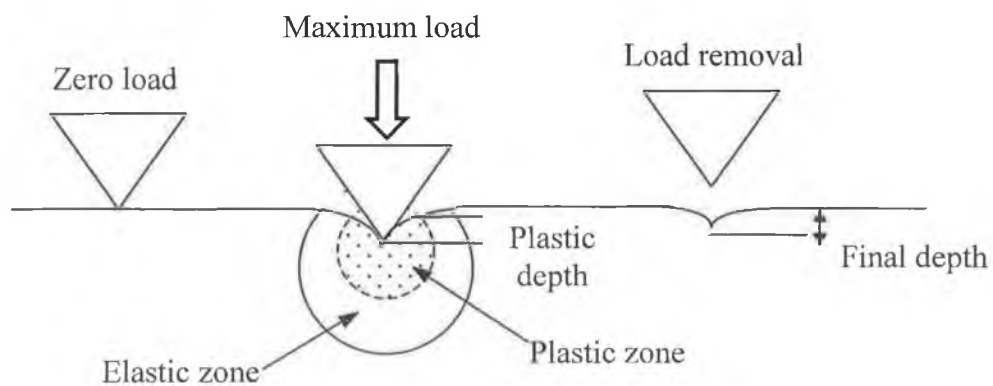


Figure 3.8: Schematic of the nanoindentation technique showing the surface indenter interaction

The Nanoindentation test is very straightforward where contact is usually made by sharp indenter, modelled in figure 3.8, as a cone. Because of this, the contact area is initially small and there is no distinct elastic region at the beginning of the test, i.e., the deformation has both elastic and plastic displacements from the outset. Furthermore, the

contact area continuously changes as the indenter is driven into and withdrawn from the specimen and these factors complicate the analysis of the data. These problems could be avoided with the use of an indenter with a flat-ended geometry. But such indenters are rarely used in practice for two reasons. First, as mentioned previously, in order to achieve a high degree of spatial resolution, it is usually desirable to make the contact area as small as possible, and this is the best accomplished using sharp indenter. Second, it is difficult to assure that the contact between a flat-ended indenter and the specimen is uniform, i.e., due to surface roughness and misalignment of the indenter, contact does not occur uniformly between the specimen and the indenter. Diamond is the most frequently used indenter material, because its high hardness and elastic modulus minimise the contribution of the indenter itself to the measured displacement [195]. For probing properties such as hardness and elastic modulus at the smallest possible scales, the Berkovich triangular pyramidal indenter is preferred over the four-sided Vickers or Knoop indenter because a three-sided pyramid is more easily ground to a sharp point [194,195,199]. It could also overcome the above problems. Another three-sided pyramidal indenter, the cube corner indenter, can displace more than three times the volume of the Berkovich indenter at the same load, thereby producing much higher stresses and strains in the vicinity of the contact and reducing the cracking threshold. This makes this indenter for the estimation of fracture toughness at relatively small scales.

3.8.2 Hardness and Elastic Modulus Measurement

Nanoindentation is a technique being used to measure the elastic modulus, E and hardness, H of thin films. For much thicker coatings ($>5\mu\text{m}$) it is possible to use microindentation test to determine the hardness and hence assess the plastic deformation and fracture properties of the coating [206]. However, as the coating thickness is reduced, much smaller indentation depths (lower loads) are required, and it is no longer possible to make accurate measurements of the indentations by conventional optical methods. In such cases nanoindentation tests, in which the displacement of the indenter is measured as a function of load are necessary [206]. In order to obtain measurements which are not influenced by the presence of the substrate, it is usually necessary to ensure that the indenter penetration is less than 10% of the coating thickness [207]. However, this rule-of-thumb is not universal. According to Pollock et al. [208] the penetration depth could be considered up to 25% of the coating thickness. Prior to embarking on a test programme, it would be

interesting to estimate the required threshold ratio of indenter penetration to coating thickness for a given coating/substrate system.

Oliver and Pharr in 1992 [198] proposed a commanding method for measuring hardness and modulus using nanoindentation methods involves making a small indentation in the thin, usually with a Berkovich indenter, while continuously recording the indentation load, P , and displacement, h , during one complete cycle of loading and unloading.

The conical indenter is another choice since, like Berkovich indenter, its cross sectional area varies as the square of the depth of contact and its geometry is unique at the tip. The load displacement relationships are nonlinear and the contact area changes continuously during unloading.

Figure 3.9 shows a cross section of an indentation and identifies the parameters used in the analysis. As the indenter is first driven into the film, both elastic and plastic deformation occurs. At any time during loading, the total displacement h is written as [198],

$$h = h_c + h_s \tag{3.8}$$

where h_c is the vertical distance along which contact is made (called contact depth) and h_s is the displacement of the surface at the perimeter of the contact. At peak load, the load and displacement are P_{max} and h_{max} respectively and the radius of the contact circle is a . Upon unloading, the elastic displacement are recovered and when the indenter is fully withdrawn, the final depth of the residual hardness impression is h_f .

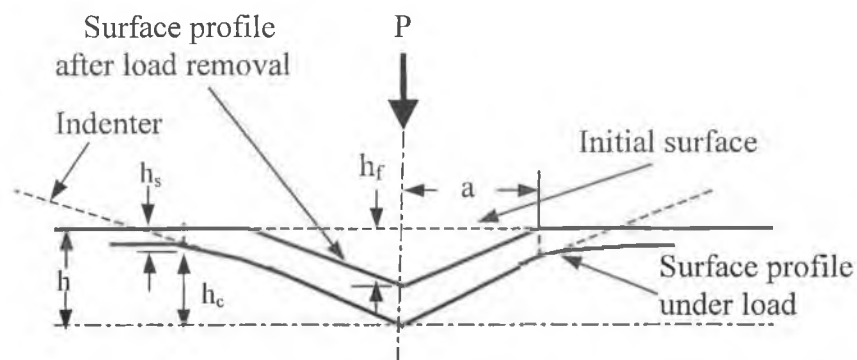


Figure 3.9: The deformation pattern of an elastic-plastic sample during and after indentation [198].

The experimental parameters needed to determine hardness and modulus are shown in the schematic load displacement data shown in figure 3.10. The three key parameters are the peak load (P_{\max}), the depth at the peak load (h_{\max}) and the initial unloading contact stiffness (S_{\max}). It should be noted that the contact stiffness is measured only at the peak load and no restrictions are placed on the unloading data being linear during any portion of the unloading. The key to the analysis procedure is that as the indenter is withdrawn, the elastic displacements are recovered and an analysis of the elastic unloading data can then be used to relate experimentally measured quantities to the projected area, A , and effective elastic modulus. For any axisymmetric indenter the relationship is

$$S = \frac{dp}{dh} = \frac{2}{\sqrt{\pi}} E_r \sqrt{A} \quad 3.9$$

where the reduced modulus, E_r , accounts for the fact that measured elastic displacement includes contributions from both the specimen and the indenter. The reduced modulus is given by [198]

$$\frac{1}{E_r} = \frac{(1-\nu_f^2)}{E_f} + \frac{(1-\nu_i^2)}{E_i} \quad 3.10$$

where E_f and ν_f are the elastic modulus and Poisson's ratio for the film, and E_i and ν_i are the same quantities for the indenter (for diamond, $E_i=1141$ GPa and $\nu_i=0.07$, data given by Simmons et al. [209]).

The equation 3.9 relates the reduced modulus, E_r , to the contact area, A , and the measured stiffness, S . The relationship holds for any indenter that can be described as a body of revolution of a smooth function and is thus not limited to a specific geometry [198]. Measurement of the initial unloading slope can thus be used to determine the reduced modulus if the contact area at peak load can be measured independently.

The area of contact at peak load is determined by the geometry of the indenter and the depth of contact, h_c . Following Oliver et al. [199,210] it is assumed that the indenter geometry can be described by an area function $F(h)$ which relates the cross-sectional area

of the indenter to the distance from its tip, h . Given that the indenter does not itself deform significantly, the projected contact area at peak load can then be computed from the relation [198]

$$A = F(h_c) \quad 3.11$$

The functional form of F must be established experimentally prior to analysis. To determine the contact depth from the experimental data, it is noted that [198]

$$h_c = h_{\max} - h_s \quad 3.12$$

which follows directly from equation 3.8. Since h_{\max} can be experimentally measured, the key to the analysis then becomes how the displacement of the surface at the contact perimeter, h_s , can be ascertained from the load-displacement data.

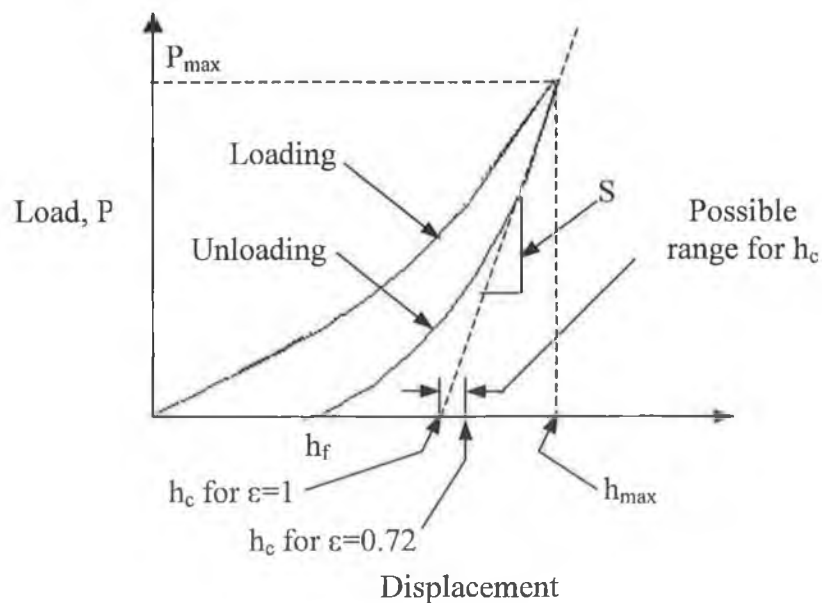


Figure 3.10: Schematic representation of a typical load-displacement curve showing quantities used in the analysis as well as a graphical interpretation of the contact depth [198]

The deflection of the surface at the contact perimeter depends on the indenter geometry. For a conical indenter, Sneddon's expression [211] for the shape of the surface outside the area contact can be used to give [198]

$$h_s = \frac{(\pi - 2)}{\pi}(h - h_f) \quad 3.13$$

The quantity $(h-h_f)$ appears in this expression rather than h by itself since Sneddon's solution applies only to the elastic component of the displacement. In addition, Sneddon's force-displacement relationship for the conical indenter yield [198]

$$(h - h_f) = 2 \frac{P}{S} \quad 3.14$$

where S is the stiffness. Substituting equation 3.13 into equation 3.14 and noting that the contact area of the interest is that at peak load, one obtains [198]

$$h_s = \varepsilon \frac{P_{\max}}{S} \quad 3.15$$

where the geometric constant ε for the conical indenter is given by [198]

$$\varepsilon = \frac{2}{\pi}(\pi - 2) \quad 3.16$$

For the flat punch, $\varepsilon=1$, and for the paraboloid of revolution, $\varepsilon=0.75$ or $\varepsilon=0.72$.

The graphical interpretation of equation 3.15 is shown in figure 3.10. For $\varepsilon=1$, the value for the flat punch, $h_s = P_{\max}/S$, and the contact depth h_c is given by the intercept of the initial unloading slope with the displacement axis. Interestingly, this is precisely the depth used by Doerner and Nix [212] in their analysis based on the flat punch approximation. Thus the current method is consistent with the Doerner and Nix approach when the flat punch geometry is assumed. For the conical and paraboloid indenters, however, the contact depths are greater than those for the flat punch, and this must be accounted for in analyses using these indenter geometries if accurate measurements are to be obtained. The range of h_c for the indenters considered here is shown in figure 3.10.

In addition to the modulus, the data obtained using the current method can be used to determine the hardness, H . It is defined that the hardness as the mean pressure the material will support under load. With this definition, the hardness is computed from [198]

$$H = \frac{P_{\max}}{A} \quad 3.17$$

where A is the projected area of contact at peak load evaluated from equation 3.11. It should be noted that hardness measured using this definition may be different from that obtained from the more conventional definition in which that area is determined by direct measurement of the size of the residual hardness impression. The reason for the difference is that, in some materials, a portion of the contact area under load may not be plastically deformed, and as a result, the contact area measured by observation of the residual hardness impression may be less than at peak load.

3.9 Atomic Structure and Characterisation

3.9.1 Bonding

According to hybridization theory (section 2.2.3), it is clearly to say that in the sp^3 configuration, a carbon forms four sp^3 orbitals which makes a strong σ bonds to an adjacent atom. In the sp^2 configuration, a carbon atom makes three sp^2 orbitals to form σ bonds and the fourth pi orbital forms a π bond with a neighboring π orbital. In the sp^1 configuration, there are two σ bonds along $\pm x$ - axis and there are pi bonds in the y and z planes. The σ bonds of all carbon sites and C-H bonds form occupy σ states in the valence band and empty σ^* states in the conducting band, separated by a wide σ - σ^* gap (Fig. 3.11) [128]. The π bonds of sp^2 and sp^1 sites form filled π states and empty π^* states which a much narrower π - π^* gap [213].

A very simple model of the atomic structure was developed some years ago, based on the properties of σ and π bonds [213]. It was argued that maximising the π bonding energy tends to cause sp^2 sites to form π bonded clusters within a sp^3 bonded matrix. The ternary phase diagram of the C-H system (Fig. 2.4) emphasises that two key parameters determine the structure and properties of DLCs; the fraction of sp^3 bonded carbon sites and the hydrogen content. Structural characterisation of DLCs focuses strongly on these two

parameters. The ordering of sp^2 sites is a third significant factor particularly for the electronic properties.

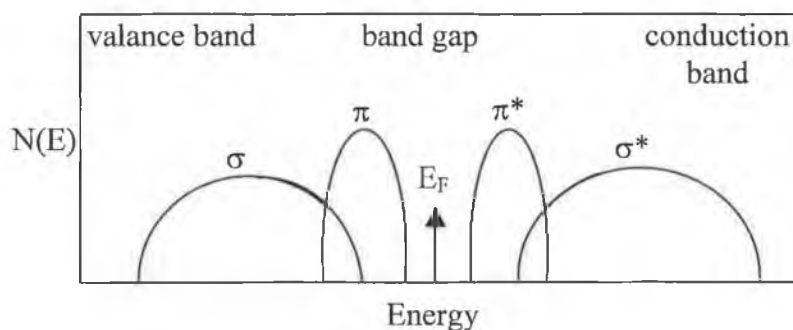


Figure 3.11: Schematic DOS of a carbon showing σ and π states [214].

Various characterisation methods have been used to determine those structural parameters. One should distinguish between methods for detailed studies such as diffraction and more routine methods for repeated monitoring which concentrate on the sp^3 content and hydrogen content. Table 3.2 compares the effectiveness and disadvantages of various routine methods to determine the sp^3 content and hydrogen content.

Table 3.2: Comparison of characterisation methods for bonding in amorphous carbon and their advantages and disadvantages

Method	Comments
NMR	Large sample needed, C^{13} , dephasing
X-ray diffraction	Not useful for amorphous structures
ESCA	Small peak shifts, due to homopolar bonding
C-H models, IR	Only sites bonded to H
ϵ_2/N_{eff}	Ok if wide spectral range
Spectroscopic ellipsometry	Useable in situ, but small spectral range
EELS	Good, but destructive and time consumable
Visible Raman	Indirect, sp^3 site invisible
UV Raman	Future method of choice
NEXAFS [215,216]	Can detects π bond and can be calculated bond length from the position of the σ^* resonance

3.9.2 Raman Spectroscopy

Raman spectroscopy is the best way to obtain the detailed bonding structure of DLCs. Raman is the most popular method and widely used, being a routine, non-destructive way to characterize the structural quality of diamond [217], graphite, DLCs and carbon nanotubes [218-230]. The Raman spectra of diamond, graphite and some disordered carbons are compared in figure 3.12.

Diamond has a single Raman active mode at 1332 cm^{-1} , which is zone center mode of T_{2g} symmetry. Single crystal graphite has a single Raman active mode, which is the zone center mode at 1580 cm^{-1} of E_{2g} symmetry labeled 'G' for 'graphite' (there is a second Raman active E_{2g} mode at 42 cm^{-1} due to interplane vibrations). Disordered graphite has a second mode at around 1350 cm^{-1} of A_{1g} symmetry labeled 'D' for 'disorder'. It corresponds to breathing vibrations rings at the K zone boundary.

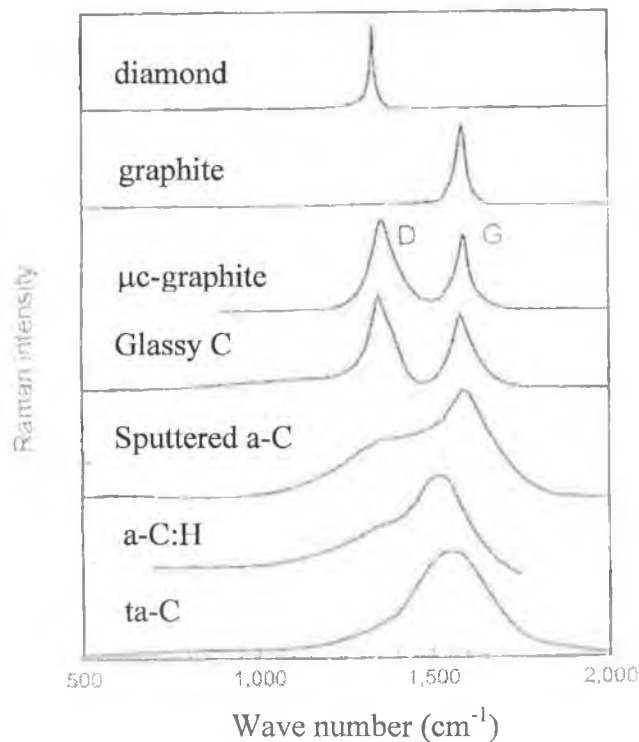


Figure 3.12: Comparison of typical Raman spectra of carbons.

An unusual and significant fact is that the Raman spectra of most disordered carbons remain dominated by these two G and D modes of graphite even when the carbon do not have particular graphitic ordering [231]. It is therefore of interest to explain this fact and

then if possible to find how Raman can be used to derive the structural information of DLCs and if possible their sp^3 fraction.

Raman is light scattering by the change in polarisability χ due to the lattice vibration [233],

$$\chi(k) = \chi_0 + \frac{d\chi}{dq} Q(k, q) \quad 3.18$$

where χ is the polarisability at wavevector k and Q the amplitude of a phonon of wavevector q . This change in polarisability causes an inelastic scattering of an incident photon (ω, k) into the scattered photon (ω', k') . Here ω is the phonon frequency. The Raman cross-section can be expressed as

$$C = k \left(\frac{\delta\chi}{\delta\omega} \right)^2 \quad 3.19$$

The polarization can occur by excitation of the electronic ground state into virtual states at energy E or into real states at E . The latter case is called resonant Raman [232].

In an amorphous material, there is a complete loss of periodicity and a breakdown of the k selection rule of optical and phonon transitions. In this case, the IR and Raman spectra of an amorphous network correspond to the vibrational density of states (VDOS) $G(\omega)$ weighted by the appropriate matrix element $C(\omega)$. This is the Shuker-Gammon formula for the Raman spectrum [233],

$$I(\omega) = \frac{n(\omega)+1}{\omega} C(\omega) G(\omega) \quad 3.20$$

where $(n(\omega) + 1)$ is the boson occupation factor.

The Raman and IR spectra should be relatively smooth and will resemble each other. This occurs in a-Si [233,234], but it is not true for the Raman spectrum of a-C. One reason for the dominance of the G and D modes is that the Raman spectra of a-Cs are dominated by

scattering of the sp^2 sites. The π states are lower energy than the σ states and so they are much more polarisable [213]. This gives the sp^2 sites at 50-230 times larger Raman cross-section than sp^3 sites [235,236]. So they dominate the Raman spectra of even ta-C, which only has a residual 10-15 % sp^2 content. Nevertheless, the Raman spectra does not simply follow the vibrational density of states of sp^2 sites. The deeper reason is that the matrix element has a much stronger effect than in σ bonded networks. The Raman spectrum becomes controlled by the order of the sp^2 sites, not by the sp^2 fraction [231]. Note that the G mode is actually the stretching vibration of any pair of sp^2 sites, whether in C=C chains or in aromatic rings [231], as shown in figure 3.13. This occurs in ethylene as well as graphite (but a high wave number). Thus G does not only mean ‘graphite’. The D mode is the breathing mode of those sp^2 sites only in rings, not in chain.

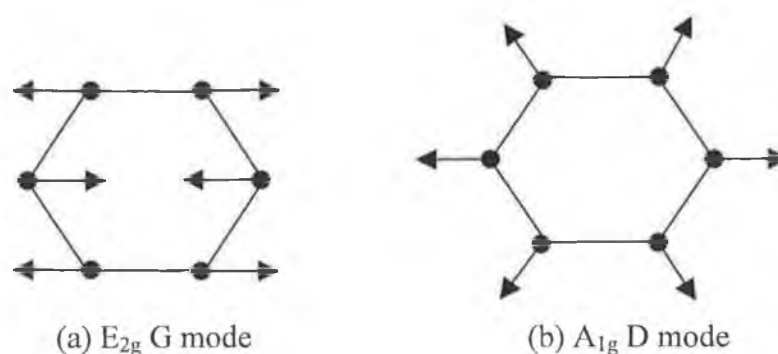


Figure 3.13: Carbon motions in the (a) G and (b) D modes. Note that the G mode is just due to the relative motion of sp^2 carbon atoms and can be found in chains as well.

There are three basic causes of the unusual Raman behavior of a-C [231].

1. Conjugated π bonds create long range polarisability. While the phonon spectrum of Si can be fitted by a nearest neighbour force field, graphite requires force up to 12th neighbours in conventional fits [237]. Recently, Mapelli et al [238] made a force field based of the π bond order and polarisability. This includes long range forces, but they are each directly derived from nearest neighbour interactions. Thus, a short range field gives rise to long range forces. The polarisability of π states is also long ranged and this gives modes quite large effective changes.
2. Both the G and D modes are bound stretching modes, which have the largest matrix element for π states. Long range polarisability further enhances their intensity. The D mode is particularly intense because it is a breathing mode of six-fold ring. In a

graphite layer, there is a constructive interference of the eigenvectors of each rings and destructive interference for rings of other orders.

3. The D mode is a double resonance [239] as described in detail shortly.

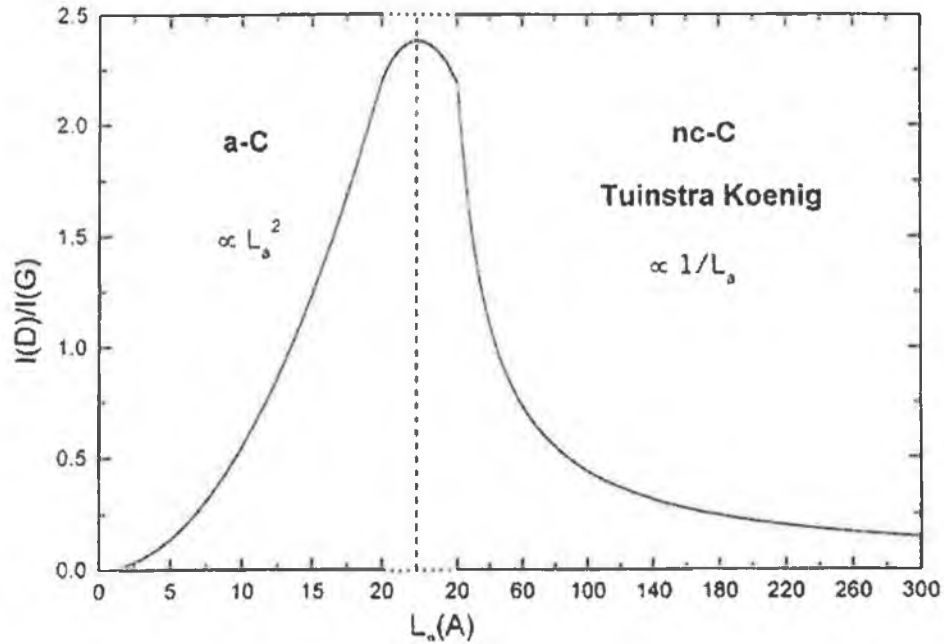


Figure 3.14: Variation of the $I(D)/I(G)$ ratio with L_a . The broad transition between two regimes is indicated.

These factors intensify the G and D breathing modes and tend to suppress modes of other symmetries. The variation of the intensity of the D mode with atomic order is interesting. Some years ago, Tuinstra and Koenig [240] noted that the intensity ratio of the D and G modes, $I(D)/I(G)$, varies inversely with the in-plane correlation length L_a or grain size of the graphite (Fig. 3.14),

$$\frac{I(D)}{I(G)} = \frac{c}{L_a} \quad 3.21$$

This means that $I(D)/I(G)$ is proportional to the number of rings at the edge of the grain. It is clear that this relationship cannot extend down to zero L_a . Recent data on the high temperature deposition of ta-C suggests that for L_a below 2 nm, the ratio decreases according to (Fig. 3.14) [231,241],

$$\frac{I(D)}{I(G)} = cL_a^2 \quad 3.22$$

The G peak is due to all sp^2 sites, but the D peak is only due to six-fold rings, so $I(D)/I(G)$ falls as the number of rings per cluster falls and the fraction of chain groups rises [231]. The important factor for DLCs is that L_a is always less than 1 nm, so that the Tuinstra-Koenig relationship is never valid for them, and equation 3.22 should be used instead.

Consider the overall Raman spectra of disordered carbons. The difficulty of this task is summarised in figure 3.15, which shows the various factors which can shift the G and D peaks in either direction and alter their relative intensity. One feature of Raman for visible photons is that it does not see the C-H bonds.

Before proceeding with a classification of the Raman spectra, it is important to note how the spectra were fitted, as this affects the numerical values. We fit the spectra with a skew Lorentzian (otherwise known as a Breit-Wigner-Fano, BWF) line shape for the G peak and a Lorentzian for the D peak [231]. The BWF is given by

$$I(\omega) = \frac{I_0 [1 + 2(\omega - \omega_0)/Q\Gamma]^2}{1 + [2(\omega - \omega_0)/\Gamma]^2} \quad 3.23$$

where $I(\omega)$ is the intensity of the Raman spectra as a function of Raman shift, I_0 is the maximum peak intensity, ω_0 is the peak position, Γ is the full width at half-maximum (FWHM) and Q^{-1} is the coupling or skewness coefficient. A symmetric Lorentzian corresponds to $Q = \infty$. Note that because of skewness the maximum of the BWF occurs at

$$\omega_{\max} = \omega_0 + \frac{\Gamma}{2Q} \quad 3.24$$

which is used in the following analysis, as the nominal position ω_0 has no fundamental meaning in Raman.

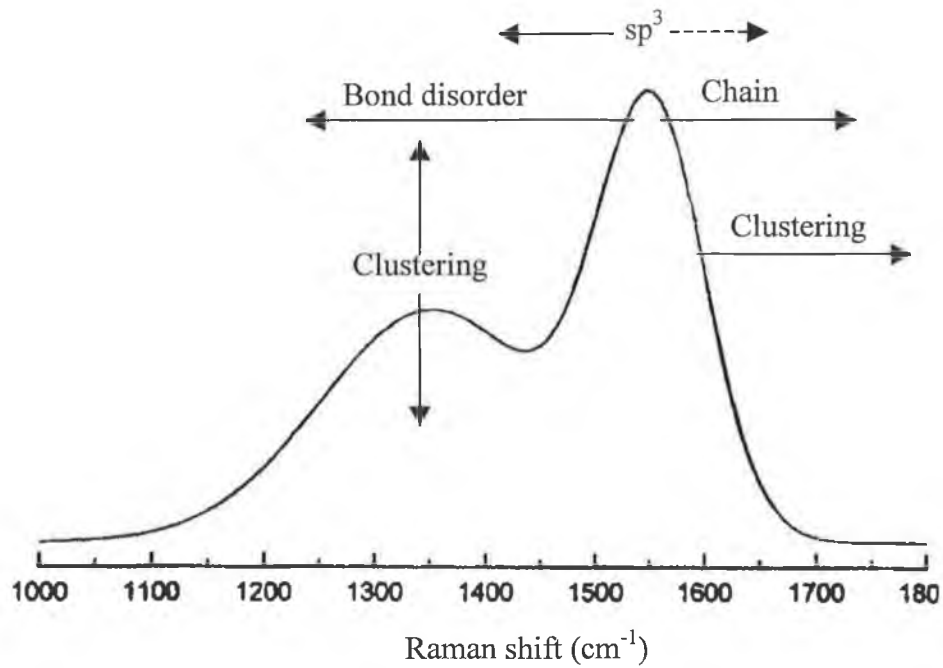


Figure 3.15: Schematic diagram of influences on the Raman spectra. A dotted arrow marks the indirect influence of the sp^3 content on increasing G position [232].

Ferrari [231] found that it is possible to classify the Raman spectra of all disordered carbons within a three-stage model of increasing disorder. The three stages are as follows (Fig. 3.16):

1. perfect graphite to nano-crystalline graphite;
2. nano-crystalline graphite to a-C, and
3. sp^2 a-C to sp^3 a-C.

Stage 1 corresponds to the progressive reduction in grain size of ordered graphite layers, while keeping aromatic rings. The VDOS is of ideal graphite. As the grain size decreases, phonon confinement causes phonons away from Γ to participate with $\Delta q = 1/L_a$. The phonon bands of graphite disperse upwards from 1580 cm^{-1} at Γ [237], so this causes an up-shift of the G peak to 1600 cm^{-1} . The D mode is forbidden in an ideal graphite layer, but the disorder causes it to appear and its intensity rises with decreasing L_a according to the Tuinstra-Koenig relation (Eq.3.21). The crossover from stage 1 to 2 is seen in ion-irradiated graphite [242].

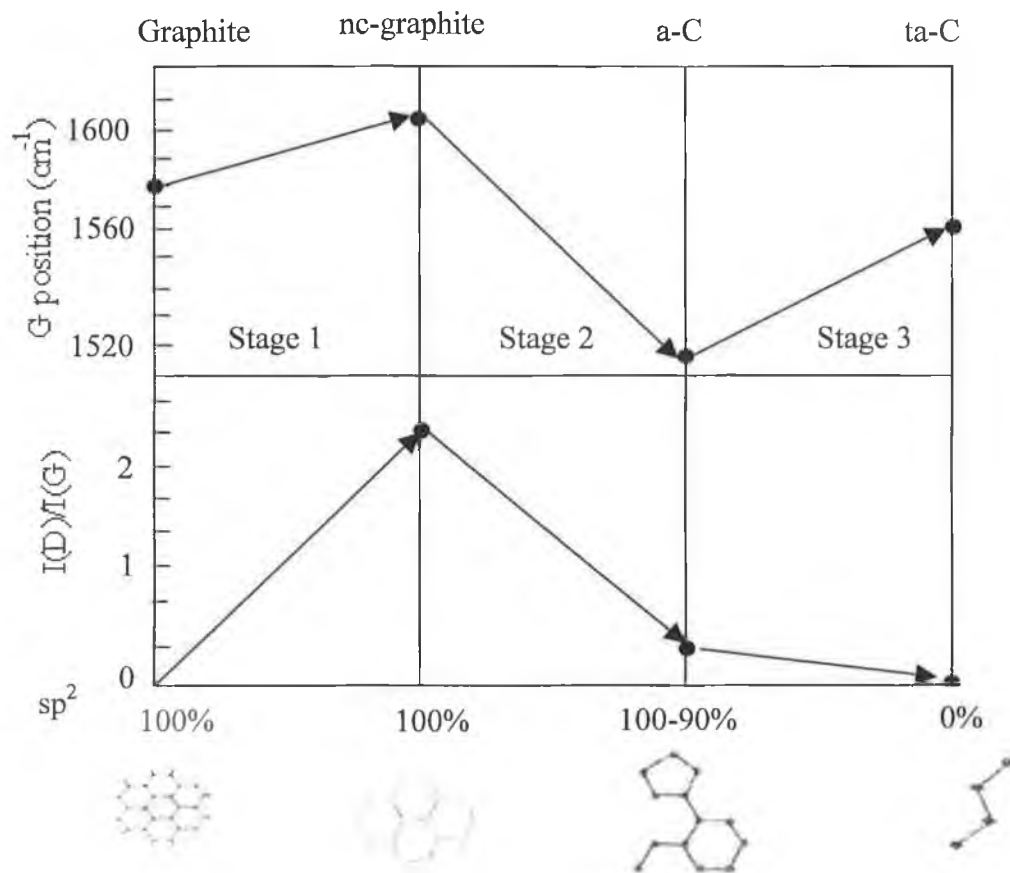


Figure 3.16: Amorphization trajectory, showing a schematic variation of the G position and $I(D)/I(G)$ ratio.

Stage 2 corresponds to the topological disordering of a graphite layer (odd membered rings) and loss of aromatic bonding, but with a purely sp^2 network. The disorder and loss of aromaticity weakens the bonds and lowers the VDOS compared to that of perfect graphite [243]. This causes the G peak to shift downwards (Fig. 3.16). The L_a is below 2 nm, so the $I(D)/(G)$ ratio falls continuously to zero. The VDOS at the end of stage 2 corresponds to sputtered a-C [244].

In stage 3, the sp^3 content increases from 0 to 100%. This changes the sp^2 configuration from mainly rings to short chains [231,243]. The bond length of chains (olefins) is shorter than that of rings, so their vibrational frequency is higher, 1640 cm^{-1} compared to $1580\text{--}1600\text{ cm}^{-1}$. These changes are seen in the VDOS [245]. Thus, in stage 3, the G mode rises, while the D peak remains at zero intensity [231]. The line-shape of the G peak becomes more symmetric as the sp^3 reaches high values [246]. Note that the maximum of the G

peak shifts up with increasing sp^3 content, but it would apparently shift downwards if a symmetric fit or the uncorrected ω_0 in equation 2.23 is used. The maximum sp^3 content corresponds to the most symmetric G peak [246].

The second major change is the absence of a D peak in a BWF fit. The G skewness falls to almost zero at high sp^3 content. Also, the G peak width first increases and then falls, as the G modes become localized on sp^2 dimers or shorter sp^2 chains with sharper length distribution. A single-Gaussian fit is poor, although it still gives a fair representation of peak position and FWHM.

This analysis allows to say that if $I(D)/I(G)$ is near zero, we are in stage 3. The G position then varies with sp^3 fraction. This is a unique relationship, which can be used to derive the sp^3 fraction from the Raman spectrum.

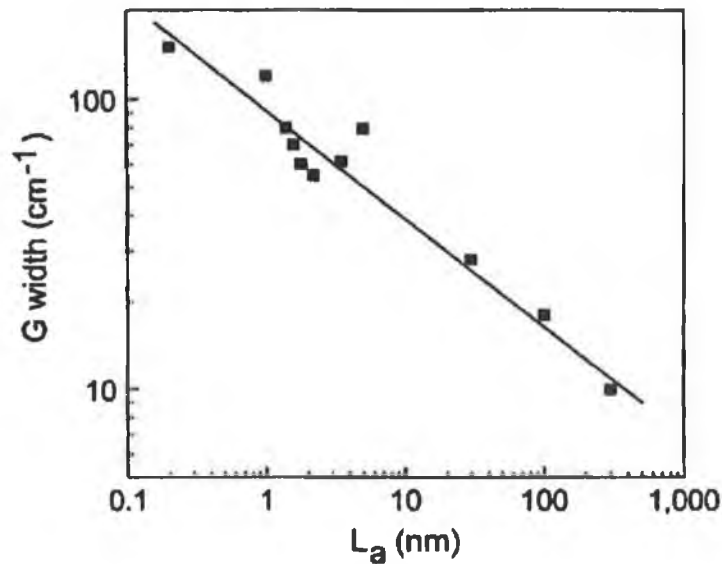


Figure 3.17: Variation of Raman G peak width with in-plane correlation length L_a , using data from Lespade et al. [248] and Schwan et al. [248].

The width of the G and D peaks scales with disorder. One way to know the correct regime is that if the FWHM of the G peak exceeds 50 cm^{-1} , then L_a is below 1 nm. Figure 3.17 shows that the G width varies in a power law fashion with L_a , using data for microcrystalline graphite, disordered C and a-C, using data from Lespade [247] and Schwan [248].

3.10 Biomedical Application of Biomaterials, DLC and Diamond

3.10.1 Biomaterials

Biomaterials have been studied for many years, but their exact definition is still controversial. One current definition is that a biomaterial is any material, natural or man made, that comprises a whole or part of a living structure or a biomedical devices that performs, augments, or replaces a natural function [249]. Ratner et al. define that a biomaterial is a non-living material used in a medical device and intended to interact with a biological system [250]. Another definition is "either naturally occurring material in living organisms or materials designed to repair humans". There are naturally many other definitions and descriptions proposed by people in the field.

Many types of biomaterials are being used, including metals, alloys, polymers, ceramics, composites and glasses. A single biomaterial or its synthetic product is used in replacements heart valves, artificial hip joints and dental implants. The design of each type of biomaterial or device has its own challenge based on the intended function and biological site. Biomaterials research is, thus, interdisciplinary in nature and in order to succeed, there must be close collaboration among people in materials science, physics, biochemistry, medicine and other fields. In spite of encouraging developments, routine long-term in vivo applications still have a mountain to climb and there is an urgent need to design and develop new suitable biomaterials. Much effort is going into the design, synthesis, and fabrication of the biomaterials and devices to ensure that they have the appropriate mechanical properties, durability and functionality [249-251]. For instance, a hip joint ought to be able to withstand high stress, an artificial heart valve should have good antithrombotic properties, a hemodialyzer should have the requisite permeability characteristics and a pump bladder in an artificial heart should flex for millions of cycles without failure [249]. The bulk structures of the materials partly govern these properties. The biological responses to biomaterials and devices, on the other hand, are largely controlled by their surface chemistry and structure. That is to say, the surface characteristics play a vital role in the functioning of a biomaterial. The rationale for the surface modification of biomaterials is straightforward. The key physical properties of a biomaterial can be retained while only the outmost surface is modified to tailor to the bio-interactions. Hence, if surface modification is properly carried out, the mechanical properties and functionality of the device will be unaffected but tissue interface-related

biocompatibility can be improved [250]. For instance, in the design of medical devices, it is necessary to consider potential corrosion and degradation due to the exposure to a variety of body liquids. There are two methods of prevention by either selecting a resistant material or protecting the material, and the latter is often chosen [251].

Materials used for body implants include metal alloys such as cobalt-chrome, stainless steel (316L and 304) and titanium alloy and a variety of ceramics and polymers. The use of prosthetic implants is increasing rapidly. Hip replacements alone now exceed 200 000 annually in the USA with a similar number in Europe [63]. Failures of such joints are however still common with average lifetimes for artificial hips of around 10 years for patients over 70 years of age. The failure rate is even more in knee implants. The major concern is increasing total joint replacements in younger patients, which requires more demanding and longer term performance criteria for these implants. Materials suited for prosthesis are those which have good biotolerance, corrosion resistance, low coefficient of friction and can withstand cyclic loading in the presence of body fluids. Prosthetic implants today are commonly made of cobalt-chrome alloy, 318 titanium (Ti-6Al-4V) or 304 stainless steel (Fe-18Cr-8Ni) with ball sockets or tibia head usually made of a polymer such ultra high molecular weight polyethylene (UHMWPE). Recently a new alloy of titanium, Ti-13Nb-13Zr has been suggested [252]. This alloy is yet to be commercialised.

3.10.2 Biocompatibility of DLC

Biomedical materials have become very important subjects in the modern medicine. Before any material is used for the medical purpose, it is necessary to have a series test in terms of its biocompatibility and toxicity to the tissue.

It is now widely accepted that for any medical device, it is difficult to combine in one material all the properties required for excellent in functionality and biocompatibility. As a result, compromises may have to be made or combinations of two or more materials used to develop the best overall properties. Because biocompatibility is most frequently controlled by the characteristics of the materials surface, an increasingly common solution to this dilemma is to select an appropriate engineering material to provide the general functional properties and to modify the surface in some way in order to optimise the biocompatibility. Moreover, the functionality itself may be better achieved through the use of surface characteristics that are quite different to those of interior, involving perhaps a

hard, wear resistance surface on a softer but tough substrate, or a lubricious surface on a flexible material. There are, of course, several constraints to the use of such combinations, including the need to achieve bonding between substrate and coating and the practicality and cost implication of the more complex production. However, medical device manufacturers have already shown considerable interest in the possibilities offered by state of the art surface treatment.

There are two fundamental reasons why an inert impervious coating is needed for materials planned in the body: first, because corrosion is one of the major causes of the failure of metal implants and second, because it is suspected that tumours may be caused by the release of ions or small particles from some metal implants [253, 254].

It has been known for a long time that carbon, in the form of pyrolytic graphite for example, can be applied to several types of material to improve either overall biocompatibility or specially blood compatibility. Several new methods and improvements are now available for the application of different forms of carbon. In particular, so called diamond-like carbon is currently the most popular form and widely described as a major advance for the surface treatment of biomaterials. DLC coatings adheres strongly to the various metals and alloys used as implants and as they are unreactive and impermeable could protect such implants against corrosion and act as a diffusion barrier. It is of course essential that DLC is acceptable to the body and its biocompatibility was therefore investigated using cell-culture techniques. [255].

3.10.3 Diamond Like Carbon and Diamond

In spite of development of new materials, often better functionality can be achieved by having a surface, which is quite different to the interior. Coatings are increasingly being used in the medical related applications as enhancement rather than protective layers. For example, prosthetic implants can be coated to ensure biocompatibility to improve corrosion resistance and wear resistance or to act as a diffusion barrier.

Diamond and DLC films have the combination of properties, which make them a very attractive industrial material. Table 3.1 lists the properties and few applications of these coatings. Several excellent reviews detailing the applications of the diamond and DLC

films are available in literature [120,256-262]. However, there is a great potential to use these coatings for biomedical applications.

DLC coatings, because of their mechanical and wear resistance properties [263,264], low coefficient of friction [264], corrosion resistance and biocompatibility [264-267] are of interest as a protective coating in biomedical applications [268,269]. Of prime importance is the strong adhesion of DLC to various metals and plastics used in bioengineering [270]. Areas where DLC films are being considered for biomedical applications are as coating for metallic orthopaedic pins [269], heart pace makers [123], surgical needles [268], impervious film to improve biocompatibility and prosthetic implants [63,271]. It is expected that a DLC film will substantially reduce, may be eliminate altogether, metal-ion release from implanted alloys, protect degradable polymers from tissue fluids, reduce tissue damage during surgery and control the release of leachables. Several research groups are investigating films for biomedical applications [63, 272,273].

Recently the use of a-SiC:H [274] and TiN [275] coating for artificial heart valves to improve blood compatibility has been suggested. Since both the structure and electronic properties of DLC coatings are better than those of above coatings, it can also be used to coat artificial hart valves with improved results [276]. DLC coatings deposited on stainless steel and titanium alloys used for components of artificial heart valves has been found to improve mechanical reliability and satisfy biological requirements [123]. Mitura et al. [272] have studied the wear behaviour of DLC coated stainless steel orthopaedic screws and found that there was no significant wear even after 100 subsequent screwing operations into the bone. They also found very good biotolerance and no corrosion. DLC coated dental prosthesis in humans have also been found to show no change after several months [273].

In prosthetic implants the major cause for failure is corrosion of the implant by the hostile environment in the body [267]. Another causes of implant failure is wear resulting in release of wear particles inside the joint. It is well established that the biological response to particulate wear debris can be very different to that of the corresponding bulk material [277-279]. The wear particles are often softer material (such as UHMWPE) and are produced as a result of friction between two components. Such particles can stimulate inflammatory response in the joint. The corrosion of the implant can lead to increase wear

causing severe body reactions and failure of the implant. In theory both the corrosion resistance and the wear resistance can be increased by covering the surface of the implant with a suitable impervious coating. It has been suggested that thin hard coatings with low coefficient of friction can be used to solve these problems of excessive corrosion and wear in prosthetic implants.

Diamond like films have the right combination of properties to be used as protective wear resistance coatings for the prosthetic implants. However, with regards to wear, inspite of many predictions there is no clear indication that DLC will improve the long term wear performance of joint replacements and indeed there is great danger that the performance could be reduced. *In-vitro* [280] and *in-vivo* [281] studies on the performance characteristics of DLC coated knee joints are being done. Results of these experiments will help decide the future of DLC coated prosthetic implants. Even though DLC is biocompatible [265-267], its adhesion behaviour in fluid is unknown and is matter of great concern. Any delamination of DLC coating in service as a prosthetic implant can cause enhanced abrasion of the polyethylene, perhaps catastrophically.

On the biomedical front diamond films have had limited attention. It has been proposed as surgical blade coatings to be used in ophthalmology and cardio-thoracic surgery [282]. Diamond surfaces are generally hydrophobic and have low friction against living tissue. They are also biocompatible, but their extreme hardness makes them unsuitable for many biomedical applications.

3.10.4 Environmental Stability of Coating

Whatever be the application, stability of diamond and DLC coatings during service is essential, particularly so when the coated component is exposed to different environments. Applications such as cutting tools, drilling tools, windows in aircraft and missile seekers, in pipes for carrying slurry or chemicals or for biomedical applications like prosthetic implants, require that coating should have both the desired combination of mechanical and corrosion resistance properties and mechanical stability during exposure to fluids during applications. In most of the above applications corrosion and wear are the biggest problem. If the coatings degrade or delaminate during service, it can cause enhanced wear and loss of other mechanical properties. Therefore, it is essential to study the effect of various environments on the adhesion strength of diamond and DLC coatings.

The diamonds like hydrocarbon films are extremely inert to many aggressive chemical reagents [283]. For example, organic solvents and inorganic acids including HF at room temperature do not attack them. The films are unaffected by a solution of three parts H₂SO₄ and one part HNO₃ (concentrated acid) at 80 °C. This reagent will dissolve all other hydrocarbon polymer and graphitic carbon. The chemical inertness of these DLC may cause by their extreme impermeability. As a result of their chemical resistance, DLC films can be used as corrosion-resistant coatings. The films and their modifications can be removed from a substrate by exposure to atomic oxygen or fluorine species generated in a plasma, which react with the carbonaceous films to produce volatile CO_x and CF_y species which are pumped out of the system. Reactive ion etching in oxygen- or fluorine-containing plasmas can be used to pattern DLC films. The film also trap argon for several years [284].

3.11 Summary

Diamond like carbon and diamond films have a unique set of properties, which make them very attractive as an industrial material and open up new avenues of applications. The deposition techniques are now more or less standardized and good quality films can be easily achieved (see chapter 2). Almost all metals and several plastics and ceramics can be easily coated. However, the limiting factors are residual stresses in the films and its effect on adhesion strength. Though thermal stresses that develop in diamond deposition are well understood and often clearly identified, there is very little known about the development of intrinsic stresses in these coating, especially for DLC films. Knowledge of what causes these stresses in DLC and diamond films, how the deposition conditions affect them or how to control or reduce them is very limited and often contradictory [156,285,286]. A clear cut understanding in this direction is needed to realize all the potential applications of these coatings. At present there is little quantitative agreement in stress measurement and adhesion strength value obtained from different tests methods by different groups. Rather, individual test to measure residual stress and adhesion are tailored for comparison of the same film substrate combination prepared in different way.

New areas of application for DLC coatings are being proposed. Biomedical application of these films seems to have the potential but proper and detail investigations of film quality need to be done. It is important not only to get the set of optimum film properties but also

to see there is no loss of adhesion strength and other mechanical properties of the coatings on biomedical application.

Chapter 4
DLC Deposition Equipment

4.1 Introduction

This chapter introduces the operation of the DLC film deposition equipment. A neutral beam saddle field fast atom source (Microvac 1200 DB, Ion Tech Ltd.) is used to deposit DLC thin films. A carbon containing gas introduced into the chamber and becomes energetic neutral particles. These energetic neutral particles are directed towards the substrates to form the films. The equipment is detailed in accordance with its two primary functions: one is the chamber pump down equipment and the other is saddle field fast atom equipment. The system is depicted in figure 4.1.

4.2 History

The experimental equipment was custom built by Ion Tech Ltd. for Pfizer Ltd. in 1989. Howmedica commenced work on deposition DLC films on to articulating surfaces of artificial hip and knee implants. Two upgrades were subsequently made to the equipment which included the addition of the 'roots blower' to aid a faster and more efficient pump down of the chamber and the upgrading of the power supply for the source. The equipment was donated to Dublin City University (DCU) in 1997 for continued production of good quality DLC.

4.3 Pump Down Chamber

Three pumps are diffusion pumps (vapor pump E0400/7000), rotary pump (E2M80 series) and roots blower (EH250 series) are connected to the deposition chamber for pump down the chamber. The schematic of the pump down in this experimental system is shown in figure 4.2.

4.4 Coating Equipment

The coating as well as etching equipment of the Microvac 1200 DB is based on saddle field source which both produces a neutral beam at low temperatures. The sources are the B95 and the FAB 104. Only the B95 was used in this project. The source has its own power supply and the cooling water supply. The source's configuration is relatively simple in construction as can be seen in figure 4.3.

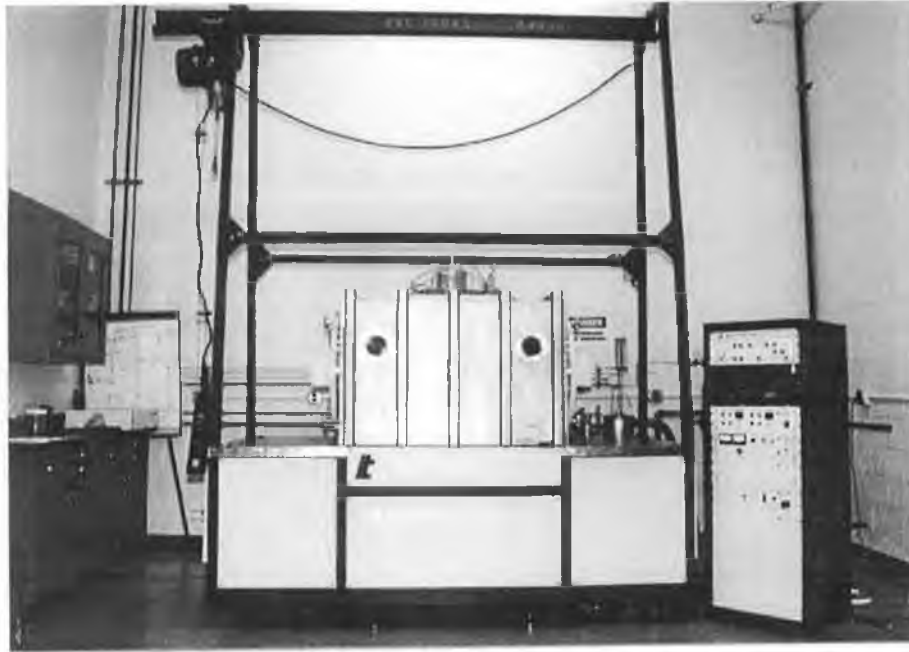


Figure 4.1: DLC film deposition system.

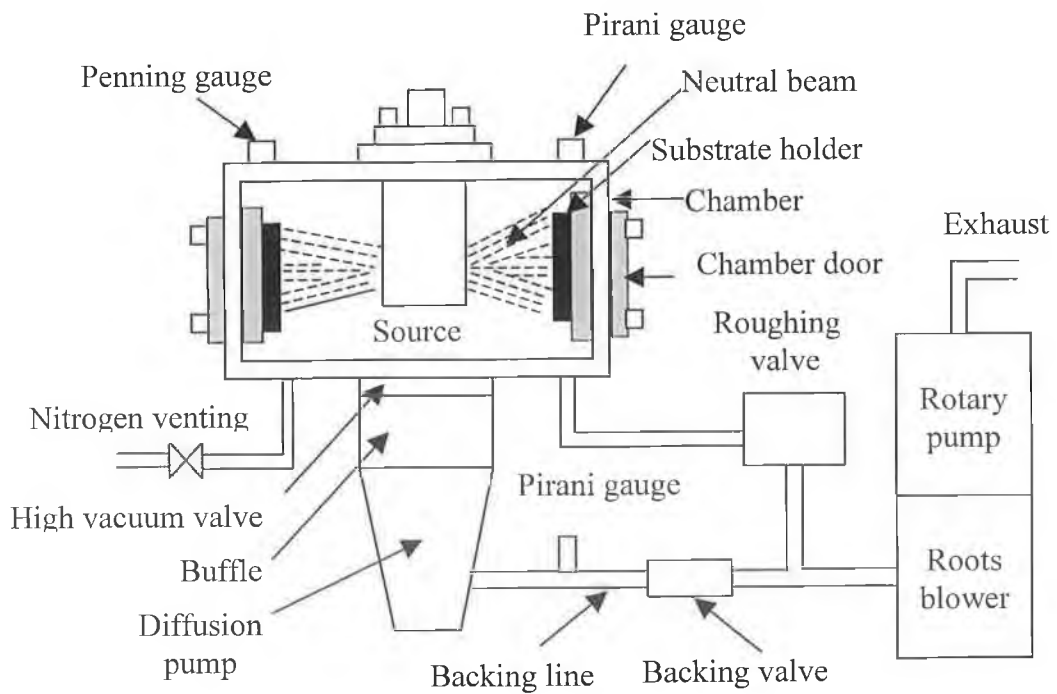


Figure 4.2: Schematic of pump down of the DLC deposition chamber.

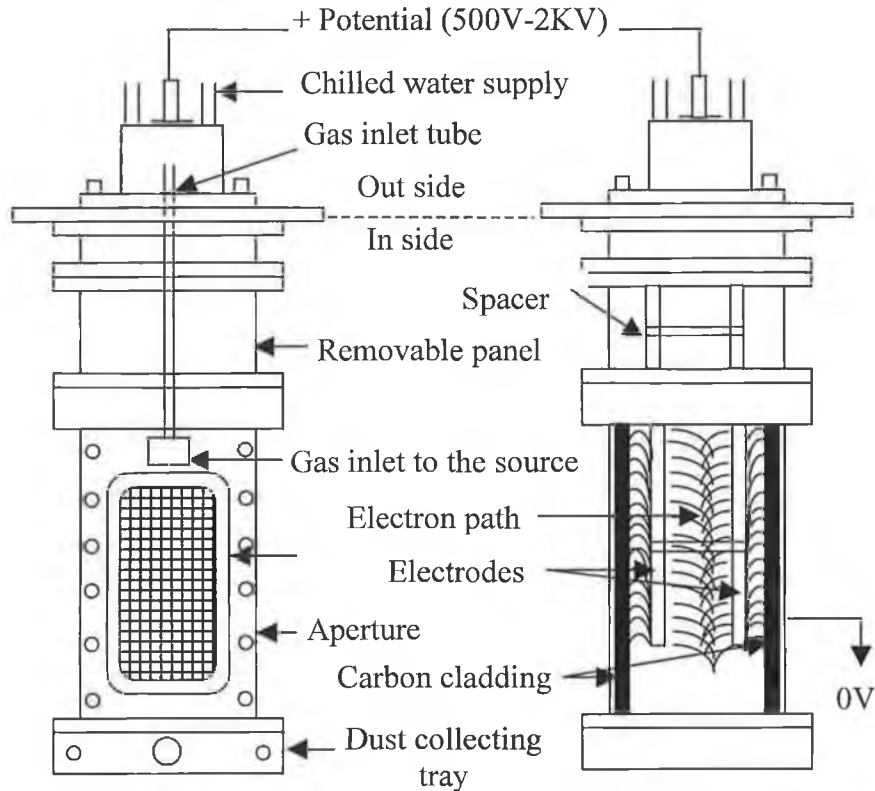


Figure 4.3: Schematic of the fast atom (FAB) beam source.

4.5 Fast Atom Beam (FAB)

A fast atom beam defined as energetic neutral particles ranging in energy from a few electron volts to several thousand electron volts [287,288]. The development of the saddle field fast atom beam source allows material processing of amorphous thin films in a very uncomplicated manner. Glow discharged (GD) decomposition by either dc or rf (radio frequency) excitation of the hydrocarbon gases is the more conventional technique. Both of these methods of plasma excitation have certain draw backs and one would prefer to have advantages specific to both these techniques and none of their inherent disadvantages. It may, at first sight, appear to be a rather strange idea. However, saddle field source deposition does indeed come very close to this idea. The potential profile [289] of the saddle field FAB discharge together with that dc and rf plasma enhanced chemical vapour deposition discharge are shown in figure 4.4. From this figure it is clear that the potential distribution in the saddle field source somewhat similar to that in the rf diode. Therefore this system achieves some of the advantages of the rf source but only requires dc supply.

Earlier FAB sources were used for cleaning, milling, etching, thinning (the specimen prepared for TEM) and sputtering applications and also for a variety of surface analysis techniques. Franks [291] first used the source to deposit DLC films. His attempts to deposit DLC films using methane (CH_4) as the source gas led to the etching of the substrates.

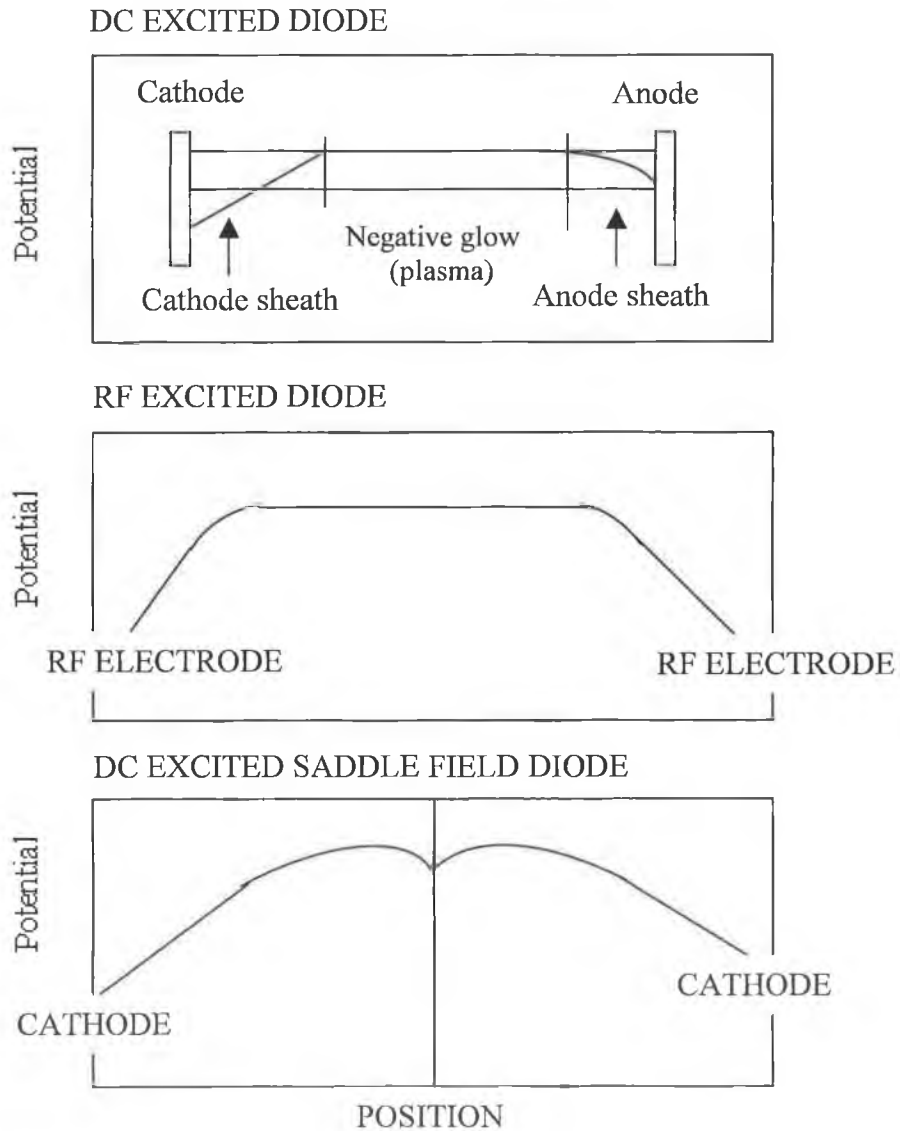


Figure 4.4: Potential profile of saddle field FAB discharge together with that of dc and rf PECVD discharges [290].

4.6 Evaluation of FAB Source

The principle of saddle field source is based on McIlraith's discovery of the electron electrostatic oscillator in 1965 [292-294]. Ion sources are known to accumulate charge at the surface of the film, which adversely effect deposition rate and properties of the film. A neutral beam source was developed in the early 1970s [294], which does not have this problem. The saddle field source configuration was subsequently developed between the 1970s and 1980s. The working model of a FAB source is shown in figure 4.5.

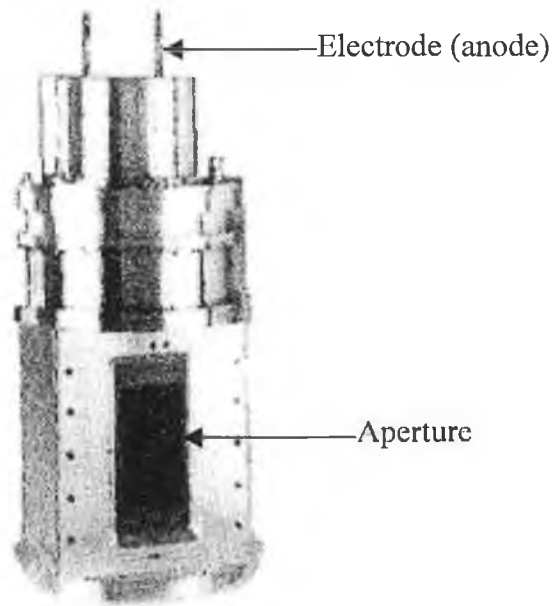


Figure 4.5 (a): Saddle field source type B95 with a beam aperture of 75x150 mm.

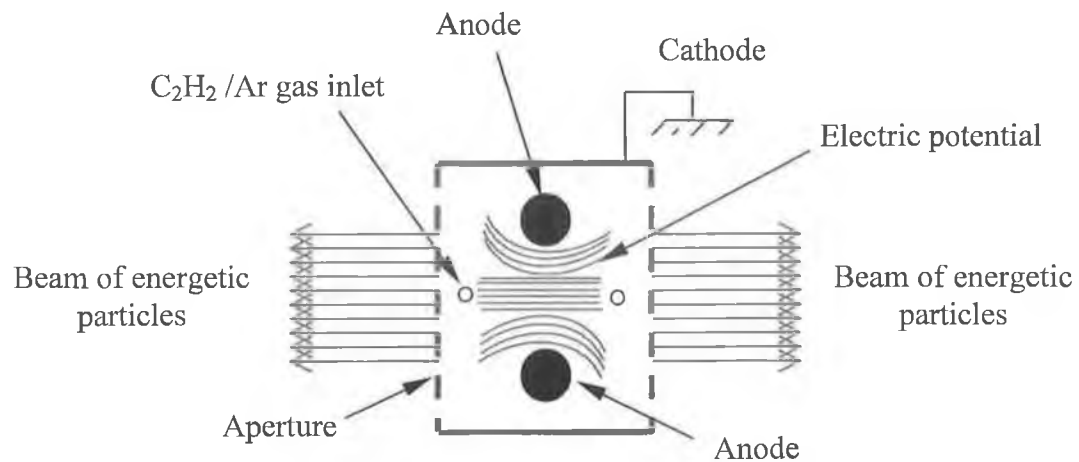


Figure 4.5 (b): Schematic of plan view of the saddle field fast atom beam (FAB) source.

When a positive high voltage is applied to the rod anodes, cold cathode discharge occurs between the anodes and cathode. Electrons produced during the glow discharge oscillate at high frequency backward and forward through the anode (Barkhausen-Kurtz Oscillation). The axial magnetic field, which is produced by the current from the anodes increases the path length of the electrons by making them travel in a helix about the axis. A large number of ions are produced when these electrons collide with gas molecules. These ions are then accelerated towards the cathode. Most of these ions are converted into fast atoms via two processes: the ions are neutralised in resonant charge transfer collisions with gas molecules, or recombine with low energy electrons near the cathode ends. The fast atoms thus produced are emitted through the apertures in the cathode.

The FAB source were also claimed by the manufacturer to be almost free of ions, which were thought to be neutralised by recombination with emitted secondary electrons produced by the collisions of ions with the cathode near the exit aperture. The symmetric resonance charge exchange between fast ions and slow neutrals can be the mechanism of neutralisation [294]. The mechanism does not require the matching of momentum of high energetic ions and slow secondary electrons and is considered as the more probable one. A high concentration of the ions with low energies in the source output region can be predicted from this suggestion. The detailed studies of the high energy fluxes produced by both cylindrical and spherical FAB sources revealed that the ion to neutral ratio and energy distribution of ejected particles is greatly determined by the voltage supply to the anode, gas pressure in the source and type of gas. Fusao Shimokawa et al. [287,295] in figure 4.6 compares the energy distributions of the residual ions and the fast atoms. In both cases, the main peak in the energy distribution coincides with the discharge voltage of the FAB source. This suggests that the kinetic energy of the original ions is retained when they become fast atoms. Thus the fast atom beam is produced by collisions with no energy losses. Therefore fast atoms are probably formed from resonant charge transfer collisions and electron ion recombination near the beam-emitted aperture. Nevertheless, saddle field source produces ion and atom beams with a relative content of energetic neutrals higher than any known sources.

Different electrode (anode) configurations do not change the energy distributions. Fusao Shimokawa et al. [287] proposed that the energy distributions for a twin rod anode configuration and a ring anode are similar, indication that the potential distributions of the

source are almost the same. Figure 4.7 shows the energy distribution and compared for different FAB source electrode configurations for a constant FAB source discharge voltage of 1.5 kV.

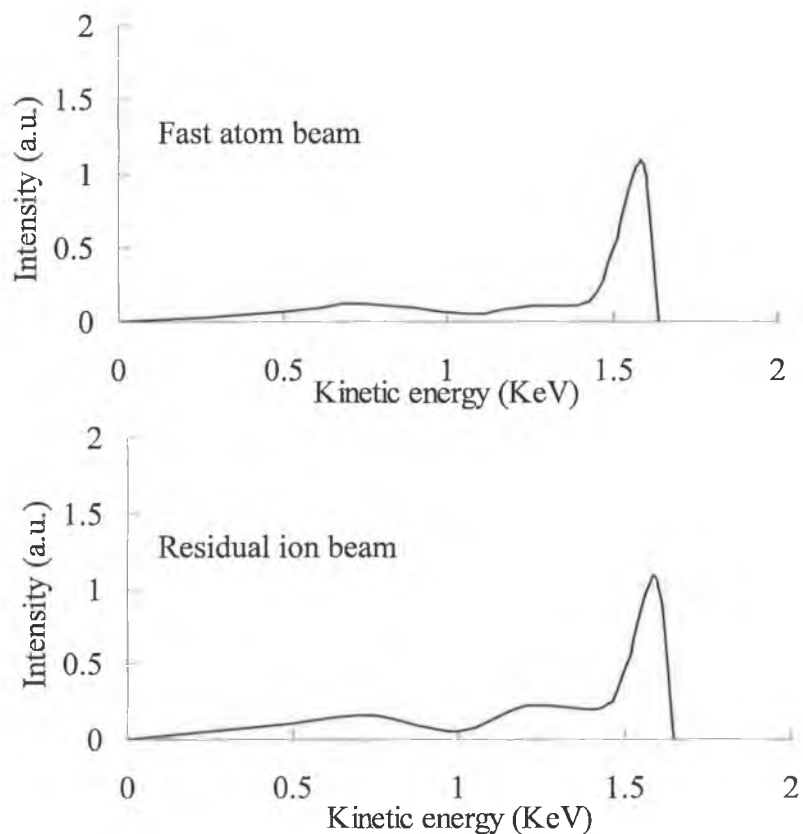


Figure 4.6: Energy distribution spectra of residual ions and fast atoms in the beam; Argon gas pressure 8×10^{-3} Pa and discharge voltage 1.6 kV.

4.7 Beam Neutralisation

To measure beam neutralisation, a deflector made of a Mo target and electrodes with a slit can be used. Deflector arrangement provides in front of the aperture of the FAB source allows the separation of radicals. When no voltage is applied to the deflector both residual ions and fast atoms bombard the Mo target. The residual ion current and a secondary electron current flowing through the target are given by,

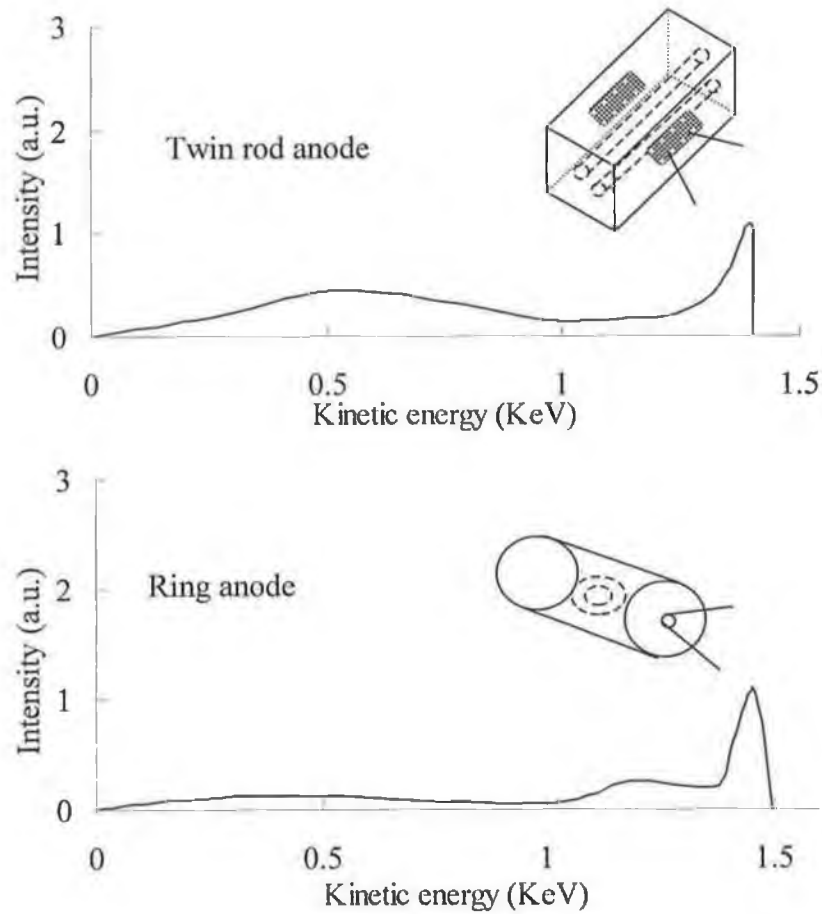


Figure 4.7: Energy distribution of fast atoms for two different electrode configurations: discharge voltage 1.5 kV [287].

$$I = N_i + \gamma_i N_i + \gamma_0 N_0 \quad 4.1$$

where N_i is the number of ions per second, N_0 is the number of energetic neutral particles per second, γ_i is the yield of secondary electrons from target surface under ion bombardment and γ_0 is the yield of secondary electrons under energetic neutral particle bombardment. When several kV are applied to the deflector, the residual ions are eliminated and only fast atoms bombard the Mo target. The secondary electron current flows through target. This current is expressed by

$$I_0 = \gamma_0 N_0 \quad 4.2$$

The beam current density is calculated as $I_0 / (S\gamma_0)$, where S is the target area. The beam neutralisation coefficient can be estimated by calculating the current with the deflector off and on, and from secondary electron yield from the Mo target under bombardment by ions and fast atoms. The beam neutralisation coefficient is determined by combining equation 4.1 and 4.2 [295, 296],

$$\eta = N_o / (N_i + N_o) \quad 4.3$$

$$\text{or, } \eta = I_o (1 + \gamma_i) / [I_o (1 + \gamma_i) + \gamma_o (I - I_o)]$$

Saranghi et al. [296] was used argon gas for the estimation of beam neutralisation coefficient. The neutralisation coefficient was estimated to be $\approx 90\%$ and was found to be almost independent of the power applied to the FAB source.

4.8 Advantage of Saddle Field Source

DLC films are commonly prepared by the plasma enhanced chemical vapour deposition (PECVD) technique or by using ion sources of different kinds. In all these techniques, ions play an important role in the formation of DLC films. The presence of significant amount of unbound hydrogen in these DLC films has been identified to cause high compressive stress [297]. It is believed that DLC films prepared by the rf self-bias technique incorporate more unbound hydrogen than the films prepared by the dc discharge technique. This is because to develop sufficient high self-bias voltage, one is often required to input higher rf power than in the case of dc PECVD. The dc technique also has certain inherent limitations, the most important one being charging of insulating substrates. Another disadvantage in using ion sources is the accumulation of the positive charge on the film surface when the film and/or substrate have high ohmic resistivity [294]. This leads to a worsening in both film deposition rate and its properties after a certain thickness. The saddle field fast atom technique (FAB) can eliminate all these problems in an elegant fashion. FAB bombardment can be used instead of ion beam bombardment in sputter deposition, etching and surface analysis [298]. The source operates on a dc power supply and the beam that comes out from the source is almost neutral so that insulating substrate can easily be coated without any charging effect. FAB techniques are also better for forming fine patterns because there is little repulsion between particles in the beam, which

causes beam spreading in an ion beam. Furthermore, a FAB source does not need a hot filament to induce plasma and it has a long operational life time when used with reactive gases. The advantages of using of FAB source to grow DLC films as compared to conventional rf self-technique are: (1) no rf matching problem, (2) uncomplicated power supply, (3) ease of scale up (modular design) and (4) no need to take care the system geometry to realise the needed asymmetry (simplified system geometry) [290,297].

Dry etching technology has become key process for producing devices and for manufacturing intricated circuits [288]. Various etching techniques such as reactive ion etching (RIE), reactive ion beam etching (IBAE) are used to produce these devices. Because these techniques are based on ions, charge assisted damage caused by energetic particles in metal-oxide-semiconductor device fabrication is also a serious problem that essentially cannot be avoided. FAB bombardment techniques are advantageous for etching, insulator and composite materials, because the specimen surface does not become charged. Since in FAB there are no space charge effect, fine patterns can be formed because beam particles do not repel each other.

The production of saddle field source could be possible near room temperature that is in the range $\sim 20-100$ °C [299]. This facilitates the deposition on polymeric substrate (e.g. UHMWPE, PTFE etc.) and other temperature dependent substrates. Another advantage of this type of source is the fact that the beam is almost 100% neutral [296], which ensures there is a reduction in the surface damage on the substrate due to energetic neutral particle bombardment.

Chapter 5
Experimental Procedure

5.1 Introduction

This chapter describes the experimental procedure including sample preparation, deposition method and mechanical and chemical characterisations of DLC films.

5.2 Materials Used

Three different implant quality materials; 316L stainless steel, cobalt chrome alloy (CoCr; wt %: 69 % Co, 25 % Cr and 5% Mo) and titanium alloy (Ti6Al4V) were considered for the deposition of DLC films. Two different substrates in the form of round disks with diameter 25 mm and thickness 8 mm (316L stainless steel, CoCr and Ti6Al4V alloys) and 0.2 mm (316L stainless steel only) were used. The chemical composition of the 316L stainless steel is given in table 5.1. Glass substrates with dimension 76 mm x 26 mm x 0.75 mm also used to characterise the uv absorption of DLC films.

Table 5.1. Chemical composition of AISI 316L stainless steel (wt.%)

C	Cr	Ni	Mo	Fe
0.03 max	18	10	3	bal

5.3 Sample Preparation

The test samples with the dimension of 8 mm thickness and 25 mm diameter had their surface smoothed by polishing with different grade of emery papers. The samples were wet polished by the emery paper of grid no. 240, 600, 800 and 1200. Final polishing was carried out (both thick and thin samples) with 0.25 μm diamond suspension on Chemomet velvet cloth to get similar substrate surface roughness. The Buehler Motopol 2000 semiautomatic specimen preparation unit was used to polish the samples. After polishing, the substrates were then cleaned consecutively in acetone and 1-1-1 trichloroethane at 40 $^{\circ}\text{C}$ for 30 minutes each in an ultrasonic bath, in order to remove any chemical residue. They were subsequently dried in air prior to conducting the experiments. Pre-cleaned glass substrates were used in their supplied condition. The substrates were placed on the

substrate holder (see Appendix A2) which 400 mm distance from the source in the chamber.

5.4 Current -Voltage (A_c - A_v) Characteristics

To investigate the current-voltage characteristics, argon and acetylene gas were used with different source voltage (discharge voltage) and current (discharge current). Argon was used for etching while acetylene was the feed gas for deposition. The pressure level was in the range of 1.8×10^{-3} to 4.6×10^{-3} mbar. Discharge currents with respect to discharge voltages were recorded during etching and deposition.

5.5 UV Absorption of DLC Films

Glass substrates were used to investigate the ultraviolet absorption of DLC film. The deposition chamber was initially pumped down to $<6 \times 10^{-7}$ mbar. The films were deposited at a pressure range of 1.8×10^{-3} to 4.6×10^{-3} mbar and the anode currents were 0.4, 0.6 and 0.8 A. The anode voltage varied in the range of 0.75 to 1.5 KV. The deposition time was kept constant at one hour. All samples were placed on the substrate holder which was 400 mm away from the source. The absorbance of deposited films was measured by UV-VIS spectrometer (Shimadzu UV-1201). The photon energy, E (eV), of the films at different absorption wavelength was calculated by well-known equation, $E(eV) = hc/\lambda e$. Where h is the Planck's constant (6.626×10^{-34} Js), c is the speed of light (2.998×10^8 ms⁻¹), λ is the wavelength used at the range of 400 to 1100 nm and e is the electronic charge (1.602×10^{-19} C). The UV absorption vs E (eV) were plotted to investigate absorption characteristic of the films. The optical band gap E_g for these films was measure by well-known Tauc formula [300].

5.6 DLC Films Deposition on Implant Metals

Before etching and the deposition, the vacuum chamber was initially pumped down to $<6 \times 10^{-7}$ mbar. In order to study the influence of pressure and current, the samples were etched with the pressure level at 1.5×10^{-3} , 2.8×10^{-3} , 3.6×10^{-3} and 4.8×10^{-3} mbar and current at 0.6A and 1A. Etching time was kept constant at 10 minutes in this experimental part. In

order to study the influence of sputter cleaning, the substrates were *in situ* etched in an argon by bombardment with energetic argon atoms from the source using pressure level at 1.5×10^{-3} and 4.8×10^{-3} mbar and etching times of 0, 5, 10, 15 and 20 minutes prior to deposition.

During deposition, the pure acetylene (C_2H_2) and acetylene-argon gas mixtures (90% C_2H_2 +10%Ar) were used as process gases. To study the effect of surface treatment on the adhesion of films on these substrates they were also deposited using pure acetylene gas only. The anode currents in the source were 0.6A and 1.0 A and the anode voltage varied in the range of 0.95 to 1.7 kV. It has been shown that the energy of the atoms in the neutral beam under these anode voltage conditions is approximately equal to the anode voltage when they leave the source [295]. To investigate the substrate temperature during etching and deposition, they were placed in the deposition chamber with two different ways. The 8 mm thick substrates were placed in the deposition chamber in direct contact with the substrate holder whereas the 0.2 mm thick substrates were thermally insulated from the holder, to some degree, by a polymeric spacer. A type K thermocouple was placed in contact with the substrate surface on which etching and deposition took place. Temperature was recorded every 1 minute during etching and deposition. The deposition time was kept constant at 1 hour.

To measure the cohesive strength of the films, 316L stainless with dimensions of 50 mm x 4 mm x 0.25 mm substrate has also been deposited with those parameters.

The operation procedures of the etching and deposition are mentioned in appendix A3.

5.7 Physical and Mechanical Characterisations

5.7.1 Film Density

The density of the coatings was determined by measuring the increase in mass of the substrate after deposition and dividing it by the volume of the film [302]. The mass gain of the samples was measured with a digital balance nearest to ± 0.0001 g. Assuming sputter weight loss negligible.

5.7.2 Film Thickness

The film thickness of the coating was measured by surface profilometry. In this process, film was deposited on to the substrate surface with part of the surface protected by a mask to create a step on the substrate surface. In that case some part of the substrate surface was uncoated during film deposition. When stylus of the profilometer was moved from coated to uncoated area, the slope in the trace on both sides of the step was recorded on the chart recorder. The film thickness corresponds to the vertical distance between linear extrapolations of the lower and upper portions of the trace calculated from the chart recorder (according to Fig. 3.7).

5.7.3 Determination of Stress in Films

All the films exhibited compressive stress. The films were limited to thickness of less than $1\mu\text{m}$ [307,308] to avoid film shattering and so avoid confusing film adhesion and film stress [309]. The internal residual stress of DLC deposited 316L stainless steel (0.25 mm thickness) was obtained quantitatively by the bending beam method from well-known Stoney equation 3.1.

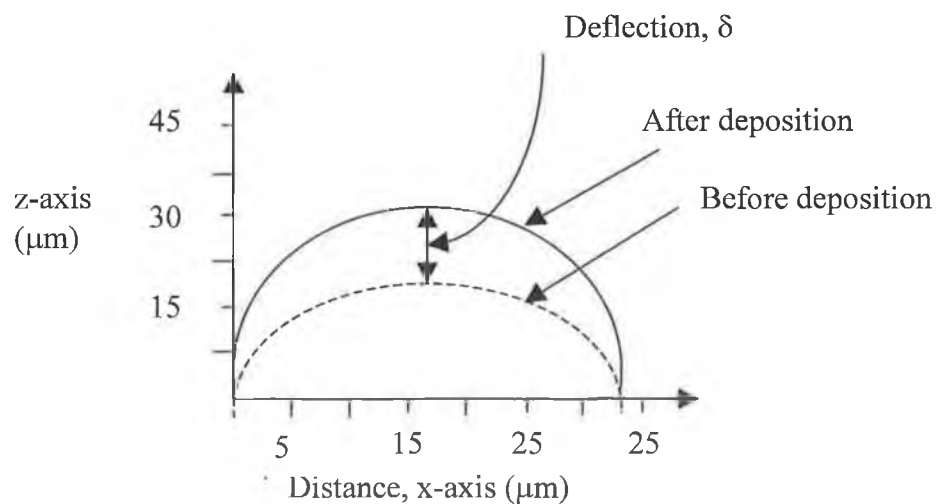


Figure 5.1: Schematic diagram to measure the curvature of 316L stainless steel (0.2mm thickness) before and after deposition of DLC film.

where σ is the internal stress, E_s is the Young's modulus of the substrate, ν_s is the Poisson's ratio of the substrate, t_s and t_f are the thickness of the substrate and film respectively, l is the length of the substrate segment and δ is the largest deflection (usually the central

deflection) in the segment measured by surface profilometry after the film deposition with reference to initial deflection (Fig. 5.1).

For 316L stainless steel $E_s = 200\text{GPa}$, $\nu_s = 0.29$ [310,311] was considered to measure the residual stress in film.

5.7.4 Determination of Films Adhesion

Two types of film adhesion were measured. One is quantitative adhesion called pull-off adhesion and other is qualitative adhesion called Rockwell C adhesion.

5.7.4.1 Pull-off Adhesion

The pull-off adhesion strength of the DLC coatings was measured in tension using the Sebastian® II stud pull test. The flat face of a solid cylinder (the stud) of 3.6 mm diameter was attached perpendicularly to the DLC coated surface using Sebastian 5-epoxy glue. The sample and stud fixture were heated to 150 °C for one hour then cooled to room temperature. The stud was placed in the chunk of the pull test machine and tightly bounded. A gradually increasing downward force was applied to the stud while holding the sample stationary. The instrument recorded the highest value of force applied before failure. On each sample at least three tests were carried out and a mean value and standard deviation were calculated.

5.7.4.2 Rockwell C Adhesion

In Rockwell C adhesion test, a standard Rockwell-C hardness tester with maximum applied force 1471 N causing layer damage adjacent to the boundary of the indentation. After indentation, an optical microscope with a magnification of x 80 was used to evaluate the test results. On each sample three indentations were produced. The damage of the coating was compared with a defined adhesion strength quality [309,312]. HF1-HF4 defines a sufficient adhesion whereas HF5 and HF6 represent insufficient adhesion (see Fig. 3.6).

5.7.5 Determination of Film Hardness and Young's modulus

The mechanical properties of the films were determined from nanoindentation using a CSEM nanohardness tester. Films were measured with an indenter of the Berkovich type.

Load-displacement curves were obtained, from which the hardness and Young's modulus of elasticity were calculated using the method of Oliver and Pharr [198]. The loading and unloading rates were 150 mN/min each. In order to estimate the influence of the penetration depth of the calculated mechanical properties, three different loads were applied (5, 8, and 10 mN). For each load at least three measurement were performed and a mean value and the standard deviation were calculated. The penetration depth was equal to or less than 25% of the film thickness because the apparent hardness of DLC films is dependent on the substrate [313,314]. For the determination of the Young's modulus, it is necessary to keep the penetration depth as small as possible [315]. In agreement to that, we usually found a clear dependence of Young's modulus on the penetration depth. For film stiffer than the substrate, the Young's modulus decreased with the penetration depth while for less stiff films an increase was observed. Therefore, the Young's modulus determined at the lowest load should be most representatives for the film. However, for the very low load the error from the surface roughness is highest. Therefore, decided to use always the mean value calculated from all three loads. For this reason, Young's moduli of stiffer or less stiff films than the substrate could be slightly underestimated and overestimated, respectively.

5.8 Determination of Bonding Structure of DLC Films

5.8.1 Raman Spectroscopy

The film structure was investigated using a Jobin-Yvon Micro-Raman Spectroscopy system HR-800 using 488 nm wavelength excitation. After that the bonding structure and sp^3/sp^2 content in films has been investigated by curve fitting process software. The Raman spectra of the films prepared under different etching and deposition parameters were fitted with a Breit-Wigner-Fano (BWF) line shape centred at approximately 1550 cm^{-1} ("G" peak, symbolised as peak 1) with an additional Lorentzian peak centred at approximately 1350 cm^{-1} ("D" peak, symbolised as peak 2). A peak at $\sim 1200\text{ cm}^{-1}$ corresponding to peak 3 has been considered as due to nanocrystalline or amorphous diamond [303-306]. The BWF shape has been considered for physical reasons to be a better approximation to the measured curve for amorphous carbon films [231] and its line shape is described by equation 3.23.

Chapter 6
Results and Discussion

6.1 Current vs. Voltage (A_c - A_v) Characteristics

The variations of the discharge voltage (anode voltage, A_v) with the discharge current (anode current, A_c) of the saddle field FAB source used are shown in figure 6.1 and figure 6.2. Figure 6.1 shows the variation of A_v with A_c when argon gas was used as the source gas at different pressure level. It is evident from this figure that the value of A_v increased approximately linearly with the value of A_c for all pressure level conditions and the value of A_v decreased with the increase of pressure for a particular value of A_c . It is very important to mention at this stage that the power supply used to operate the FAB source is a current controlled device. It was therefore possible, by keeping all other parameters constant, for the discharge voltage to be increased suitably by increasing the discharge current only. Therefore, the decrease of discharge voltage at a particular discharge current with increase of gas pressure is due to the higher ionisation of the feed gas inside the source. This can be seen to have effectively reduced the plasma resistance.

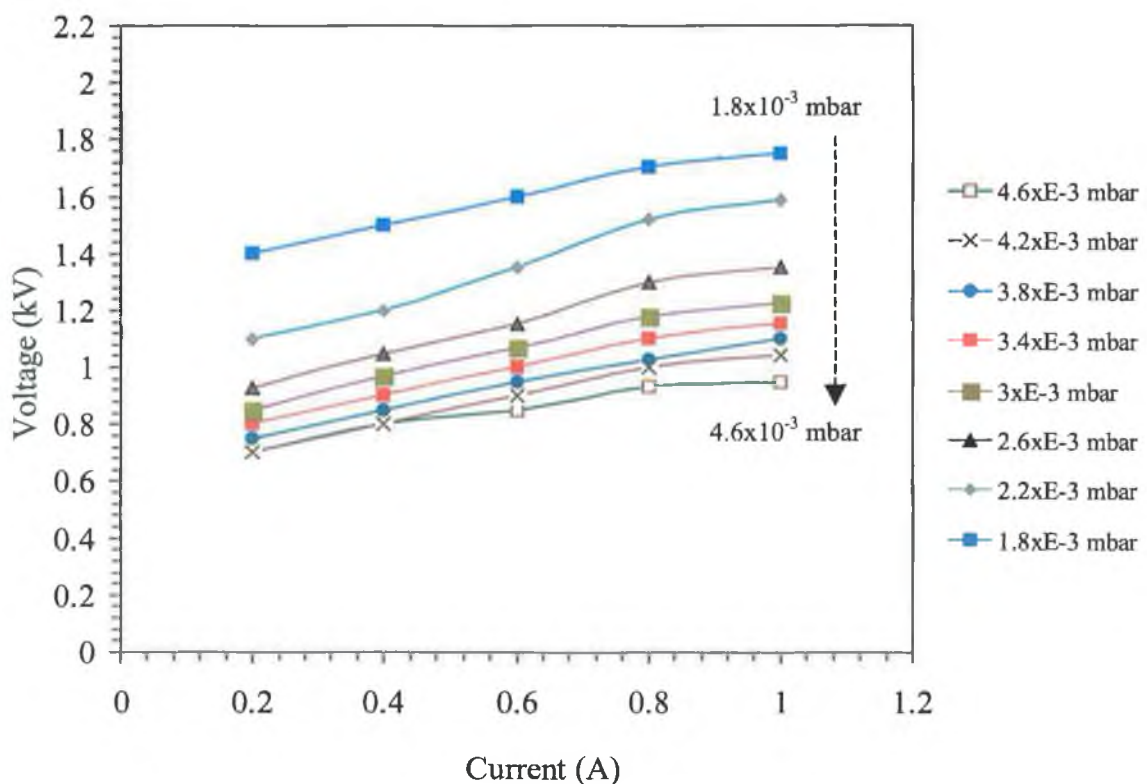


Figure 6.1: Anode current vs anode voltage with different argon (Ar) gas pressure.

Figure 6.2 shows the variation of A_v with A_c for acetylene as source gas and having a similar set of operation conditions used in the case of argon discharge. The variation of A_v with A_c is also found to be almost linear in this case as well. In the case of argon discharge, the variations are distinct in all different pressure level. But in the case of hydrocarbon (C_2H_2) discharge, the discharge voltage attains almost similar value for the higher pressure level. It can be said that at higher C_2H_2 gas pressure, the ionisation of the gas inside the source begins to saturate. The value of A_v has also been found in the range of 0.7 to 1.75 kV for argon, which is comparatively large than the acetylene gas (0.75-1.52 kV).

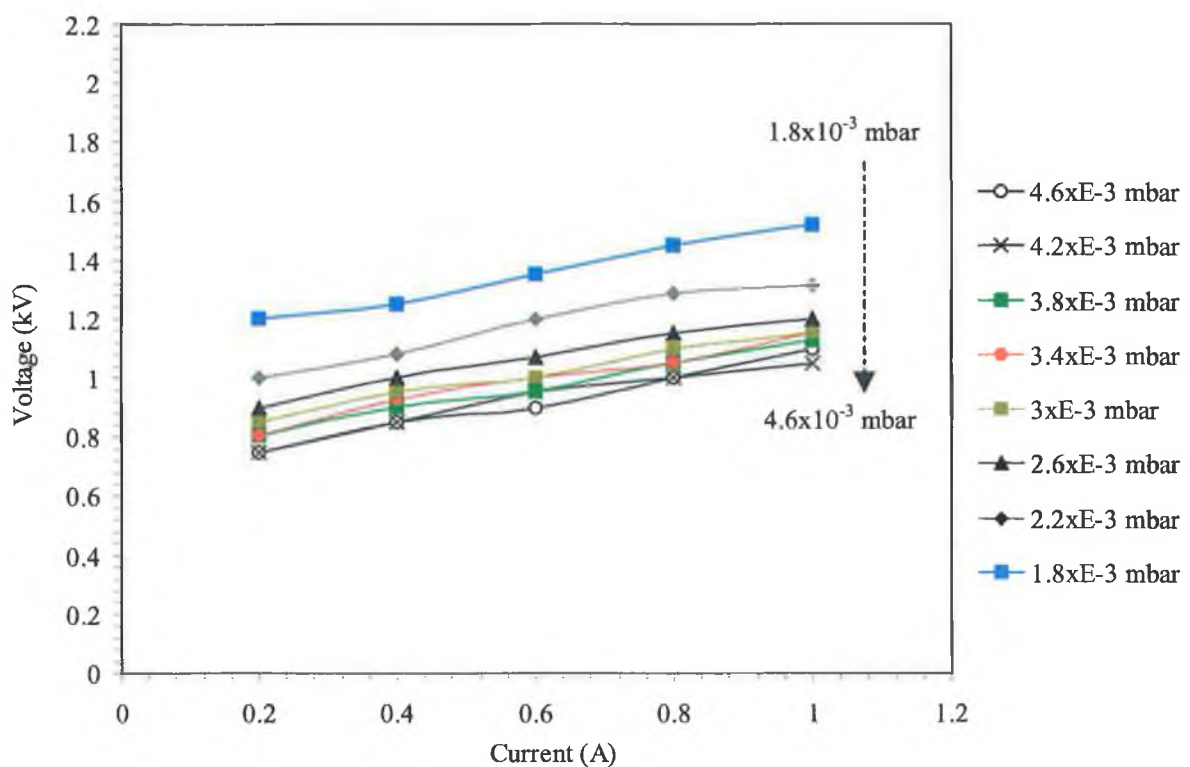


Figure 6.2: Anode current vs anode voltage with different acetylene (C_2H_2) gas pressure.

From the above observation, it is clear that discharge voltage not only depends on discharge current. It also depends on pressure and type of source gas used. According to Sarangi et al. [290] gas flow rates also influence the discharge voltage. They proposed that the value of A_v decreased with the increase of gas flow rate for a particular value of discharge current when argon gas used as the source gas. This is because of higher ionisation of the argon feed gas inside the source which can reduce the plasma resistance. On the other hand, for C_2H_2 source gas, dependence of the discharge voltage on discharge

current appears to have two distinct patterns; one for flow rate below 1 sccm and other above that. In this case, the discharge voltage attains almost similar value for the flow rate above 1 sccm because of the ionisation of the gas inside the source begins to saturate. It is therefore concluded that the saddle field FAB discharges using argon and acetylene gases as source gas are, indeed, different.

6.2 UV Absorption Spectra

In figure 6.3 typical absorption spectra of DLC films deposited on a glass substrate is presented. The uv absorption of the films grown at lower deposition current (0.4A) as lower for the whole wave number range investigated. The variation of the photon energy with uv absorption spectra (log scale) of films deposited with different pressure level and three different currents is shown in figure 6.4 (a-c). All curves show characteristically a similar performance. However, there is important difference in the absorption range with the deposition current. The absorption value is strongly dependent on deposition current and has been found to increase with the increase of current. At lower deposition current (0.4A), the absorption at 3.1 eV was found in the range of $\sim 1.57-2.31$ whereas at higher deposition current it is in the range of $\sim 3.2-3.55$. At lower deposition current (Fig. 6.4-a), a clear distinction of the variation of absorption with photon energy has been observed for different deposition pressure used. But as shown in figure 6.4 (c) any specific trend in this variation is not discernible. It is abundantly clear from this figure that uv absorption with photon energy does not appear to depend so much at different deposition pressure level for higher deposition current. Therefore, while dealing with higher deposition current, pressure does not constitute a critical process parameter.

Uv absorption spectra can also be influenced by the film thickness. The film thickness of the deposited sample with different deposition pressure and current was found less than $0.4 \mu\text{m}$. According to Gabriel Lazăr [316], the absorption spectra are not depending on the smaller film thickness (below $0.4 \mu\text{m}$). So it can be say that there is no effect the absorption with film thickness.

From the above observation it is clear that the uv absorption spectra strongly depends on all range of deposition current but only depends on pressure at lower deposition current.

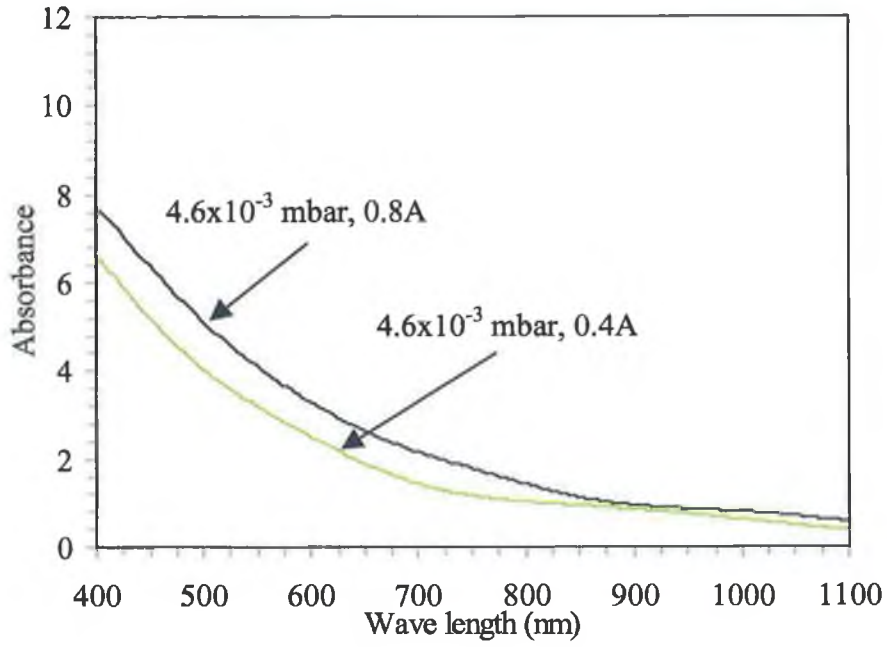


Figure 6.3: Typical absorption spectra of DLC films deposited on glass substrates: film thickness for 0.8A deposition current is $0.38\mu\text{m}$ and for 0.4A is $0.20\mu\text{m}$.

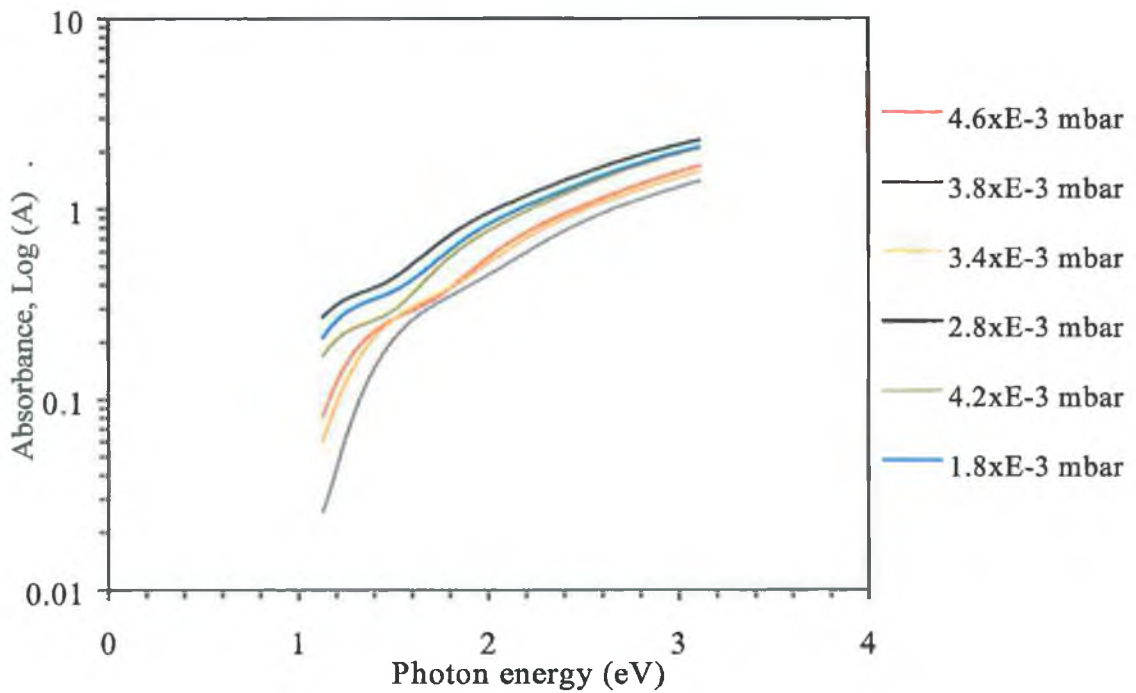


Figure 6.4 (a): Variation of the photon energy with uv absorption spectra (log scale) of films deposited on glass substrates with different pressure level and 0.4 A current.

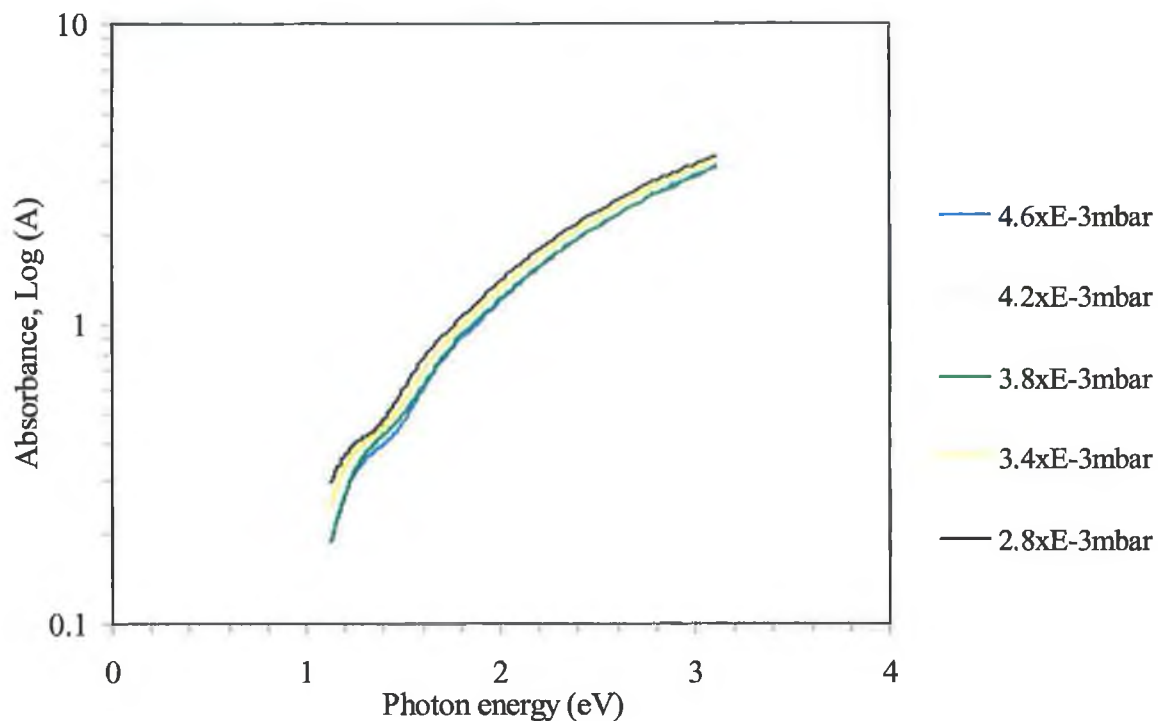


Figure 6.4 (b): Variation of the photon energy with uv absorption spectra (log scale) of films deposited on glass substrates with different pressure level and 0.6 A current.

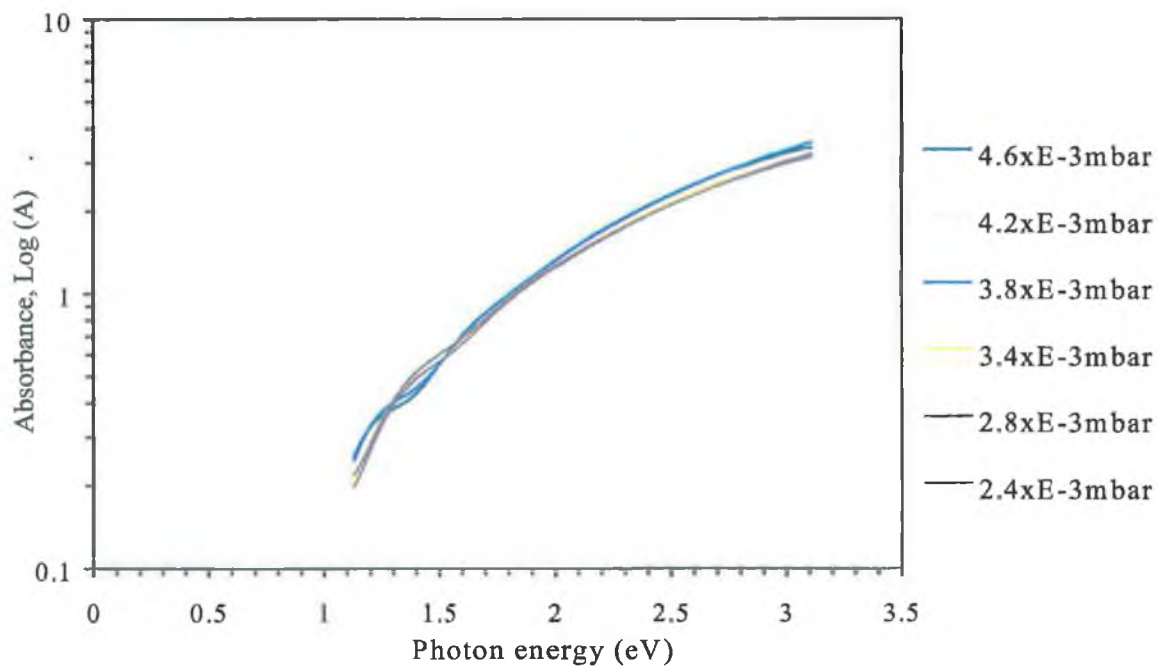


Figure 6.4 (c): Variation of the photon energy with uv absorption spectra (log scale) of films deposited on glass substrates with different pressure level and 0.8 A current.

The optical properties of DLC films were measured by the well-known Tauc equation,

$$\alpha = (h\nu - E_g)^2 \frac{A}{h\nu}$$

where A is a constant, $h\nu$ the photon energy, α the absorption and E_g the optical band gap [300]. E_g is defined as the energy gap between the valence and the conduction band. A typical graph of $(\alpha h\nu)^{1/2}$ versus $h\nu$ for one of our DLC films is shown in figure 6.5. Extrapolation of this plot to $\alpha^{1/2} = 0$ gives the optical band gap E_g for indirect transitions.

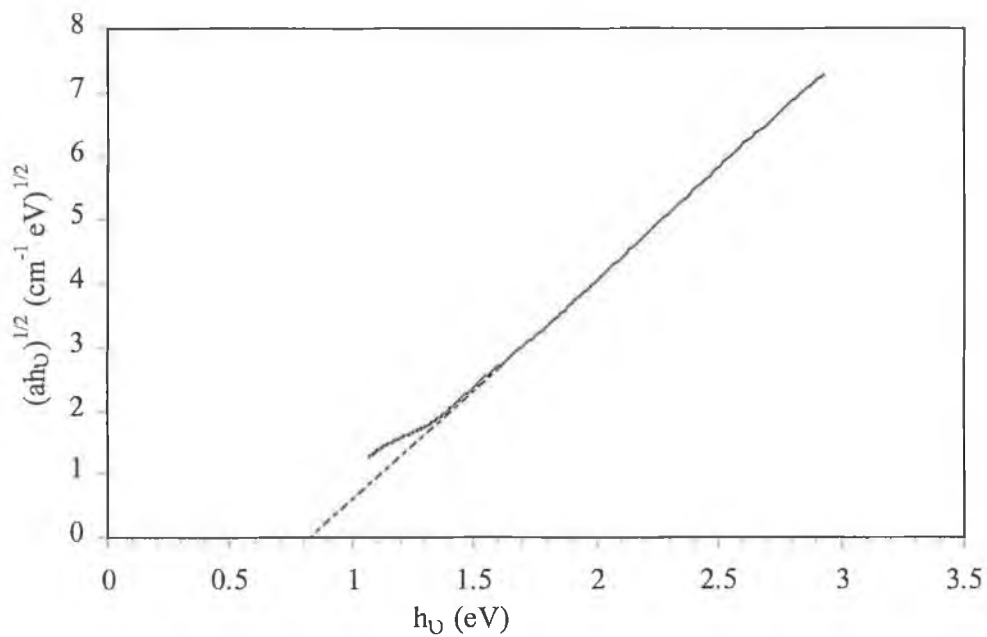


Figure 6.5: A typical $(\alpha h\nu)^{1/2}$ vs. $h\nu$ plot: deposition current 0.4 A and deposition pressure 3.8×10^{-3} mbar.

Figure 6.6 shows the optical band gap of DLC films as a function of deposition pressure and current. The value of E_g for DLC films has been found by other authors to be in the range of 0.7-3 eV (see table 3.1). The band gap E_g obtained here for as deposited DLC films was ~ 0.85 eV for 0.4 A deposition current. For higher deposition currents (0.6 and 0.8 A) the band gap E_g was found to be in the range of 0.85-0.97 eV, which is within the typical range of DLC films. Ferrari et al. proposed the relationship between the optical band gap and sp^3 fraction inside the films [232]. They said that a higher sp^3 is achieved

mainly by hydrogen saturating C=C bonds as $\equiv\text{CH}_x$ groups, rather than by increasing the fraction of C-C bonds. The sp^3 percentage and the sp^3/sp^2 ratio of DLC films grown at higher deposition current are significantly high, which indicates that the films grown by the saddle field FAB source techniques exhibit more diamond-like behaviour and this behaviour might be enhanced with the increase of carbon to hydrogen ratio in the hydrocarbon gas. More diamond-like films with less hydrogen content also increase optical band gap because of increasing the fraction of the C-C sp^3 bond. Sarangi et al. [297] proposed that the sp^2 percentage in the DLC film deposited by saddle field fast atom beam source is lower than other deposition techniques, for example rf self-bias techniques and decreases with the increase of carbon to hydrogen ratio in the hydrocarbon source gases. Films grown by the saddle field FAB source exhibit more diamond like behaviour and this behaviour is enhanced with increase of carbon to hydrogen ratio. It is noted that acetylene (C_2H_2) has the highest carbon to hydrogen ratio (1:1) compared with other hydrocarbon source gases. They also showed that with the increase of power applied to the saddle field FAB source, the bonded hydrogen content decreased. Similar behaviour was also reported by Walters et al. [301,317] in their FAB grown DLC films using acetylene source gas. According to their work, for FAB grown DLC films using acetylene as the feedstock, a minimum of 22 at.% of hydrogen was reported when beam energies of 0.8 kV were used to grow the films. The atomic percentage of hydrogen was found to be significantly lower when they used up to 2 kV beam energies. This is because an increasing bombardment of the film during growth with rising energy appears to remove the weakly bound hydrogen from the films. It is noted that the total amount of hydrogen content inside the DLC films is the sum of bonded and unbound hydrogen. Sarangi et al. found the total hydrogen content to be 7-8 at.% for CH_4 grown DLC films and 5-6 at.% for C_2H_2 grown DLC films whereas unbound hydrogen in these films was found to be 1.5-2.0 at.% for CH_4 grown DLC films and 2.5-3.0 at.% for C_2H_2 grown DLC films. The amount of bonded and total hydrogen can said to be more in CH_4 grown DLC films than the amount of bonded and total hydrogen present in C_2H_2 grown DLC films. From the above observation it is clear that the hydrogen content, both bonded and total, decreases in DLC films as the carbon to hydrogen ratio increases in the hydrocarbon gases using the saddle field FAB source. Higher deposition current means higher power, which also decreases the hydrogen content and increase C-C sp^3 bond inside the film.

Any sp^3 phase change would affect the gap between the conduction and valence band in the films. For higher deposition current 0.8A, sp^3 content inside the films was found to be higher which affects the optical band gap.

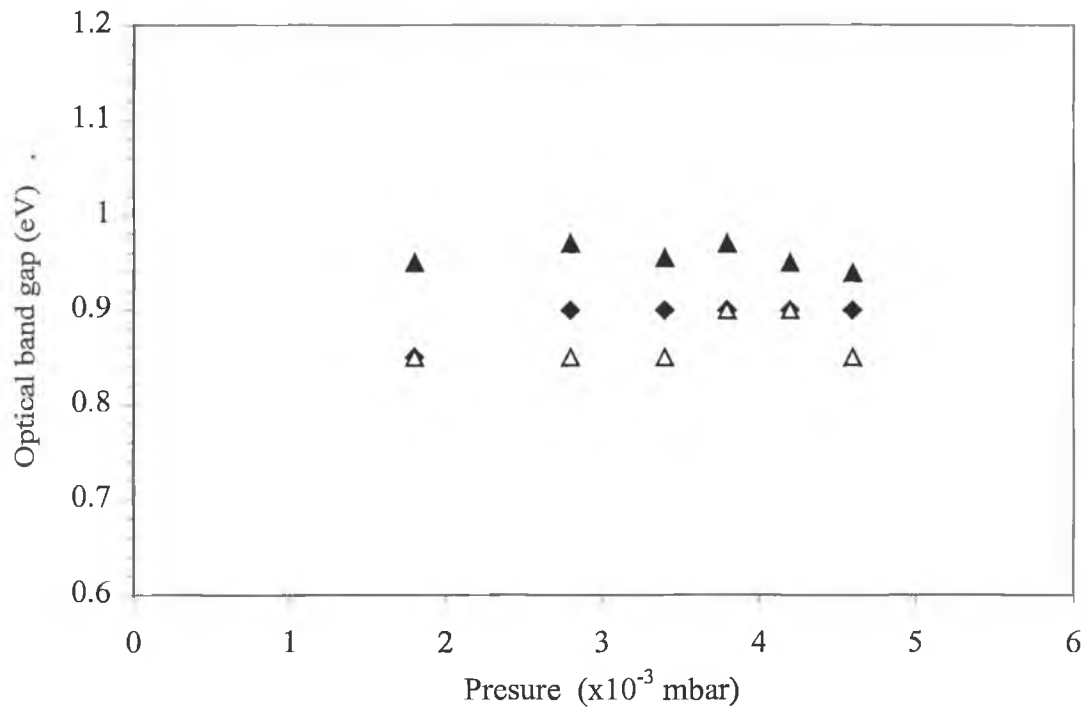


Figure 6.6: Optical band gap of films as a function of deposition conditions: Δ 0.4 A, \blacklozenge 0.6 A and \blacktriangle 0.8 A.

6.3 Effect of Process Parameters

The previous part of this chapter discussed the current-voltage characteristic, which can be helped to control the current with voltage during the coating as well as etching. It is of interest to see the effect of process parameters, e.g. deposition pressure, deposition current, process gas and gas mixture, etc. on bonding structure and adhesion of the films. A clear understanding of the process parameters are required to have control on deposition of DLC thin films. It is of interest to find a way to increase the sp^3 bonding in the films and good adhesion with the substrates. This part discusses the effect of process parameters on the films characteristics: (1) the growth rate (deposition rate), (2) films adhesion, (3) the sp^3/sp^2 ratio since it is of interest to increase the ratio as far as possible for good quality of

DLC films, (4) films stress and (5) hardness. The part also discusses the correlation between the stress and adhesion of the films. The process parameters have been used to deposition DLC films were discussed in experimental part.

6.3.1 Deposition Rate

The deposition rate was found to vary only slightly with chamber pressure and source current as shown in figure 6.7. The deposition rate mainly varies in proportion to the flux of acetylene atoms which is directly related to the source current and the proportion of acetylene in the gas mixture. It is clear that there is some variation in deposition rate with gas pressure with mid-range pressures showing a slightly lower growth rate. The reason for this is not clear but is presumably due to a combination of the characteristics of the neutral beam source and the scattering of the particles on their way to the substrate.

The density of the films was found to be in the range of $2.24\text{-}2.36\text{ g cm}^{-3}$ which is in the typical range for DLC films.

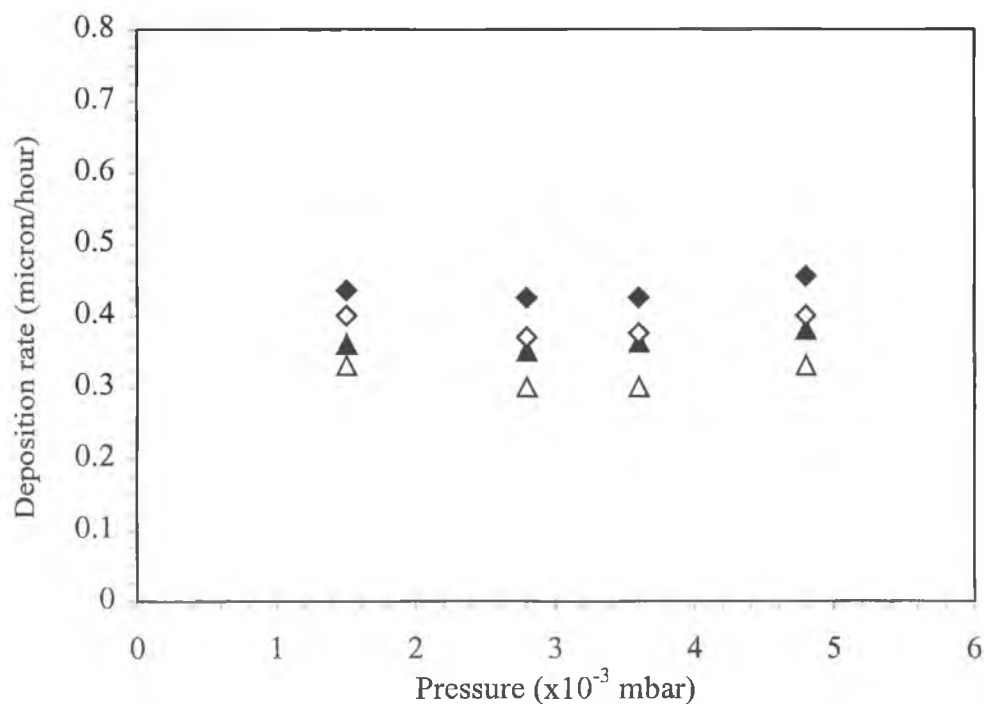


Figure 6.7: Deposition rate of films as a function of source current, chamber pressure and process gas. \blacklozenge 100% C_2H_2 , 1A; \blacktriangle 100% C_2H_2 , 0.6A; \diamond (90% C_2H_2 +10%Ar), 1A; \triangle (90% C_2H_2 +10%Ar), 0.6A.

6.3.2 Raman Spectroscopy

A typical Raman spectra of films deposited on 316L stainless steel is shown in figure 6.8. It can be seen that there is one main peak with a broad shoulder on the low frequency side. The position and size of the component peaks were determined by a curve fitting process using the method of Ferrari and Robertson [231] where the main peak is fitted with a Breit-Wigner-Fano (BWF) asymmetrical curve and the shoulders by Lorentzian curves. The lack of clear features in the curve makes the fitting process somewhat subjective and unreliable but consistent fits could be achieved using a combination of three peaks.

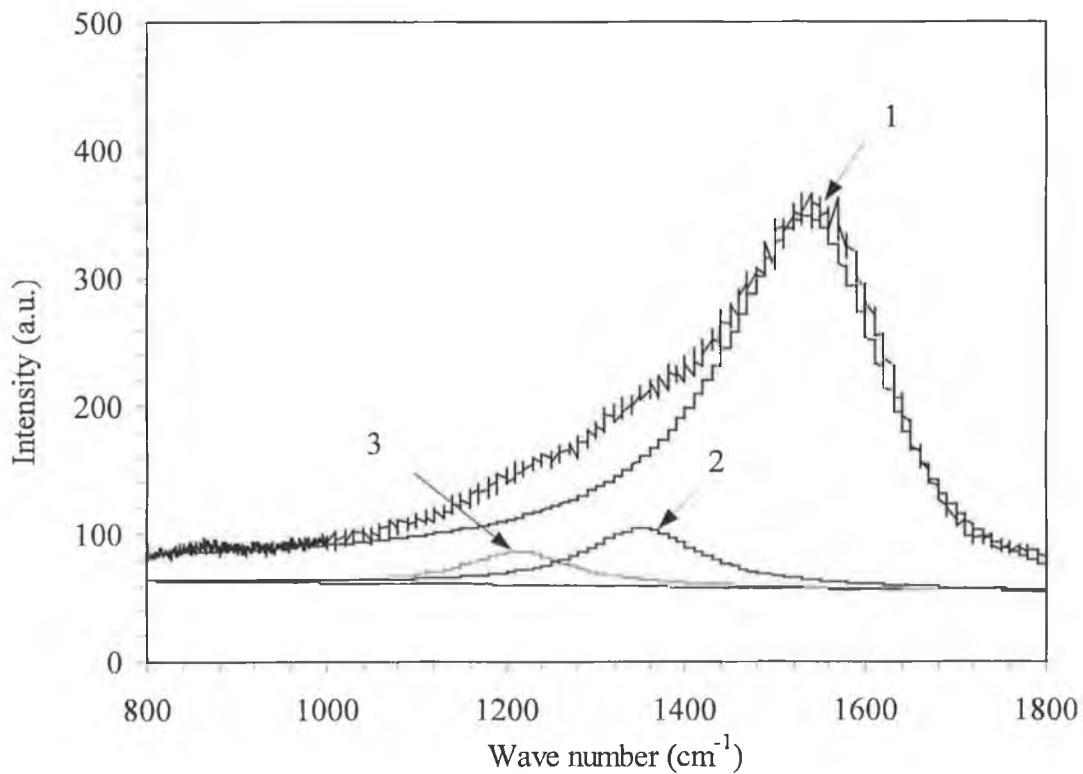


Figure 6.8: Typical Raman spectrum of DLC film: 1.5×10^{-3} mbar, 0.6 A and 100% C_2H_2 gas.

Figure 6.9 (a-b) shows the peak area ratio ((peak 2+peak 3)/ peak1) as a function of deposition conditions using the pure acetylene and acetylene-argon (90% C_2H_2 + 10% Ar) process gas. It can be seen that for 0.6A deposition current the peak area ratio increases with increasing deposition pressure whereas for 1A deposition current there is more complex behaviour. The area ratio is higher for the 1 A films compared with the 0.6 A films with a peak at 2.8×10^{-3} mbar indicates that the sp^3 content is highest at this point. The

peak area ratio for acetylene-argon gas mixture has also been found higher both in 1 and 0.6 A deposition current. It can be averred that argon can influence to increase the sp^3 during deposition process.

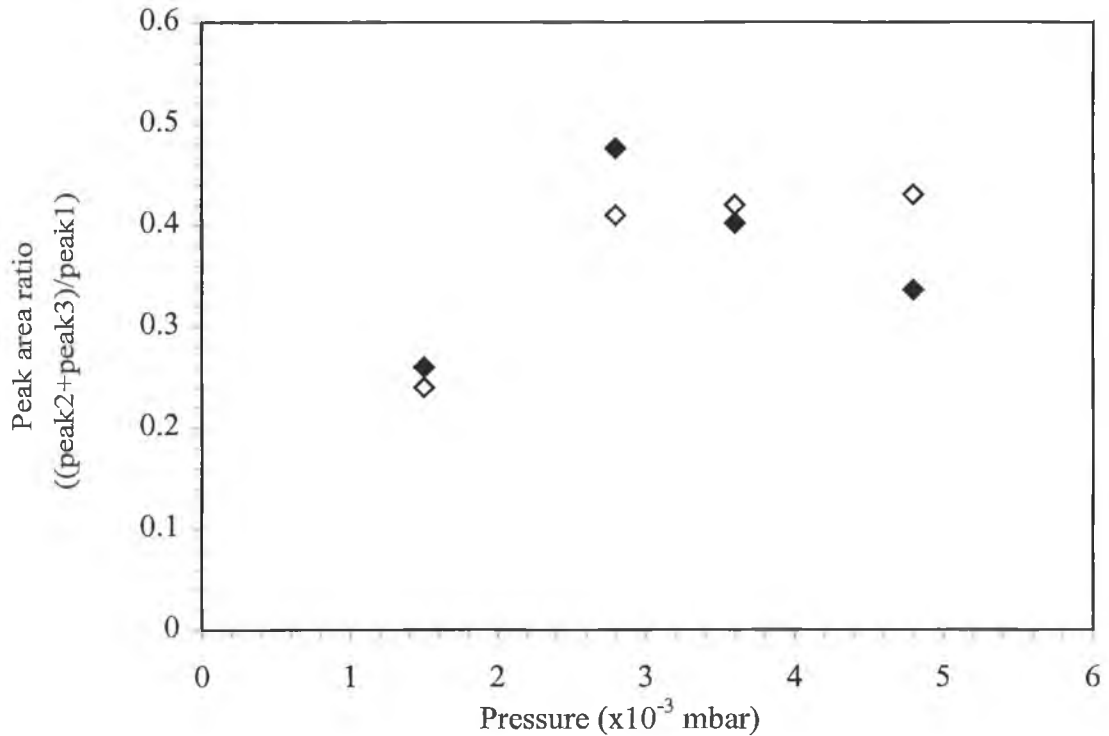


Figure 6.9 (a): Variation of peak area ratio as a function of deposition conditions: ◆ 90% C_2H_2 + 10%Ar gas mixture and 1 A current; ◇ 100% C_2H_2 gas and 1 A current.

The variations of the coupling coefficient (Q) with deposition conditions are shown in figure 6.10 (a-b). The value of Q decreases with increasing deposition pressure for 0.6 A current whereas for 1A, it increasing up to 2.8×10^{-3} mbar deposition pressure and then decreasing. According to Yoon and Praver et al. [318,319] the Q value is correlated with the sp^3/sp^2 ratio with a decrease in the magnitude of the Q value (i.e. a more negative value) indicating an increase in the sp^3 content. Both the peak area ratio and the coupling coefficient, Q, show similar behaviour in that the sp^3/sp^2 ratio is maximised at higher deposition pressure and lower deposition current (0.6A) whereas at pressure of 2.8×10^{-3} mbar for 1 A current. For both the deposition currents, coupling coefficients have also been found slightly higher for argon-acetylene process gas.

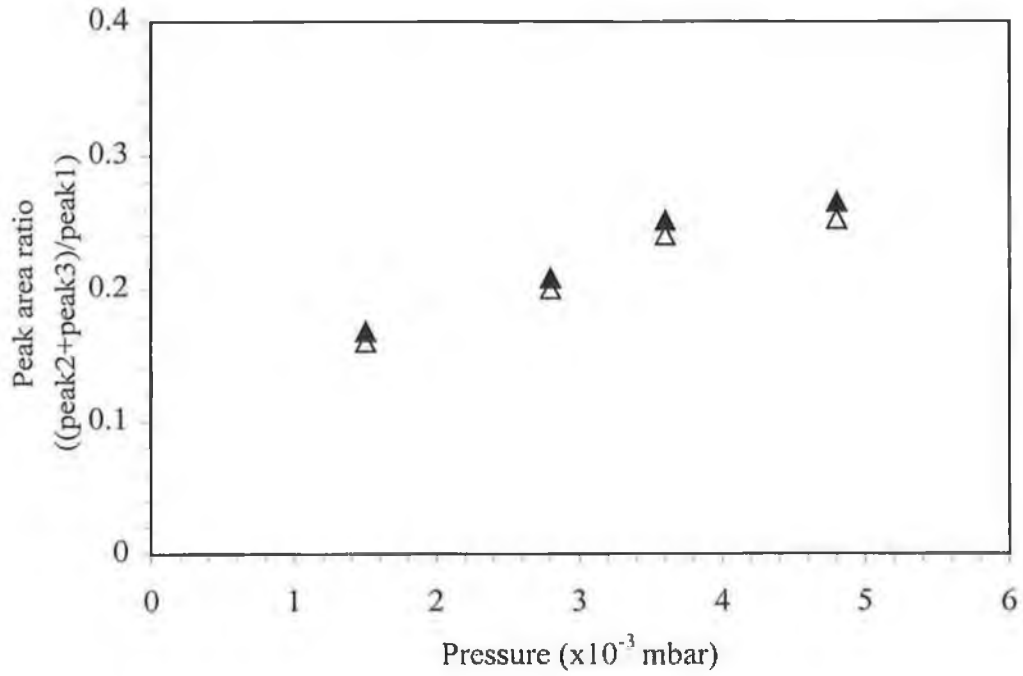


Figure 6.9 (b): Variation of peak area ratio as a function of deposition conditions: ▲90% C_2H_2 +10%Ar gas mixture and 0.6 A current; Δ100% C_2H_2 gas and 0.6 A current.

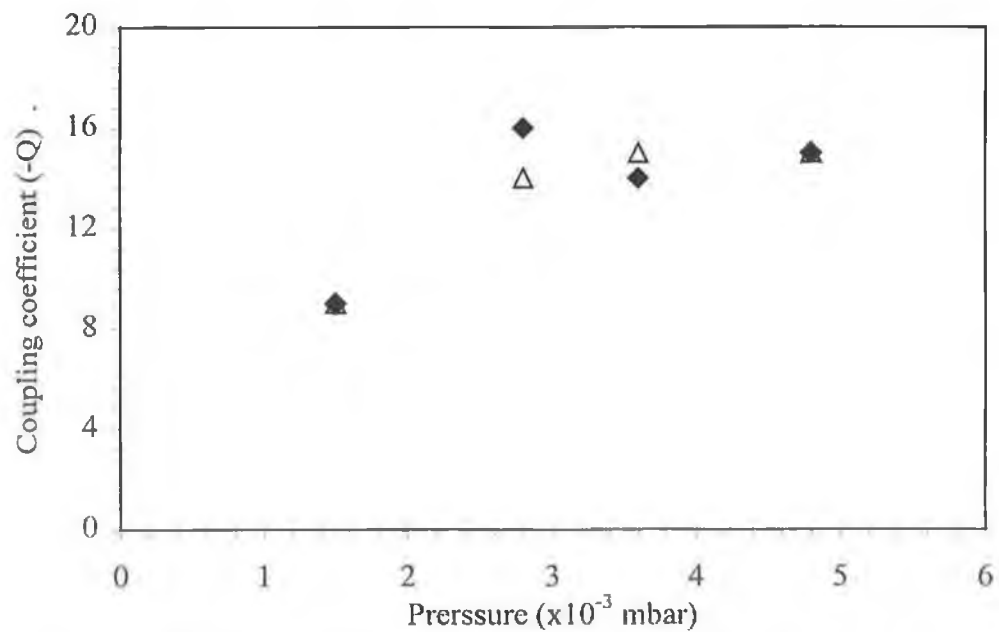


Figure 6.10 (a): Coupling coefficient, Q , as a function of deposition conditions: ◆90% C_2H_2 +10%Ar gas mixture and 1 A current; Δ 100% C_2H_2 gas and 1 A current.

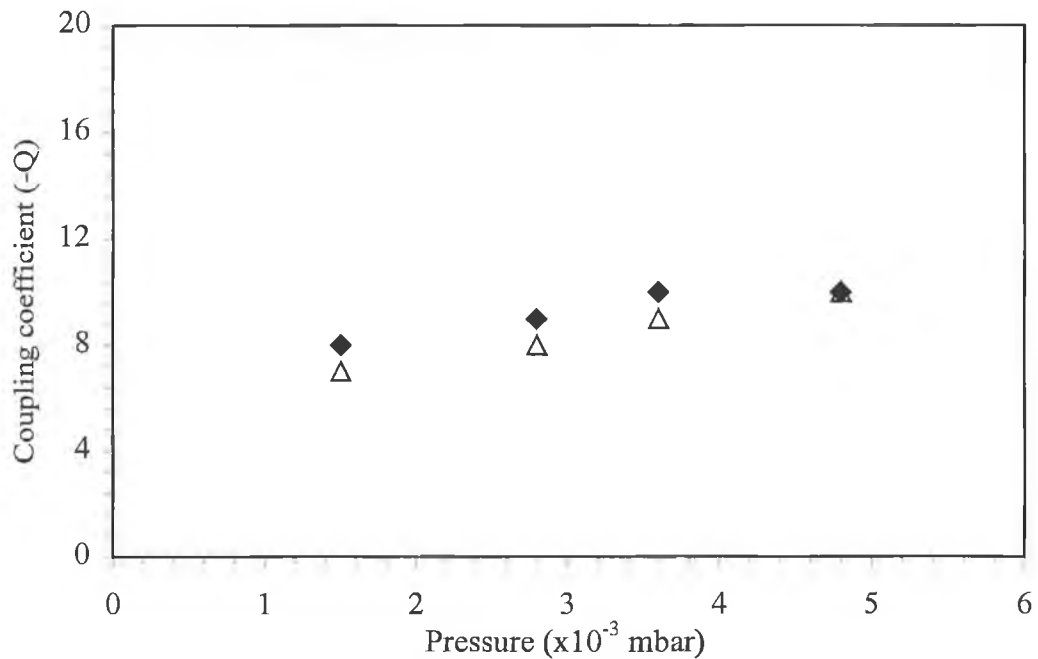


Figure 6.10 (b): Coupling coefficient, Q , as a function of deposition conditions: ◆90% C_2H_2 +10%Ar gas mixture and 0.6 A current; Δ 100% C_2H_2 gas and 0.6 A current.

6.3.3 Films Stress and Adhesion

Figure 6.11 (a-b) shows the residual stress as a function of the deposition conditions. For all films, the stress is in the range 0.8 to 1.6 GPa. For the 0.6 A films (Fig. 6.11-b) the stress increases as the chamber pressure is increased while for the 1 A deposition films (Fig. 6.11-a) the behaviour is more complex. Here maximum stress was generated at the deposition pressure of 2.8×10^{-3} . A clear correlation could be seen between the Raman peak area ratio (Fig. 6.9) and residual stress. This is due to the residual stress inside the films, which increases with increasing sp^3 -bonding fraction.

Figure 6.12 shows the pull-off adhesion strength as a function of deposition conditions. Using 100% C_2H_2 process gas, it can be seen that the adhesion behaves in an inverse manner to the stress as shown in figure 6.11. This is not unexpected since stress and adhesion are intimately connected. This relation can be clarified if the adhesion strength is plotted against the inverse of the residual stress as shown in figure 6.13. The linear relationship shows that

$$\text{Adhesion} \times \text{Stress} = \text{Constant}$$

Adhesion measurements using a Rockwell C indenter were also carried out. The adhesion of the various films is shown in table 6.1. It can be seen that there is a strong correlation between the two assessment methods; the HF2 samples also show the highest adhesion strength. The similar results can be obtained using the 90% C_2H_2 +10%Ar process gas. The adhesion strength of the films cannot be easily related to the structure as determined by Raman spectroscopy or density. However, certain points are clear. Generally the best adhesion can be obtained at the lowest deposition pressure (pressures lower than 1.5×10^{-3} mbar could not be investigated due to instability of the neutral beam source). It is also striking that the intrinsic stress is an absolute predictor of the pull-off adhesion strength.

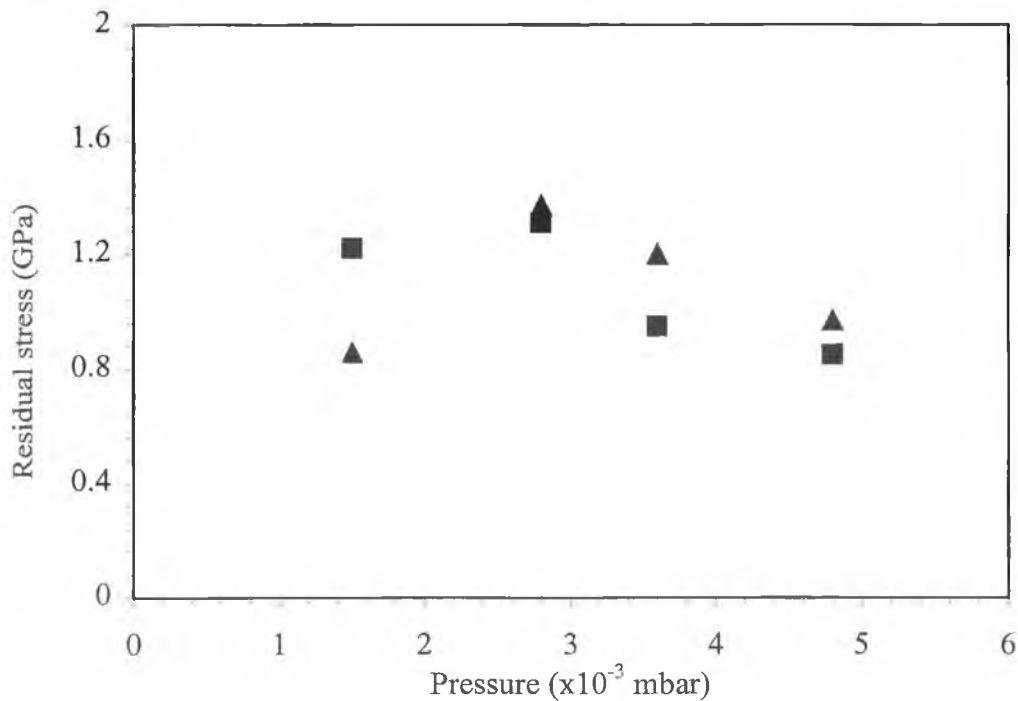


Figure 6.11 (a): Residual stress as a function of deposition conditions: ▲100% C_2H_2 , 1A
■ (90% C_2H_2 +10%Ar), 1A.

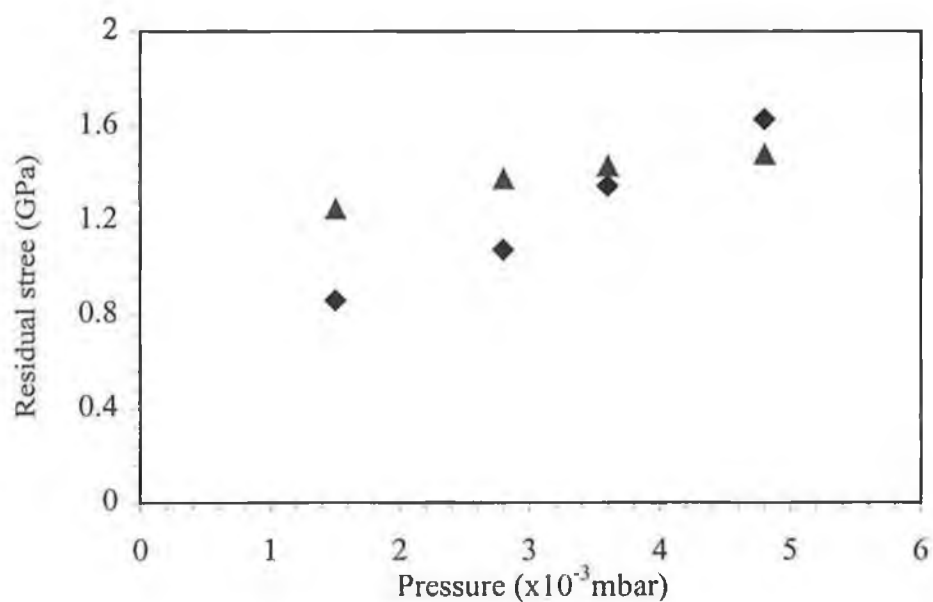


Figure 6.11 (b): Residual stress as a function of deposition conditions: \blacklozenge 100% C_2H_2 , 0.6A
 \blacktriangle (90% C_2H_2 +10%Ar), 0.6A.

Table 6.1: Rockwell and pull-off adhesion properties of films (100% C_2H_2 process gas).

Source current (A)	Pressure (mbar)	Rockwell adhesion	Pull-off adhesion (kg/cm ²)
0.6	1.5×10^{-3}	HF2	310
0.6	2.8×10^{-3}	HF3	257
0.6	3.6×10^{-3}	HF5	190
0.6	4.8×10^{-3}	HF5	150
1.0	1.5×10^{-3}	HF2	310
1.0	2.8×10^{-3}	HF4	186
1.0	3.6×10^{-3}	HF5	250
1.0	4.8×10^{-3}	HF2	275

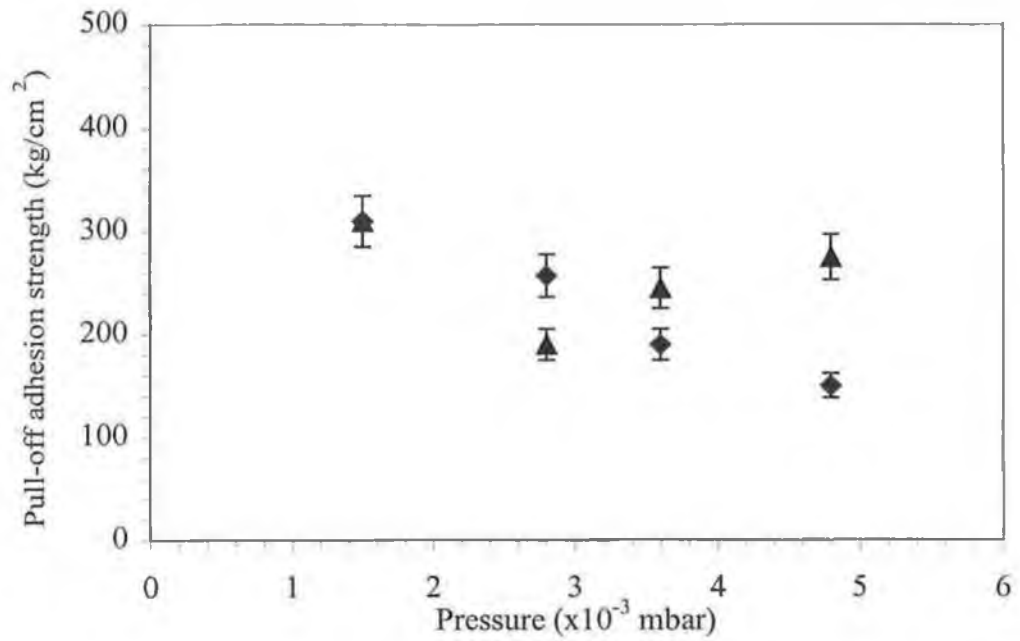


Figure 6.12: Pull-off adhesion strength as a function of deposition conditions for 100% C_2H_2 process gas: ◆ 0.6A, ▲ 1A.

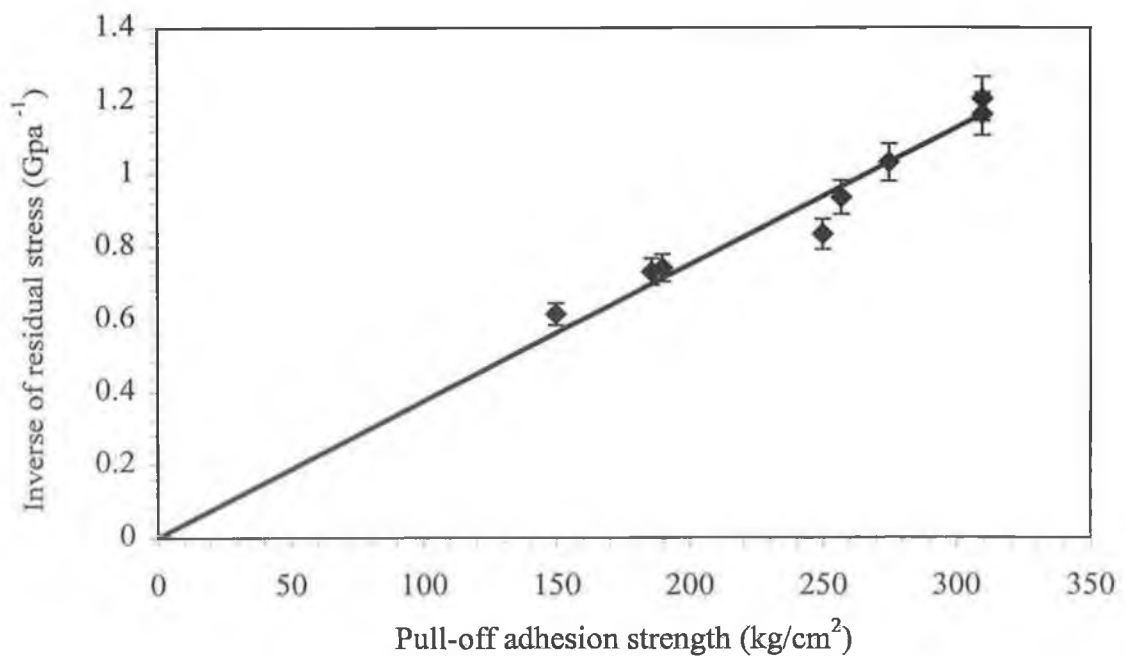


Figure 6.13: Relationship between the inverse of the residual stress and the pull-off adhesion strength.

6.3.4 Films Hardness and Young's Modulus

Hardness (H) and Young's modulus (E) of the films were measured using load-displacement curve. Figure 6.14 (a) shows a typical load-displacement curve. The hardness of the films was found to be in the range of 18 to 22 GPa, which is the typical range of hard carbon films. Figure 6.14 (b-c) shows plots of the hardness and elastic modulus as a function of the deposition pressure, which were deposited with 1 and 0.6 A current. The maximum H (E) value of the films is ~22 (230) GPa was found at the deposition current of 0.6A and pressure 4.8×10^{-3} mbar (Fig.6.14-c), whereas for a film deposited with 1A and 4.8×10^{-3} mbar pressure was found 18 (193) GPa (Fig. 6.14-b). For 0.6A deposition current H (E) increases with increasing deposition pressure. This might be attributed to the increase in sp^3 content in the film. These results support the Raman spectroscopy as well as stress results, which is discussed in the previous section. Similar behaviour according to Raman spectroscopy and stress with hardness has also been observed at 1A current. It also logical to compare the hardness of the films with the surface hardness of the respective substrate (316L stainless steel: 5.5 Gpa [320]). The hardness of DLC films on the substrate shows that the differences are less significant and within the error limit.

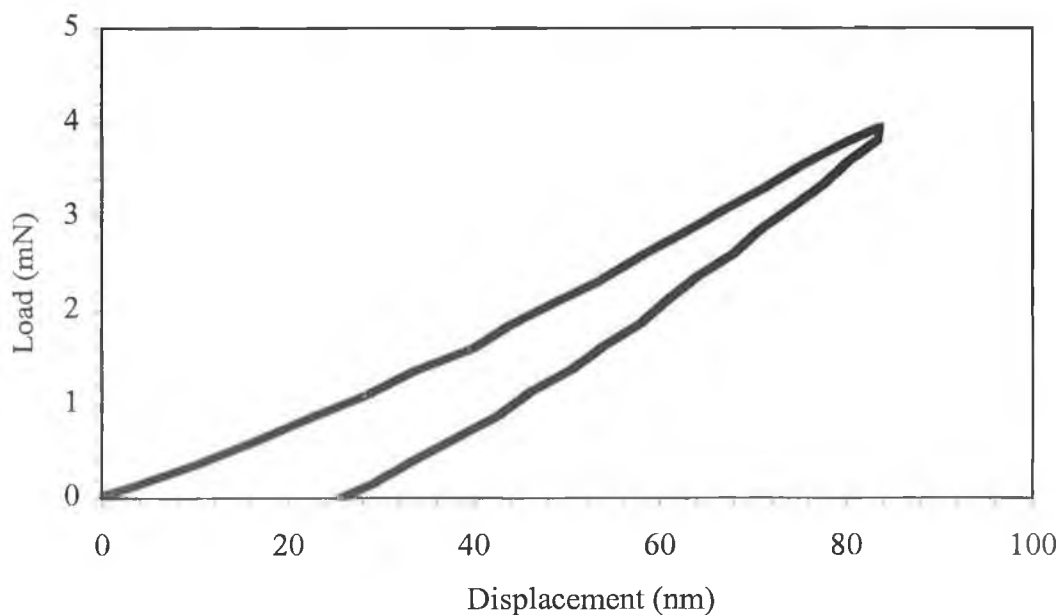


Figure 6.14 (a): A typical load-displacement curve of DLC film.

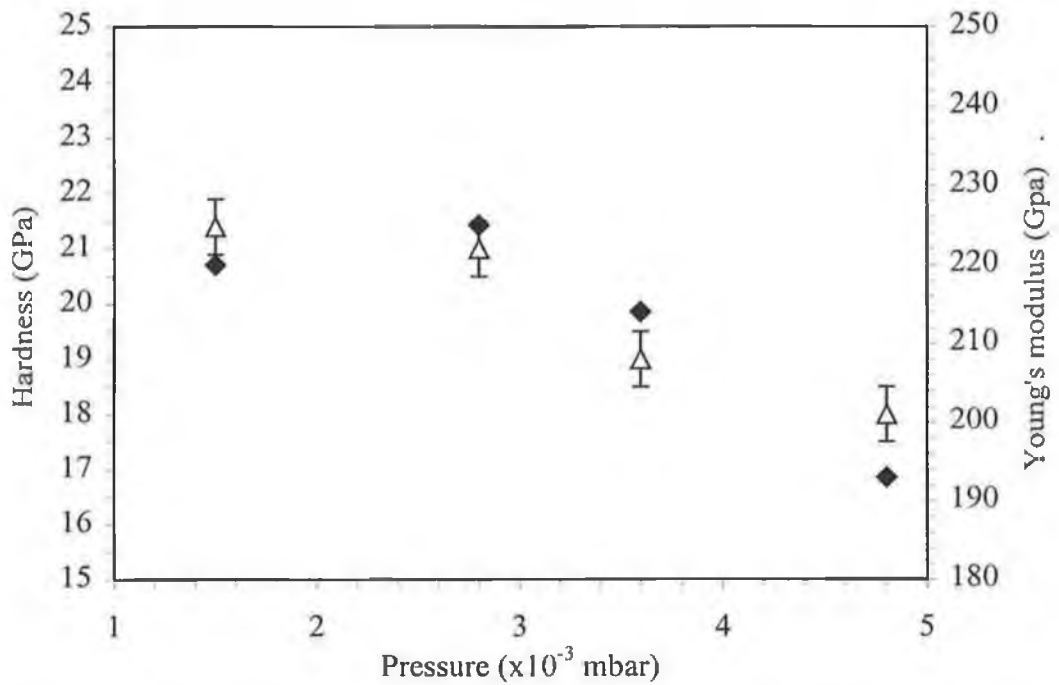


Figure 6.14 (b): Hardness (H) and Young's modulus (E) of DLC film deposited on 316L stainless steel as a function of deposition conditions: Δ Hardness; \blacklozenge Young's modulus; 1A.

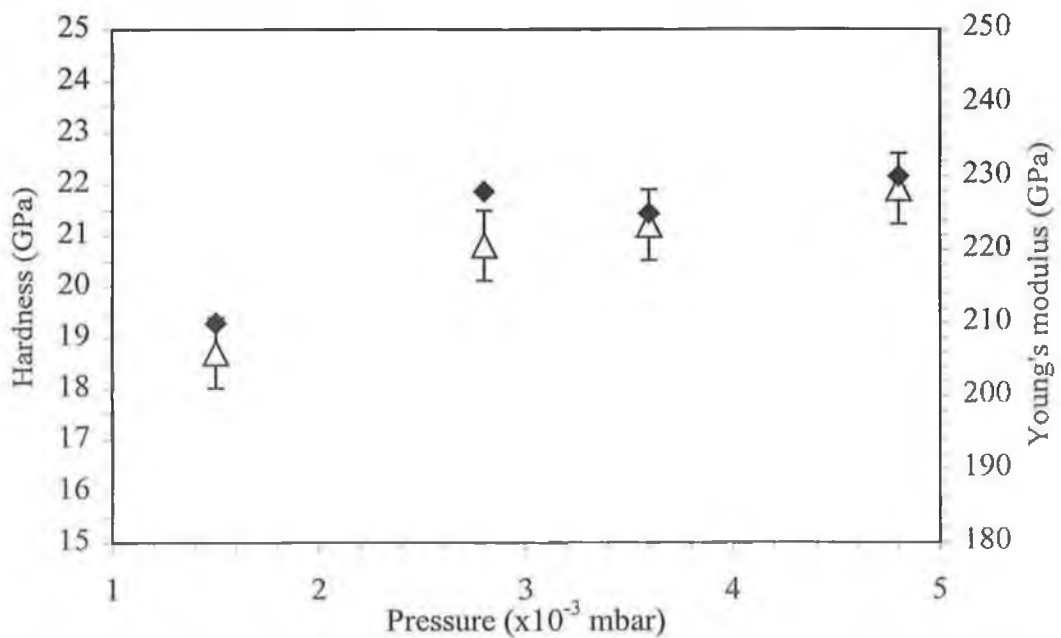


Figure 6.14 (c): Hardness (H) and Young's modulus (E) of DLC film deposited on 316L stainless steel as a function of deposition conditions: Δ Hardness; \blacklozenge Young's modulus; 0.6A.

The reason for the peak in sp^3 contents at 1 A source current and 2.8×10^{-3} mbar chamber pressure is not clear at this stage. The energy of the molecules bearing the neutral beam system is approximately 1000 eV [295]. It is known that particle energies in the range 100-150 eV are most favourable for obtaining sp^3 bonding in the carbon films. Higher energies lead to graphitisation and lower energy can not cause sufficient bond rearrangement [42]. The particles will of course lose energy due to scattering between the source and the substrate and this loss will depend on pressure. It may be that a pressure of 2.8×10^{-3} mbar gives the optimum particle energy, however, this does not explain why no such effect is seen at 0.6 A. It is also interesting that the same effect is seen whether 100% C_2H_2 is used or 10% Ar is included in the process gas.

6.4 Effect of Surface Treatment of 316L Stainless Steel

In this section DLC films have been deposited on to substrate of 316L stainless steel with two different deposition pressures, 1.5×10^{-3} and 4.8×10^{-3} mbar and constant source current, 1A. The substrate was argon pre-etched for investigating the effect of surface treatment on the adhesion of films. Etching time and other deposition parameters have been discussed in experimental part.

6.4.1 Raman Spectroscopy

The Raman spectra of the films prepared under different etching time were fitted with a BWF line shape centred with additional Lorentzian distribution centred. A peak at ~ 1200 cm^{-1} has also been considered as due to nanocrystalline or amorphous diamond [321-326]. The background has been subtracted for best fit. A typical Raman spectra and fitted curve of films deposited on 316L stainless steel are shown in figure 6.8. Figure 6.15 shows the peak area ratio $((\text{peak 2} + \text{peak 3}) / \text{peak 3})$ as a function of deposition condition. It can be seen that for 1.5×10^{-3} and 4.8×10^{-3} mbar deposition pressure films the peak area ratio increases with increasing substrate etching time up to 15 minutes and then decreases. The peak area ratio is indicative of a change in the bonding structure of the films. The area ratio is higher for the higher deposition pressure compared with the lower deposition pressure films with a peak at 15 minutes etching time in both cases. The variation of the coupling coefficient (Q) with deposition conditions are shown in figure 6.16. It is noted

that Q is the BWF coupling coefficient and represents the degree symmetry of the G peak. Large negative Q value indicates increased asymmetry of the peak.

The value of Q decreases with increasing etching time up to 15 minutes and then increases. The Q value is correlated with the sp^3/sp^2 ratio with a decrease in Q value indicating a decrease in the sp^2 content. Both the peak are ratio and the coupling coefficient, Q , show similar behaviour in that the sp^3/sp^2 ratio is maximised for an etching time of 15 minutes. It is not, however, clear at this stage how the etching should influence significantly the bulk structure of an amorphous film. This is investigated and discussed in to the next section.

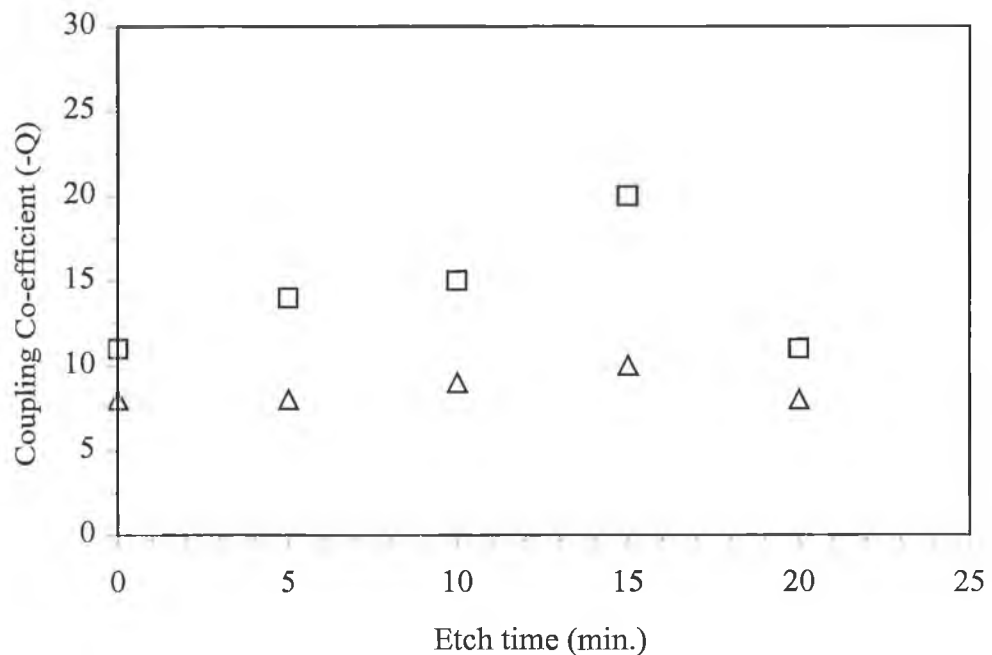


Figure 6.15: Ratio of Raman peaks in film as a function of argon etch time: $\Delta 1.5 \times 10^{-3}$ mbar, $\square 4.8 \times 10^{-3}$ mbar.

6.4.2 Films Stress and Adhesion

Figure 6.17 shows the pull-off adhesion strength of DLC films deposited on substrates as a function of argon etch time. The results are the average of three tests and the error bars show the standard deviation of the results. The maximum adhesion of the film was found at 15min etching time. The same result was found for Rockwell adhesion shown in figure

6.18. The points on this graph show the results of two tests; each test giving the same result.

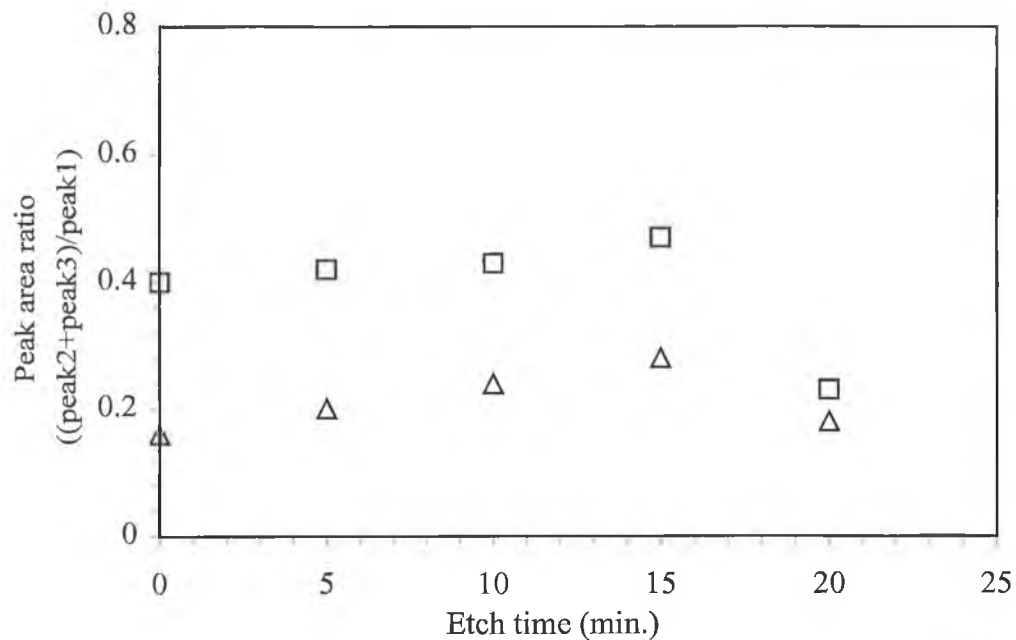


Figure 6.16: Coupling coefficient, Q , as a function of argon etch time: $\Delta 1.5 \times 10^{-3}$ mbar, $\square 4.8 \times 10^{-3}$ mbar.

Even without any adhesion layer between the steel and the DLC, a Rockwell figure HF2 is obtained indicating good adhesion whereas HF6 indicates poor adhesion (Fig: 6.19). Figure 6.19 (d) shows a typical failure, which can be related to the adhesion quality HF6 that has been mentioned in previous section. This shows lateral cracking, which forms circumferentially around the indentation and leads to large circular delamination by piling up the substrate. It is clear that the pressure under which etching and deposition were carried out had little effect on the adhesion within the range of experiment, even though there were significant differences in film structure and stress. In all cases the surface on the substrates was the same since they were all polished and prepared by the same process.

As stated previously, the film hardness showed little variation with deposition conditions therefore, this confirms that the effect on the substrate surface rather than the film structure has the major effect on adhesion. Figure 6.20 shows the stress of the films as a function of argon etch time. The minimum stress is also seen to occur at 15 min. argon etch time,

consistent with the best adhesion. The film hardness showed little variation with film structure and stress variations, having values in the range ~18-22 GPa.

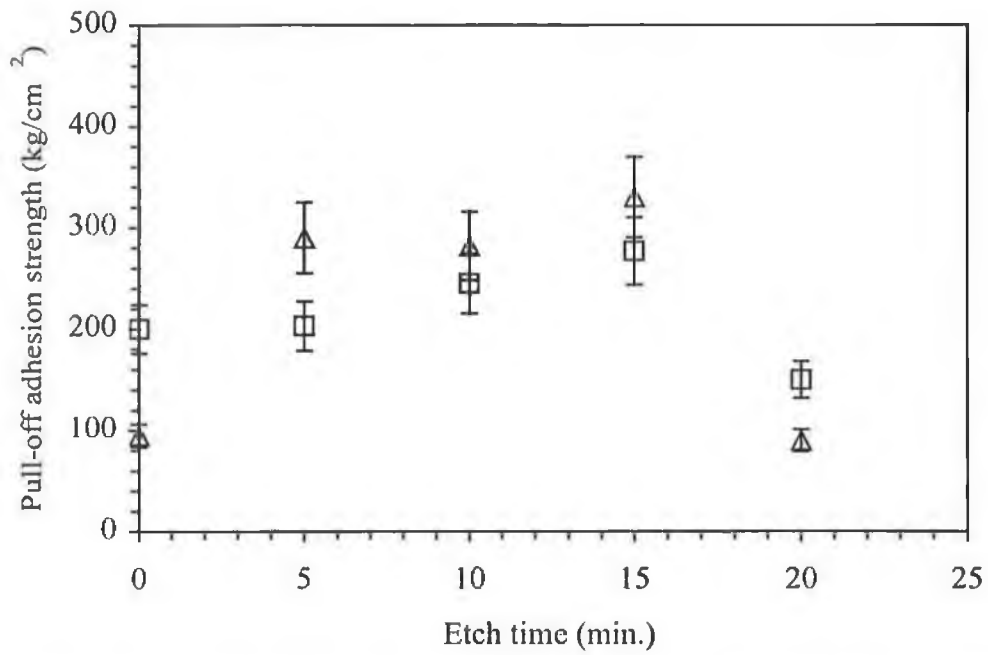


Figure 6.17: Pull-off adhesion strength of films as a function of argon etch time: $\Delta 1.5 \times 10^3$ mbar, $\square 4.8 \times 10^3$ mbar. Error bars show the standard deviation.

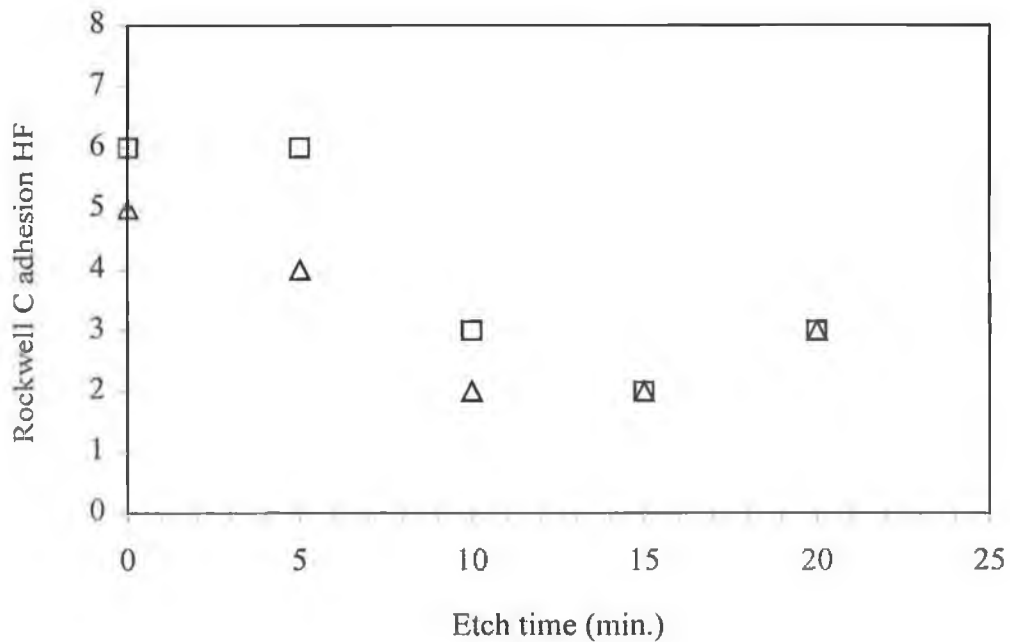


Figure 6.18: Rockwell C adhesion of films as a function of argon etch time: $\Delta 1.5 \times 10^3$ mbar, $\square 4.8 \times 10^3$ mbar.

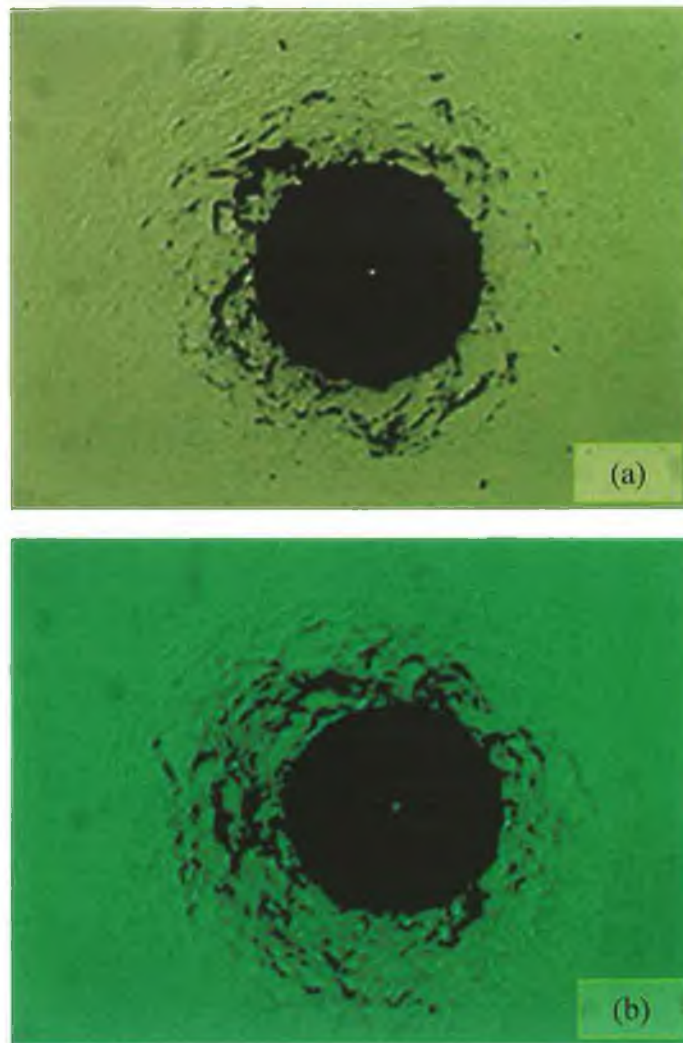


Figure 6.19: Rockwell indentation for adhesion evaluation of DLC films deposited on 316L stainless steel: (a) film deposited with 4.8×10^{-3} mbar pressure and 15 min. etch time, the feature represents adhesion in HF2 Rockwell indentation scale and shows cracks of the films surrounding the indenter; (b) film deposited with 4.8×10^{-3} mbar pressure and 10 min. etch time, the feature represents adhesion in HF3 Rockwell indentation scale and shows large amount of cracks (compare to Fig; 6.19-a) of the films surrounding the indenter. The fragments of the films are due to indentation (small spots). Magnification 80x.

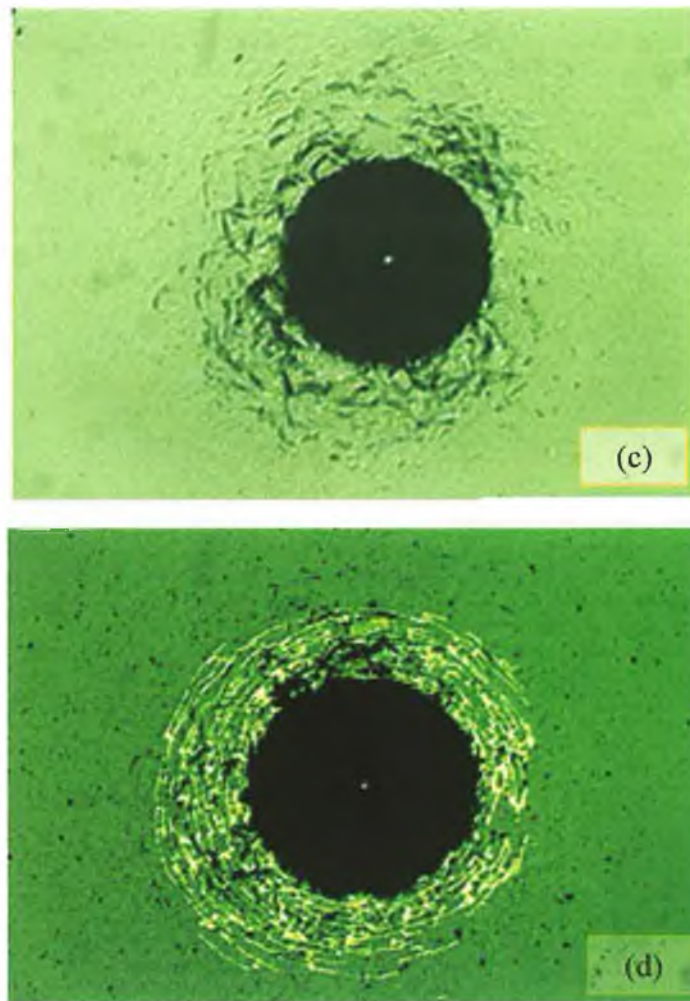


Figure 6.19: Rockwell indentation for adhesion evaluation of DLC films deposited on 316L stainless steel: (c) film deposited with 1.5×10^{-3} mbar pressure and 05 min. etch time, the feature represents adhesion in HF4 Rockwell indentation scale and shows slight delamination of the film at the edge of the indenter; (d) film deposited with 1.5×10^{-3} mbar pressure and 0 min. etch time, shows lateral cracking which forms circumferentially around the indenter and leads to large circular delamination by pilling up the substrate. This feature represents adhesion in HF6 Rockwell indentation scale. The fragments of the films are due to indentation (small spots). Magnification 80x.

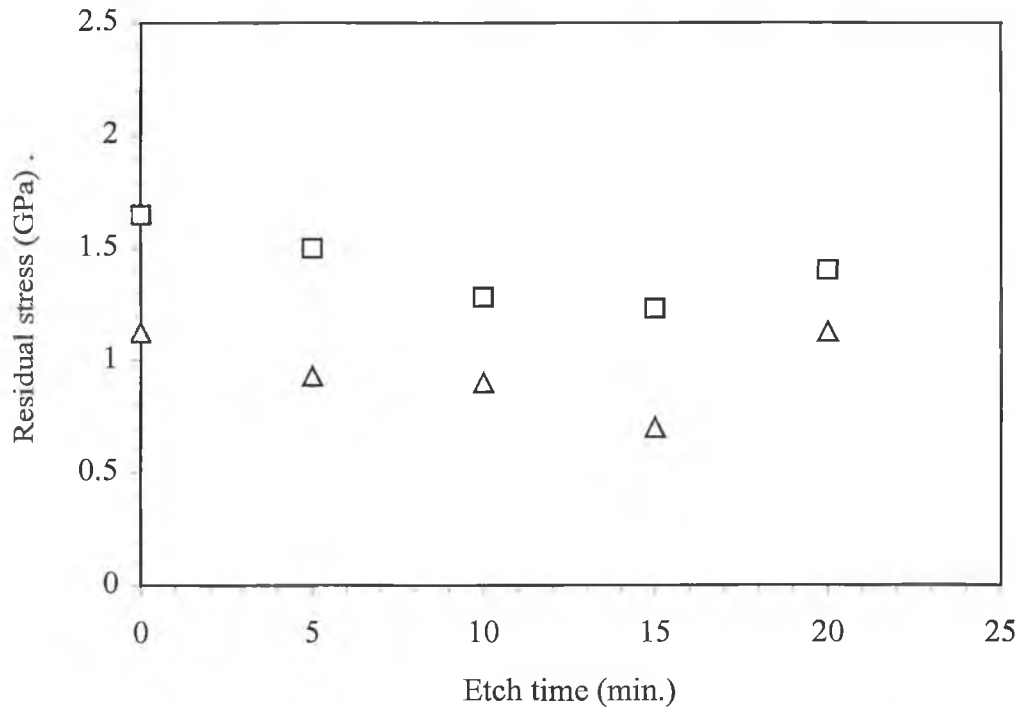


Figure 6.20: Film intrinsic stress as a function of argon etch time: $\Delta 1.5 \times 10^{-3}$ mbar, $\square 4.8 \times 10^{-3}$ mbar.

6.4.3 FTIR

In order to investigate the surface changes which occurred during etching gave rise to these variations in adhesion and film structure the composition of the surface oxide layer on the substrate was determined by measuring the FTIR transmission of the oxide layer in the reflection mode. The FTIR spectra of substrate surfaces with different etching times are shown in figure 6.21. The prominent features in the spectrum from the unetched substrate are two peaks at 405 and 430 cm^{-1} which can be ascribed to Cr_2O_3 bond absorption [327]. There are a number of other peaks which are more difficult to identify; they could be a combination of iron and nickel oxides, but those at 475 and 504 cm^{-1} may be related to the iron oxide Fe_2O_3 . As etching proceeds, these bands reduce until after 15 mins etching there is only a small trace of the 405 cm^{-1} band and the main absorption peak

occurs at $\sim 450 \text{ cm}^{-1}$. This may be due to the nickel oxide Ni_2O_3 . With increased etching time the spectrum reverts to that more characteristic of $\text{Cr}_2\text{O}_3 + \text{Fe}_2\text{O}_3$. Analytical and structural investigations of the oxide layer formed on 316L stainless steel after oxidation under various conditions have shown that it does not have homogeneous composition; the outermost part of oxide film consists of mixed iron-nickel oxide whereas innermost part of the film consists of chromium oxide film [328,329]. The results given here suggest also that the oxide layer is inhomogeneous and that adhesion is best when only a nickel oxide layer remains on the surface. However, this does not explain why the $\text{Cr}_2\text{O}_3 + \text{Fe}_2\text{O}_3$ layer should redevelop after longer etching times. It should be mentioned that these FTIR measurements were done *ex-situ* immediately after deposition, which implies that there will be some re-oxidation of the surface by exposure to air. The evolution of this layer with time was observed and it was found to take several hours before the steel returned to its pre-etched state. It is possible that the longer etch time totally removes any surface oxide which leaves the steel surface in a very reactive condition so that on exposure to air a $\text{Cr}_2\text{O}_3 + \text{Fe}_2\text{O}_3$ layer is rapidly produced whereas the existence of a nickel oxide layer maintains passivation and only allows slow reoxidation.

The argon etching of the film therefore has two effects; (i) it improves the film adhesion significantly as shown by the Rockwell C test results changing from HF6 to HF2 and (ii) it affects the bulk film properties as shown by the changes in their Raman spectra. It has to be considered whether it is solely the bulk properties that affect the adhesion, however, the fact that the film hardness does not vary and the film stress only varies by $\sim 30\%$ is not enough to give the large changes in adhesion which were found.

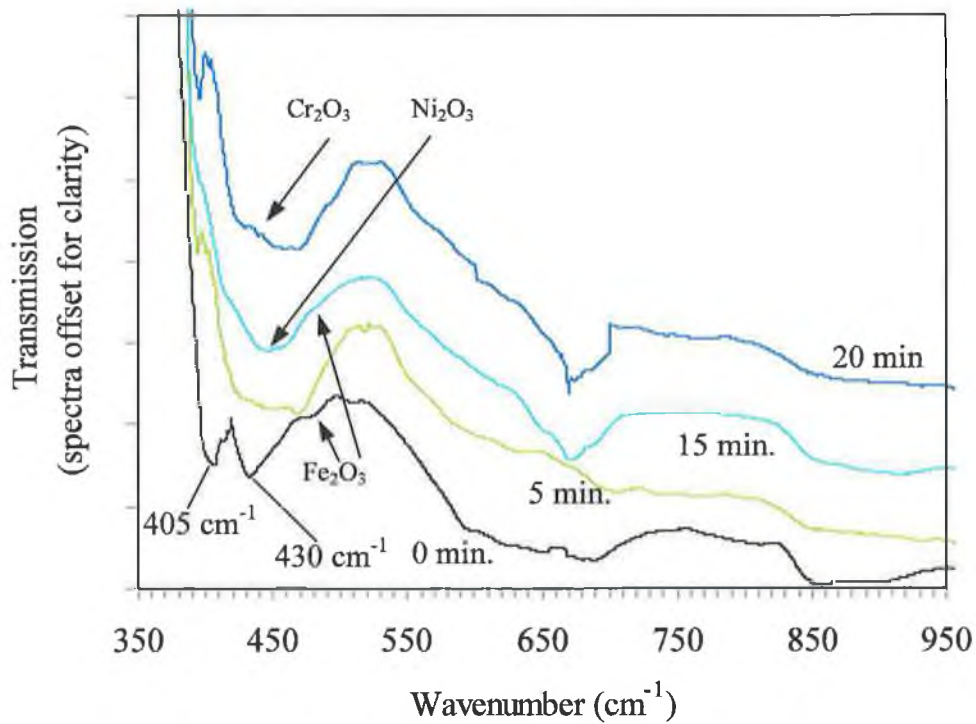


Figure 6.21: FTIR transmission spectra of surface oxide as a function of argon etch time: 80 degree incidence angle and reflection from substrate.

6.5 Effect of Surface Treatment of 316L stainless steel, CoCr and Ti6Al4V Alloys

In this section DLC films have been deposited on to substrates of 316L stainless steel, cobalt-chrome and titanium alloy with constant deposition pressure, 1.5×10^{-3} and source current, 1A. Substrates were argon pre-etched and the etching time and other deposition parameters have been discussed in experimental part.

6.5.1 Raman Spectroscopy

Figure 6.22 shows the peak area ratio ((peak 2+peak 3)/peak 1) as a function of deposition condition for 8 mm thick substrates. It can be seen that the peak area ratio increases with increasing substrate etching time up to 15 minutes and then decreases. The peak area ratio is indicative of a change in the bonding structure of the films. The area ratio is higher for the CoCr alloy followed by titanium alloy and finally the 316L substrates. The variations

of the coupling coefficient (Q) with deposition conditions are shown in figure 6.23. The value of Q decreases with increasing etching time up to 15 minutes and then decreasing. The Q value is correlated with the sp^3/sp^2 ratio with a decrease in the magnitude of the Q value (i.e. a more negative value) indicating an increase in the sp^3 content [318,319]. Both the peak area ratio and the coupling coefficient, Q , show similar behaviour in that the sp^3/sp^2 ratio is maximised for an etching time of 15 minutes.

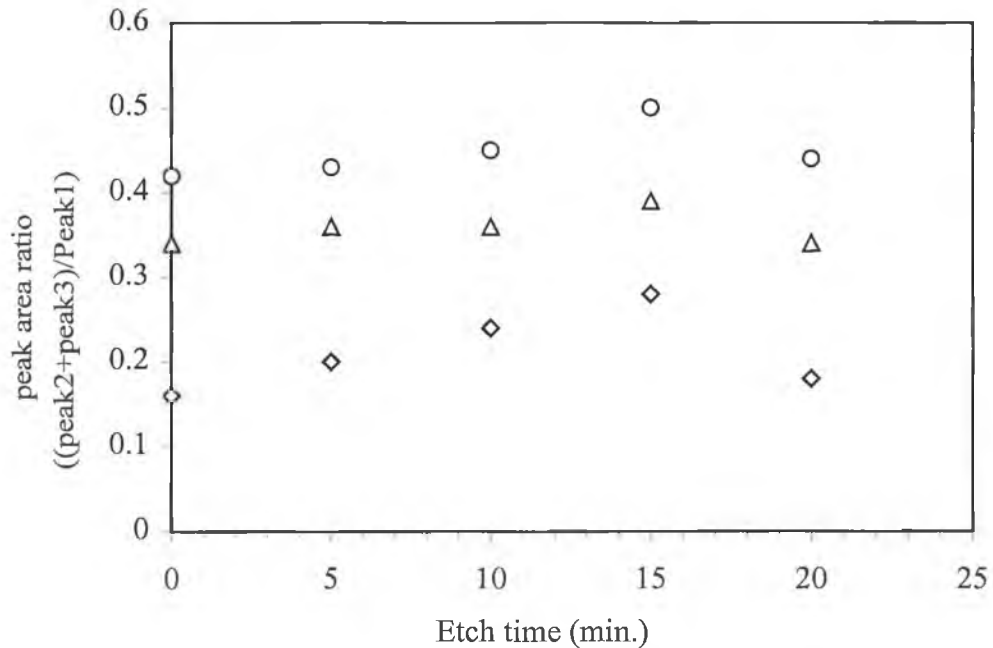


Figure 6.22: Ratio of Raman peaks in films as a function of argon etch time: ◇316L stainless steel, ○ CoCr alloy and △ Ti6Al4V alloy (8 mm thickness substrates).

6.5.2 Adhesion

Figure 6.24 shows the pull-off adhesion strength of DLC films deposited on substrates as a function of argon etch time. The maximum adhesion of the film was found at 15 min. etching time. The same result was found for Rockwell adhesion shown in figure 6.25. Even without any adhesion layer between the substrates and the DLC, a Rockwell figure HF1 is obtained on CoCr alloy substrates indicating good adhesion. It is clear that there is a direct relationship between the adhesion and the film structure in terms of sp^3 content as shown by both the peak area ratio and the coupling coefficient.

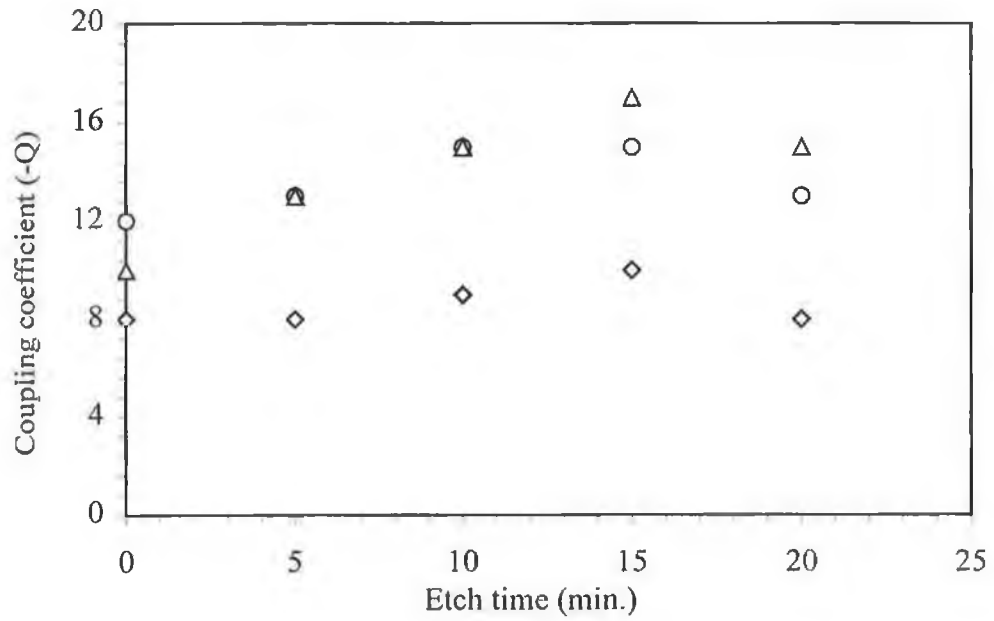


Figure 6.23: Coupling coefficient, Q , as a function of argon etch time: ◇ 316L stainless steel, ○ CoCr alloy and △ Ti6Al4V alloy (8 mm thickness substrates).

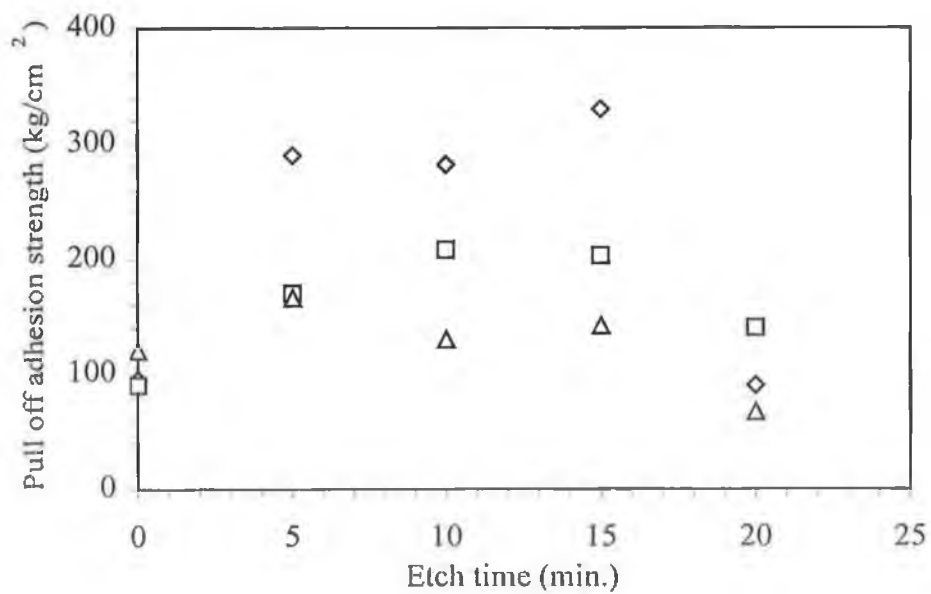


Figure 6.24: Pull-off adhesion strength of films as a function of argon etch time: ◇ 316L stainless steel, □ CoCr alloy and △ Ti6Al4V alloy (8 mm substrates).

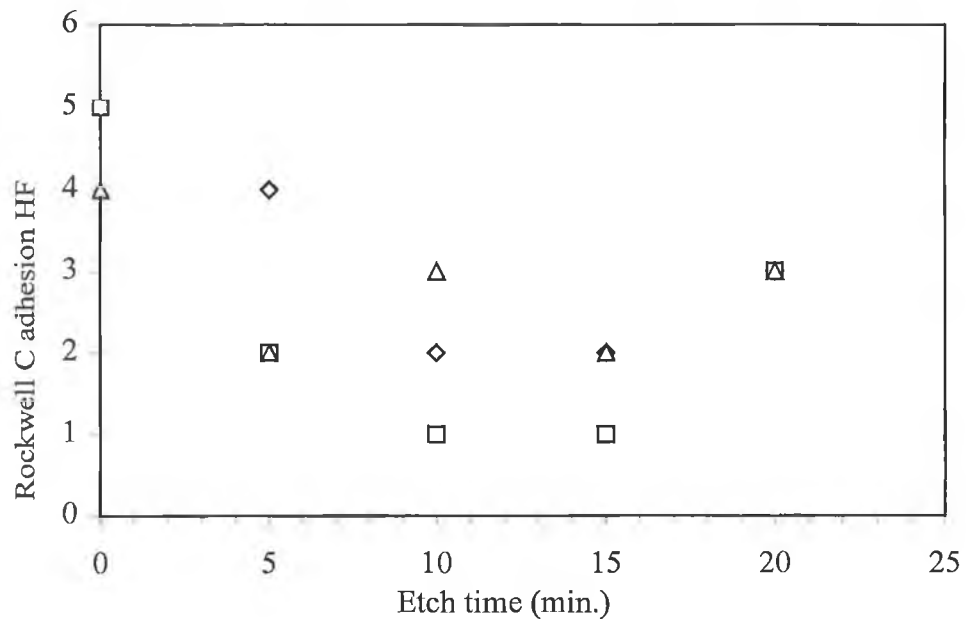


Figure 6.25: Rockwell C adhesion of films as a function of argon etch time: ◇316L stainless steel, □ CoCr alloy and △ Ti6Al4V alloy (8 mm substrates).

Figure 6.26 (a-d) shows the typical Rockwell indentation photographs of DLC films deposited on Ti6Al4V and Co-Cr alloys with the magnification of 80x in all cases.

6.5.3 Effect of Temperature

Fig. 6.27 shows the temperature generated as a function of etching and deposition times with contact and non contact substrate. Note that between etching and deposition the substrates were allowed to cool to the ambient temperature. Consequently the temperature reached during deposition was independent of etching time. The temperature increased to ~110 °C and ~81 °C during the etching and the deposition respectively of the better-insulated substrates compared to ~79 °C and ~65 °C for the less well insulated substrates. The evolution of the film structure with argon etch time for the higher temperature 316L substrates is shown in figure 6.28. Here it can be seen that the peak of sp^3 content occurs at shorter times compared to the measurements on the less-insulated substrates. This indicates that the temperature of the substrate during etching affects the film structure and consequently adhesion; all films experienced the same deposition conditions. If the point

of maximum adhesion is compared to the temperature during etching, it is clear that there is a narrow “window” during which best results are achieved. At etch times of 15 mins. (cooler) and 5 mins. (hotter) substrates this equates to a temperature of ~ 75 °C. The peak area ratios and coupling coefficients of the hotter compared to the cooler substrates (0.37 v. 0.28 for peak area ratio and -14 v. -10 for Q) show that the higher temperature during etching produces a significant increase in the sp^3 content. It is not clear if this difference is caused by the etching alone; it may also be influenced by the temperature during deposition.

The adhesion of DLC films to different substrates is related to chemical interaction between the film and substrate surfaces, microstructural defects in the film-substrate interface and compressive stress levels in the film. A clean surface is vital for good adhesion of the film as oxide and other contaminant layers are known to have a detrimental effect on film adhesion. Even in the case of clean substrate surfaces, the adhesion strength will depend both on the nature of the substrate material, and on the deposition conditions due to the change in initial growth mechanisms as the growth kinetics are altered. Titanium and chromium are known to form carbide interlayers, poor adhesion of DLC to the titanium alloy may be due to a thicker than expected oxide layer as observed by others [330]. Argon sputter etch cleaning can be used to remove oxides, however excessive sputter etching can introduce sputter-induced defects which have been shown to be a factor in the reduced adhesion strength of the CH_4/Ar produced films [330].

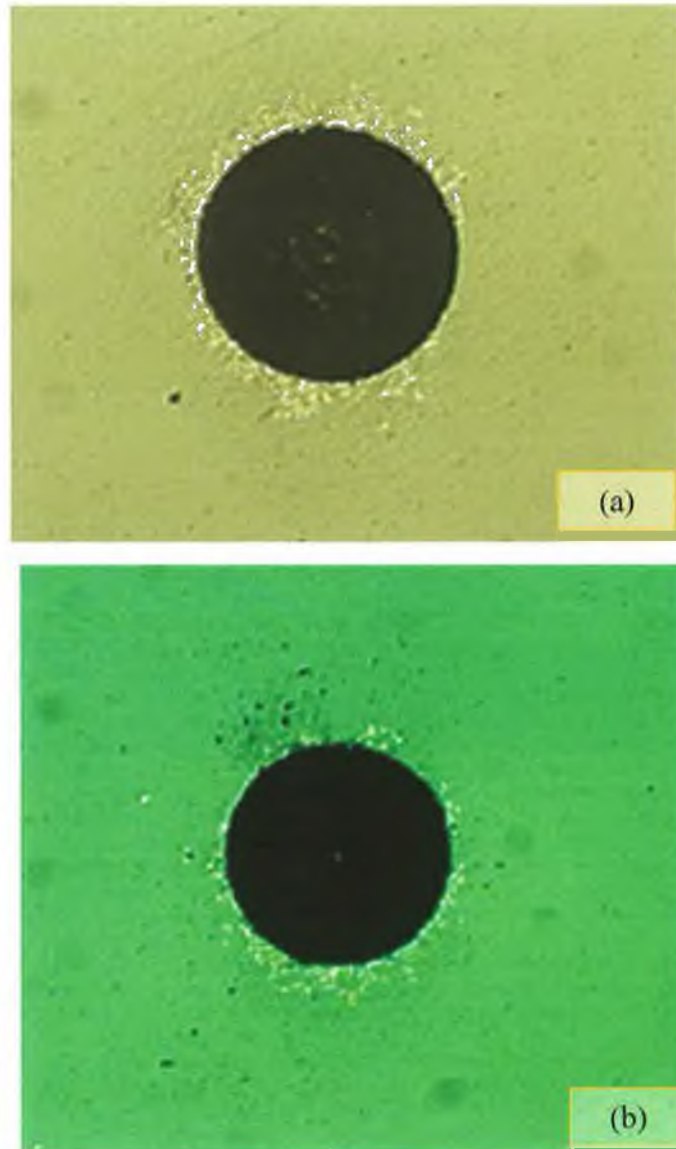


Figure 6.26: Rockwell indentation for adhesion evaluation of DLC films deposited Ti6Al4V alloy: (a) film deposited with 1.5×10^{-3} mbar pressure and 0 min. etch time, the feature represents adhesion in HF4 Rockwell indentation scale and shows slight delamination of the film at the edge of the indenter; (b) film deposited with 1.5×10^{-3} mbar pressure and 10 min. etch time, the feature represents adhesion in HF3 Rockwell indentation scale and shows cracks and little delamination of the films surrounding the indenter. The fragments of the films are due to indentation (small spots). Magnification 80x.

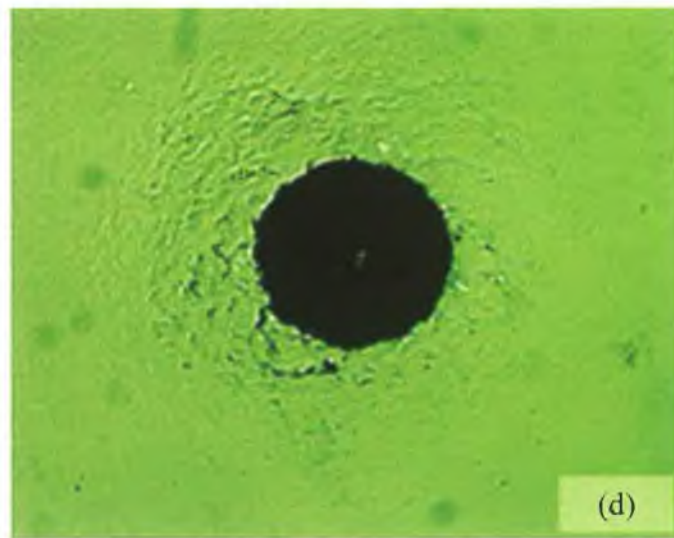
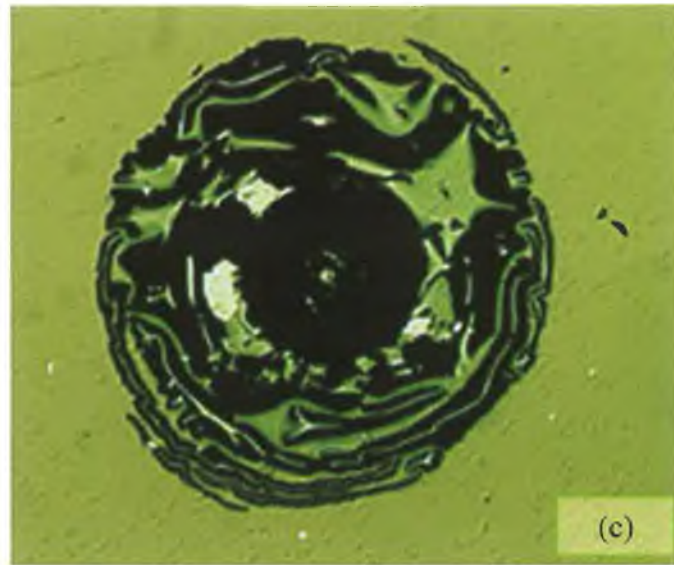


Figure 6.26: Rockwell indentation for adhesion evaluation of DLC films deposited cobalt chrome (CoCr) alloy: (c) film deposited with 1.5×10^{-3} mbar pressure and 0 min. etch time, the feature represents adhesion in HF5 Rockwell indentation scale and shows circumferential cracks surround the indenter and films is not completely delaminated; (d) film deposited with 1.5×10^{-3} mbar pressure and 10 min. etch time, shows a typical failure which can be related to the adhesion strength quality HF1. The fragments of the films are due to indentation (small spots). Magnification 80x.

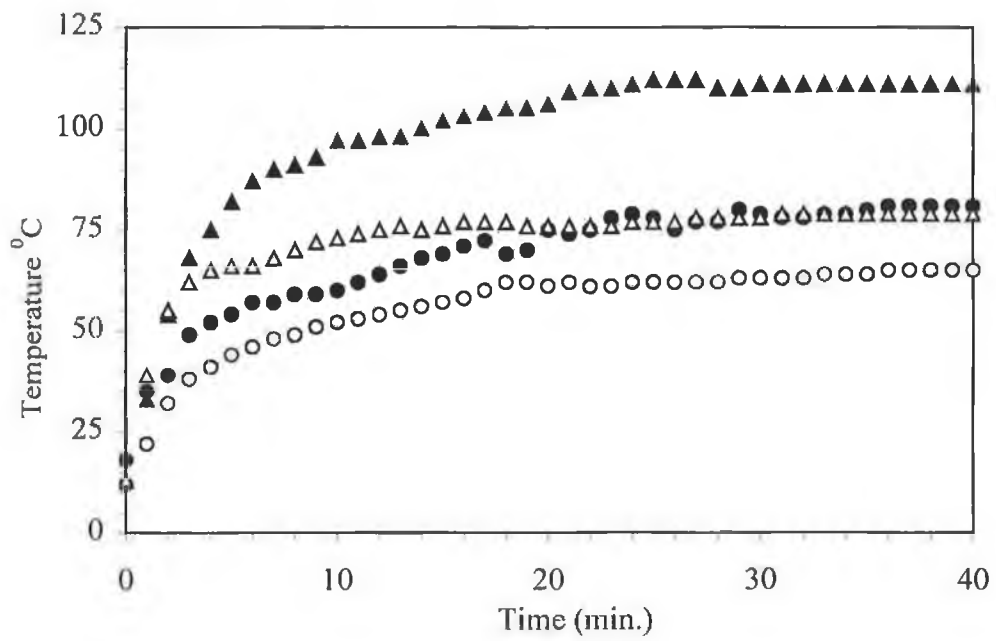


Figure 6.27: Temperature as a function of etching and deposition time: ● etching (8 mm substrate), ▲ etching (0.2 mm substrate), △ deposition (0.2 mm substrate) and ○ deposition (8 mm substrate).

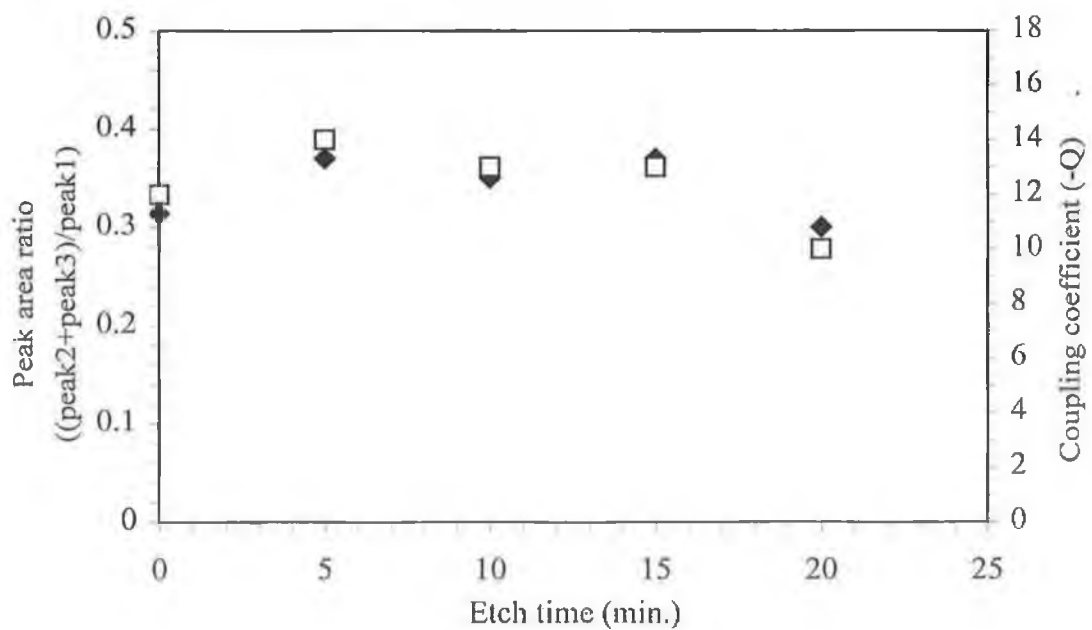


Figure 6.28: Peak area ratio, ◆, and coupling coefficient, □, of 0.2 mm substrates as a function of argon etch time.

Chapter 7

Modelling for Cohesive Strength of DLC Thin Film

7.1 Finite Element Analysis (FEA)

The finite element method is a numerical procedure that can be used to solve many of the problems encountered in engineering analysis, including stress analysis, joint displacement, heat transfer, fluid flow, electromagnetism and solid mechanics problems. In thin film coating of metal substrate, FEA is used to validate and predict the experimental results through the numerical formulation. Film-substrate adhesion as well as cohesion is a major problem in thin film technology. Several methods can be used to measure cohesive strength of the films. The four point bend test (FPB) is one of the simplest and easiest method than can be used to measure the cohesive strength of films. FEA may help researchers to understand where the maximum stress arises in film substrate component and hence helps to identify cracking during the test. The load, which produces the cracks, called critical load (P_{cr}) can be used in mathematical equation as well as FEA to measure the cohesive strength of films. In this a way FEA may support experimental work and to observe the stress distribution across the coating thickness.

There are many finite element method software programs available to provide various engineering solution. However, the ANSYS program has been used in the current research, as it is widely available within the university.

The origin of the modern finite element method may be traced back to the early 1900s, when some investigators approximated and modelled elastic continua using discrete equivalent elastic bars. The ANSYS finite element method software was released in 1971 for the first time. Every year this software package is upgraded and the current version of ANSYS contains multiple windows incorporating a Graphical User Interface (GUI), pull-down menus, dialog boxes and a tool bar. The following section is to introduce the basic concepts of FEA.

Some of FEA's limitations arise from difficulties in creating an adequate model of the complex geometries (e.g., heavily contoured resonators or composite resonators) that require three-dimensional models. The model is often simplified in order to reduce modeling and computing time. Such a model will always give somewhat limited or incomplete results. The FEA engineer must have sufficient experience to estimate the effect of such simplifications.

7.2 Engineering Problems

Engineering problems can be described in general as being mathematical models of physical situations [331]. The mathematical model generally comprises numerous differential equations with sets of corresponding initial and boundary conditions. The differential equations are derived by applying fundamental laws and principles of nature to an engineering system. These equations represent the balance of mass, force or energy. When possible, the solution of these equations renders a detailed behaviour of a system under a given set of conditions.

Analytical solutions show the exact behaviour of a system at any point within the system. An analytical solution may be composed of two parts: firstly, homogeneous part and secondly, a particular part. In any engineering system, there are two sets of parameters that influence the way a system behaves. Firstly there are those parameters that provide information regarding natural behaviour of a given system and always appear in the homogenous part of the solution. Examples of these parameters include modulus of elasticity, viscosity and thermal conductivity of a material. On the other hand, there are parameters that produce disturbance in a system and they appear in the particular part of the solution. Examples of disturbing parameters include external force, pressure difference in fluid flow and temperature difference across the medium.

7.3 Numerical Method

Many practical engineering problems can only be solved approximately. This inability to obtain an exact solution may be attributed to either the complex nature of the governing differential equation or the difficulties that arises from the dealing with initial and boundary conditions [331]. To deal with such problems, numerical approximations are used. In contrast to analytical solutions, which show the exact behaviour of a system at any point within the system, numerical solutions approximate exact solutions only at discrete points. The first step in the numerical procedure is to discretize (divide) a system into small subsystems known as elements whose shape is described by discrete points known as nodes.

There are two types of numerical methods, finite difference method and finite element method. With finite difference method, the differential equation is written at each discrete point (node) and the derivatives are replaced by difference equations. This approach results in a set of simultaneous linear equations [332]. The finite difference method is easy to apply to a simple system. However, it becomes difficult to apply to a system with complex geometries or with complex boundary conditions. An example of this would be a system involving nonisotropic material properties.

The finite element method uses integral formulation rather than difference equations to create a system of algebraic equations. Moreover, an approximate continuous function is assumed to represent the solution for each element. The complete solution is generated by connecting or assembling the individual solutions allowing for continuity at the inter elemental boundaries.

7.4 Steps in the Finite Element Method

The basic steps in any finite element analysis consist of the following [333]:

a) Preprocessing Phase

- i) Create and discretize the solution domain into finite elements, that is the system is subdivided into nodes and elements.
- ii) Assume a shape function to represent the physical behaviour of an element; that is an approximate continuous function is assumed to represent the solution of an element.
- iii) Develop the element equations.
- iv) Arrange and assemble the elements to represent the entire system. Construct the global stiffness matrix.
- v) Apply boundary conditions, initial conditions and loading.

b) Solution Phase

- i) Solve a set of linear and nonlinear algebraic equations simultaneously to obtain nodal results, such as displacement values at different nodes or temperature values at different nodes in a heat transfer problem.

Postprocessor Phase

- i) Using the nodal values and interpolation functions, other parameters such as strain, stress etc. inside each element may be determined.

7.5 Four Point Bend Test (FPB)

Three types of strength are important for coating materials: bond (adhesive) strength, cohesive strength and in-plane strength. The distinction between the first two can be made by failure location. If failure occurs at the coating-substrate interface, the corresponding strength value is adhesive and if it occurs within the coating, the strength value is cohesive. Of the two, adhesive strength is the most important since coatings often fail by debonding at the interface. Therefore, a systematic investigation of the decohesion mechanism and determination of adhesion strength of DLC coating on 316L stainless steel are necessary and the results will give guidelines on the coating procedure for further improvement of their performance behaviour.

Various mechanical test methods such as tension, plane bending, torsion and four point bend test have been conventionally used to characterise the mechanical properties of materials. Amongst these tests, the four point bend test is of practical interest and offers a number of advantages over the other testing methods. Firstly, it produces a uniform moment between the two inner loading rollers in the specimen, which gives rise to a uniform maximum tensile stress in the specimen surface. Secondly, no special sample gripping is needed for the four-point bend test, which makes it possible to test brittle materials in tension, and sample preparation is relatively simple since a specimen with uniform rectangular cross section is usually used in the test. Thirdly, sample mounting and dismounting is fairly straightforward in a four point bend which makes it very convenient compared to the other mechanical test methods [334].

7.5.1 Theoretical Background of Four Point Bend Test

The loading arrangement for the four point bend test is as shown in figure 7.1. The maximum bending moment in a four point bend test is given by,

$$M = \frac{P(L_0 - L_1)}{4} \quad 7.1$$

where P, L_0 and L_1 are the applied load, outer and inner loading span distance, respectively.

The stress is maximum along the top and bottom surface of the beam and is given as,

$$\sigma = \frac{My}{I} \quad 7.2$$

where I is the second moment of area for the beam cross-section and y represents the position of the neutral axis with respect to the top or bottom surface of the beam. In the present case, since the beam consist of two layers, individual components of stress and moment of inertia for coating and the substrate have to be considered.

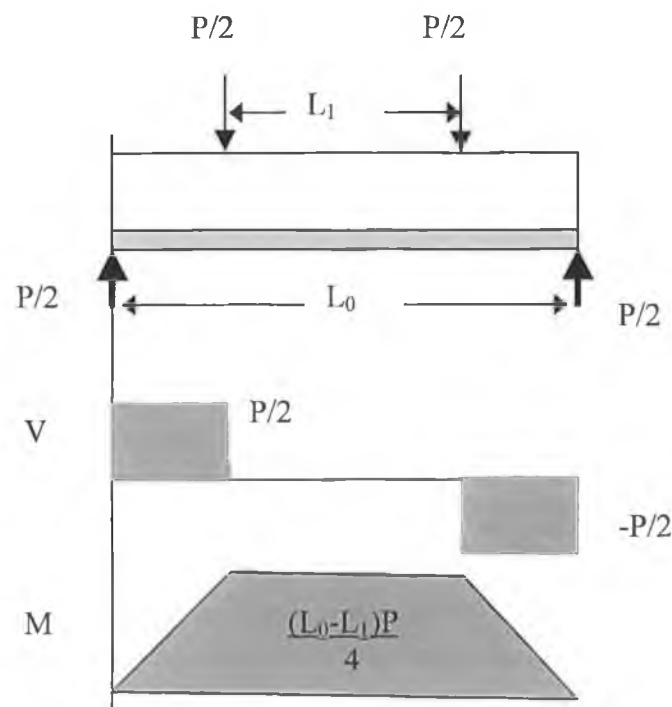


Figure 7.1: The loading arrangement for the four-point bend test.

Since the coating and substrate are of different material having different Young's moduli, there will be a shift in the neutral axis of the rectangular cross-section under the bending load. Using the strength of materials approach, the actual cross-section can be transformed into an equivalent cross-section in terms of its two components [335]. Figure 7.2 (a) shows

the sketch of the cross-section of coating-substrate material, whereas figure 7.2 (b-d) shows the transformed cross-section. This transformation depends only on the elastic modulus.

The elastic modulus ratio, n , is given as

$$n = \frac{E_c}{E_s} \quad 7.3$$

where E_c and E_s are the elastic modulus of coating and substrate respectively.

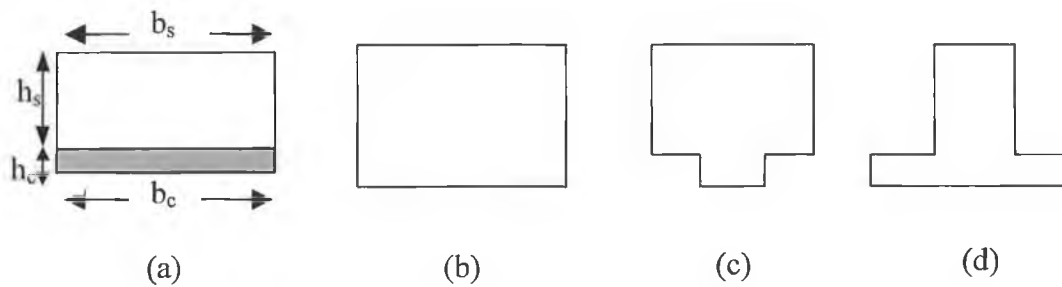


Figure 7.2. Cross section of coating-substrate material system: (a) original cross-section; (b) transformed cross-section ($E_s = E_c$ (trivial)); (c) transformed cross section ($E_s > E_c$) and (d) transformed cross section ($E_s < E_c$).

In the transformed cross-section the first parameter to be calculated is the position of the neutral axis, y_c , and can be written with respect to the coating surface as follows,

$$y_c = \frac{\sum_{i=c,s} M_i}{\sum_{i=c,s} A_i} = \frac{M_{coating} + M_{substrate}}{Area_{total}} = \frac{M_c + M_s}{A_t} \quad 7.4$$

$$y_c = \frac{h_c^2 b_c / 2 + h_s b_s (h_s / 2 + h_c)}{h_c b_c + h_s b_s} \quad 7.5$$

where h and b are the height and width of the constituents respectively, while the subscripts c and s signify the coating and substrate respectively. The next step is to calculate the second moment of area, I . Since the neutral axis is not at the geometric centre, a parallel axis theorem must be used to shift the I -values of each constituent area to

the neutral axis and therefore total moment of inertia I_t of the entire coating-substrate system is given by the following relationship,

$$I_t = \sum_{i=c,s} (I_i + A_i d_i^2) \quad 7.6$$

$$I_t = \left[\left(\frac{b_c h_c^3}{12} \right) + h_c b_c \left(y_c - \frac{h_c}{2} \right)^2 \right] + \left[\left(\frac{b_s h_s^3}{12} \right) + h_s b_s \left(y_c - \left(h_c + \frac{h_s}{2} \right) \right)^2 \right]$$

The maximum stress on the substrate surface is given as,

$$\sigma_s = \frac{M y_s}{I_t} = \frac{P(L_0 - L_1) y_s}{4I_t} \quad 7.7$$

and the maximum stress in coating surface is given by Hooke's law as,

$$\sigma_c = E_c \varepsilon_c$$

but,

$$\sigma_s = E_s \varepsilon_s$$

Therefore,

$$\sigma_c = n \sigma_s \left(\frac{\varepsilon_c}{\varepsilon_s} \right) \quad 7.8$$

$$\text{or, } \sigma_c = n \sigma_s \left(\frac{y_c}{y_s} \right)$$

where ε_c and ε_s are strains in coating and substrate respectively and y_s is the distance between the substrate surface and neutral axis.

Thus by substituting the Eq. (7.7) into Eq. (7.8), an analytical solution to calculate the strength of coating, σ_{cr} , at critical load P_{cr} , is obtained.

$$\sigma_{cr} = n \left[\frac{(L_0 - L_1) y_c}{4I_t} \right] P_{cr} \quad 7.9$$

P_{cr} is to be determined experimentally from the load displacement curves (LVDT technique) during four point bend test. This load corresponds to the point on the curve where deviation linearity occurs.

7.6 Experimental Procedure

The specimen prepared from 316L stainless steel used in the four point bend test consists of straight beam of rectangular cross section with dimension 50 mm x 4 mm x 0.25 mm. Before deposition, substrates were prepared in the same way used for deposition tests as described the experimental section. Substrates were coated under same deposition parameters.

The coated samples were subjected to four point bend test with a 26 mm inner span and a 40 mm outer span using LVDT technique. Load and displacement during tests were recorded by an in built computer data acquisition system. From the load-displacement plots, the initiation of first crack can be found by observing the point at the plot where deviation from the linearity occurs. The value of the load corresponding to this point was then further used to calculate cohesive strength of the coating using Eq. 7.9 to obtain accuracy results. At least three tests were carried out for each parameter. It should be noted that this method of calculation of cohesive strength of the coating is valid only if the initiation of the crack occurs within the coating. Finite element analysis (FEA) has been used to verify location where maximum stress generated across the coating thickness and can produce initial crack during the test. The accuracy of strength formula (Eq. 7.9) has also been checked by FEA.

After the test was carried out, Stereoscan 440 (developed by Leica Cambridge Ltd.) scanning electron microscope (SEM) was used to reveal the crack.

7.7 Results and Discussion

Figure 7.3 shows a typical load-displacement curve obtained during the four point bend test. It was observed that the load-displacement behaviour displayed by all the samples was similar in general nature. From figure 7.3, it can be seen that the initial part of curve is linear indicating an elastic behaviour of the beam. However, the point where inelastic behaviour starts as a result of the crack initiation in the coating is considered as critical load P_{cr} , which determines the cohesive strength of the coating. At the point after the crack has propagated through the entire thickness of the coating and reached the interface, the load tends to become constant suggesting the beginning of the load via plastic deformation of the substrate material. The values for critical load obtained for the various deposition

conditions tested on the four point bend test are given in table 7.1. This table also provides the values of cohesive strength of the films calculated by equation 7.9. The thickness and elastic modulus of the films with different deposition conditions have also been mentioned in table 7.1. From table 7.1 it is observed that as the deposition pressure increase, the cohesive strength of 0.6 A film increase. For 1A deposition current, these values do not increase with increasing deposition pressure. Along with pressure variables, the cohesive strength values calculated by the beam theory method are inclusive of the effect due to residual stresses incorporated during film growth and the residual stress is a predominant factor affecting the cohesive strength of the coating. By convention, a negative sign indicates compressive stress whereas positive sign indicates tensile stress. Compressive stress adds up to the cohesive strength of the coating and is beneficial in enhancing the surface properties and interfacial strength. On the other hand, tensile stress decreases the strength of the coating and interfacial strength and is undesirable for coating performance. It is noted that the residual stress generated in DLC coatings during film growth is compressive and the coated samples were tested in a configuration to place the coating in tension.

The behaviour of the cohesive strength as a function of a source current and pressure is very similar to changes in sp^3 content (see Fig. 6.9). Higher proportion of covalent bonds in sp^3 rich material probably accounts for this.

Figure 7.4 shows typical cracks, which were formed at critical load P_{cr} (Fig. 7.3). The verification of crack initiation at the surface is very important. But, it is difficult to observe the crack across the film thickness. It is believed that the crack had initiated on the surface of the DLC film and once the crack reached the interface, further loading lead to the formation of interface cracks. This has been proven by finite element analysis where the maximum stress generated to the outer surface of the film, which can provide crack initiation.

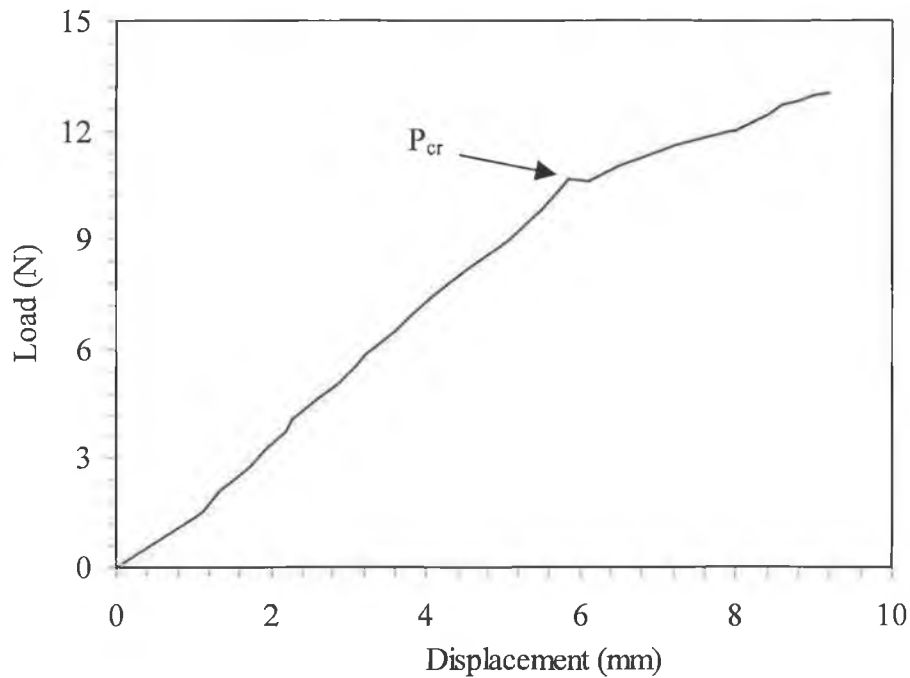


Figure 7.3: Typical load-displacement curve obtained during the four point bend test. (1.5×10^{-3} mbar, 1 A and 100% C_2H_2 gas).

Table 7.1: Properties of DLC films, which were deposited with 100% C_2H_2 process gas and with different deposition parameters.

Source current (A)	Pressure (mbar)	Film thickness, t (micron)	Young's modulus, E (GPa)	Critical load, P_{cr} (N)	Cohesive strength, σ_{cr} (GPa)	Maximum stress by FEA (GPa)	Residual stress (GPa)
0.6	1.5×10^{-3}	0.36	210	11.15	0.980	0.982	0.864
0.6	2.8×10^{-3}	0.35	228	12.5	1.193	1.195	1.078
0.6	3.6×10^{-3}	0.362	225	15.6	1.47	1.472	1.348
0.6	4.8×10^{-3}	0.38	230	18.2	1.752	1.755	1.63
1.0	1.5×10^{-3}	0.435	220	10.60	0.976	0.977	0.858
1.0	2.8×10^{-3}	0.425	225	15.75	1.4833	1.486	1.36
1.0	3.6×10^{-3}	0.425	214	14.72	1.3212	1.321	1.20
1.0	4.8×10^{-3}	0.455	193	-	-	1.104*	0.97

* At the interface



Figure 7.4: Typical SEM micrograph shows cracks obtained during the four point bend test of DLC film (1.5×10^{-3} mbar, 1 A and 100% C_2H_2 gas).

7.8 Study of the Stress Distribution Across the Coating Thickness by FEA

A two dimensional finite element technique is considered to analyse the stress distribution across the coating thickness. This result can help the exact location of crack initiation during the four point bend test. Three different specimen geometries have been considered in this model to investigate the change of stress distribution across the coating thickness.

Specimen geometry one: The film and substrate are perfectly bonded and considered a single beam.

Specimen geometry two: The film and substrate are perfectly bonded and considered a single beam but one element on the outer surface of the central point of the film was considered to be very soft (i.e. $E \ll \ll 1$) that is considered as a notch effected beam.

Specimen geometry three: There is no coated materials at the central point (25 mm from one end of the substrate) of the substrate.

The following assumptions have also been considered to create these models.

1. Film and substrate are perfectly bonded.
2. Film is uniformly deposited on the substrate, i.e., there is no thickness variation over the substrate.
3. There is no friction between the loading points and beam, and supporting points and beam.
4. Film is considered to be in a stress (intrinsic compressive stress) free condition, i.e., there is no stress between the film and the substrate before external loading is applied.

The dimension of the substrate and film were considered as 50 mm x 4 mm x 0.25 mm and 50 mm x 4 mm x 0.000435 mm, respectively. The Young's modulus, Poisson ratio and density of the substrate are 200 GPa, 0.29 and 7.79 gm/cm³, and for coating, two Young's modulus 220 GPa and 193 GPa and Poisson ratio 0.25 and density 2.24gm/cm³ have been considered in these models.

Due to the symmetry of the problem, half of the specimen is analysed with PLANE82 - 2-D 8-node structural solid (Fig. 7.5) using commercial FE software ANSYS 5.5. The schematic diagram of the FE model is shown in figure 7.6.

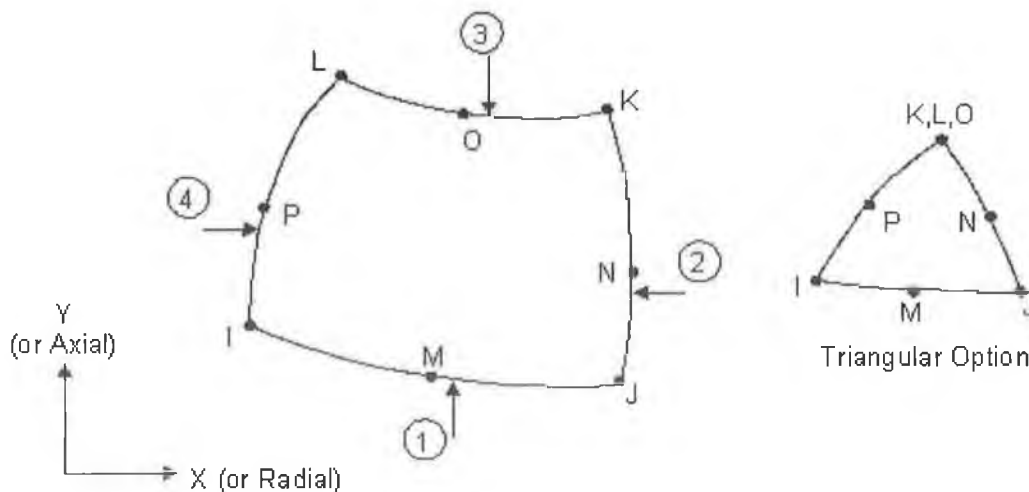


Figure 7.5: PLANE82 is used for 2-D modeling of solid structures. The element is defined by eight nodes having two degrees of freedom at each node: translations in the nodal x and y directions.

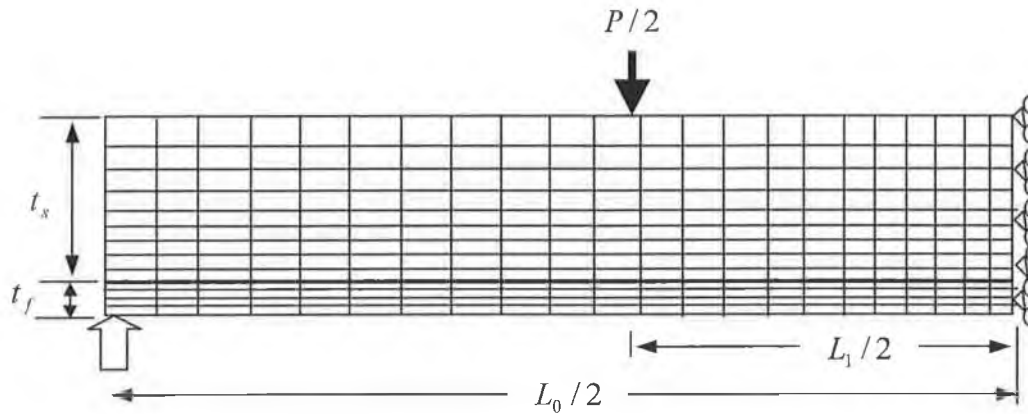


Figure 7.6: A schematic illustration of the FE model.

For a finite element model to produce the correct results, it must be both valid, i.e. properly represent the physical problem (geometry, material properties, loading and boundary conditions) and accurate, i.e. being at or near convergence. The effect of model size was thoroughly examined in this study and the loading and boundary conditions are believed to correct. The accuracy of a finite element model will depend on the type of element used in the model and the fineness of the mesh, and is best evaluated by observing the convergence of the solution as the number of elements defining the problem is increased. This is particularly difficult however, because of number of elements are limited to 32,000 in the ANSYS software. The accuracy (convergence) of the model was confirmed by examining the effect of increasing mesh density and comparing the results with known analytical values. The element type and spacing of element, all influenced the results to some extent. The mesh design used plane82, which can provide automatic meshes and can tolerate irregular shapes without as much loss of accuracy. The meshing spacing was biased towards the beam length and coating thickness. The model was built with the largest possible number of elements in order to improve the accuracy of the solution. The models used approximately 5600 elements and 17629 nodes, and 6000 elements and 18831 nodes for without and with interface beams respectively. The point load of 0.0053 kN was applied to the node of the upper surface of the beam, which is 12 mm from the edge of the model geometry. The point load and the boundary condition of the model are shown in figure 7. 7.

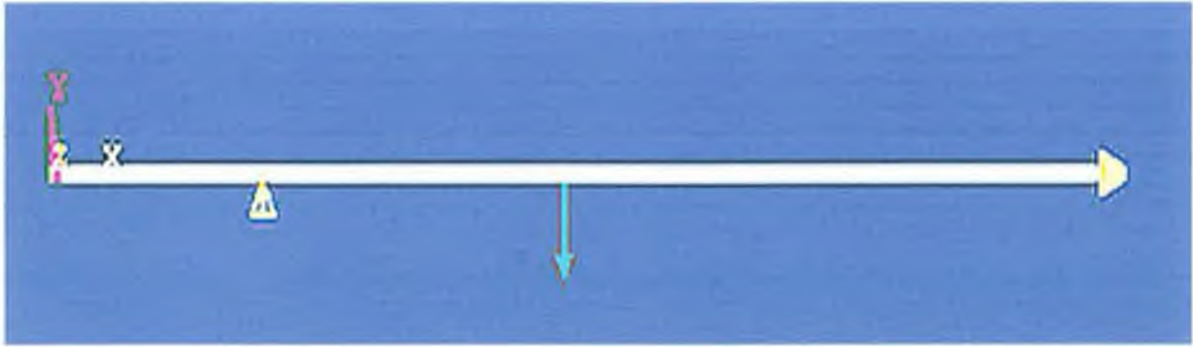


Figure 7.7: Finite element model of coated substrate beam (specimen geometry one, applied load 10.6 N, coating thickness and young's modulus are 0.000435 mm and 220 GPa respectively).

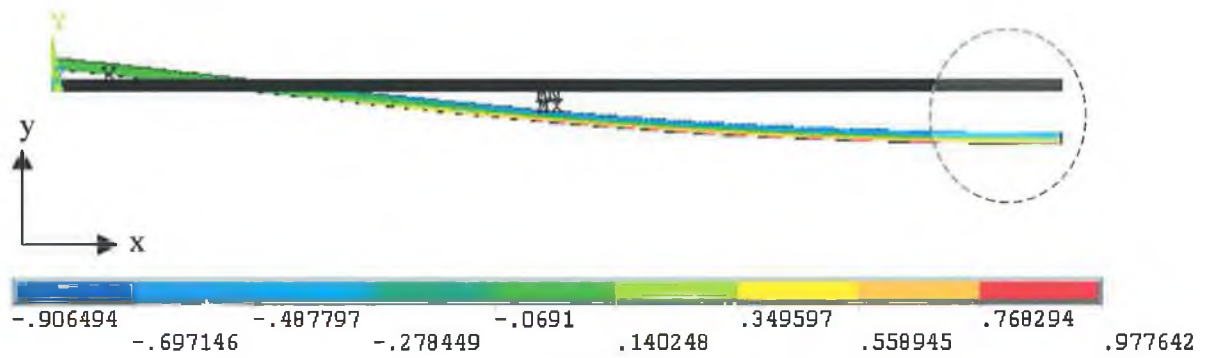


Figure 7.8 (a): Stress distribution of coated substrate along the x direction.

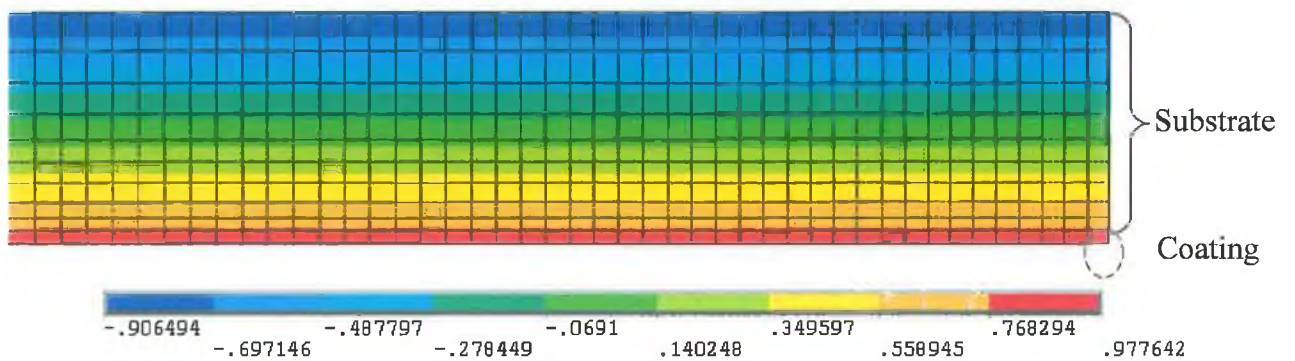


Figure 7.8 (b): Stress distributions along the x direction of enlarged part of figure 7.8(a).

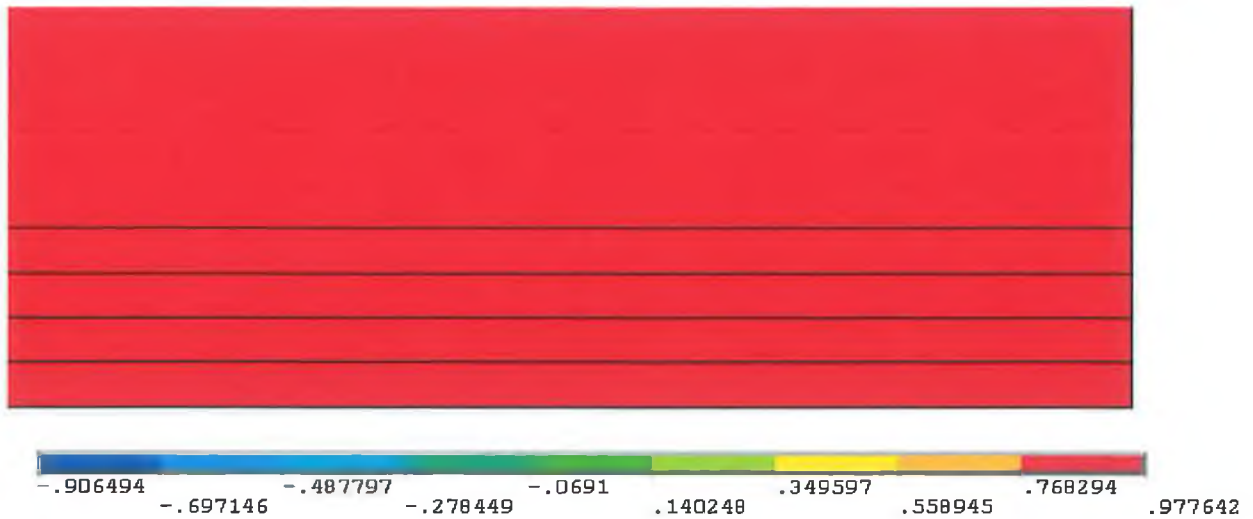


Figure 7.8 (c): Stress distributions along the x direction of enlarged part of figure 7.8 (b).

Figure 7.8 shows the stress distribution across the film thickness in the middle of the beam. Bending is primary deformation made in the outer surface of the film. It causes bending stress of up to 0.977 GPa, which is most likely to initiate crack and propagate through the film thickness.

7.9 Results and Discussion

Figure 7.9 (a-c) shows the stress distribution across the coating thickness, which has been taken from outer surface of the central part of the film. Figure 7.9 (a) shows stress distribution for specimen geometry one and figure 7.9 (b) and (c) show the stress distribution for specimen geometry two and three respectively. In all cases, the stress distribution across the coating thickness for low Young's modulus film (i.e. $E_c < E_s$) was found different behaviour compared with higher Young's modulus ($E_c > E_s$) film. Figure 7.9 (a) shows maximum stress is concentrated at the outer surface of the film for higher E_c . The stress is gradually decreased up to three-fourth of the film thickness. This change is not so far but consistent. Beyond this point, the stress is abruptly falling down up to the film-substrate interface. This is because the change of Young's modulus of film and substrate. After the interface, the stress also decreased linearly and come down to zero at

neutral axis. This part is not important to analyse stress in this section. So, it can be avoided during analysis. For lower Young's modulus film ($E_c < E_s$), the stress distribution was found in reverse way up to film-substrate interface which indicates that maximum stress is concentrated at film-substrate interface. Figure 7.10 shows the deflection along the beam length. The maximum deflection occurred at the middle of the beam, which is slightly higher than experimental result. It could be possible because of the friction between supporting points.

If one element at the bottom surface of the film is considered to be very of soft property ($E \ll 1$), the stress distribution across the film thickness is increased linearly from the outer surface to half of the film thickness in both higher and lower Young's modulus film (in Fig. 7.9 (b)). After that the stress distribution behaviour is similar to figure 7.9 (a). Figure 7.9 (c) shows the variation of the stress across the film thickness. Maximum stress is concentrated at the outer surface (symbolised 1) of the film. The stress decreased linearly until one-fourth of film thickness reached and it starts to increase linearly up to one-fourth of film thickness and then increased again to the interface. It has been found for lower Young's modulus film. On the other hand, the stress distribution for higher Young's modulus film has shown different behaviour after one-fourth of film thickness. The stress appears to reach a plateau and then starts to decrease with the minimum observed stress at the interface (Fig. 7.9 (a-b)).

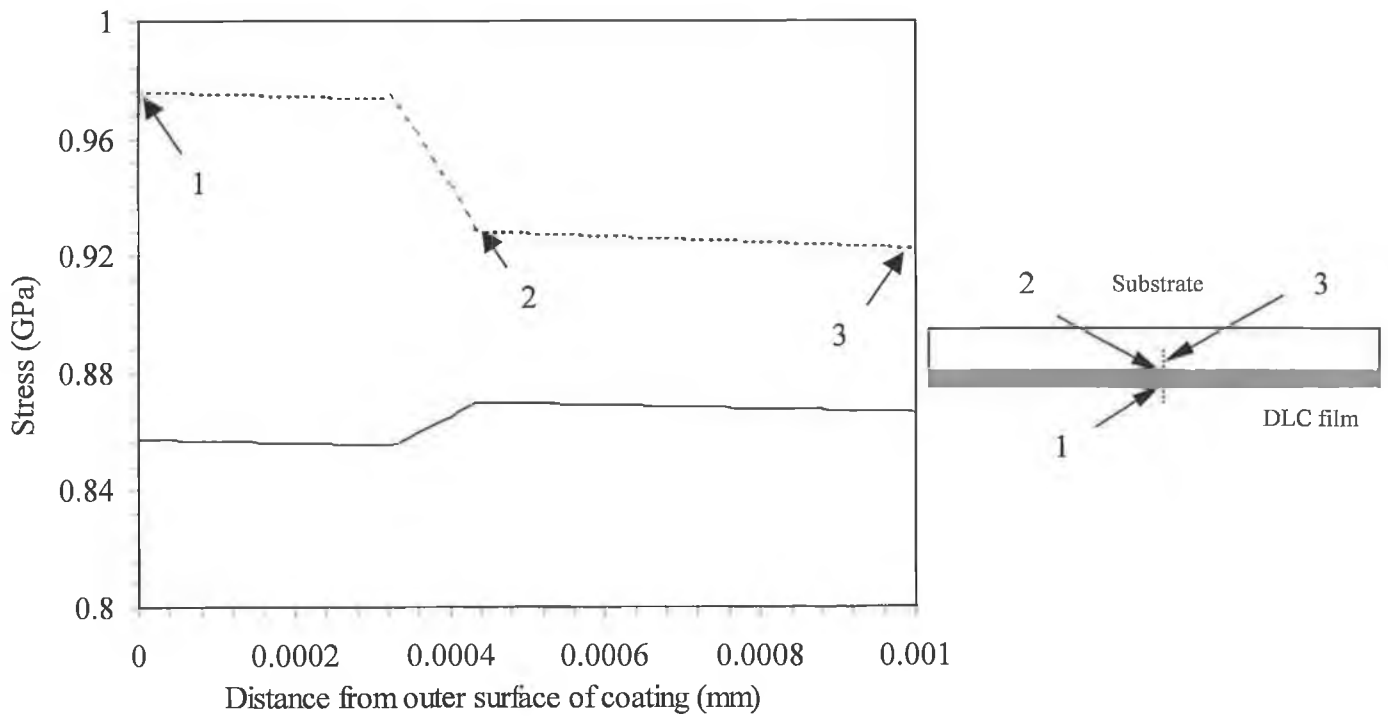


Figure 7.9 (a): Stress distribution across the film thickness with applied load, 10.6 N: solid line for $E_c=193$ GPa and dotted line for $E_c=220$ GPa (specimen geometry one).

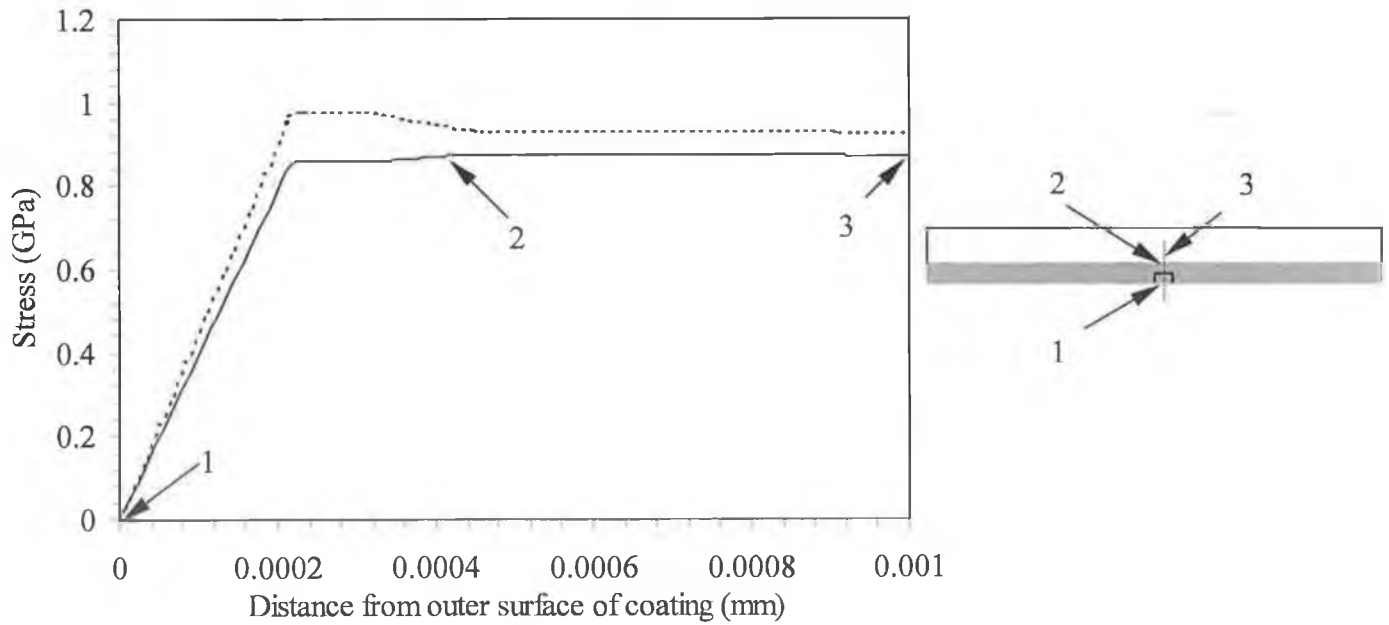


Figure 7.9 (b): Stress distribution across the film thickness with applied load, 10.6 N: solid line for $E_c=193$ GPa and dotted line for $E_c=220$ GPa (specimen geometry two).

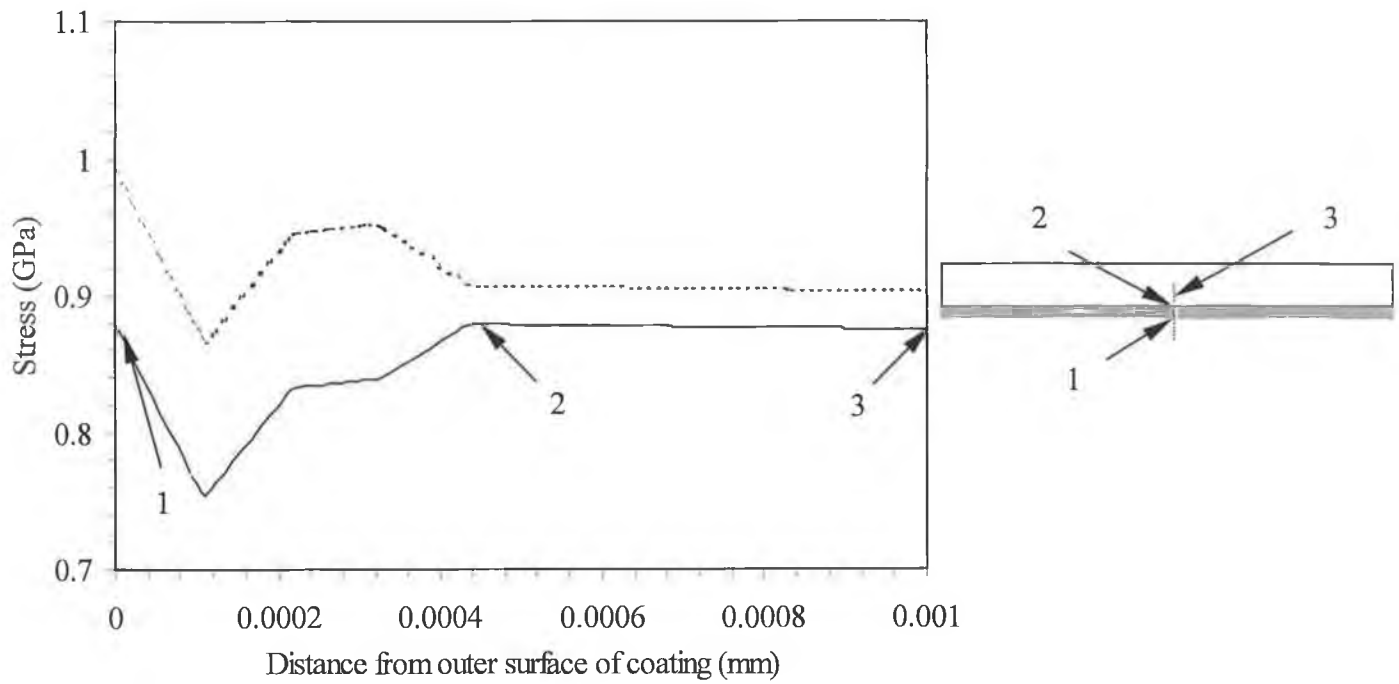


Figure 7.9 (c): Stress distribution across the film thickness with applied load, 10.6 N: solid line for $E_c=193$ GPa and dotted line for $E_c=220$ GPa (specimen geometry three).

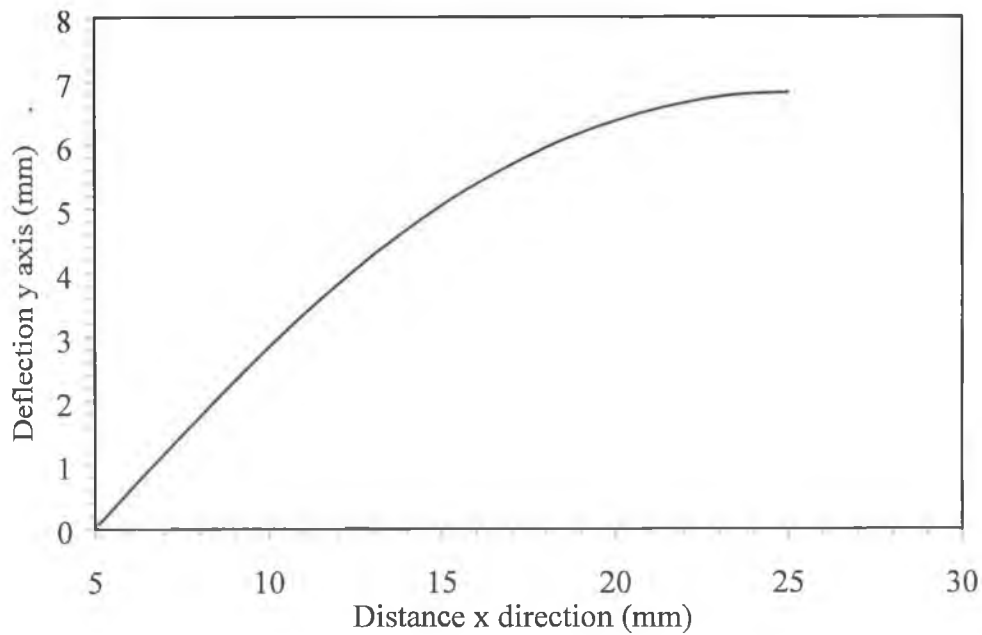


Figure 7.10: Deflection in the outer surface along the beam with applied load 10.6 N for specimen geometry one.

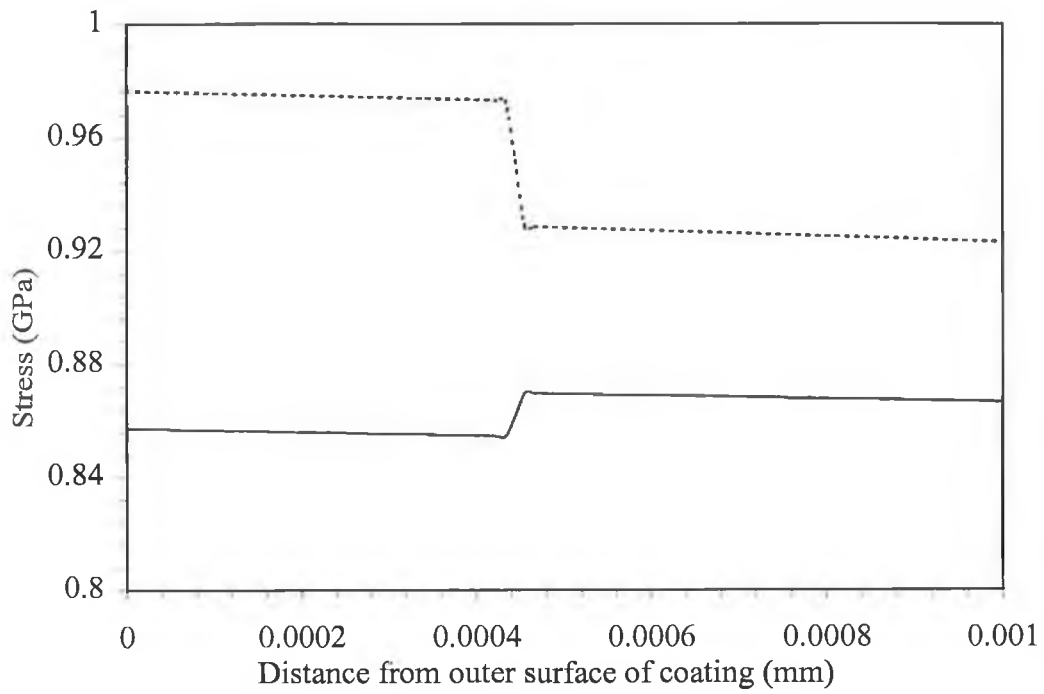
In the following section, two different specimen geometries have been considered to investigate the change of stress distribution across the coating thickness. Three layers; substrate, film and interface have been considered in these models. The dimension and the properties of film and substrate are same as previous work whereas the dimension of the interface is 50 mm x 4 mm x 20×10^{-6} mm. Two different interfacial properties have been considered. One is similar to the film property and other is different Young's modulus, 16 GPa and Poisson ratio, 0.44 that is very soft compared with film property.

Specimen geometry one: Film, substrate and interface are perfectly bonded and considered a single beam.

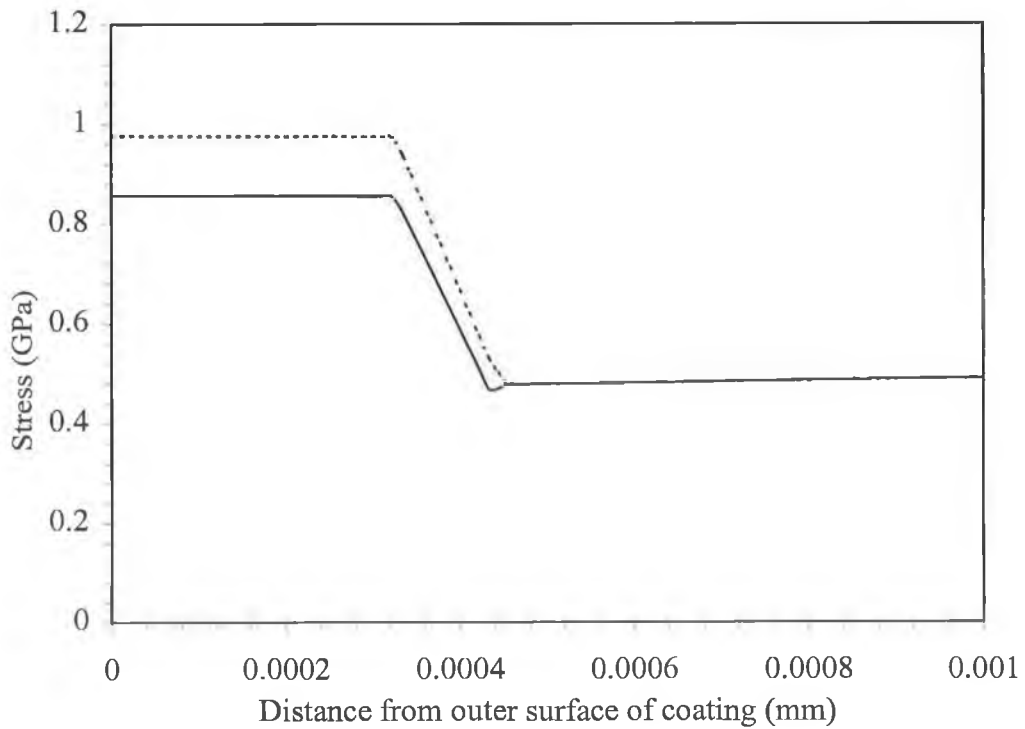
Specimen geometry two: Film, substrate and interface are perfectly bonded and considered a single beam but one of the elements in the outer surface of the central point of the film has considered very soft (i.e. $E \ll \ll 1$) which is assumed as a notch effected beam.

Figure 7.11 (a-d) shows the stress distribution across the film thickness as a function of interfacial properties. In figure 7.11 (a), the stress distribution behaviour is similar to figure 7.9 (a). Figure 7.11 (b) shows the different mode because of its soft interfacial property. Here stress is gradually increased until it reached to 3.22×10^{-4} mm film thickness. Stress from 3.22×10^{-4} mm thickness was found to decrease linearly near the upper surface of the interface. This happened because of soft interfacial property (low Young's modulus). The stress is then increased gradually because of higher Young's modulus of the substrate. Figure 7.11 (c-d) has considered one element at the middle of bottom surface of coating is very soft property ($E \ll \ll 1$). The stress distribution behaviour across the coating shown in figure 7.11 (c) is almost similar to that shown in figure 7.9 (b) because of similar material properties.

Figure 7.11 (d) shows the stress near the interface changed due to different properties between film and interface. Stress is increased linearly across the film thickness until it reached to half of film thickness (0.000222 mm) and then remain almost constant up to two third of coating thickness. After that the stress is decreased linearly because of lower Young's modulus interface. After crossing the interface, it increased gradually due to the substrate.



7.11 (a) Stress distribution across the film thickness with applied load, 10.6 N: solid line for $E_c=193$ GPa and dotted line for $E_c=220$ GPa (specimen geometry one, DLC interface).



7.11 (b): Stress distribution across the film thickness with applied load, 10.6 N: solid line for $E_c=193$ GPa and dotted line for $E_c=220$ GPa (specimen geometry one, soft interface).

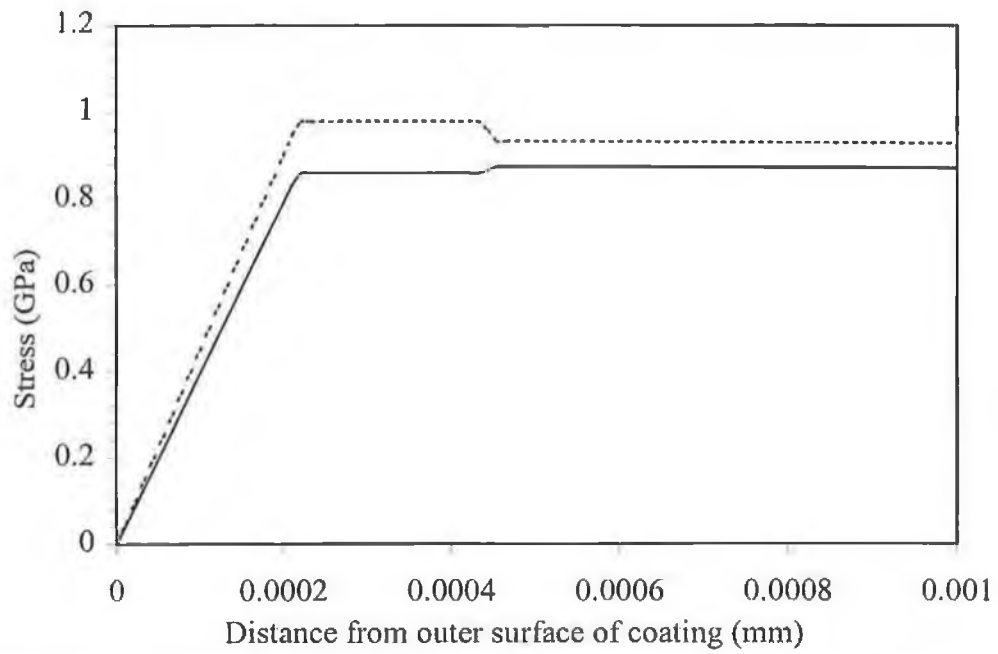


Figure 7.11 (c): Stress distribution across the film thickness with applied load, 10.6N: solid line for $E_c=193$ GPa and dotted line for $E_c=220$ GPa (specimen geometry two, DLC interface).

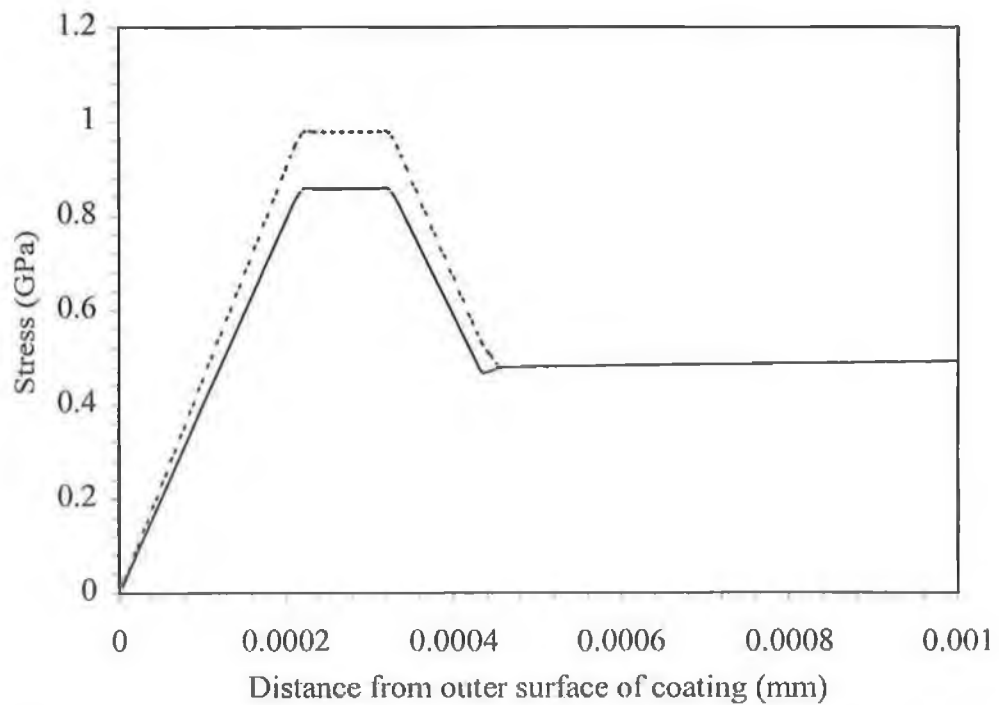


Figure 7.11(d): Stress distribution across the film thickness with applied load, 10.6N: solid line for $E_c=193$ GPa and dotted line for $E_c=220$ GPa (specimen geometry two, soft interface).

Chapter 8
Conclusions

8.1 Conclusions

Good DLC-substrate adhesion, low coefficient of friction and the early indications of the biocompatible nature of DLC will provide an attractive solution for higher quality production of surgical cutting tools and other implant devices. Polyethylene and stainless steel has been the gold-standard coupling pair used in total joint replacement for the past forty years. There is, however, increasing use of cobalt chrome and titanium alloy steels as a substitute for stainless steel [336]. Cobalt chrome alloys are used for their superior strength due to the constituent elements of cobalt and tungsten, while titanium alloys are popular because of their low modulus, high strengths and osseointegrative properties. Surface modification of these materials by application of coatings such as DLC can improve the properties for the application of biomedical field. DLC films have successfully been deposited on biomaterials viz. 316L stainless steel, cobalt-chrome alloy and Ti6Al4V alloy with a saddle field fast atom beam source. Different deposition parameters have been used to investigate the quality of the DLC films. The spectral absorbance of DLC films was measured in the wavelength range 400-1100 nm by UV-vis spectrometer. The optical band gap of the deposited films was measured. The effect of *in situ* argon etching pre-treatment of the surface on the sp^3 content of the films has been measured. Adhesion is always a key factor in making thin film to be used biomedical applications and has been investigated. Quantitative pull-off and qualitative Rockwell C tests have been used to measure adhesion of films. Residual stress is the major problem for adhesion of the films. The compressive stress inside the films increases with increase of sp^3 bonding fraction. Raman spectroscopy together with a curve fitting process has been used to estimate the trends in the sp^3 fraction inside the films. The bending beam method was used to measure the residual stress inside the films. The values of internal stress of these DLC films were found to be in the range of 0.8 to 1.6 GPa. Etching also improved the adhesion of the DLC films. It may be noted that the stress values reported here are very much less than the stress values generated in films that are deposited with deposition system like the rf-self bias technique. The effect of process parameters and substrate treatment that affect the films' adhesion and the quality of films are summarised below. Finite element analysis has been used to analysis the stress distribution in the coated substrate which has helped to identify the location of initial crack during four point bend test.

8.1.1 Current vs. Voltage (A_c - A_v) Characteristics

The variation of the discharge voltage (anode voltage, A_v) with the discharge current (anode current, A_c) of the saddle field FAB source has been investigated in this present study and found to be the same as reported by Sarangi et al. [291]. During the operation of saddle field FAB source the discharge voltage was not only found to depend on the discharge current but also on chamber pressure and type of source gas. It is not strongly depends on flow rate.

It is clearly apparent that discharge voltage, A_v increased almost linear fashion with the discharge current, A_c for all pressure level conditions. On the other hand, A_v decreased with the increase of pressure for a particular value of A_c . These type of behaviours were found in both argon and acetylene gas as the source gas. The distinct variations in all different pressure level were found for argon discharge whereas, for acetylene source gas, the discharge voltage was found almost similar value for higher pressure level.

8.1.2 UV Absorption of DLC Films

The uv absorption for sub-band gap energies of DLC films was observed to depend on deposition current and has been found higher with higher deposition current. Uv absorption did not appear to depend on different deposition pressure with higher deposition current, but there was significant variation with pressure at lower currents.

The value of optical band gap of these films calculated by Tauc's relation are found to be in the range of 0.85-0.87 and \sim 0.85 eV for higher (0.8A) and lower (0.4A) deposition current respectively, which are within the typical range of DLC films. Higher deposition current increased the sp^3 content in the films. By comparison with other reports, this is due to an increased diamond like nature and not an increased C-H bonding. This also causes a slight increase in optical band gap.

8.1.3 Effect of Process Parameters

The parameters that affect deposition rate and adhesion have been determined and it has been shown that the adhesion strength is directly proportional to the inverse of the residual stress. The intrinsic stress levels correlate with the sp^3 content of the films as measured by Raman spectroscopy. In both acetylene and acetylene-argon (90% C_2H_2 + 10% Ar) process gas, the peak area ratio which is an indicatar of the sp^3 content increases with

increasing deposition pressure for lower deposition current, 0.6A. But for higher deposition current, 1A the area ratio behaviour is more complex. The peak area ratio that means sp^3 content inside the films was found higher for 1 A deposition current compared to 0.6 A current. Acetylene-argon process gas has also been influenced to increase sp^3 content inside the films. The highest levels of sp^3 content and stress occurred with high source current at lower pressures. The direct relationship between stress and adhesion has been shown. The film hardness and the Young's modulus were in the range 18-22 GPa and 193-230 GPa, which is consistent with other deposition technique.

8.1.4 Effect of Surface Treatment of 316L Stainless Steel

The adhesion of DLC films on 316L stainless steel has been shown to be dependent on the length of the etching time with an argon atom beam. It has been shown by FTIR studies that the composition of surface oxide is altered during argon etching and there is an optimum etch time to maximise adhesion consistent with removal of chromium and iron oxides from the surface leaving a residue of nickel oxide. It has been shown that the initial etching of the substrate affects the bulk structure of the films; etching for optimum adhesion maximise the sp^3/sp^2 ratio and also minimise intrinsic stress without significantly affecting the film hardness.

8.1.5 Effect of Surface Treatment of 316L stainless steel, Co-Cr and Ti6Al4V Alloys

The adhesion of DLC films on orthopaedic biomaterials viz. 316L stainless steel, cobalt-chrome alloy and Ti6Al4V alloy has also been shown to be dependent on the length of the etching time with an argon atom beam. Etching and deposition temperature with insulating and non-insulating substrate has also been influenced the adhesion and sp^3 content inside the films. It has been shown that there is an optimum etch time to maximise adhesion regardless of the type of substrate metal alloy, hence, it is not only a function of the details of the surface oxide layer but also temperature. This variation of adhesion correlates with the film structure in terms of the sp^3 content. The optimum time for improved adhesion has been shown to be related to the temperature of the substrate during etching and there appears to be a “window” centred around 75 °C during which best adhesion can be achieved.

8.1.6 Finite Element Analysis

Finite element analysis has been used to identify the location of maximum stress generated during the four point bend test. The first crack initiated at the location of maximum stress and it has been confirmed that the crack initiated at the outer surface of the film and propagated through the film thickness during the bend test. This result has been valid only for higher Young's modulus coatings compared with the substrate.

The changes in the behaviour of the cohesive strength as function of a source current and pressure were found to be related to changes in sp^3 content. Higher proportion of covalent bonds in sp^3 rich material probably accounts for this.

8.2 Recommendation and Future work

In recent years significant progress in the understanding of DLC film deposition processes has been made. This can be used to explore additional aspects that have not yet been properly addressed. The author believes that research efforts in the next decade will improve our basic understanding and will solve some problems relevant to the use to DLC films in a variety of practical applications. The saddle field fast atom beam process has demonstrated the capability of fine tuning the properties of DLC films to meet specific requirements. It is still a challenge to apply these capabilities to commercially available deposition system where the process could be industrialises and scale up. Among the more technical issues that should be addressed, we may include (i) the problem of stress which limits the thickness of DLC films that can be deposited in many systems, (ii) the applicability of DLC deposition to a variety of substrates which still maintaining good adhesion and optimal DLC properties and (iii) control of homogeneity and reproducibility of DLC films in practical process. Another issue, which should also be addressed, is characterisation methods. A better standardisation of the characterisation methods with help of numerical analysis (FEA) is needed to avoid the large number of erroneous interpretations characteristic of the field of DLC deposition.

A coating of DLC+M, where M is an added element would significantly enhance the properties of the surface and create a surface with the ideal futures. This coating is a surface impregnation, not a bonded coating. So the coating can not peel-off. The component M is an element that can be added in small proportions to give specific surface

energy properties, which could be designed to minimise attraction or even to repel specific particles. Element M such as fluorine and nitrogen will give the properties needed but the selection of the most suitable element and the proportion to be used in DLC composite for this application needs to be investigated.

REFERENCES

- [1] Hsiao-chu Tsai and D. B. Bogy, Characterization of diamondlike carbon films and their application as overcoat on thin-film media for magnetic recording, *J. Vac. Sci. Technol.*, 5 (1987) 3287.
- [2] N. Savvides and B. Window, Diamondlike amorphous carbon films prepared by magnetron sputtering of graphite, *J. Vac. Sci. Technol.*, 3 (1985) 2386.
- [3] A. H. Lettington, in: Y. Tzeng, M. Yoshikawa, M. Murakawa and A. Feldman (Eds.), *Application of diamond films and related materials*, Elsevier, New York, (1991), p703.
- [4] K. J. Clay, S. P. Speakman, N. A. Morrison, N. Tomozeiu, W. I. Milne and A. Kapoor, Materials properties and tribological performance of rf-PECVD deposited DLC coatings, *Diam. Relat. Mater.* 7 (1998) 1100.
- [5] N. A. Morrison, I. C. Drummond, C. Garth, P. John, D. K. Milne, G. P. Smith, M. G. Jubber and J.I.B. Wilson, Growth of CVD diamond films over bio-medical materials, *Diam. Relat. Mater.* 5 (1996) 1118.
- [6] Veli-Matti Tiainen, Amorphous carbon as a bio-mechanical coating — mechanical properties and biological applications, *Diam. Relat. Mater.* 10 (2001) 153.
- [7] Kari Koski, Jorma Hölsä, Jacques Ernoult, André Rouzaud, The connection between sputter cleaning and adhesion of thin solid films, *Surface and Coating Technology*, 80 (1996) 195.
- [8] G. Lenzen, *The History of Diamond Production and the Diamond Trade*, trans by F. Bradley, Praeger, New York, (1970).
- [9] E. Streeter, *The Great Diamond of the World: Their History and Romance*, George Bell and Sons, London, (1971).
- [10] R. C. Majumdar, *Ancient India*, 6th rev. ed., Motilal Banarasidas, Delhi, (1971).
- [11] S. Tolansky, *The History and Use of Diamond*, Mathuen & Co. Ltd., London, (1962).
- [12] W. Büchner, R. Schliebs, G. Winter and K.H. Büchel, *Industrial Inorganic Chemistry*, Published jointly by VCH Verlagsgesellschaft, Weinheim (Federal Republic of Germany) and VCH publishers, New York, USA, (1989) p. 470.

- [13] M. N. Yoder, The Vision of Diamond as an Engineered Material, in Synthetic Diamond: Emerging CVD Science and Technology, K. E. Spear and J. P. Dismukes (Eds.), John Wiley & Sons, New York, (1994), p. 3.
- [14] Y. U. Orlov, Occurrence of Diamonds in Nature, in The Mineralogy of the Diamond, Y. U. Orlov (Ed.), John Wiley & Sons, New York, (1973), p. 154.
- [15] J. W. Harris, Diamond Geology, in The Physical Properties of Natural and Synthetic Diamond, J. E. Field (Ed.), Academic Press, London, (1992), p. 345.
- [16] J. W. Harris, The Geology of Diamond: Time and depth profiles from inclusions, *Diam. Relat. Mater.* 2 (1993) 75.
- [17] B. Bhushan, B. K. Gupta, Handbook of Tribology: Materials, Coatings and Surface Treatment, McGraw-Hill, New York, (1991), reprint ed. Krieger, Malabar, FL, (1997).
- [18] B. Bhushan, Principles and Applications of Tribology, Wiley, New York, (1999).
- [19] Hugh O Pierson, Handbook of Carbon, Graphite, Diamond and Fullerenes, Noyes Publications, USA, (1993), p.360.
- [20] Bharat Bhushan, Chemical, mechanical and tribological characterization of ultra-thin and hard amorphous carbon coatings as thin as 3.5nm: recent development, *Diam. Relat. Mater.* 8 (1999) 1985.
- [21] J. C. Angus, Y. Wang and M. Sunkara, in Annual Review of Materials Science, edited by Robert A. Huggins, Joseph A. Giordmaine and John B. Wachtman, Annual Reviews, Vol.21 (1991), Palo Alto, CA, p.221.
- [22] M. S. Dresselhaus, G. Dresselhaus, P. C. Eklund, Science of Fullerenes and Carbon Nanotubes, Academic Press, London, (1996).
- [23] J. E. Field, Properties of Diamond, Academic Press, London, (1993).
- [24] B. Bhushan, B. K. Gupta, G. W. VanCleeef, C. Capp and J. V. Coe, Fullerene (C₆₀) films for solid lubrication, *Tribol. Trans.* 36 (1993) 537.
- [25] B. K. Gupta, B. Bhushan, C. Capp and J. V. Coe, Material characterization and effect of purity and ion implantation on the friction and wear of sublimed fullerene films, *J. Mater. Res.* 9 (1994) 2823.

- [26] B. K. Gupta and B. Bhushan, Fullerene particles as an additive to liquid lubricant and greases for low friction and wear, *Lubr. Eng.* 50 (1994) 524.
- [27] J. Robertson, Amorphous carbon, *Adv. Phys.* 35 (1986) 317.
- [28] J. Robertson, Deposition of diamond-like carbon, in *Thin film diamond*, A. Lettington (Ed.), Chapman & Hall, London, (1994), p. 107.
- [29] W. Jacob and W. Möller, On the structure of thin hydrocarbon films, *Appl. Phys. Lett.* 63 (1993) 1771.
- [30] D. R. McKenzie, Tetrahedral bonding in amorphous carbon, *Rep. Prog. Phys.* 59 (1996) 1611.
- [31] Rainer Hippler, Sigismund Pfau, Martin Schmidt and Karl H. Schoenbach (Eds.), *Low Temperature Plasma Physics*, Printed in the Federal Republic of Germany (2001), p.482.
- [32] Alfred Grill, Diamond-like carbon:state of the art, *Diam. Relat. Mater.* 8 (1999) 4 28.
- [33] M. Weiler, S. Sattel, K. Jung, H. Ehrhardt, V. S. Veerasamy, and J. Robertson, Highly tetrahedral diamond-like amorphous hydrogenated carbon prepared from a plasma beam source, *Appl. Phys. Lett.* 64 (1994) 2797.
- [34] P. Koidl, C. Wild, R. Locher, R. E. Sah, in: R. E. Clausing, L. L. Horton, J. C. Angus, P. Koidl (Eds.), *Diamond and diamond like films and coatings*, NATO-ASI SeriesB: Physics, Plenum, New York, (1991), p.243.
- [35] P. W. Bridgman, *Synthetic Diamonds*, *Sci. Am.*, 193 (November) (1955), p. 42.
- [36] F. P. Bundy, H. T. Hall, H. M. Strong and R. J. Wontorf, Man-made diamonds, *Nature* 176 (1955) 51.
- [37] W. G. Eversole, US Patent No.3030188, (1962).
- [38] J. C. Angus and C. C. Hayman, Low-Pressure, Metastable growth of diamond and "diamondlike" Phases, *Science* 241 (1988) 913.
- [39] J. C. Angus and Y. Wang, Diamondlike hydrocarbon and carbon films, in *NATO Advanced Study Institute on Diamond and Diamondlike Materials* (1990), Italy, R. E. Clausing, L. L. Horton, J. C. Angus and P. Koidl (Eds.), Vol. 266, NATO ASI Series B (Physics), Plenum Press, USA (1991), p. 173.
- [40] S. Aisenberg and R. W. Chabot, Ion beam deposition of thin diamondlike carbon, *J. App. Phys.* 42 (1971) 2953.

- [41] J. C. Angus, P. Koidl and S. Domitz, in: J. Mort (Ed.), Plasma deposition thin films, CRC Press, Boca Raton, (1986).
- [42] J. Robertson, Deposition mechanisms for promoting sp_3 bonding in diamond-like carbon, *Diam. Relat. Mater.* 2 (1993) 984.
- [43] V. Liebler, H. Baumann and K. Bethge, Characterisation of ion-beam-deposited diamond-like carbon films, *Diam. Relat. Mater.* 2 (1993) 584.
- [44] A. Erdemir, S. M., R. Wei and P. Wilbur, A tribological investigation of the graphite-to-diamond-like behaviour of amorphous carbon films ion beam deposited on ceramic substrates, *Surf. Coat. Technol.* 50 (1991) 17.
- [45] Y. Lifshitz, G. D. Lempert, S. Rotter, I. Avigal, C. Uzan-Saguy and R. Kalish, The influence of substrate temperature during ion beam deposition on the diamond-like or graphite nature of carbon films, *Diam. Relat. Mater.* 2 (1993) 285.
- [46] S. Scaglione and G. Emiliani, Mechanical properties (hardness and adhesion) of a-C:H thin films produced by dual ion beam sputtering, *J. Vac. Sci. Technol. A* 7 (1989) 2303.
- [47] G. F. Huang, Zhou Lingping, Huang Weiqing, Zhao Lihua, Li Shaolu and Li Deyi, The mechanical performance and anti-corrosion behavior of diamond-like carbon film, *Diam. Relat. Mater.* (2003) to be published.
- [48] L.-P. Andersson, A review of recent work on hard i-C films, *Thin Solid Films*, 86 (1981) 193.
- [49] B. Ollivier and A. Matthews, Adhesion assessment of DLC films on PET using a simple tensile tester; Comparison of different theories, *J. Adhes. Sci. Technol.* (1995).
- [50] Y. Catherine, Preparation techniques for diamond-like carbon, in *The NATO Advanced Study Institute on Diamond and Diamond-Like Films and Coatings* (1991), Il Ciocco, Italy, R. E. Clausing, L. L. Horton, J. C. Angus and P. Koidl (Eds.), Plenum Press, USA, p. 193.
- [51] R. Hauert, J. Patscheider, K.-H. Ernest and M. Tobler, Interface properties of a-C:H on Al and Al_2O_3 , in *Third Int. Symposium on Diamond Materials* (1993),

- Honolulu, USA, J. P. Dismukes and K. V. Ravi (Eds.), The Electrochemical Society, p. 483.
- [52] A. Grill and V. Patel, Diamond-like and nitrogen doped diamond-like carbon deposited by DC PACVD, in Third Int. Symposium on Diamond Materials (1993), Honolulu, USA, J. P. Dismukes and K. V. Ravi (Eds.), The Electrochemical Society, p. 442.
- [53] S. Hoshino, K. Fujii, N. Shohata, H. Yamaguchi, Y. Tsukamoto and M. Yanagisawa, Mechanical properties of diamond-like carbon films, *J. App. Phys.*, 65 (1989) 1918.
- [54] H.-J. Scheibe, P. Siemroth, B. Schoneich and A. Mucha, Diamond-like carbon film preparation by laser arc, *Surf. Coat. Technol.* 52 (1992) 129.
- [55] C. B. Collins, F. Davanloo, E. M. Juengerman, D. R. Jander and T. J. Lee, Preparation and characterization of thin films of amorphous diamond, in *Diamond Optics II* (1989), San Diego, California, A. Feldman and S. Holly (Eds.), Vol. 1146, SPIE, p. 37.
- [56] J. Robertson, Properties of diamond-like carbon, *Surf. Coat. Technol.* 50 (1992) 185.
- [57] J. Robertson, Mechanical properties and structure of diamond-like carbon, *Diam. Relat. Mater.* 1 (1992) 397.
- [58] H. Tsai and D. B. Bogy, Critical review-characterization of diamond-like carbon films and their application as overcoats on thin-film media for magnetic recording, *J. Vac. Sci. Technol.*, A5 (1987) 3287.
- [59] J. C. Angus, Diamond and diamond-like films, *Thin Solid Films* 216 (1992) 126.
- [60] J. C. Angus, Empirical categorization and naming of "diamond-like" carbon films, *Thin Solid Films* 142 (1986) 145.
- [61] C. V. Deshpandey and R. F. Bunshah, Diamond and diamondlike films: Deposition processes and properties, *J. Vac. Sci. Technol. A* 7 (1989) 2294.
- [62] C. B. Collins, F. Davanloo, T. J. Lee, J. H. You and H. Park, The production and use of amorphous diamond, *Am. Ceram. Soc. Bull.* 71 (1992) 1535.

- [63] J. Narayan, W. D. Fan, R. J. Narayan, P. Tewari and H. H. Stadelmaier, Diamond, diamond-like and titanium nitride biocompatible coatings for human body parts, *Mater. Sci. Eng. B* 25 (1994) 5.
- [64] A. A. Voevodin and M. S. Donley, Preparation of amorphous diamond-like carbon by pulsed laser deposition: A critical review, *Surf. Coat. Technol.* 82 (1996) 199.
- [65] F. Davanloo, E. M. Juengerman, D. R. Jander, T. J. Lee and C. B. Collins, Amorphous diamond films produced by a laser plasma source, *J. Appl. Phys.* 67 (1990) 2081.
- [66] David L. Pappas, Katherine L. Saenger, John Bruley, William Krakow, Jerome J. Cuomo, Tierr Gu, and Robert W. Collins, Pulsed laser deposition of diamond-like carbon films, *J. Appl. Phys.* 71 (1992) 5675.
- [67] Fullin Xiong, Y. Y. Wang and R. P. H. Chang, Complex dielectric function of amorphous diamond films deposited by pulsed-excimer-laser ablation of graphite, *Phys. Rev. B* 48 (1993) 8016.
- [68] Peter Kovarik, E. B. D. Bourdon and R. H. Prince, Electron-energy-loss characterization of laser-deposited a-c, a-c:H, and diamond films, *Phys. Rev. B* 48 (1993) 12123.
- [69] Y. Huai, M. Chaker, J. N. Broughton, E. Gat, H. Pépin, T. Gu, X. Bian and M. Sutton, Study of density in pulsed-laser deposited amorphous carbon films using x-ray reflectivity, *Appl. Phys. Lett.* 65 (1994) 830.
- [70] M. P. Siegal, J. C. Barbour, P. N. Provencio, D. R. Tallant and T. A. Friedmann, Amorphous tetrahedral diamondlike carbon layered structures resulting from film growth energetics, *Appl. Phys. Lett.* 73 (1998) 759.
- [71] M. P. Siegal, L. J. Martinez-Miranda, J. N. DiNardo, D. R. Tallant, J. C. Barbour and P. N. Provencio, in *High Powered Laser Ablation*, SPIE, (1998).
- [72] Vladimir I. Merkulov, Douglas H. Lowndes, G. E. Jellison, Jr., A. A. Puretzky and D. B. Geohegan, Structure and optical properties of amorphous diamond films prepared by ArF laser ablation as a function of carbon ion kinetic energy, *Appl. Phys. Lett.* 73 (1998) 2591.
- [73] I. I. Aksenov, S. I. Vakula, V. G. Padalka, R. E. Strelnitski and V. M. Khoroshikh, High-efficiency source of pure carbon plasma, *Soviet Phys. Tech. Phys.*, 25(9) (1980) 1164.

- [74] Y. Lifshitz, Hydrogen-free amorphous carbon films: Correlation between growth conditions and properties, *Diam. Relat. Mater.* 5 (1996) 388.
- [75] Y. Lifshitz, Diamond-like carbon — present status, *Diam. Relat. Mater.* 8 (1999) 1659.
- [76] Y. Lifshitz, S. R. Kasi, J. W. Rabalais and W. Eckstein, Subplantation model for film growth from hyperthermal species, *Phys. Rev. B* 41 (1990) 10468.
- [77] Y. Lifshitz, G. D. Lempert and E. Grossman, Substantiation of subplantation model of diamondlike film growth by atomic force microscopy, *Phys. Rev. Lett.* 72 (1994) 2753.
- [78] H. Hofsass, C. Ronning, *Beam Processing of Advanced Materials*, ASME, Cleveland, (1995).
- [79] F. Jansen, M. Machonkin, S. Kaplan, S. Hark, The effect of hydrogenation on the properties of ion beam sputter deposited amorphous carbon, *J. Vac. Sci. Technol. A* 3 (1985) 605.
- [80] N. Savvides, Deposition parameters and film properties of hydrogenated amorphous silicon prepared by high rate dc planar magnetron reactive sputtering, *J. Appl. Phys.* 55 (1984) 4232.
- [81] N. Savvides, Optical constants and associated functions of metastable diamondlike amorphous carbon films in the energy range 0.5-7.3 eV, *J. Appl. Phys.* 59 (1986) 4133.
- [82] S. M. Rossnagel, M. A. Russak, J.J. Cuomo, Pressure and plasma effects on the properties of magnetron sputtered carbon films, *J. Vac. Sci. Technol. A* 5 (1987) 2150.
- [83] J. Schwan, S. Ulrich, H. Roth, H. Ehrhardt, S. R. P. Silva, J. Robertson, R. Samlenski and R. Brenn, Tetrahedral amorphous carbon films prepared by magnetron sputtering and dc ion plating, *J. Appl. Phys.* 79 (1996) 1416.
- [84] Jerome J. Cuomo, James P. Doyle, John Bruley and Joyce C. Liu, Sputter deposition of dense diamond-like carbon films at low temperature, *Appl. Phys. Lett.* 58 (1991) 466.
- [85] S. Logothetidis, Hydrogen-free amorphous carbon films approaching diamond prepared by magnetron sputtering, *Appl. Phys. Lett.* 69 (1996) 158.

- [86] P. J. Fallon, V. S. Vecerasamy, C. A. Davis, J. Robertson, G. A. J. Amaratunga, W. I. Milne and J. Koskinen, Properties of filtered-ion-beam deposited diamondlike carbon as a function of ion energy, *Phys. Rev. B* 48 (1993) 4777.
- [87] D. R. McKenzie, D. Muller and B. A. Pailthorpe, Compressive-stress-induced formation of thin-film tetrahedral amorphous carbon, *Phys. Rev. Lett.* 67 (1991) 773.
- [88] Richard Lossy, David L. Pappas, Ronnen A. Roy, Jerome J. Cuomo and Vivek M. Sura, Filtered arc deposition of amorphous diamond, *Appl. Phys. Lett.* 61 (1992) 171.
- [89] Simone Anders, André Anders and Ian Brown, Macroparticle-free thin films produced by an efficient vacuum arc deposition technique, *J. Appl. Phys.* 74 (1993) 4239.
- [90] André Anders, Simone Anders and Ian Brown, Focused injection of vacuum arc plasmas into curved magnetic filters, *J. Appl. Phys.* 75 (1994) 4895.
- [91] André Anders, Simone Anders and Ian G. Brown, Effect of duct bias or transport of vacuum arc plasmas through curved magnetic filters, *J. Appl. Phys.* 75 (1994) 4900.
- [92] M. M. M. Bilek, The effect of magnetic field configuration on plasma beam profiles in curve magnetic filters, *J. Appl. Phys.* 85 (1999) 6385.
- [93] B. Schultrich, P. Siemroth and H. J. Scheibe, High rate deposition by vacuum arc methods, *Surf. Coat. Technol.* 93 (1998) 64-68.
- [94] Shi Xu, B. K. Tay, H. S. Tan, Li Zhong, Y. Q. Tu, S. R. P. Silva and W. I. Milne, Properties of carbon ion deposited tetrahedral amorphous carbon films as a function ion energy, *J. Appl. Phys.* 79 (1996) 7234.
- [95] B. K. Tay, G. F. You, S. P. Lau and X. Shi, Plasma flow simulation in an off-plane double beam magnetic filter, *Surf. Coat. Technol.* 133 (2000) 593.
- [96] M. Chhowalla, J. Robertson, C. W. Chen, S. R. P. Silva, G. A. J. Amaratunga and W. I. Milne, Influence of ion energy and substrate temperature on the optical and electronic properties of tetrahedral amorphous carbon, *J. Appl. Phys.* 81 (1997) 139.
- [97] André Anders, Approaches to rid cathodic arc plasmas of macro-and nano particles: a review, *Surf. Coat. Technol.* 121 (1999) 319.

- [98] M. C. Polo, J. L. Andújar, A. Hart, J. Robertson and W. I. Milne, Preparation of tetrahedral amorphous carbon films by filtered cathodic vacuum arc deposition, *Diam.Relat. Mater.* 9 (2000) 663.
- [99] B. F. Coll, in: S. R. P. Silva, et al. (Eds.), *Amorphous Carbon*, World Scientific, Singapore, (1998).
- [100] B. F. Coll and M. Chhowalla, Amorphous diamond film by enhanced arc deposition, *Surf. Coat. Technol.* 79 (1996) 76.
- [101] I. G. Brown, Cathodic arc deposition of films, *Ann. Rev. Mater. Sci.* 28 (1998) 243.
- [102] Y. Catherine, *Diamond and diamond-like carbon thin films*, NATO ASI 266 (1991) 193.
- [103] A. Bubenzer, B. Dischler, G. Brandt and P. Koidl, R.F. plasma deposited amorphous hydrogenated hard carbon thin films, preparation, properties and applications, *J. Appl. Phys.* 54 (1983) 4590.
- [104] Ch. Wild and P. Koidl, Structured ion energy distribution in radio frequency glow-discharge systems, *Appl. Phys. Lett.* 54 (1989) 505.
- [105] C. Wild and P. Koidl, Ion and electron dynamics in the sheath of radio-frequency glow discharges, *J. Appl. Phys.* 69 (1991) 2909.
- [106] J. W. Zou, K. Reichelt, K. Schmidt and B. Dischler, The deposition and study of hard carbon films, *J. Appl. Phys.* 65 (1989) 3914.
- [107] J. W. Zou, K. Schmidt, K. Reichelt and D. Dischler, The properties of a-C:H films deposited by plasma decomposition of C₂H₂, *J. Appl. Phys.* 67 (1989) 487.
- [108] M. A. Lieberman and A. J. Lichtenberg, *Principles of Plasma Discharges and Materials Processing*, Wiley, New York, (1994).
- [109] M. Zarrabian, N. Fourches-Coulon, G. Turban, C. Marhic and M. Lancin, Observation of nanocrystalline diamond in diamondlike carbon films deposited at room temperature in electron cyclotron resonance plasma, *Appl. Phys. Lett.* 70 (1997) 2535.
- [110] M. Weiler, S. Sattel, T. Giessen, K. Jung, H. Ehrhardt, V. S. Veerasamy and J. Robertson, Preparation and properties of highly tetrahedral hydrogenated amorphous carbon, *Phys. Rev. B* 53 (1996) 1594.

- [111] M. Weiler, K. Lang, E. Li and J. Robertson, Deposition of tetrahedral hydrogenated amorphous carbon using a novel electron cyclotron wave resonance reactor, *Appl. Phys. Lett.* 72 (1998) 1314.
- [112] N. M. J. Conway, A. C. Ferrari, A. J. Flewitt, J. Robertson, W. I. Milne, A. Tagliaferro, and W. Beyer, Defect and disorder reduction by annealing in hydrogenated tetrahedral amorphous carbon, *Diam. Relat. Mater.* 9 (2000) 765.
- [113] P. Koidl, C. Wagner, B. Dischler, J. Wagner, M. Ramsteiner, *Mater. Sci. Forum* 52 (1990) 41.
- [114] Leon I. Maissel and Reinhard Glang, *Handbook of Thin Film Technology*, McGraw-Hill, Inc., USA, (1983).
- [115] David Brandon and Wayne D. Kaplan, *Joining Process: An Introduction*, (1997), Wiley and Sons Ltd., West Sussex PO19 IUD, England.
- [116] B. Bhushan and B. K. Gupta, *Handbook of Tribology*, McGraw-Hill, New York, (1991).
- [117] G. J. Jorgenson, G. K. Wehner, *Trans. 10th AVS Symp.*(1963), p.338, The McMillan Company, New York, (1964).
- [118] R. C. DeVries, Synthesis of Diamond under metastable conditions, *Ann. Rev. of Mater. Sci.* 17 (1987)161.
- [119] K. E. Spear, Diamond-ceramic coating of the future, *J. Am. Ceram. Soc.* 72 (1989) 171.
- [120] W. A. Yarbrough, Vapor-phase-deposited diamond-problems and potential, *J. Am. Ceram. Soc.* 75 (1992) 3179.
- [121] J. E. Field, Appendix, in *The Properties of Natural and Synthetic Diamond*, Academic Press, London, (1992), p. 668.
- [122] F. Davanloo, T. J. Lee, D. R. Jander, J. H. You, H. Park and C. B. Collins, Mechanical and adhesion properties of amorphous diamond films, *Thin Solid Films* 212 (1992) 216.
- [123] A. Grill and B. S. Meyerson, Development and status of diamondlike carbon, in *synthetic diamond: Emerging CVD Science and Technology*, K. E. Spear and I. P. Dismukes (Eds.), John Wiley & Sons, New York, (1994), p. 91.

- [124] K. V. Ravi, Technological application of CVD diamond, in synthetic diamond: Emerging CVD Science and Technology, K. E. Spear and J. P. Dismuks (Eds.), John Wiley and Sons, New York, (1994), p.533.
- [125] K. Enke, Some new results on the fabrication of and the mechanical, electrical and optical-properties of i-carbon layer, *Thin Solid Films* 80 (1981) 227.
- [126] R. Memming, H. J. Tolle and P. E. Wierenga, Properties of polymeric layers of hydrogenated amorphous-carbon produced by a plasma-activated chemical vapor-deposition process .2. Tribological and mechanical-properties, *Thin Solid Films* 143 (1986) 31.
- [127] M. Hilden, J. Lee, G. Ouano, V. Nayak and J. B. Wu, Sputtered carbon on particulate media, *IEEE Trans. Magnetics* 26 (1990) 174.
- [128] J. Robertson, Amorphous-carbon, *Advances in Physics* 35 (1986) 317.
- [129] A. Matthews and S. S. Eskildsen, Engineering applications for diamond-like carbon, *Diam. Relat. Mater.* 3 (1994) 902.
- [130] E. Gheeraert, A. Deneuille and A. M. Bonnot, Defects and stress analysis of the Raman spectrum of diamond films, *Diam. Relat. Mater.* 1 (1992) 525.
- [131] R. E. Clausing, L. Heatherly, E. D. Specht, K. L. More and G. M. Begun, Growth mechanisms, film morphology, texture and stresses for 3 types of HFCVD diamond film growth, *Carbon* 28 (1990) 762.
- [132] G. A. J. Amaratunga, A. Putnis, K. Clay and W. Milne, Crystalline diamond growth in thin films deposited from a CH₄/Ar RF plasma, *Appl. Phys. Lett.* 55 (1989) 634.
- [133] D. Nir, Summary abstract: Energy dependence of the stress in diamondlike carbon films, *J. Vac. Sci. Technol. A* 4 (1986) 2954.
- [134] G. G. Stoney, The tension of metallic films deposited by electrolysis, *Proc. R. Soc. Lond. A* 82 (1909) 172.
- [135] D. W. Hoffmann, Film stress diagnostic in the sputter deposition of metals, in *Proc. 7th ICVM* (1982), Tokyo, Iron & Steel Inst. Japan, p. 145.
- [136] J. A. Thornton and D. W. Hoffman, Stress-related effects in thin films, *Thin Solid Films* 171 (1989) 5.

- [137] F. M. d'Heurle and J. M. E. Harper, Note on the origin of intrinsic stresses in films deposited via evaporation and sputtering, *Thin Solid Films* 171 (1989) 81.
- [138] R. W. Hoffman, Stresses in thin films: The relevance of grain boundaries and impurities, *Thin Solid Films* 34 (1976) 185.
- [139] B. J. Pond, Characterisation and control of stress in optical films, in *Characterisation of Optical Materials*, G. J. Exarhos (Ed.), Butterworth-Heinemann, Boston, (1993) p. 117.
- [140] J. W. Ager and M. D. Drory, Quantitative measurement of residual stress by Raman-spectroscopy in diamond grown on a Ti Alloy by chemical vapour deposition, *Phys. Rev. B -Cond. Matter* 48 (1993) 2601.
- [141] R.W. Hoffman, in "Thin Films", American Society for Metals, Metals Park, Ohio, (1963), p.99.
- [142] R.W. Hoffman, in J. C. Anderson (ed.), *The use of Thin Films in Physical investigations*, Academic Press Inc., New York, (1996), p.261.
- [143] R.W. Hoffman, *Physics of Thin Films*, Vol.3, Academic Press Inc., New York, (1966), p.211.
- [144] W. J. Meng, J. A. Sell, G. L. Eesley and T. A. Perry, Measurement of intrinsic stresses during growth of aluminium nitride thin films by reactive sputter deposition, *J. Appl. Phys.* 74 (1993) 2411.
- [145] D. W. Hoffman and C. M. Kukla, Determination of film stresses during sputter deposition using an *in-situ* probe, *J. Vac. Sci. Technol.* A3 (1985) 2600.
- [146] P. J. Fallon, V. S. Veerasamy, C. A. Davis, J. Robertson, G. A. J. Amaratunga W. I. Milne and J. Koskinen, Properties of filtered-ion-beam-deposited diamondlike carbon as a function of ion energy, *Phys. Rev. B* 48 (1993) 4777.
- [147] E. I. Bromley, J. N. Randall, D. C. Flanders and R. W. Mountain, A Technique for the determination of stress in thin films, *J. Vac. Sci. Technol.* B 1 (1983) 1364.
- [148] M. G. Allen, M. Mehrengany, R. T. Howe and S. D. Senturia, Microfabricated structures for the *in situ* measurement of residual stress, young's modulus, and ultimate strain of thin films, *Appl. Phys. Lett.* 51 (1987) 241.

- [149] G. F. Cardinale and R. W. Tutison, Mechanical property measurement of polycrystalline diamond films, in *Diamond Optics III* (1990), San Diego, California, A. Feldman and S. Holly (Eds.), Vol. 1325, SPIE, p. 90.
- [150] G. F. Cardinale and R. W. Tutison, Biaxial modulus measurement of chemical vapor deposited polycrystalline diamond films, *J. Vac. Sci. Technol. A* 9 (1991) 2204.
- [151] G. F. Cardinale and C. J. Robinson, Fracture strength measurement of filament assisted CVD polycrystalline diamond films, *J. Mater. Res.* 7 (1992) 1432.
- [152] J. E. Field, E. Nicholson, C. R. Seward and Z. Feng, Strength, fracture and erosion properties of CVD diamond, *Phil. Trans. R. Soc. London, A* 342 (1993), p. 261.
- [153] L. Chandra and T. W. Clyne, Mechanical properties of diamond films deposited on metallic substrates, University of Cambridge, Internal Report to Howmedica Int., (1993).
- [154] H. Behnken and V. Hauk, Influence of elastic and plastic strain on the stress state of the thin film, *Thin Solid Films* 193/194 (1990) 333.
- [155] J. A. Baglio, B. C. Farnsworth, S. Hankin, G. Hamill and D. O'Neil, Studies of stress related issues in microwave CVD diamond on <100> silicon substrates, *Thin Solid Films* 212 (1992) 180.
- [156] P. R. Chalker, A. M. Jones, C. Johnston and I. M. Buckley-Golder, Evaluation of internal stresses present in chemical vapor deposition diamond films, *Surf. Coat. Technol.* 47 (1991) 365.
- [157] A. R. Badzian, T. Badzian, R. Roy, R. Messier and K. E. Spear, Crystallization of diamond crystals and films by microwave assisted CVD (Part II), *Mat. Res. Bull.* 23 (1988) 531.
- [158] K. Fabisiak, M. Maar-Stumm and E. Blank, Defects in CVD diamond films studied by ESR and Raman spectroscopy, *Diam. Relat. Mater.* 2 (1993) 722.
- [159] J. Diaz, J. A. M. Gago, S. Ferrer, F. Comin L. Abello and G. Lucazeau, Raman spectroscopy of carbon films grown by pulsed laser evaporation of graphite, *Diam. Relat. Mater.* 1 (1992) 824.

- [160] D. S. Knight and W. B. White, Characterization of diamond films by Raman spectroscopy, *J. Mater. Res.* 4 (1989) 385.
- [161] W. Wanlu, L. Kejun, G. Jinying and L. Aimin, Internal stress analysis in diamond films formed by DC plasma chemical vapour deposition, *Thin Solid Films* 215 (1992) 174.
- [162] G. J. Exarhos, Raman determination of molecular structure and physical properties of dielectric coatings, *J. Vac. Sci. Technol. A* 4 (1986) 2962.
- [163] D. K. Sood, W. R. Drawl and R. Messier, The effect of carbon ion implantation on the nucleation of diamond on Ti-6Al-4V alloy, *Surf. Coat. Technol.* 51 (1992) 307.
- [164] M. Yoshikawa, G. Katagiri, H. Ishida, A. Ishitani, M. Ono and K. Matsumura, Characterization of crystalline quality of diamond films by Raman spectroscopy, *App. Phys. Lett.* 55 (1989) 2608.
- [165] H. Boppart, J. V. Straaten and I. F. Silvera, Raman-spectra of diamond at high-pressures, *Phys. Rev. B* 32 (1985) 1423.
- [166] P. W. Carey, D. C. Cameron, Plasma deposition of hard carbon films as wear protective coatings, *J. Mater. Proces. Technol.* 26 (1991) 117.
- [167] P. A. Flinn, D. S. Gardner and W. D. Nix, Measurement and interpretation of stress in aluminium-based metallization as a function of thermal history, *IEEE Trans. Elect. Devices*, ED-34 (1987), p. 689.
- [168] D. Schwarzbach, R. Haubner and B. Lux, Internal stresses in CVD diamond layers, *Diam. Relat. Mater.* 3 (1994) 757.
- [169] L. Schafer and C.-P. Klages, Growth and properties of diamond films prepared by microwave plasma chemical vapour deposition using different oxygen containing source gases, *Surf. Coat. Technol.* 47 (1991) 13.
- [170] P. J. Martin, R. P. Netterfield, T. J. Kinder and V. Stambouli, *In situ* stress measurements of ion- assisted MgF_2 and SiO_x thin films, *Appl. Phys. Lett.* 58 (1991) 2497.
- [171] C. F. M. Borges, S. Schelz, L. Martinu and M. Moisan, Adhesion of CVD diamond films on silicon substrates of different crystallographic orientations, *Diam. Relat. Mater.* 5 (1996) 1402.

- [172] M. Ohring, Mechanical properties of thin films, in *The Materials Science of Thin Films*, Academic Press, San Diego, California, (1992).
- [173] P. A. Steinmann and H. E. Hintermann, A review of the mechanical tests for assessment of thin- film adhesion, *J. Vac. Sci. Technol. A* 7 (1989) 2267.
- [174] K. L. Mittal, in *Adhesion measurement of thin films, thick films, and bulk coatings*, edited by K. L. Mittal, ASTM Spec. Tech. Publ. 640 (ASTM) Philadelphia, PA (1978)), p.5.
- [175] R. Ramesham, T. Roppel and R. W. Johnson, Characterization of polycrystalline diamond thin films grown on various substrates, *Thin Solid Films* 212 (1992) 96.
- [176] H. Chen, M. L. Neilsen, C. J. Gold, R. O. Dillon, J. DiGregorio and T. Furtak, Growth of diamond films on stainless steel, *Thin Solid Films* 212 (1992) 169.
- [177] K. Kurihara, K. Sasaki, M. Kawarada and Y. Goto, Formation of functionally gradient diamond films, *Thin Solid Films* 212 (1992) 164.
- [178] Karl E. Spear and John P. Dismukes, *Synthetic diamond: Emerging CVD Science and Technology*, John Wiley & Sons, Inc., New York, (1994), p 125.
- [179] J. Valli, A review of adhesion test methods for thin hard coatings, *J. Vac Sci. Technol. A* 4 (1986) 3007.
- [180] R. Jacobson, Measurement of adhesion of thin films, *Thin Solid Films* 34 (1976) 191.
- [181] R. C. McCune, D. W. Hoffman, T. J. Whalen and C. O. McHugh, Adherence of diamond films produced by microwave plasma deposition on SiAl on tool inserts., in *Thin Films: Stresses and mechanical properties* (1989), *Mat. Rev. Soc. Symp.*, Vol. 130, p. 261.
- [182] C. Kuo, T. Yen and T. Huang, Adhesion and tribological properties of diamond films on various substrates, *J. Mater. Res.* 5 (1990) 2515.
- [183] M. D. Drory, M. D. Thouless and A. G. Evans, On the decohesion of residually stressed thin films, *Acta Metall.* 36 (1988) 2019.
- [184] VDI Guideline 3198, *VDI-Handbuch für Betriebstechnik, Teil 3*, Verein Deutscher Ingenieure, Dusseldorf, August, (1992), p.7.

- [185] H. Jehn, G. Reiners and N. Siegel (Eds.), DIN Fachbericht 39, Characterisierung dinner Schichten, Beuth Vergin, Berlin, (1993).
- [186] H. Ollendorf and D. Schneider, A Comparative study of adhesion test for hard coatings, Surf. Coat. Technol. 113 (1999) 86.
- [187] W. Heinke, A. Leyland, A. Matthews, G. Berg, C. Friedrich and E. Broszeit, Evaluation of PVD nitride coatings using impact, scratch and Rockwell-C adhesion tests, Thin Solid Films 270 (1995) 431.
- [188] M. Lindstam, O. Wånstrand, M. Boman and K. Piglmayer, Mechanical and tribological aspects on a a-C films deposited by lamp assisted chemical vapour deposition, Surf. Coat. Technol. 138 (2001) 264.
- [189] D. C. Agrawal and R. Raj, Measurement of the ultimate shear strength of a metal ceramic interface, Acta Metall. 37 (1989) 1265.
- [190] M. D. Bentzon, C. Barholm-Hansen and J. B. Hansen, Interfacial shear strength of diamond-like carbon coatings deposited on metals, in numerical predictions of deformation processes and the behaviour of real materials (1994), Riso National Laboratory, Denmark, S. I. Andersen, J. B. Bilde-Sorensen, T. Lorentzen, O. B. Pedersen and N. J. Sorensen (Eds.), Riso International Symposium on Materials Science, p. 243.
- [191] L. Chandra and T. W. Clyne, Characterisation of the strength and adhesion of diamond films on metallic substrates using a substrate plastic straining technique, Diam. Relat. Mater. 3 (1994) 791.
- [192] J. Yuan and V. Aupta, Measurement of interface strength by the modified laser spallation technique. I. Experiment and simulation of the spallation Process, J. Appl. Phys. 74 (1993) 2388.
- [193] D. J. Gillespie, in B. Schwartz and N. Schwartz (eds.), Measurement techniques for thin films, The Electrochemical Society, New York, (1967), p.102.
- [194] D. Tabor, The hardness of metals. Oxford: Oxford University Press, (1951).
- [195] B. Bhushan, Handbook of micro/nanotribology, (2nd ed.), Boca Raton (FL): CRC Press, (1999).
- [196] D. Tabor, Indentation hardness: fifty years on a personal view, Philos Mag A 74 (1996) 1207.

- [197] JB Pethica, R. Hutchings and WC Oliver, Hardness measurement at penetration depths as small as 20 nm, *Philos Mag A* 48 (1983) 593.
- [198] WC Oliver, GM Pharr, An improved technique for determining hardness and elastic- modulus using load and displacement sensing indentation experiments, *J. Mater. Res.* 7 (1992) 1564.
- [199] GM Pharr, Measurement of mechanical properties by ultra-low load indentation, *Mater. Sci. Eng. A* 253 (1998) 151.
- [200] SI Bulychev, VP Alekhin, MKH Shorshorov, AP Ternovskii and GD Shnyrev, Determining Young's modulus from the indenter penetration diagram, *Zavod Lab* 41 (1975) 1137.
- [201] B. Bhushan, AV Kulkarni, W. Bornin and JT Wyrobek, Nanoindentation and picoindentation measurements using a capacitive transducer system in atomic force microscopy, *Philos Mag A* 74 (1996) 1117.
- [202] B. Bhushan, *Mechanics and reliability of flexible magnetic media*, (2nd ed.), New York: Springer-Verlag, (2000).
- [203] Li X, D. Diao and B. Bhushan, Fracture mechanism of thin amorphous carbon films in nanoindentation, *Acta Mater* 45 (1997) 4453.
- [204] Li X and B. Bhushan, Measurement of fracture toughness of ultra-thin amorphous carbon films, *Thin Solid Films* 315 (1998) 214.
- [205] Li X and B. Bhushan, Evaluation of fracture toughness of ultra-thin amorphous carbon coatings deposited by different deposition techniques, *Thin Solid Films* 355-356 (1999) 330.
- [206] T. F. Page, In *Solid State Interactions*, Proceedings of First Royal Society-Unilever Indo-Anglo Forum in Materials Science and Engineering, London, September 1994, ed. M.J. Adams, B.J.Broscoe and S.K.Biswas, World Scientific Publishing, Singapore, (1996).
- [207] H. Buckle, In *Science of Hardness Testing and its Research Applications*, ed. J. H. Westbrook and H. Conrad, ASM, Metal Park, Ohio, (1973), p.453.
- [208] H. M.Pollock, D. Mangis and M. Barquins, in *Microindentation Techniques in Materials Science and Engineering*, (ASTM STP 889), P. J. Blau, B. R. Lawn edn., ASTM, Philadelphia, (1986), p.47.
- [209] G. Simmons and H. Wang, *Single Crystal Elastic Constants and Calculated Aggregate Properties: A Handbook*, 2nd edn., The M. I. T. Press, Cambridge, Massachusetts, (1971).

- [210] W. C. Oliver, R. Hutchings, J. B. Petchica, in ASTM STP 889, P. J. Blau and B. R. Lawn edn., ASTM, Philadelphia, (1986), p.90.
- [211] I. N. Sneddon, The relation between load and penetration in the axisymmetric boussinesq problem for a punch of arbitrary profile, *Int. J. Engng. Sci.* 3, (1965) 47.
- [212] M. F. Doerner and W. D. Nix, A method for interpreting the data from depth-sensing indentation instruments, *J. Mater.Res.*, 1, (1986) 601.
- [213] J. Robertson, E. P. Ó Reilly, Electronic and atomic structure of amorphous carbon, *Phy.Rev.B* 35 (1987) 2946.
- [214] J. Robertson, *Prog. Solid State Chem.* 21 (1991) 199.
- [215] J. M. Ripalda, E. Román, N. Díaz, L. Galán, I. Montero, G. Comelli, A. Baraldi, S. Lizzit, A. Goldoni and G. Paolucci, Correlation of x-ray absorption and x-ray photoemission spectroscopies in amorphous carbon nitride, *Phys. Rev. B* 60, R 3705 (1999).
- [216] J. Stöhr, *NEXAFS Spectroscopy*, Springer, Berlin, (1992).
- [217] B. S. Elman, M. Shayegan, M. S. Dresselhaus, H. Mazurek and G. Dresselhaus, Structural characterization of ion-implanted graphite, *Phys. Rev. B* 25 (1982) 4142.
- [218] J. Robertson, in: S.R.P. Silva, et al. (Eds.), *Amorphous carbon: State of the art*, World Scientific, Singapore, (1998), p.32.
- [219] M. A. Tamor, J. A. Haire, C. H. Wu and K. C. Hass, Correlation of the optical gaps and Raman spectra of hydrogenated amorphous carbon films, *Appl. Phys. Lett.* 54 (2) (1989) 123.
- [220] R. J. Nemanich, J. T. Glass, G. Lucovsky, R. E. Scroder, Raman scattering characterization of carbon bonding in diamond and diamond like thin films, *J. Vac. Sci. Technol. A* 6 (3) (1998) 1783.
- [221] R. E. Shroder, R. J. Nemanich, J. T. Glass, Analysis of the composite structures in diamond thin films by Raman spectroscopy, *Phy. Rev. B* 41 (1990) 3738.
- [222] M. Ramsteiner, J. Wagner, Resonant Raman scattering of hydrogenated amorphous carbon: Evidence for π -bonded carbon clusters, *Appl. Phys. Lett.* 51 (17) 1335.
- [223] J. Wagner, M. Ramsteiner, C. Wild and P. Koidl, Resonant Raman scattering of amorphous carbon and polycrystalline diamond films, *Phy. Rev. B* 40 (1989) 1817.
- [224] M. Yoshikawa, N. Nagai, M. Matsuki, H. Fukada, G. Katagiri, H. Ishida, A. Ishitani and I. Nagai, Raman scattering from sp^2 carbon clusters, *Phy. Rev.B* 46 (1992) 7169.

- [225] Fang Li and Jeffrey S. Lannin, Disordered induced Raman scattering of nanocrystalline carbon, *Appl. Phys. Lett.* 61 (1992) 2116.
- [226] W. S. Bacsa, J. S. Lannin, D. L. Pappas, J. J. Cuomo, Raman scattering of laser-deposited amorphous carbon, *Phys. Rev. B* 47 (1993) 10931.
- [227] S. Praver, K. W. Nugent, Y. Lifshitz, G. D. Lempert, E. Grossman, J. Kulik, I. Avigal and R. Kalish, Systematic variation of the Raman spectra of DLC films as function of $sp^2:sp^3$ composition, *Diam. Relat. Mater.* 5 (1996) 433.
- [228] M. A. Tamor, W. C. Vassell, Raman "fingerprinting" of amorphous carbon films, *J. Appl. Phys.* 76 (1994) 3823.
- [229] K. W. R. Gilkes, H. S. Sands, D. N. Batchelder, J. Robertson and W. I. Milne, Direct observation of sp^3 bonding in tetrahedral amorphous carbon using ultraviolet Raman spectroscopy, *Appl. Phys. Lett.* 70 (1997) 1980.
- [230] V. I. Merkulov, J. S. Lannin, C. H. Munro, S. A. Asher, V. S. Veerasamy and W. I. Milne, uv studies of tetrahedral bonding in diamond like amorphous carbon, *Phys. Rev. Lett. A* 78 (25) (1997) 4869.
- [231] A. C. Ferrari and J. Robertson, Interpretation of Raman spectra of disordered and amorphous carbon, *Phys. Rev. B* 61 (2000) 14095.
- [232] P. Y. Yu and M. Cardona, *Fundamentals of Semiconductors*, Springer, Berlin, 1996.
- [233] R. Alben, D. Weaire, J. E. Smith and M. H. Brodsky, Vibrational properties of amorphous Si and Ge, *Phys. Rev. B* 11 (1975) 2271.
- [234] N. Maley and J. S. Lannin, Raman coupling-parameter variation in amorphous germanium, *Phys. Rev. B* 35 (1987) 2456.
- [235] R. E. Shroder, R. J. Nemanich and J. T. Glass, Analysis of the composite structures in diamond thin films by Raman spectroscopy, *Phys. Rev. B* 41 (1990) 3738.
- [236] G. Adamopoulos, K. W. R. Gilkes, J. Robertson, N. M. J. Conway, B. Y. Kleinsorge, A. Buckley and D. N. Batchelder, Ultraviolet Raman characterisation of diamond-like carbon films, *Diam. Relat. Mater.* 8 (1999) 541.
- [237] R. Al-Jishi and G. Dresselhaus, Lattice-dynamical model for graphite, *Phys. Rev. B* 26 (1982) 4514.
- [238] C. Mapelli, C. Castiglioni, G. Zerbi and K. Müllen, Common force field for graphite and polycyclic aromatic hydrocarbons, *Phys. Rev. B* 60 (1999) 12710.

- [239] C. Thomsen and S. Reich, Double resonant Raman scattering in graphite, *Phys. Rev. Lett.* 85 (2000) 5214.
- [240] F. Tuinstra, J. L. Koenig, Raman spectrum of graphite, *J. Chem. Phys.* 53 (1970) 1126.
- [241] M. Chhowalla, A. C. Ferrari, J. Robertson and G. A. J. Amaratunga, Evolution of sp^2 bonding with deposition temperature in tetrahedral amorphous carbon studied by Raman spectroscopy, *Appl. Phys. Lett.* 76 (2000) 1419.
- [242] D. G. McCulloch and S. Praver, The effect of annealing and implantation temperature on the structure of C ion-beam-irradiated glassy carbon, *J. Appl. Phys.* 78 (1995) 3040.
- [243] Th. Köhler, Th. Frauenheim, and G. Jungnickel, Stability, chemical bonding, and vibrational properties of amorphous carbon at different mass densities, *Phys. Rev. B* 52 (1995) 11837.
- [244] Fang Li and Jeffrey S. Lannin, Disorder induced Raman scattering of nanocrystalline carbon, *Appl. Phys. Lett.* 61 (1992) 2116.
- [245] G. P. Lopinski, V. I. Merkulov and J. S. Lannin, Vibrational states of tetrahedral amorphous carbon, *Appl. Phys. Lett.* 69 (1996) 3348.
- [246] S. Praver, K.W. Nugent, Y. Lifshitz, G. D. Lempert, E. Grossman, J. Kulik, I. Avigal and R. Kalish, Systematic variation of the Raman spectra of DLC film as a function of sp^2 : sp^3 composition, *Diam. Relat. Mater.* 5 (1996) 433.
- [247] P. Lespade, R. Al-Jishi, M.S. Dresselhaus, Model for Raman scattering from incompletely graphitized carbons, *Carbon* 20 (1982) 427.
- [248] J. Schwan, S. Ulrich, V. Batori, H. Ehrhardt and S. R. P. Silva, Raman spectroscopy on amorphous carbon films, *J. Appl. Phys.* 80 (1996) 440.
- [249] J. Enderle, S. Blanchard and J. Bronzino, *Introduction to Biomedical Engineering*, Academic Press, New York, (1999), p.538.
- [250] B. D. Ratner, A. S. Hoffman, F. J. Schoen and J. E. Lemons, *Biomaterials Science: An Introduction to Materials in Medicine*, Vol.2, Academic Press, New York, (1996).
- [251] D. Hill, *Design Engineering of Biomaterials for Medical Devices*, Wiley, London, (1998)
- [252] J. A. Davidson, A. K. Mishra, P. Kovacs and R. A. Poggie, New surface-hardened, low modulus, corrosion-resistant Ti-13Nb-13Zr alloy for total hip anthroplasty, *Bio-Med. Mater. Eng.* 4 (1994) 231.

- 253] L. Anne Thomson, Frances C. Law, Neil Rushton and J. Frank, Biocompatibility of diamond-like carbon coating, *Biomaterials* 12 (1991) 37.
- [254] W. J. Gillespie, C. M. A. Framton, R. I. Henderson, P. M. Ryan, The incidence of cancer following total hip replacement, *J. Bone Joint Surg.* 70 B (1988) 539.
- [255] Luo Lu and Michael W. Jones, Diamond-like carbon as biological compatible material for cell culture and medical application, *Bio-Med. Mater. Eng.* Vol. 3. No.4, (1993) 223.
- [256] J. V. Busch and J. P. Dismukes, Trends and market perspectives for CVD diamond, *Diam. Relat. Mater.* 3 (1994) 295.
- [257] C. J. Russell, CVD Diamond markets in the 21st century, in *Synthetic Diamond: Emerging CVD Science and Technology*, K. E. Spear and J. P. Dismukes (Eds.), John Wiley & Sons, New York, (1994), p. 625.
- [258] S. J. Bull and A. Matthews, Diamond for wear and corrosion applications, *Diam. Relat. Mater.* 1 (1992) 1049.
- [259] S. J. Bull, Tribology of carbon coatings: DLC, diamond and beyond, *Diam. Relat. Mater.* 4 (1995) 827.
- [260] C. A. Klein, Diamond windows for IR applications in adverse environments, *Diam. Relat. Mater.* 2 (1993) 1024.
- [261] K. A. Snail, Growth, processing and properties of CVD diamond for optical applications, *Optical Materials* 1 (1992) 235.
- [262] M. N. Yoder, Diamond: Potential and status, in *diamond and diamond-like films and coatings* (1990), Pascoli, Italy, R. E. Clausing, J. C. Angus, L. L. Horton and P. Koidl (Eds.), Plenum Press, USA, p. 1-16.
- [263] J. C. Pivin, Tribology of amorphous diamond films grown or modified by ion implantation, *J. Mater. Sci.* 27 (1992) 6735.
- [264] K. Miyoshi, R. L. C. Wu and A. Garscadden, Friction and wear of diamond and diamondlike carbon coatings, *Surf. Coat. Technol.* 54/55 (1992) 428.
- [265] L. Lu, M. W. Jones and R. L. C. Wu, Diamond-like carbon as biological compatible material for cell Culture and medical application, *Bio-Med. Mater. Eng.* 3 (1993) 223.

- [266] T. L. Parker, K. L. Parker, I. R. McColl, D. M. Grant and J. V. Wood, The biocompatibility of low temperature diamond-like carbon films: A transmission electron microscopy, scanning electron microscopy and cytotoxicity study, *Diam. Relat. Mater.* 3 (1994) 1120.
- [267] L. A. Thomson, F. C. Law, N. Rushton and J. Franks, Biocompatibility of diamond-like carbon coating, *Biomaterials* 12 (1991) 37.
- [268] D. M. Grant, I. R. McColl, M. A. Golozar and J. V. Wood, Plasma assisted CVD for biomedical applications, *Diam. Relat. Mater.* 1 (1992) 727.
- [269] A. H. Lettington, Applications of diamond-like carbon thin films, *Phil. Trans. R. Soc. London, A* 342 (1993) 287.
- [270] A. C. Evans, J. Franks and P. J. Revell, Diamond-like carbon applied to bioengineering materials, *Surf. Coat. Technol.* 47 (1991) 662.
- [271] D. Williams, Diamond-like carbons and other thin films, *Medical Device Technol.*, October (1993), p. 8.
- [272] E. Mitura, S. Mitura, P. Niedzielski, Z. Has, R. Wolowiec, A. Jakubowski, J. Szmidt, A. Sokolowska, P. Louda, J. Marciniak and B. Koczy, Diamond-like carbon coatings for biomedical applications, *Diam. Relat. Mater.* 3 (1994) 896.
- [273] A. Olborska and M. Swider, Amorphous carbon -biomaterial for implant coatings, *Diam. Relat. Mater.* 3 (1994) 899.
- [274] A. Bolz and M. Schaldach, Artificial heart valves: Improved blood compatibility by PECVD a- SiC:H coating, *Artificial Organs* 14 (1990) 260.
- [275] I. Dion, F. Rouais, L. Trut, C. Baquey, J. R. Monties and P. Havlik, TiN coating: Surface characterization and hemocompatibility, *Biomaterials* 14 (1993) 169.
- [276] I. Dion, X. Roques, C. Baquey, E. Baudet, B. B. Cathalinat and N. More, Hemocompatibility of diamond-like carbon coating, *Bio-Med. Mater. Eng.* 3 (1993) 51.
- [277] D. W. Howie and B. Verno-Roberts, Synovial macrophage response to aluminium-oxide ceramic and cobalt chrome alloy wear particles in rat, *Biomaterials* 9 (1988) 442.

- [278] D. W. Howie and B. Verno-Roberts, The synovial response to intra-articulate cobalt chrome wear particles, *Clinical Orthopaedics and Related Research* 232 (1988) 244.
- [279] N. Rushton and T. Rae, The intra-articulate response to particulate carbon fiber reinforced high-density polyethylene and its constituents-An experimental study in mice, *Biomaterials* 5 (1984) 352.
- [280] M. Choudhury, Tribological investigation of artificial knee-joints, University of Cambridge, Internal Report 1 (1995).
- [281] M. Allen, Diamond like carbon as wear retardant coating for arthroplasty components, PhD Thesis, Orthopaedic Research Unit, Addenbrookes Hospital, University of Cambridge, (1995).
- [282] M. Seal, High technology applications of diamond, in the properties of natural and synthetic diamond, J. E. Field (Ed.), Academic Press, London, (1992), p. 607.
- [283] Karl E. Spear, John P. Dismukes, Synthetic Diamond: Emerging CVD science and technology, John Wiley & Sons, Inc. New York, (1994), p.123.
- [284] J. C. Angus and F. Jansen, American Vacuum Society Meeting, Anaheim, CA, Nov.4, 1987, To appear in *J. Vac. Sci. Tech. A*, May-June (1988).
- [285] H. Guo and M. Alam, Strain in CVD diamond films: Effects of deposition variables, *Thin Solid Films* 212 (1992) 173.
- [286] L. Schafer and C.-P. Klages, Growth and properties of diamond films prepared by microwave plasma chemical vapour deposition using different oxygen containing source gases, *Surf. Coat. Technol.* 47 (1991) 13.
- [287] Fusao Shimokawa and Hiroki Kuwano, Energy distribution and formation mechanism of fast atoms in a fast atom beam, *J. Appl. Phys.* 72 (1) (1992) 13-17.
- [288] Fusao Shimokawa, High-power fast-atom beam source and its application to dry etching, *J. Vac. Sci. Technol. A* 10 (1992) 1352.
- [289] Kruzelecky R.V., Zukotynski S., In: Plasma properties deposition and etching, *Materials Science Forum*, Vol.89 Aedermanns dorf, Switzerland: Trans Tech, 1993, p.140-142.

- [290] D. Sarangi, O. S. Panwar, Sushil Kumar and R. Bhattacharyya, Characterisation of a saddle field fast atom beam source and its application to the growth of diamond-like carbon films, *Vacuum* 58 (2000) 609-627.
- [291] J. Franks, Preparation and properties of diamond like carbon films, *J. Vac. Sci. Technol. A* 7 (3) (1989) 2307.
- [292] A. H. McIlraith, 1965 British Patent No. 20592/65.
- [293] A. A. Voevodin, J. M. Schneider, C. Caperaa, P. Stevenson and A. Mathews, Studies of atom beam produced by a saddle field source used for deposition diamond-like carbon films on glass, *Vacuum* 46 (1995) 299-303.
- [294] A. A. Voevodin, J. M. Schneider, C. Caperaa, P. Stevenson and A. Mathews, Characterisation of a saddle field source for deposition of diamond-like carbon films, *Ceramics International* 22 (1996) 1-5.
- [295] Fusao Shimokawa and Hiroki Kuwano, New high-power fast atom beam source, *J. Vac. Sci. Technol. A* 12 (1994) 2739.
- [296] D. Sarangi, O.S.Panwar, Sushil Kumar, P.N.Dixit and R. Bhattacharyya, Filtered saddle field fast atom beam deposition of diamond like carbon films, *J. Vac. Sci. Technol. A* 16 (1998) 203-206.
- [297] D. Sarangi, O.S.Panwar, S. Kumar, and R. Bhattacharyya, Characterization studies of diamond-like carbon films growth using a saddle-field fast-atom-beam source, *J. Vac. Sci. Technol. A* 18 (2000) 2302-2311.
- [298] H. Kuwano and K. Nagai, Ion Mass Spectroscopy, SIMS iv, edited by A. Benninghoven, J. Okana, R. Shimizu and H.W. Werner, Springer, Berlin (1994) p.448.
- [299] D.P. Dowling, A.J.Betts, C. Pope, M.L.McConnell, R. Eloy and M.N Arnaud, Anti-bacterial silver coatings exhibiting enhanced activity through the addition of platinum, *Surface and Coatings Technology* 163-164 (2003) 637-640.
- [300] J. C. Tauc, *Optical Properties of Solids*, North-Holland, Amsterdam, (1972).
- [301] J. K. Walters, R. J. Newport, S. F. Parker and W. S. Howells, *J. Phys.:* *Condens. Matter* 7 (1995) 10059.
- [302] J. -P. Hirvonen, J. Koskinen, J. R. Jervis and M. Nastasi, Present progress in the development of low friction coatings, *Surf. Coat. Technol.* 80 (1996) 139.

- [303] M. I De Barros, L. Vandenbulcke, J. Fontaine, G. Farges, M. Vayer and R. Erre, Tribological performance of diamond-coated Ti-6Al-4V alloy with respect to diamond characteristics, *Surf. Coat. Technol.* 127 (2000) 193.
- [304] M. I. De Barros and L. Vandenbulcke, Plasma-assisted chemical vapor deposition process for depositing smooth diamond coatings on titanium alloys at moderate temperature, *Diam. Relat. Mater.* 9 (2000) 1862.
- [305] M. Zarrabian, N. Fourches-Coulon, G. Turban, M. Lancin and C. Marhic, Effect of negative bias voltage on a-C:H films deposited in electron cyclotron resonance plasma, *Diam. Relat. Mater.* 6 (1997) 542.
- [306] Y. Konishi, I. Konishi, N. Sakauchi, S. Hayashi, A. Hirakimoto and J. Suzuki, *Nucl. Instr. Meth. Phys. Res. B* 118 (1996) 312.
- [307] J. A. Mclaughlin, B.Meena, P.Maguire and N.Jamieson, Properties of diamond like carbon thin film coatings on stainless steel medical guidewires, *Diam. Relat. Mater.* 5 (1996) 486.
- [308] M. Hakovitra, Adhesion of amorphous diamond-like film on sputtered hard metal (WC—Co) cutting tools, *Diam. Relat. Mater.* 5 (1996) 186.
- [309] W. Heinke, A. Leyland, A. Matthews, G. Berg, C. Friedrich and E. Broszeit, Evaluation of PVD nitride coatings, using impact, scratch and Rockwell-C adhesion tests, *Thin Solid Films* 270 (1995) 431.
- [310] ASM Hand Book, ASM Int., Metals Park, Ohio, Vol. 18 (1992) 659.
- [311] A. M. Howatson, P. G. Lund and J.D. Todd, *Engineering tables and data*, 2nd edition, Chapman and Hall, London, (1991) 41.
- [312] H. Jehn, G. Reiners and N. Siegel (Eds.), *DIN Fachbericht 39, Charakterisierung dinner Schichten*, Beuth Vergin, Berlin, (1993).
- [313] C. J. McHargue, Diamond and Diamond-like film coatings, in: R. E. Clausing, L. L. Horton, J. C. Angus, P. Koidl (Eds.), *NATO ASI Series B 26*, Plenum, New York (1991) p. 363-375.
- [314] D. P. Dowling, K Donnelly, M. Monclous and M. McGuinness, The use of refractive index as a measure of diamon-like carbon film quality, *Diamond and Related Materials* 7 (1998) 432-434.
- [315] T. Chudoba, N. Schwarzer and F. Richter, Steps towards a mechanical modeling of layered systems, *Surface and Coating Technology*, 154 (2002) 140-151.

- [316] Gabriel Lazăr, Some peculiarities in ultraviolet absorption spectra for hydrogenated amorphous carbon thin films, *Materials Letters* 57 (2002) 586-588.
- [317] J. K. Walters and R. J. Newport, The atomic scale structure of amorphous hydrogenated carbon, *J. Phys.: Condens. Matter.* 7 (1995) 1755.
- [318] S. F. Yoon, K. H. Tan, Rusli, J. Ahn and Q. F. Huang, Effect of process pressure on diamond-like carbon deposited using electron cyclotron resonance chemical vapor deposition, *Thin solid Films* 396 (2001) 62.
- [319] S. Praver, K. W. Nugent, Y. Lifshitz, G. D. Lempert, E. Grossman, J. Kulik, I. Avigal and R. Kalish, Systematic variation of the Raman spectra of DLC films as a function of sp^2 : sp^3 composition, *Diam. Relat. Mater.* 5 (1996) 433.
- [320] D. Sheeja, B. K. Tay, X. Shi, S. P. Lau, C. Daniel, S. M. Krishnan and L. N. Nung, Mechanical and tribological characterization of diamond-like carbon coatings on orthopaedic materials, *Diamond and Related Materials* 10 (2001) 1043.
- [321] M. I De Barros, L. Vandenbulcke, J. Fontaine, G. Farges, M. Vayer and R. Erre, *Surf. Coat. Technol.* 127 (2000) 193.
- [322] M. I. De Barros and L. Vandenbulcke, *Diam. Relat. Mater.* 9 (2000) 1862.
- [323] M. Zarrabian, N. Fourches-Coulon, G. Turban, M. Lancin and C. Marhic, *Diam. Relat. Mater.* 6 (1997) 542.
- [324] Y. Konishi, I. Konishi, N. Sakauchi, S. Hayashi, A. Hirakimoto and J. Suzuki, *Nucl. Instr. Meth. Phys. Res. B* 118 (1996) 312.
- [325] M. M. Morshed, B. P. McNamara, D. C. Cameron and M. S. J. Hashmi, Stress and adhesion in DLC coatings on 316L stainless steel deposited by a neutral beam source, *Journal of Materials Processing Technology* 6779 (2003) 1
- [326] M. M. Morshed, B. P. McNamara, D. C. Cameron and M. S. J. Hashmi, Effect of surface treatment on the adhesion of DLC film 316L stainless steel, *Surface and Coatings Technology* 163-164 (2003) 541.
- [327] R. A. Nyquist and R. O. Kagel, *Handbook of infrared and Raman spectra of inorganic compounds and organic salts*, Vo. 4, Academic Press, San Diego, (1999).
- [328] M. Da Cunha Belo, M. Walls, N. E. Hakiki, J. Corset, E. Picquenard, G. Sagon and D. Noël, Composition, structure and properties of the oxide films formed on

the stainless steel 316L in a primary type pwr environment, *Corrosion Science*, Vol.40, No.2/3,(1998), p.447.

- [329] M. F. Montemor, M. G. S.Ferreira, N. E. Hakiki and M. Da Cunha Belo, Chemical composition and electronic structure of the oxide films formed on 316L stainless steel and nickel based alloys in high temperature aqueous environments, *Corrosion Science* 42 (2000) 1635.
- [330] K. J. Clay, S. P. Speakman, N. A. Morrison, N. Tomozeiu, W. I. Milne and A. Kapoor, Material properties and tribological performance of rf-PECVD deposited DLC coatings, *Diam Relat. Mater.* 7 (1998) 1100.
- [331] M. J. Fagan, *Finite Element Analysis: Theory and Practice*, John Wiley and Sons, New York (1991), ISBN 0-582-02247-9.
- [332] B. A. Boley and J. H. Weiner, *Theory of Thermal Stresses*, Dover Publications, New York (1997), ISBN 0-486-69579-4.
- [333] S. Moaveni, *Finite element analysis, Theory and Application with ANSYS*, Prentice-Hall, New Jersey, 1999.
- [334] T. Zhai, Y. G. Xu, J. W. Martin, A. J. Wilkinson and G. A. D. Briggs, A self-aligning four-point bend testing rig and sample geometry effect in four-point bend figure, *International Journal of Fatigue* 21 (1999) 889-894.
- [335] W. F. Riely and L. Zachary, *Introduction to Mechanics of Materials*, John Wiley, New York (1989) p. 274.
- [336] Urs I. Thomann and Peter J. Uggowitzer, Wear-corrosion behaviour of biocompatible stainless steels, *Wear* 239 (2000) 48.

Publications

The following publications/manuscripts resulted from this project:

Journals

1. M. M. Morshed, B. P. McNamara, D. C. Cameron and M. S. J. Hashmi, Stress and adhesion in DLC coatings on 316L stainless steel deposited by a neutral beam source, "*Journal of Materials Processing Technology*", Volume 141, Issue 1, 1 October 2003, Pages 127-131.
2. M. M. Morshed, D. C. Cameron, B. P. McNamara, and M. S. J. Hashmi, DLC films deposited by a neutral beam source: adhesion to biological implant metal, "*Surface and Coatings Technology*", Volumes 169-170, 2 June 2003, Pages 254-257.
3. M. M. Morshed, B. P. McNamara, D. C. Cameron and M. S. J. Hashmi, Effect of surface treatment on the adhesion of DLC film 316L stainless steel, "*Surface and Coating Technology*", Volumes 163-164, 30 January 2003, Pages 541-545.
4. M. M. Morshed, D. C. Cameron, B. P. McNamara, and M. S. J. Hashmi, Pre-treatment of substrates for improved adhesion of diamond like carbon films on surgically implantable metals deposited by saddle field neutral beam source, "*Surface and Coatings Technology*", Volumes 174-175, September-October 2003, Pages 579-583.
5. B. P. McNamara, H. Murphy and M. M. Morshed, Adhesion properties of diamond-like coated orthopaedic biomaterials, "*Diamond and Related Materials*", Volume 10, Issues 3-7, March-July 2001, Pages 1098-1102.

Refereed National/International Conference Proceedings

1. M. M. Morshed, D. C. Cameron, B. P. McNamara, and M. S. J. Hashmi, Implant Metal Coatings: DLC's Adhesive Value!, Proceedings of Bioengineering in Ireland (8) and The 16th Meeting of the Northern Ireland Biomedical Engineering Society - Joint conference, 26th & 27th January 2002, Sligo, Republic of Ireland, p 77.
2. B. P. McNamara, M. M. Morshed and H. Murphy, Adhesion properties of DLC coated orthopaedic biomaterials, Proceedings, 4th Annual Sir Bernard Crossland Symposium and Postgraduate Workshop at University College of Dublin, December 6-7, 2000, pp146-147.

Abstract of Oral Conference Presentation

1. M. M. Morshed, D. C. Cameron, B. P. McNamara, and M. S. J. Hashmi, Adhesion of DLC films deposited by a neutral beam source to biological implant metals, 11th Annual Conference of the Irish Plasma and Beam Processing Group in conjunction with the 10th Symposium on Fusion Research in Ireland hosted by The National Centre for Plasma science & Technology in Dublin City University, 6-7 September 2001.

Posters Presentation

1. M. M. Morshed, B. P. McNamara, D. C. Cameron and M. S. J. Hashmi, Diamond-like Carbon Films Deposited on Biomaterials, National Centre for Plasma Science & Technology, Dublin City University, 30th May 2001.
2. M. M. Morshed, B. P. McNamara, D. C. Cameron and M. S. J. Hashmi, Effect of surface treatment on the stress and adhesion of diamond-like carbon on 316L austenitic stainless steel, Presented at National Centre for Plasma Science & Technology Plenary Meeting on March 13, 2002.
3. M. M. Morshed, Halen Murphy and Brian P. McNamara, Improving Design Performance of Orthopaedic Biomaterials Through Application of DLC Coatings, Royal Irish Academy, National committee for Engineering Sciences, Engineering Design in an Academic Environment, Academy house, 19 Dawson St. Dublin-2, 12-13 October 2000.

APPENDIX A1

PERIODIC TABLE OF ELEMENTS

Group	1	2	3	4	5	6	7	8	9	10	11	12	13	14	15	16	17	18
Period																		
1	<u>1</u> <u>H</u>																	<u>2</u> <u>He</u>
2	<u>3</u> <u>Li</u>	<u>4</u> <u>Be</u>											<u>5</u> <u>B</u>	<u>6</u> <u>C</u>	<u>7</u> <u>N</u>	<u>8</u> <u>O</u>	<u>9</u> <u>F</u>	<u>10</u> <u>Ne</u>
3	<u>11</u> <u>Na</u>	<u>12</u> <u>Mg</u>											<u>13</u> <u>Al</u>	<u>14</u> <u>Si</u>	<u>15</u> <u>P</u>	<u>16</u> <u>S</u>	<u>17</u> <u>Cl</u>	<u>18</u> <u>Ar</u>
4	<u>19</u> <u>K</u>	<u>20</u> <u>Ca</u>	<u>21</u> <u>Sc</u>	<u>22</u> <u>Ti</u>	<u>23</u> <u>V</u>	<u>24</u> <u>Cr</u>	<u>25</u> <u>Mn</u>	<u>26</u> <u>Fe</u>	<u>27</u> <u>Co</u>	<u>28</u> <u>Ni</u>	<u>29</u> <u>Cu</u>	<u>30</u> <u>Zn</u>	<u>31</u> <u>Ga</u>	<u>32</u> <u>Ge</u>	<u>33</u> <u>As</u>	<u>34</u> <u>Se</u>	<u>35</u> <u>Br</u>	<u>36</u> <u>Kr</u>
5	<u>37</u> <u>Rb</u>	<u>38</u> <u>Sr</u>	<u>39</u> <u>Y</u>	<u>40</u> <u>Zr</u>	<u>41</u> <u>Nb</u>	<u>42</u> <u>Mo</u>	<u>43</u> <u>Tc</u>	<u>44</u> <u>Ru</u>	<u>45</u> <u>Rh</u>	<u>46</u> <u>Pd</u>	<u>47</u> <u>Ag</u>	<u>48</u> <u>Cd</u>	<u>49</u> <u>In</u>	<u>50</u> <u>Sn</u>	<u>51</u> <u>Sb</u>	<u>52</u> <u>Te</u>	<u>53</u> <u>I</u>	<u>54</u> <u>Xe</u>
6	<u>55</u> <u>Cs</u>	<u>56</u> <u>Ba</u>	* <u>71</u> <u>Lu</u>	<u>72</u> <u>Hf</u>	<u>73</u> <u>Ta</u>	<u>74</u> <u>W</u>	<u>75</u> <u>Re</u>	<u>76</u> <u>Os</u>	<u>77</u> <u>Ir</u>	<u>78</u> <u>Pt</u>	<u>79</u> <u>Au</u>	<u>80</u> <u>Hg</u>	<u>81</u> <u>Tl</u>	<u>82</u> <u>Pb</u>	<u>83</u> <u>Bi</u>	<u>84</u> <u>Po</u>	<u>85</u> <u>At</u>	<u>86</u> <u>Rn</u>
7	<u>87</u> <u>Fr</u>	<u>88</u> <u>Ra</u>	** <u>103</u> <u>Lr</u>	<u>104</u> <u>Rf</u>	<u>105</u> <u>Db</u>	<u>106</u> <u>Sg</u>	<u>107</u> <u>Bh</u>	<u>108</u> <u>Hs</u>	<u>109</u> <u>Mt</u>	<u>110</u> <u>Ds</u>	<u>111</u> <u>Uuu</u>	<u>112</u> <u>Uub</u>	<u>113</u> <u>Uut</u>	<u>114</u> <u>Uuq</u>	<u>115</u> <u>Uup</u>	<u>116</u> <u>Uuh</u>	<u>117</u> <u>Uus</u>	<u>118</u> <u>Uuo</u>
*Lanthanoids			* <u>57</u> <u>La</u>	<u>58</u> <u>Ce</u>	<u>59</u> <u>Pr</u>	<u>60</u> <u>Nd</u>	<u>61</u> <u>Pm</u>	<u>62</u> <u>Sm</u>	<u>63</u> <u>Eu</u>	<u>64</u> <u>Gd</u>	<u>65</u> <u>Tb</u>	<u>66</u> <u>Dy</u>	<u>67</u> <u>Ho</u>	<u>68</u> <u>Er</u>	<u>69</u> <u>Tm</u>	<u>70</u> <u>Yb</u>		
**Actinoids			** <u>89</u> <u>Ac</u>	<u>90</u> <u>Th</u>	<u>91</u> <u>Pa</u>	<u>92</u> <u>U</u>	<u>93</u> <u>Np</u>	<u>94</u> <u>Pu</u>	<u>95</u> <u>Am</u>	<u>96</u> <u>Cm</u>	<u>97</u> <u>Bk</u>	<u>98</u> <u>Cf</u>	<u>99</u> <u>Es</u>	<u>100</u> <u>Fm</u>	<u>101</u> <u>Md</u>	<u>102</u> <u>No</u>		

APPENDIX A2

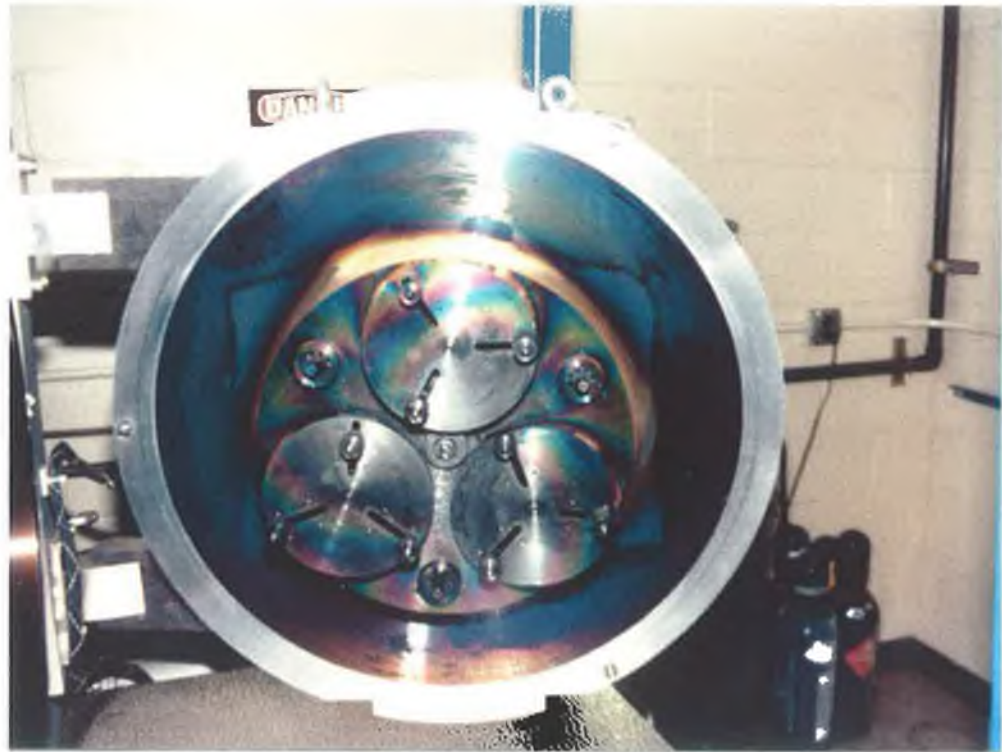


Figure A1: Planetary substrate holder (right hand side) attached to the door of DLC deposition system.

APPENDIX A3

Operation Procedure

- *Turn on* the water supply (inlet and outlet) to the chamber, diffusion pump and the source. Open all valves that control the flow of cooling water through the whole system.
- *Turn on* the air compressor to keep the air pressure at least 50 Psi.
- *Turn on* the electrical main switch. *POWER* button should be illuminated.

To pump down the chamber, it can be operate either manual or auto mode.

Pump down sequence

Auto

- *Turn on* the key switch to *AUTO* position.

Manual

- *Turn on* the key switch to *MANUAL* position.

“STOP” button should be illuminated.

- *Press “STAND-BY” button.*
 - *Press Roughing pump button*
 - *Press Diffusion pump button.*
 - *Press backing valve button.*
- Roughing pump and Diffusion pump come on. After six second, the Backing valve opens (after press the *STAND-BY* button the controller will automatically sequence the opening the appropriate valves. As a valve is opened or if pump is active, its corresponding button on the schematic flow diagram of the 624 controller will become illuminated).

Wait for an hour to allow the Diffusion pump oil to heat up. During the Diffusion pump oil warm up period, the parts or substrates that need to be coated should be prepared at this time. All substrate surfaces should be free of oil, grease and/or dust debris before being placed on the substrate holder (planetary) located on the inside of each chamber door (see figure A4). Before installing or affixing substrates to the planetary holder, *turn off* electrical power switch to the planetary motors located on the planetary motor control, which is in the middle of the instrument control cabinet panel.

Affix the pre-cleaned substrates to the holder (planetary) and close the chamber doors. Hand tightens the three clamping knobs on each door.

Turn on the planetary motor control power switch (optional). The motors will turn the planetary gears until they come to a reference position at which time the motors will stop. At this point the motor controls can be set for continuous rotation or time dwell rotations. All work can be performed to this point with the substrates in continuous rotation during the process.

- *Press* the “*START*” button on the 624 controller.
- Backing valve closes.
- Roughing valve opens. The Rotary and Roughing pump will start to pump down the chamber to a pressure of 8×10^{-2} mbar.
- The 624 controller will now close the Roughing valve, open the Backing valve between the diffusion and Rotary pump and after the proper Backing pressure has been reached, the valve to the chamber from the diffusion pump will open.
- *Press* Backing valve button to close the Backing valve.
- *Press* Roughing valve button to open the Roughing valve. The Rotary and Roughing pump will start to pump down the chamber to a pressure of 8×10^{-2} mbar.
- *Press* Roughing valve button to close the Roughing valve.
- *Press* Backing valve button to open the Backing valve.
- *Press* High vacuum valve button to open the high vacuum valve.

At this point the chamber pressure should be dropping at a very fast rate and within a couple of minutes at the starting operating point. The “*source enable light*” below the source power controller should be illuminated, which is the signal that all initiating operating parameters have been met and the system is now ready to run.

Before proceeding further, turn the three clamping knobs on each door counter clockwise. This must be performed now or the doors will be very difficult to open at the end of the coating run.

Process gas

Before starting the coating process, the process gas lines needed to be purged of all ambient gas and or water vapour that may have contaminated the gas supply line, which will interfere with the coating process and yield poor result.

Ensure that all process gases supplies (argon and acetylene) are acquit and at proper regulated pressures. Move the *Toggle switch* B95 REF on the 1105 controller from centre position to the up position. This will cause the in line air actuated gas control valve to open and allow gas to flow.

To regulate the gas flows, use the needle control valves, which are on the top right side of the chamber before each of the two mass flow meters. The gas flow for each gas type, either etch or coating must be regulated so that the chamber pressure is maintained in the range of 9×10^{-4} to 4.8×10^{-3} mbar.

Now push the “*Toggle switch*” down to the centre position and then down to the position labelled coating. At this point repeat the same steps used for the argon set up.

Power up source

Turn on the first circuit breaker (left side), which situated at the right hand side in the door of the electrical distribution box of the DLC system frame.

Etching

Move the *Toggle* and the *Gas control switch* to the position labeled etching. Allow gas (argon) to flow and the chamber pressure should rise to the pre-set range of 9×10^{-3} to 4.8×10^{-3} mbar. If the pressure is not in the correct range, adjust with needle valve if necessary.

Turn the current control knob fully counter clockwise as far as possible. The range selection switch should be on the 2A position.

Press the *ON* button located in the middle of the source power controller panel.

Slowly turn the current control knob clockwise till the current analogue meter is reading the required Ampear for the process. Keep as long as need to etch the substrate.

After complete etching, turn the current control knob fully counter clockwise as far as possible and then press *OFF* button located in the middle of the source power controller panel.

Coating

Move the *Toggle* and the *Gas control switch* to the position labeled coating. Allow gas (acetylene) to flow and the chamber pressure should rise to the pre-set range of 9×10^{-3} to 4.8×10^{-3} mbar. If the pressure is not in the correct range, adjust with needle valve if necessary.

Press the *ON* button located in the middle of the source power controller panel.

Slowly turn the current control knob clockwise till the current analogue meter is reading the required Ampear for the process. Keep as long as need to coat the substrate.

Terminating the Coating Process

Upon the completion of the coating process, *switch off* the coating gas by moving the *Toggle* and *Gas control switch* to the middle position.

Turn the current control knob fully counter clockwise as far as possible and push the "*OFF*" button in the middle of the source power controller panel.

Turn off the main electrical circuit breaker for the source.

To open the chamber

Auto

Press the *STAND-BY* button on the 624 control panel (High vacuum valve will close).

Manual

Press High vacuum valve button to close the high vacuum valve.

Open the doorknobs and ensure that they are fully opened.

Press "*VENT*" button to allow the nitrogen in to the chamber (make sure nitrogen valve on wall is opened). Allow the chamber pressure to ambient atmospheric pressure for opening the doors.

System Shut Down

Either press the *DIFF COOL* button to cool the diffusion pump or replace new substrates in the chamber and press start (auto mode) or manually pump down the chamber. When *DIFF COOL* button is pressed, automatically turn off the Diffusion pump but the Rotary pump and Roots blower will continue to operate for another hour. After the one hour cool down period the 624 controller will turn off the Rotary and Roots.

At this time the cooling water, compressed air, argon, acetylene and nitrogen gas valves can be shut off.

To off the system, turn key switch on the 624 control panel to the off position.